On
Pressure-Actuated Cellular Structures

Bei der Fakultät für Maschinenbau
der Technischen Universität Carolo-Wilhelmina zu Braunschweig

zur Erlangung der Würde

eines Doktor-Ingenieurs (Dr.-Ing.)

genehmigte Dissertation

von:	Dipl.-Ing. Benjamin Gramüller
aus:	Ingolstadt

eingereicht am:	09. Juni 2016
mündliche Prüfung am:	19. September 2016

Gutachter:	Prof. Dr.-Ing. Christian Hühne
	Prof. Dr.-Ing. Horst Baier

2016

Abstract

The herein presented investigations address the implementation of a holistic design process for *Pressure-Actuated Cellular Structures* (PACS) and include their realization and characterization. Similar to the motion of nastic plants, the actuation principle of these biologically inspired shape-variable structures bases on the controlled expansion of pressurized volumes. The advantages of fluidic actuation are combined with an adaptive single-curved structure that deforms continuously and with controllable stiffness between predefined states of shape. Benfits from the utilization of such a structure are expected within the fields of aeronautical, automobile, power and civil engineering.
The herein presented research bases on the so far purely theoretical investigations of Pagitz et al. [1]. Their work covers the description of the functional principle, the implementation of a numerical structural model, an approach for the shape-optimization procedure and the identification of structural characteristics. The preceding studies are limited to the numerical simulation on the basis of two-dimensional truss-structures. The effects of model assumptions and the validity of the underlying methods are so far not evaluated. Some substantial structural subsystems are not yet described or identified and their influence on the overall structure is not examined.

The identification of open issues, the development and the validation of design methods, as well as the evaluation of the performance of the concept of PACS are realized in consideration of the holistic system. A substantial aspect of the herein presented procedure is the verification of these methods for different system levels by numerical simulation and experimental examination of functional models at an early stage. The following core issues are addressed:
An alternative structural model is developed that provides a high grade of flexibility for the adaption of model assumptions and structural boundary conditions. It is used for the issue of shape optimization, for the computation of the highly geometrical nonlinear deformations and for the stress analysis. With utilizing the approach of virtual work (AVW), the influence of model assumptions on the deformation accuracy and on the computational efforts can be determined. Examinations about the deformation behaviour, the resulting structural stresses and ultimately the operational envelope are thereby performed. The shape-optimization process, which bases on the same structural model, profits from the model's expandability for external forces and allows for the consideration of external loads. The target deformation can thus be reached also under the influence of specifiable load conditions. Following this, the implementation of an approach for the automated load-based design of the PACS's cross section allows reducing structural stresses and deviations of deformation. A novel concept for sealing the shape-variable structure allows increasing the PACS's performance due to its low rigidity and the load-based design. It is described together with the underlying methods for the computation of the cell closure's shape. Conceptual limitations due to the manufacturing and assembly processes are identified. The investigation of alternative production processes for PACS and the development of the selected variants allow for the reduction of these limitations. In order to verify and improve the design methods, numerical and experimental investigations are performed at the subsystem level. The combination of partial solutions to a holistic design process for PACS allows for the realization of a fully-functional test specimen and thus for the experimental validation of the entire system
A holistic solution for the design of PACS is successfully implemented and applied for the profound investigation on an experimental basis. The foundation for the evaluation and utilization of such shape-variable structures is thus laid.

Kurzfassung

Die nachfolgenden Untersuchungen befassen sich mit der Entwicklung eines ganzheitlichen Entwurfsprozesses für *Druckaktuierte Zelluläre Strukturen* (PACS, engl.: Pressure-Actuated Cellular Structures), sowie deren Realisierung und Charakterisierung. Ähnlich dem Vorbild nastischer Pflanzen, basiert das Antriebsprinzip dieser biologisch inspirierten formvariablen Strukturen auf der Ausdehnung druckbeaufschlagter Volumina. Die Vorzüge fluidischer Aktuierung lassen sich dabei auf eine einfach gekrümmte Struktur übertragen, welche sich stufenlos und mit kontrollierbarer Steifigkeit zwischen spezifizierbaren Formzuständen deformieren lässt. Potentiale aus der Nutzung einer solchen Struktur ergeben sich unter anderem für die Bereiche Luftfahrt, Automobil- und Energietechnik sowie Bauwesen.
Die hier vorgestellten Forschungsinhalte knüpfen an die bislang rein theoretischen Untersuchungen von Pagitz et al. [1] an. Die Beschreibung des Funktionsprinzips der PACS, die Implementierung eines numerischen Strukturmodells und eines Ansatzes zur Formoptimierung, sowie die Ermittlung der Struktureigenschaften wurden darin erstmals behandelt. Die vorangegangenen Arbeiten beschränken sich auf die numerische Simulation auf Basis zweidimensionaler Fachwerke, wobei die Einflüsse von Modellannahmen nicht untersucht, sowie die Gültigkeit zugrundeliegender Methoden bislang nicht nachgewiesen wurden. Einige wesentliche Subsysteme wurden bisher weder beschrieben noch identifiziert und deren Einflüsse auf das Gesamtstrukturverhalten sind nicht untersucht.

Die Identifikation offener Problemfelder, die Entwicklung und Validierung von Entwurfsmethoden, sowie die Bewertung der Leistungsfähigkeit des Konzeptes der PACS erfolgen in dieser Arbeit über eine ganzheitliche Systembetrachtung. Ein wesentlicher Bestandteil der hierin umgesetzten Vorgehensweise ist die frühzeitige Überprüfung der Entwurfsmethoden anhand numerischer und experimenteller Untersuchungen auf unterschiedlichen Systemebenen. Die folgenden Kernthemen werden dabei behandelt:
Ein alternatives Strukturmodell wird entwickelt, welches eine hohe Flexibilität gegenüber der Adaptionen von Modellannahmen und strukturellen Randbedingungen aufweist. Dieses wird zur Formoptimierung, zur Berechnung hochgradig geometrisch nichtlinearer Deformationen, sowie zur Beanspruchungsanalyse verwendet. Unter Verwendung des Prinzips der virtuellen Arbeit kann damit der Einfluss von Modellannahmen auf die Genauigkeit und den Berechnungsaufwand der Struktursimulation bestimmt werden. Untersuchungen zum Deformationsverhalten, zu den resultierenden strukturellen Belastungen und letztlich zur Leistungsfähigkeit der formvariablen Struktur werden damit ermöglicht. Der ebenfalls auf dieses Modell zurückgreifende Formoptimierungsprozess erlaubt durch eine Erweiterung zur Berücksichtigung externer Kräfte und Momente das Erreichen vorgegebener Zieldeformationen auch unter Lasteinwirkung. Ein daran anknüpfender Detailentwurf, welcher auf der Bestimmung lokaler Deformationen und Lastverläufe basiert, ermöglicht die Reduktion von Spannungen und Deformationsabweichungen. Ein neuartiges Konzept zur Abdichtung druckbeaufschlagter formvariabler Strukturen verhindert durch eine geringe Eigensteifigkeit und beanspruchungsorientierte Formgebung die Limitation des Deformations-potentials der Zellstruktur. Die Zellverschlusslösung wird zusammen mit den zugrundeliegenden Berechnungsmethoden beschrieben. Fertigungs- und montagebedingte Randbedingungen werden identifiziert. Zur Verifikation und Verbesserung von Entwurfsmethoden werden numerische und experimentelle Untersuchungen auf Subsystemebene durchgeführt. Die Zusammenführung der Teillösungen zu einem ganzheitlichen Entwurfsprozess für PACS erlaubt die Realisierung von Teststrukturen und damit die experimentelle Validierung des Gesamtauslegungsprozesses.
Das Konzept der PACS kann durch den Aufbau eines ganzheitlichen Entwurfsprozesses erstmals fundiert und auf experimenteller Basis untersucht werden. Die Grundlagen zur Bewertung und Nutzung solcher formvariabler Strukturen sind damit geschaffen.

Preface

This thesis is accomplished at the department of Composite Design as part of the Institute of Composite Structures and Adaptive Systems at the German Aerospace Center (DLR) in Braunschweig. Airbus Defence and Space supported this research, which is part of the project Sagitta, with resources and large expertise. The productive cooperation with the participating research institutes allowed handling and overcoming even complex and interdisciplinary issues. The excellent teamwork and support is gratefully acknowledged.

The completion of this work is made possible only by the valuable support of great supervisors, advisors, colleagues and friends. In particular, I would like to thank:

Prof. Dr.-Ing. Christian Hühne, Institute of Adaptronics and Function Integration (iAF) at the Technical University Braunschweig and department head Composite Design (FA-FLB), DLR, for providing the opportunity to work on this innovative field of research, for the competent supervision, for the professional support and the assistance in the context of and beyond this thesis.

Prof. Dr.-Ing. Horst Baier, director of the Institute of Lightweight Structures (LLB) at the Technical University Munich, for the great preparation during studies and for assuming the supervision as second examiner.

Prof. Dr.-Ing. Michael Sinapius, director of the Institute of Adaptronics and Function Integration at the Technical University Braunschweig for being chairman of the examination board.

Prof. Dr.-Ing. Martin Wiedemann, director of the Institute of Composite Structures and Adaptive Systems, DLR, for critical observations and inspiring discussions.

Dr.-Ing. Jost Seifert, Dr.-Ing. Roland Lang, Airbus Defence and Space, and Michael Hanke, DLR, for mentoring and assistance within the framework of Sagitta.

Dr. Markus Pagitz, for providing a valuable preparatory work and motivation.

The students, which contributed to this work with great enthusiasm and professional approach, in particularly Alfred Tempel, for his work on the cell closure concepts and Johannes Boblenz, for the sustaining efforts with realizing the first PACS demonstrator.

Jochen Schmidt, my office colleague, for the friendly teamwork and numerous helpful discussions not only about manufacturing issues and Dr.-Ing. Hardy Köke, my valuable contact partner in terms of research issues, for his persistent support and clear words.

Eva, for her incredible generosity and tolerance, my parents, for their faith in me, my brothers and my friends, who complement my yang with the necessary yin.

This work is devoted to my deceased friend and brother Matthias Gramüller.

Braunschweig, September 2016

"You have power over your mind
- not outside events.
Realize this, and you will find strength."
Marcus Aurelius

Contents

List of Symbols

Symbol	Unit	Description
a	[mm]	Cell side length
$\boldsymbol{a}$	[mm]	Vector of cell side lengths
c	[Nmm]	Rotational hinge stiffness
c_{CL}	[m]	Chord length of wing profile
d	[mm]	Depth of structure
e	[mm]	Distance between flexure hinge and chord line
f	[N], [Nmm]	Scalar potential (translational / rotational)
$\boldsymbol{f}$	[N], [Nmm]	Potential vector (translational / rotational)
g	[mm/s²]	Gravitational acceleration
h	[-]	Number of cell row
h_{cat}	[mm]	Height of catenoid
i	[-]	Number of cell
j	[-]	Number of hinge or cell side
k	[-]	Position scalar
k_A	[-]	Tightening factor for seal design
$\boldsymbol{k}$	[-]	Position vector
l	[mm]	Length of element
m	[t]	Mass
n	[-]	Number of cells per cell row
n_m	[mol]	Amount of substance
p	[MPa]	Pressure
p_{int}	[MPa]	Internal cell pressure
$\boldsymbol{p}$	[MPa]	Pressure vector
q	[N/mm]	Line load
r_{cat}	[mm]	Radius of catenoid
r_H	[mm]	Radius of flexure hinge
r_{isot}	[mm]	Radius of isotensoid cell closure
$\boldsymbol{r}$	[N/mm]	Vector of cell-side-perpendicular displacement
$\boldsymbol{r}_{VM}$	[rad]	Residual shape vector
s	[mm]	Hinge length
t	[mm]	Thickness
t_{WT}	[s]	Wall-clock time
t_{opt}	[mm]	Optimal hinge thickness
$t_{NACA\ 0012}$	[mm]	Thickness of aerodynamic profile NACA 0012
u	[rad]	Angle between adjacent cell sides of a cell
u_c	[rad]	Angle of hinge element
u_ζ	[rad]	Angle of hinge crossover element
$\boldsymbol{u}$	[m/s]	Vector of rotational DOFs of hinges
v	[m/s]	Airspeed
w	[mm]	Plate deflection
$\boldsymbol{w}$	[-]	Mixed vector of design variables for shape optimization
x	[mm]	Displacement
$\boldsymbol{x}$	[-]	Vector of hinge coordinates
z	[-]	Iteration step

Symbol	Unit	Description
A	[mm²]	Cross-sectional area
C_D	[-]	Drag coefficient
C_L	[-]	Lift coefficient
D	[mm]	Diameter
$\boldsymbol{D}$	[-]	Deformation gradient
E	[GPa]	*Young*'s modulus
F	[N]	Force
F_{cl}	[N]	Clamping force for seal
F_{op}	[N]	Operating force for seal
G	[GPa]	Shear modulus
H	[J]	Enthalpy
$\boldsymbol{H}$	[-]	*Hessian* matrix
I_z	[mm^4]	Second moment of inertia (z-direction)
K	[N/mm], [Nmm/rad]	Stiffness (translational, rotational)
$\boldsymbol{K}$	[-]	Stiffness matrix
L	[N]	Aerodynamic lift force
M	[Nmm]	Momentum
N	[N]	Axial force
PF	[-]	Pressure factor
Q	[N]	Transverse force
R	[MPa]	Material strength
R_m	[J/molK]	Universal gas constant
Re	[-]	Reynolds number
S	[N/rad], [Nmm/rad²]	Sensitivity to change of cell side lengths and hinge angles
$\boldsymbol{S}$	[-]	Sensitivity matrix
SF	[-]	Safety factor
$\mathcal{S}$	[J/K]	Entropy
T	[K]	Temperature
U	[J]	Inner energy
V	[mm³]	Volume
W	[J]	Work

Symbol	Unit	Description
α	[rad]	Angle
α_{AoA}	[°]	Angle of attack
β	[°]	Maximum deflection of PACS
ε	[-]	Structural strain
ζ	[mm]	Hinge eccentricity
η	[%]	Relative deviation
θ	[rad]	Orientation of acceleration
κ	[1/mm]	Hinge curvature
κ_A	[-]	Reduction factor for seal design
ν	[-]	*Poisson*'s ratio
ν_∞	[m²/s]	Kinematic viscosity
ξ	[m/s]	Hinge orientation
Π	[J]	Potential energy
$\boldsymbol{\Pi}$	[-]	Potential energy matrix
ρ	[t/mm³]	Density
σ	[MPa]	*Cauchy* stress
σ_P	[MPa]	Principal stress
σ_{vM}	[MPa]	Equivalent stress
$\boldsymbol{\sigma}$	[MPa]	*Cauchy* stress tensor
τ	[MPa]	Adhesive shear stress
φ	[rad]	Degree of curvature
ψ	[-]	Ratio of longitudinal stiffness
ϕ	[mm]	Potential factor

Operators	Description
d	Integral operator
δ	Virtual differential amount
∂	Differential operator
Δ	Differential amount

Superscripts	Description
$\dot{(\,)}$	First derivative
$\ddot{(\,)}$	Second derivative
$(\,)^*$	Value at maximum effective overlap length of bonding

Subscripts	**Description**
$()_0$	Initial state
$()_\infty$	Ambient conditions
$()_{ad}$	Aerodynamic-load-related parameters
$()_{ana}$	Analytically computed value
$()_{ax}$	Axial component
$()_b$	Bending component
$()_c$	Hinge-stiffness-related parameter
$()_e$	Vector index
$()_{equil.}$	Equilibrium state
$()_{exp}$	Experimental value
$()_{in}$	Inertial-load-related parameters
$()_{hys}$	Hysteresis
$()_{isot}$	Isotensoid parameters
$()_l$	Cell side lateral value
$()_{le}$	Linear elastic value
$()_{max}$	Maximum value
$()_{min}$	Minimum value
$()_n$	Cell side normal value
$()_p$	Pressure-related parameters
$()_{pl}$	Point-load-related parameters
$()_{st*}$	Target state of shape *
$()_t$	Target value
$()_{thk}$	Thickness value
$()_{tot}$	Total value
$()_z$	Value at iteration step z
$()_A$	Autoclave process parameter
$()_{AC}$	Actual configuration
$()_B$	Beam parameter
$()_{Bar}$	Bar parameter
$()_{Bolt}$	Bolt parameter
$()_C$	Cohesive
$()_{CC}$	Cell closure parameter
$()_{CS}$	Cell side parameter
$()_{DSEC}$	DSEC parameter
$()_{FEM}$	FEM based value
$()_H$	Hinge parameters
$()_{Hex}$	Hexagonal cell parameter
$()_{OV}$	Overdriven DSEC parameter
$()_{Pent}$	Pentagonal cell parameter
$()_{RC}$	Reference configuration
$()_{SO}$	Shape-optimization parameter
$()_{Var*}$	Model variant *
$()_{VM}$	Approach of volume maximization
$()_{VW}$	Approach of virtual work
$()_{WC}$	Water cutting parameter
$()_{\emptyset}$	Average value

List of Acronyms

Acronym	Description
AFTI	Advanced Fighter Technology Integration
APDL	Ansys Parametric Design Language
AVM	Approach of volume maximization
AVW	Approach of virtual work
CAcD	Cellular Actuator Device
CAD	Computer-Aided Design
CFD	Computational Fluid Dynamics
CRC	Compliant Rib Cap
CRTEF	Controllable Rubber Trailing Edge Flap
CSA	Cross-sectional area
DARPA	Defence Advanced Research Projects Agency
DLR	German Aerospace Center
DOC	Direct operating costs
DOF	Degree of freedom
DP	Design point
DSEC	Deformation Supportive End Cap
DSEC_OV	Overdriven DSEC
EDM	Electrical discharge machining
EMsFEM	Extended Multiscale FEM
EPDM	Ethylene Propylene Diene Rubber
ERI	Extension-regulated isotensoid
FDM	Fused deposition modeling
FEM	Finite Element Method
FMC	Flexible Matrix Composites
FRP	Fibre-reinforced plastic
GFRP	Glass-fibre reinforced plastic
IGES	Initial Graphics Exchange Specification
IRC	Isotensoid Rib Cap
LBC	Load and boundary condition
MAS	Morphing Aircraft Structures
MAW	Mission Adaptive Wing
MFC	Macro Fibre Composites
NASA	National Aeronautics and Space Administration
NBR	Nitrile Butadiene Rubber
NRA	Non-reinforced area
PACS	Pressure-Actuated Cellular Structure
PAH	Pressure Adaptive Honeycomb
PAM	Pneumatic Artificial Muscle
PVC	Polyvinylchloride
PZT	Lead-zirconate-titanate
RCS	Radar cross section
RMS	Root mean square
SLA	Stereolithography
SLM	Selective laser melting

Acronym	**Description**
SMA	Shape memory alloy
SMP	Shape-memory polymers
STEP	Standard for the Exchange of Product Model Data
UAV	Unmanned aerial vehicle
URS	Updated Reference Strategy
VCCTEF	Variable-camber Continuous Trailing Edge Flap

1 Introduction

1.1 Problem definition and approach to solution

Shape-variable structures open up new potentials for a variety of applications. Active and passive concepts can be found in the literature, which allow for the controlled adaption of a structure's geometry. Conventional rigid structures are thereby substituted by representatives, which provide the possibility to reach even complex target shapes or allow for variable stiffness and damping properties. Highly integral implementations dissolve the differentiation between actuator, converter and structure and provide lightweight and energetically efficient solutions. The possibility to control the shape of a structure and thus to influence the interaction of structure and environment allows improving existing kinematical concepts and gives rise to completely new functionalities.
The research on shape-variable structures and on its utilization as an aerodynamic surface in aeronautical applications in particular is of high interest, as these structures hold promising advantages like the expansion of the flight envelope, efficiency increase and operating cost reduction. Nevertheless practical implementations of such concepts are still rare and primarily realized at military aircrafts. Barriers for such a realization are the increased system complexity, the need for certification, the additional weight, production costs and energy consumption. One of the very first concepts for wing-camber morphing is the Aeroplane Wing from Kientz [2], which was patented in 1931. Figure 1-1, left, depicts the working principle of this concept that allows controlling the profile's thickness and camber. In the right depiction, the F-14 Tomcat, which is in operation since 1974, is illustrated with its variable-sweep-wing mechanism that enables an expansion of the flight envelope [3].

In adavance of the herein presented research work a novel, highly integral and lightweight concept, which provides huge power density and actuation strain, is investigated theoretically. With *Pressure-Actuated Cellular Structures* (PACS), the biologically successful mechanism of the Venus flytrap's moveable trapping leaves is transferred to a technically useable concept. The outcomes of the preliminary examinations of Pagitz et al. [1] are auspicious and yield the potential to overcome present barriers.
Although an important step towards the principle design and analysis of PACS is already done by Pagitz et al., the effects of the underlying assumptions and simplifications are not investigated sufficiently to verify the concepts feasibility. Questions regarding the functional envelope, the load capacity and deformation capability are unanswered and essential subsystems are not even approached. Before the transfer of the theoretical results to a three-dimensional structural design, the realization and the experimental evaluation of PACS can be processed, fundamental issues have to be solved.

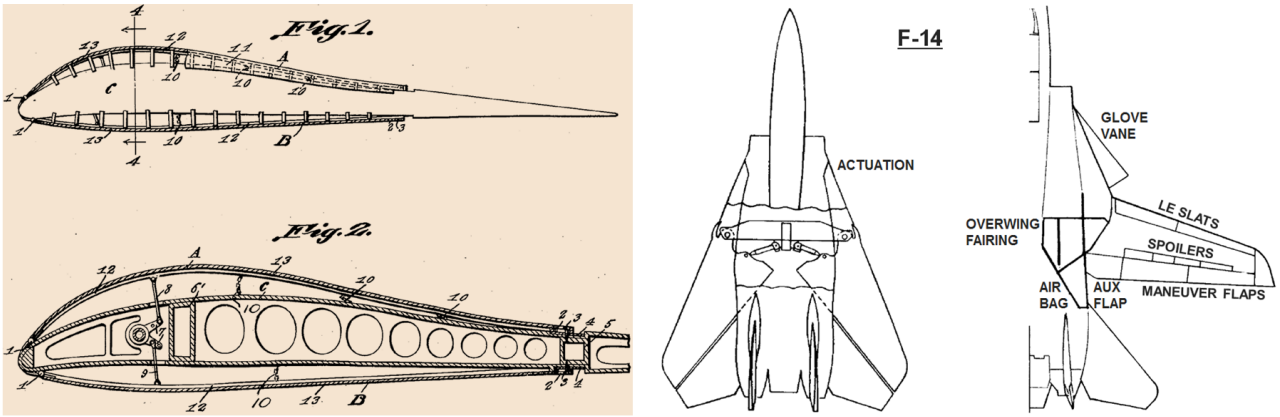

Figure 1-1: The Aeroplane Wing from Kientz, for the realization of a variable-camber wing (l.) [2]; and variable-sweep wing and actuation mechanism of F-14 Tomcat (r.) [3]

For the verification of the concept's theoretically investigated performance, PACS are dimensioned, realized and experimentally tested for the first time. The influence of the design methods, of the underlying assumptions and of not yet investigated sub-components on the concept can thus be evaluated. An iterative process is implemented, which allows for the progressive improvement of methods and helps identifying and eliminating reasons for losses of accuracy and performance. To control complexity, this process is performed at different subdivision levels, for each sub-system and for the complete design process. Relations between the structural components and also among consecutive design steps are identified.
The enhanced methods for the dimensioning of all sub-systems are combined to a toolchain for the holistic design of PACS. The full and evaluated transfer of the fundamental bio-inspired mechanism to a technically utilizable structure is thus performed for the first time. The adequacy of the design process and the underlying methods is verified by numerical investigations and experimental tests.

The introductory chapter is divided into four segments. Starting with the already presented problem definition and the approach to solution, the motivation for this work on PACS is elucidated secondly. A definition of morphing structures is given before potentials and challenges with this technology are identified. The advantages of PACS within this field give reasons for the recent research activities. Third, a brief summary of the state-of-the-art points out the relevance of the research on morphing structures. Novel high potential ideas and already realized structures, which are partially characterized in wind tunnel experiments or even proven in flight tests, are classified according to their actuation principle. The thematic classification into the research environment and the summary of research activities on PACS are essential contents of this section. Fourth, the objectives of this thesis are pointed out in detail, following the identified demands. An outline of the investigated contents is presented subsequently.

1.2 Motivation for this work on morphing structures

A definition of "Morphing structures" is provided first, before the general potentials and challenges with such a technology are identified.

1.2.1 Definition of "Morphing structures"

In advance of this work on a specific kind of morphing structure, a reliable definition shall delimit the relevant concepts. For aeronautical application, the difference between a morphing, adaptive, smart or active structure and a conventional one is so far defined in different ways. An aircraft wing with conventional slats and flaps for controlling lift forces and moments is not classified as a morphing structure, although these devices enable to change the wing's shape and thus to vary the pressure distribution, its lift and drag in wide range. The following definitions are individual attempts to differentiate between conventional and morphing structures.
The morphing aircraft is defined by Seigler [4]. He characterizes such structures as "flight vehicles that change their shape to effectuate either a change in mission and/or to provide control authority for manoeuvring, without the use of discrete control surfaces or seams." McGowan et al. [5] postulates that "conventional airplanes are generally optimized with a bias towards a single [design point]", whereas "morphing vehicles are optimized for multiple [design points]". Similarly, Weisshaar [6] defines morphing aircrafts as "multi-role aircrafts that change their external shape substantially to adapt to a changing mission environment during flight". Besides these expositions, a widely recognized und uniform definition for morphing aircraft structures is not available.

The combination of the referenced descriptions of aeronautical morphing structures with an approach for general usage, including ground-based implementations, can lead to the following definition:

A morphing structure for general application extends the capabilities of rigid structures by the ability to release specific translational or rotational structural degrees of freedom (DOFs) in discrete or distributed manner in order to achieve specified shape variations.

Shape-changing skins in the automotive sector, soft robots, which are addressed in medical and robotic research and multi-stable fibre-reinforced plastics (FRP) for adaptive winglets, are included by this definition of morphing structures. Hinge-based conventional slats and flaps of an aircraft wing are considered as well as mechanisms for varying the sweep of a wing (see Figure 1-1, right). Additional limitations that supplement the given definition allow specifying the regarded branch of morphing structures. Frequently used categories thereby distinguish between target application, actuation principles, deformation mechanism, amplitude und frequency of the shape variation and types and amount of DOFs that can be modified.

1.2.2 Need for improvement

The design of conventional structures is usually driven by two groups of requirements. The first one is of programmatic manner, ensures economic success and holds general demands like low costs, high quality and reduced development and manufacturing expense. As a second group, structural demands with reference to structural mechanics are determined by the expected loads and in addition by geometrical requirements. As these needs are also valid for shape-variable structures, they have to withstand the design loads and simultaneously ensure to keep deformations in a tolerable range. In addition to these general demands, the development and implementation of an effective morphing structure requires to overcome additional challenges.
Each actuator or active shape-variable structure can be divided in two functional elements, the energy adjusting element (e.g. compressor), which transforms energy (e.g. electrical energy) from the auxiliary energy source into a usable energy form (e.g. pressure and volume) and the energy converter, that modifies the received energy in order to obtain the desired energy driven effects (e.g. deformation) [7]. Each of these elements and their sub-elements own a particular efficiency coefficient, which has to be as high as possible and affects the overall power demand of the active structure. Together with the increased complexity the power demands and the additional weight of the energy converter, the adjusting element and the peripheral sub components like wiring, the first basic problem about shape-variable active structures appears. It can be condensed to the 1st challenge on shape-variable structures, specifying the general demand:

1st basic challenge: *The development and implementation of a concept for morphing structures is only reasonable if the anticipated benefit outweighs the invested efforts.*

Moreover, morphing structures are usually accompanied by risen system complexity, and the related additional sources of error (see Figure 1-2). Airborne-specific challenges like the certification process complicate the launch of novel structural solutions and mechanisms especially when safety critical components are involved. An increase of maintenance efforts, which affects the life-cycle costs unfavourably, can disqualify an otherwise valuable concept.

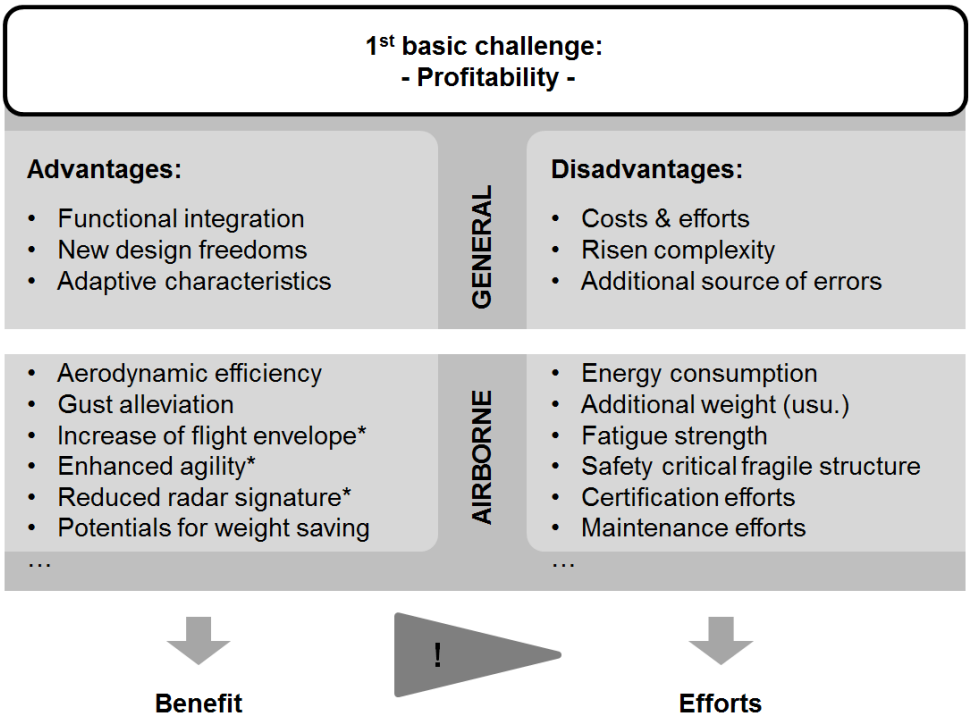

Figure 1-2: Challenge of creating profitable morphing structures, (*) indicates military application

The reason for the highly increasing research efforts on morphing structures (cf. Figure 1-7) lies in the diverse fields of potential advantages. Functional integration enables to combine actuator, converter and structure in an advantageous composition to substitute redundant components. As an enabling technology that provides new design freedoms for novel structures and tools, the morphing structures cover unsatisfied desires regarding adaptive shape and stiffness. New possibilities regarding design aspects are attractive and promotionally effective features for the architecture and the automotive industry, as the concept car *BMW GINA Light Vision* [8] demonstrates. Substantial advantages for airborne applications are presented in the following.

Aerodynamic benefits

The impact of a variable-camber morphing structure on the aerodynamic efficiency is investigated by Szodruch [9] with respect to civil transport aircraft for transonic flight. As depicted in Figure 1-3 an increase of the lift-to-drag ratio of 9 % and of the maximum lift coefficient of 12 % can be reached theoretically. With the reduction of drag, the enhanced aerodynamic efficiency leads to reduced fuel consumption and increasing endurance, which is evaluated by Gano [10] for a NACA 23015 profile to be +22.0 %. The flight envelope is expanded by over 25 % [11] due to the increased maximum lift value. Especially military aircrafts profit from a reduced turn radius and roll rate. Additional cost savings result from the operational flexibility of a variable-camber wing. Regarding this, development, manufacturing and maintenance costs can be reduced, when several aircrafts within a product line are equipped with the same wing [12]. The substitution of conventional control surfaces by a mechanism which additionally allows a variation of the camber in spanwise direction enables load control. A root bending moment reduction of $13 - 24$ % [13] can be achieved. The suitability for manoeuver load reduction is successfully verified in flight tests with an *F-111 Aardvark* by Thornton [14]. The benefits of pressure-actuated structures with regard to gust alleviation are further described in [15]. A detailed numerical and experimental aerodynamic study by Breitsamter [16] at the exemplary military aircraft structure of the canard-delta wing type *Eurofighter Typhoon* provides similar results for a variable trailing edge flap. A reduction of dynamic loads at the blade root of a wind turbine is measured by Madsen et al. [17].

Tani et al. [18] and Ai et al. [19] investigated the effects of shape-variable trailing edge flaps on noise emission. A noise reduction of up to 6 dB resulted for their morphing concept.

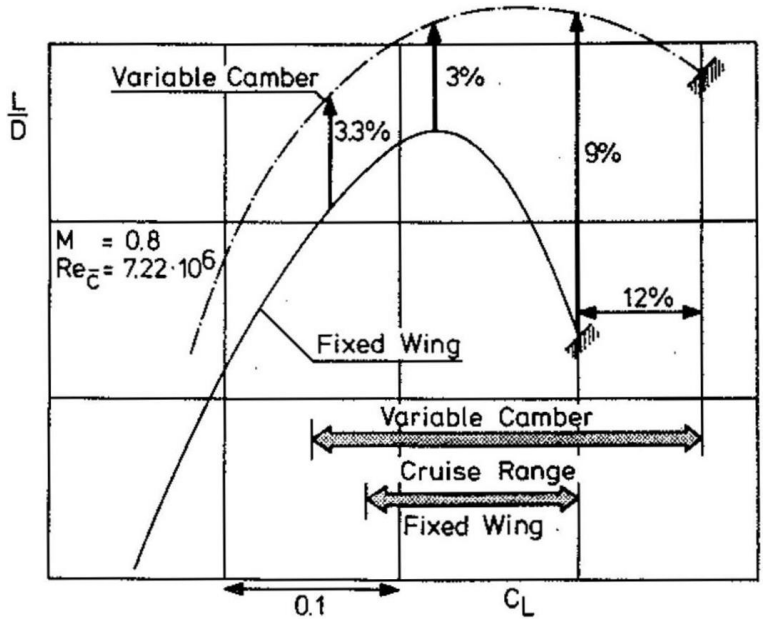

Figure 1-3: Influence of variable caber on lift-to-drag ratio [9]

Influence on radar signature

According to Knott et al. [20], the radar cross section (RCS) or the backscatter characteristic of a body or target scanned by radar beam results from the interaction of six mechanisms. Radar echoes originating from reentrant structure reflections, specular scattering and body interactions require major interventions in the design of an aircraft. Morphing structures can be used to efficiently avoid surface discontinuities, edges and vertexes in military aircraft structures. Scattering of incident, traveling and creeping waves can be reduced by avoiding gaps, seams or changes of curvature. Conventional control surfaces are particularly affected by these three mechanisms. Shape-variable wings can thus significantly enhance the radio signature of military aircrafts.

Rütten et al. [21] investigated the effects of a shape-variable trailing edge on the aerodynamic behaviour of Delta- and Lambda-wing configurations under consideration of RCS reduction. The influence of a variable-sweep wing on the RCS and the detection probability is investigated by Chen et al. [22]. By simulation and experimental measurements in a microwave chamber, the backscatter characteristic of the aircraft is examined. The morphing structure thereby reduces the probability of detection for increasing sweep angles. RCS peaks appear in leading-edge-perpendicular direction. The variable-sweep-wing allows adapting the wing's orientation according to the specific threat scenario.

Morphing mechanisms become particularly valuable when multiple advantages can be reached with one and the same structure. The unmanned aerial vehicle (UAV) *Sagitta*, a technology demonstrator of Airbus Defence and Space, the *German Aerospace Center* (DLR) and other German research institutes [23], is a diamond-shaped aircraft in blended-wing-body configuration. For reasons of camouflage, all service and maintenance covers as well as landing gear doors are positioned on the lower side of the aerodynamic skin. After take-off *Sagitta* turns upside down and profits from its smooth upper surface, which is now directed to possible ground-based radar scanners. Morphing flaps, as intended but not implemented for this project, reduce the radar signature and additionally allow for wing-camber variation. For *Sagitta* this means that the aerodynamically inefficient but necessarily symmetrical profile could be changed during flight to show positive camber.

Figure 1-4: Structural model of *Sagitta* at ILA2014 in Berlin (r.) [24] and roll-out at DLR in Braunschweig, 2015 (l.) [23]

Efficiency of actuation

Besides the enhancing effects on aerodynamics, loads, noise and camouflage, an integral design that merges structure and actuator provides potentials for increased efficiency and weight saving. The necessary actuation energy for morphing a trailing edge flap of a blended wing body aircraft under consideration of structural and aerodynamic work is investigated by Gern et al. [25]. The underlying structural and aerodynamic loads together with the required displacements are either directly borne by the actuator or converted by gearboxes or lever systems, which cause additional weight and dissipation. The selection of the actuation principle is thus essential for the efficiency of the overall morphing structure. Further criterions are power density, which includes information about the actuator weight and traverse speeds, the maximum actuation strain and frequency.
Huber et al. [26], Hollerbach et al. [27] and Hunter et al. [28] compared fluidic, electric, polymeric, piezoelectric, magnetostrictive, shape memory alloy (SMA) and thermal expansion actuators. The actuator characteristics, which are identified in their investigations, are summarized in Figure 1-5. The efficiency data in particular is taken from Huber et al. as the information of both references in this case does not match perfectly. The main information that is provided in Figure 1-5 is about power density and actuation strain. For each group of actuators the solid lines show their performance limits. The line colour specifies the efficiency of the actuation principle. Depending on the requirements on actuation strain, the selection of piezoelectric, magnetostrictive or fluidic actuators is most beneficial. The high power density and efficiency give advantage to these types of actuators. For the utilization of weight saving potentials this selection is fundamental. Subsequent structural optimization on the morphing mechanism holds further potentials but is also influenced by the selected actuation system regarding bearing and geometrical boundary conditions. Further details on actuators and their utilization in morphing structures are given in chapter 1.3.

Vos [29] utilizes the aerostatic pressure change in different flight altitudes to actuate the *Pressure Adaptive Honeycomb* (PAH). Experimental investigations of a PAH flap within a low speed wind tunnel validate the concept's functionality. A very special method for pressurizing soft robots (see chapter 1.3.4) is realized by Shepherd et al. [30]. They use methane explosions for the pressure generation, thus substitute conventional compressors and show the possible improvement potentials by technologically already realizable solutions.

Economical profitability

A holistic consideration of the profitability of morphing mechanisms for aircraft structures is performed as part of the *Mission Adaptive Wing* (MAW) project. A summary of the project's objectives, a description of the morphing mechanism and flight test results are published by Moorhouse et al. [11]. Besides the aerodynamic advantages of increased manoeuvrability and gust alleviation, a reduction of fuel consumption of approximately 22 % is examined.

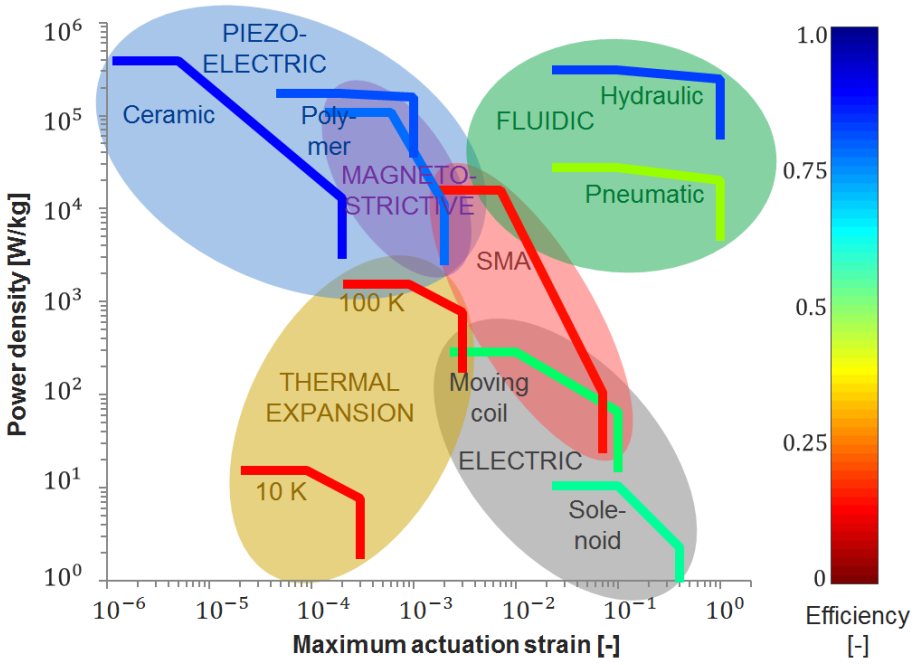

Figure 1-5: Power density over actuation strain and efficiency (coloured lines) for electric, fluidic, piezoelectric, SMA, thermal expansion and magnetostrictive actuators

The assessment of the variable-camber wing for application to transport aircraft of Brissenden R.F. et al. [31] exceeds the investigational outcomes of the MAW project. With a simple, reliable, low-maintenance mechanism which allows for independent wing leading and trailing edge deflections, the possibility for camber optimization is provided. The performance of the adaptive system should enable camber optimization for the flight conditions take-off, climb, cruise, descent and landing. Subsonic domestic (range: 3,700 km) and intercontinental (range: 10,200 km) transport aircraft (payload: 200 passengers) configurations are considered for the comparative examination in order to evaluate the profitability of the morphing wing. Although fuel savings of 4.0 % are computed, a benefit for the direct operating costs (DOC), basing on 1977 operational costs and fuel price, could not be discovered for the domestic variant. Due to increased empty weight and life cycle costs, including development, production, operation and maintenance, the increased aerodynamic efficiency and reduced fuel consumption could not lower the DOC.

The potential fuel savings for the intercontinental mission is 3.1 %. For this scenario, the DOC decreases by 1.5 % for a fuel price of 0.42 $\$/gal$. With a significant price increase since 1977 to 1.73 $\$/gal$ in June 2015, the profitability of morphing is given today more than ever. This financial motivation gives reason for the increasing research efforts on morphing aircraft structures since the 1990s, as shown in Figure 1-7.

The reduction of operating costs resulting from fuel savings due to the application of an adaptive contour bump is further examined by Stanewsky [32] in 2000 for transonic transport aircraft. With this concept for the reduction of the shock strength in transonic flows a decrease of DOC of 1.3 % for laminar-type transport aircraft and 0.8 % for Airbus A3xx-type designs is calculated.

1.2.3 Structural dilemma

The energy consumption and related weight of the actuator and the peripheral systems depends on the required forces and travel ranges that are needed to deform the structure. Common concepts for aeronautical shape-variable structures like the ripless plain flap [33], the active *Flexspar* actuator [34] and the vertebrate structure [35] utilize stiff and heavy structural components to withstand aerodynamic forces. On the contrary Barrett et al. [15] even describe the possibility of reducing structural weight by adaptive structures.

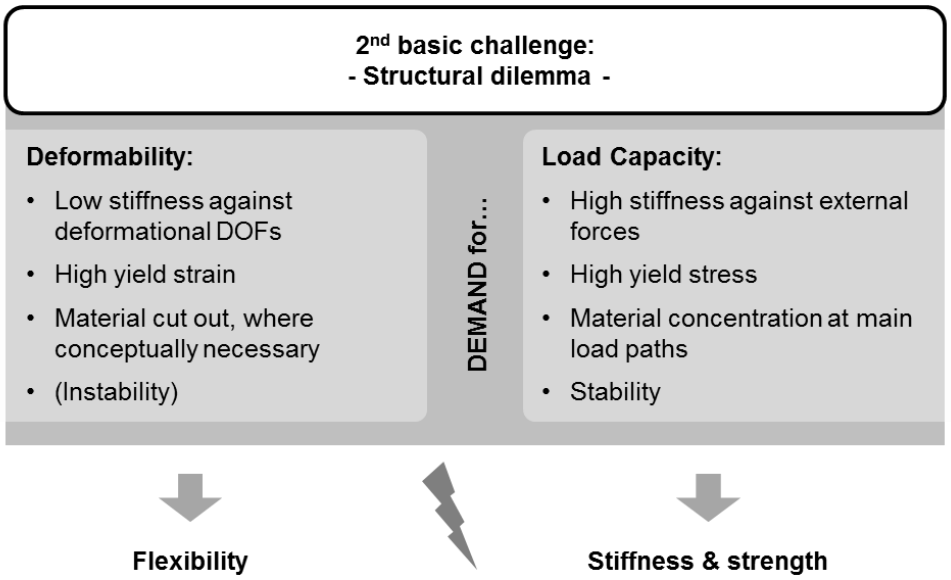

Figure 1-6: Morphing concepts and structural dilemma

Their artificial cell structure that bases on a pressure driven honeycomb benefits of its weight-efficient structural-integrated actuator and provides the non-concentrated forwarding of distributed aerodynamic loads. Structural hard points can thus be eliminated for further weight reduction and provide an additional contribution to the advantages for airborne applications.
A raise of structural stiffness enhances the capacity for bearing external forces on the corresponding structure but also increases the necessary efforts for changing the structure's shape and limits the boundaries of tolerable deformation. Thus the 2nd challenge for developing a profitable morphing concept can be formulated (cf. Figure 1-6):

2nd basic challenge: *An efficient concept for morphing structures circumvents the seeming contradiction of the competitive demands for structural stiffness and flexibility.*

Further concepts that consider this relation are the flexible rib from Monner [36], the topology-optimized cellular morphing structure from Vasista et al. [37], the tendon-actuated compliant cellular trusses [38] or the *Zigzag Wingbox* [39]. The common principle behind these examples is a steered release of specific DOFs by integrating hinges, compliant mechanisms or linear bearings.
The actuation system of such an energetically efficient and lightweight morphing structure can thus be conceived to only overcome primarily external, e.g. aerodynamic, loads. Internal loads caused by structural strains due to the deformation are minimal. In this case, the stiffness of the morphing structure is established by the actuation mechanism or additional locking mechanisms. The resulting weight and energy savings ultimately increase the profitability of the shape-variable structure.

1.3 Morphing structures and actuation

A review of the most important topics allows to position the herein presented work about PACS within the scientific landscape and to evaluate the related objectives with the research on morphing structures. In the following, morphing structures are classified according to the utilised actuation principles. Relevant representatives for morphing concepts basing on conventional actuators and so-called smart materials are listed together with exemplary realizations. Concepts using structurally integrated fluidic actuation and cellular actuators are introduced subsequently. The functional principle and characteristics of PACS are presented together with the related state of research.

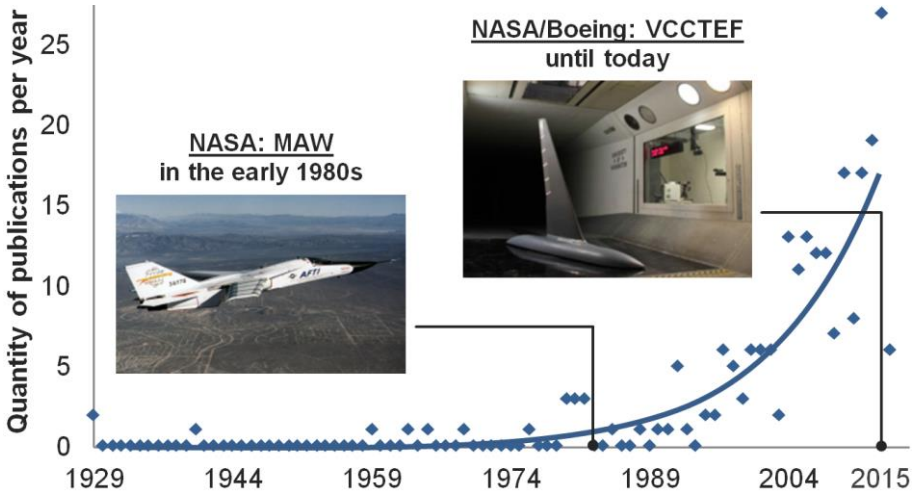

Figure 1-7: International comparison of research activities on morphing structures between 1929 and 2015 showing a substantial increase of research activities about morphing structures in the last twenty years; MAW (l.) [6], VCCTEF (r.) [40]

1.3.1 Research landscape

One of the very first concepts for wing camber morphing is the *Aeroplane Wing* from Kientz [2] (see Figure 1-1). This concept allows for controlling the profile's thickness and camber. Researchers have reached plenty of aims in this field during the last century. Thereof, the most important achievements are presented in the following. Analysing the origin of the related publications, it can be found that there are two hotspots for such research: North American (49.5 %) and European (38.7 %) researchers published almost 90 % of the articles on morphing issues. This analysis bases on the evaluation of the herein referenced publications on morphing structures under consideration of the year of publication and the location of the first authors' research institutes. The requirements for the selection of a publication for this statistic, besides the topic, were the international availability and the English script. Important North American projects are performed by the *National Aeronautics and Space Administration* (NASA) and the *Defence Advanced Research Projects Agency* (DARPA) in terms of aeronautical application and by the *University of Harvard* regarding robotics and medical tools. European efforts concentrate at the DLR and at the *Swansea University*. Extensive information about publications in the field of morphing structures can furthermore be obtained from the review work of Barbarino et al. [41], McGowan et al. [42], who summarizes the results of the NASA's morphing projects and Thill et al. [43].

The statistic about research publications also provides an insight into the topicality of morphing structures. Until the 1980s there was only marginal interest in such technologies. With the MAW, the NASA developed a shape-variable aircraft wing for the F-111, which allowed for a gapless modification of the wing camber [6]. In this context a first peak of research efforts is initiated. At the end of the 20th century the desire of aircraft producers and their customers for aerodynamic improvement, noise reduction, decreased fuel consumption and ultimately for reduced costs revitalized the demand for morphing structures. Figure 1-7 visualizes this trend that is at least partially driven by the financially oriented reasons that are presented in chapter 1.2.
In cooperation of Boeing and NASA the Variable-Camber Continuous Trailing Edge Flap (VCCTEF) is developed for substituting conventional trailing edge flaps. The segmented design allows bending of the wing in case of high lift and gust loads and facilitates to achieve uneven deflections in spanwise direction.
The following subsections shall provide a summary of the state-of-the-art and discuss the relevance of the presented concepts for morphing structures.

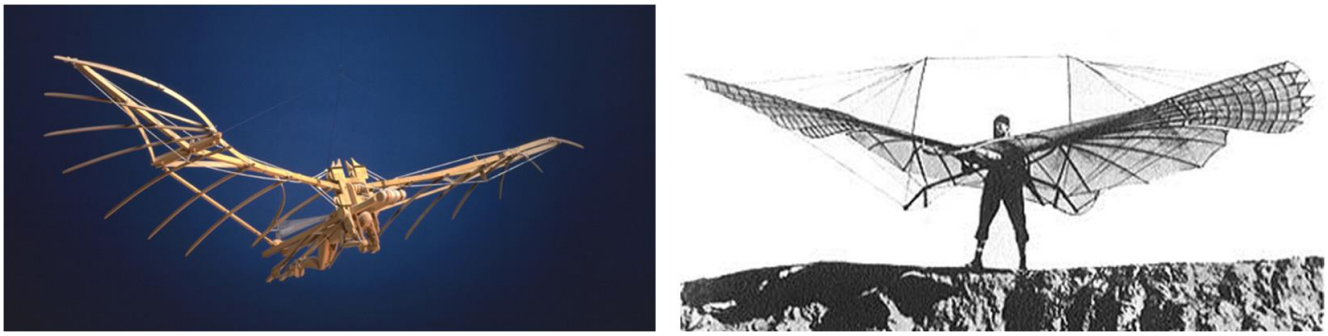

Figure 1-8: Leonard da Vinci's *Ornithopter* (l.) [44]; Otto von Lilienthal's *Kleiner Schlagflügelapparat* (r.) [45]

1.3.2 Conventional actuation

The research for morphing mechanisms for aeronautical applications is as old as the history of aviation. In the 15th century Leonardo da Vinci's enthusiasm for the flight of birds resulted in the first design for a shape-variable aeronautical structure. With the inspiration to emulate the motional mechanism of birds he designed the *Ornithopter*. Figure 1-8, left, shows a reproduction of da Vinci's flying machine. The movement of the wings hereby is conceived to be driven by human muscle power. Flight tests with a similar flying apparatus are executed by Otto von Lilienthal in 1894 (see Figure 1-8, right). A carbon dioxide driven motor enabled Lilienthal to reach the required forces for actuating the wing mechanism. Subsequently to the research achievements on the variable-camber wing, concepts for varying the shape of a leading and trailing edge are presented in the following. Wing twist and sweep solutions are further complemented by supplementary examples considering rotating-wing morphing concepts and aerospace implementations. Conventional actuators for the further considerations are understood as electric and fluidic actuators as these are standardly used and certified for today's aircrafts.

Variable-camber wing

An early implementation of a variable-camber wing is conceived and filed for patenting in 1929 by Kientz [2]. Powered by a profile-internally positioned drive shaft, a lever system is used to lift and lower a flexible aerodynamic skin, which lies above the rigid core structure. Huge variations of the profile thickness thus allow adjusting the aerodynamic properties of the aerofoil. The increase of aerodynamic efficiency for a range of flight conditions and an expansion of the flight envelope are the key drivers for this technology. An alternative solution for realizing a variable-camber wing is given by Hannah [46] in 1929. Without the usage of flexible materials a linear drive actuating a knee lever provides the forces for lifting the guided upper segment of the aerofoil. Increased surface-perpendicular aerodynamic loads can be borne compared to a concept utilizing a non-rigid skin. The *Variable Shaped Airfoil* of Lyon [47] exploits the energetically favourable bending of the thin aerodynamic skin to alter the wing camber hydraulically. Overlapping sheets near the trailing edge avoid extensional deformations by allowing slipping between upper and lower wing skin.

A straightforward concept for morphing a profile at multiple discrete positions over the chord length with a completely internal spindle drive is patented by Frost et al. [48]. In order to assess the potentials of a variable-camber wing the NASA together with the US Air Force compared different morphing concepts for their efficiency at the use case of a transport aircraft. After an evaluation of aerodynamics, weight, manufacturing and operating costs for a given set of flight missions and generic aircraft platforms, camber morphing was assessed as potentially useful [49]. Advances from the increase of aerodynamic efficiency over a range of lift coefficients and flight speeds surpass the penalties due to risen system complexity and cost. The MAW concept within the *Advanced Fighter Technology Integration* (AFTI) project is established thereupon. The morphing concept of the MAW bases on a flexible panel at the upper wing side, which is made from glass-fibre reinforced plastic (GFRP), for

structural compliance [50]. The shape variation is achieved by bending of this flexible segment through hydraulic actuation. Four modes of operation, manoeuvre camber control, cruise camber control, manoeuvre load control, and manoeuvre enhancement and gust alleviation are planned within the respective research activities. After the successful wind tunnel experiments, the theoretically deduced enhancement perspectives are evaluated at the test vehicle F-111 Aardvark [51]. The proof of concept is shown effectively by flight tests (see Figure 1-7, left). The aerodynamic results are summarized in [52]. Actual research activities at the ETH Zurich investigate the efficiency of a completely compliant wing for camber morphing [53].

Shape-variable leading edge

Research efforts on a gapless-lowerable leading edge device are made since the early 1980s. The front segment of the before mentioned MAW initiated the research activities of the aircraft manufacturer *Boeing*. Two lever-mechanism-driven variants for the "continuous skin, variable-camber leading edge" are invented by Statkus et al. [54] and Cole [55] and patented by *Boeing* in this time. Basing on the idea of a variable profile airplane wing from the Dornier Company [56], Kintscher et al. [57] continues the investigations on a closed compliant GFRP leading edge and realized a concept which is called the *Droop Nose* (see Figure 1-9, left). Starting with the preliminary design by Monner et al. [58] and first realizations by Heintze et al. [59] at the DLR, the reliability of the concept is improved and verified by ground tests [60]. The optimization potentials for the flexible GFRP skin are meanwhile investigated by Thuwis et al. [61]. Aerodynamic efficiency enhancements by substituting conventional high-lift systems as well as noise reduction during take-off and landing are significant aims of the respective research project. A full-scale model is investigated in a low-speed wind tunnel. The research proceedings for multi-material laminates to increase the strength of the flexible skin at bird strike, to protect against erosion and to integrate functionalities like de-icing are given in [62]. A competitive concept with a similar deformation characteristic is realized and presented by the *Fraunhofer Institute* for *Structural Durability and System Reliability* [63] in 2014.

In addition to lever-driven morphing structures, compliant mechanisms are investigated to substitute conventional kinematics. Santer et al. [64] and Saggere et al. [65] implemented a beam-element-based strategy for computing an optimal design for compliant leading edge morphing structures. Vasista et al. [66] combined static topology optimization methods with the possibility to include deformational boundary conditions in order to calculate compliant-hinge-based mechanisms. With the ability to actuate complex shape variations with a single force or torque input the objectives of weight and complexity reduction shall be reached.

Shape-variable trailing edge

Structurally integrated shape control is attracting interest in the wind power sector. Peak loads due to gusts highly strain essential components of a wind power plant, from the wing to the gearbox, the generator and the tower. The maximum wing span and thus the maximum capacity of the plant is limited by these gust loads and the resulting deformations. Trailing edge flaps shall allow for the realization of active load control. Morphing structures in this area of application offer the possibility for an integral solution for realizing a lightweight device with high aerodynamic efficiency. The exemplary structure, which is presented by Berg et al., bases on a conventional belt driven actuator design [67] and is already realized for experimental operation on a test plant [68].

For being able to adjust the wing camber in chordwise and spanwise direction, Monner et al. [69] examined a morphing concept for shape-variable *Fowler flaps*. A flexible deformation of the last 30 % to 40 % of the chord length of these flaps is according to Monner et al. sufficient to reduce the aerodynamic drag notably, enlarge the operative range and reduce the wing root bending moments and thus the overall structural weight of the aircraft. Strength investigations for this mechanism are processed theoretically and by experiment [36]. A similar morphing mechanism, basing on interlocking slides is recently taken up by Wang et al. [70]. Developed for trailing and leading edge morphing, their work is additionally motivated by the aim of shortening the required length of runways.

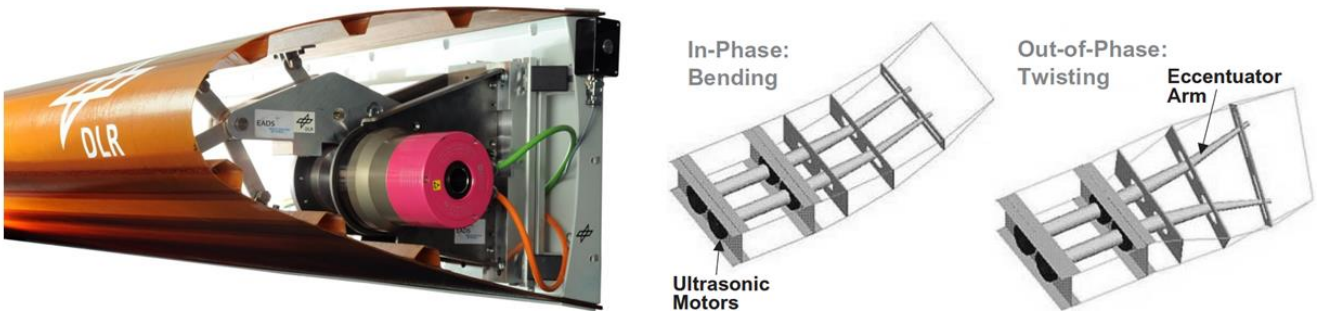

Figure 1-9: Realization of *Droop Nose* by Kintscher et al. (l.) [71]; the *Eccentuator* within smart wing project (r.) [72]

Another special variant of conventionally actuated morphing structures is the *Eccentuator*. The relative pivotal movement of the two adjacent segments wing and trailing edge flap is realized by an eccentrically deviating bolt. The concept is filed for patent in 1974 by Musgrove [73] from the *LTV Aerospace Corporation*. After Musgrove [74] published his research results the concept is taken up again in phase 2 of the DARPA Smart Wing project [75] (cf. Figure 1-9, right). Wind tunnel experiments [76] verified the functionality of this concept for morphing trailing edge flaps [72]. Recent investigations for this kind of morphing structure are performed by Di Matteo et al. [77] and Bei et al. [78]. A very similar concept is published as *Hornkonzept* by Müller [12]. Müller's morphing structure is made of carbon-FRP (CFRP) and driven by a linear hydraulic actuator. This solution profits from the lightweight design and the high power density of the hydraulic actuation.
A compliant morphing structure for shape control at the trailing edge flap is conceived by Bauer [33]. Flexible webs within a ripless trailing edge flap thereby allow deforming the rear 50 % of the chord of a trailing edge flap. Liu [79] and De Gaspari [80] combined this idea with the *Droop Nose* concept to a compliant-mechanism-based morphing-trailing-edge concept for single-point actuation. Topology optimization is used for designing the underlying mechanism and to save weight.

Wing sweep, span, chord and twist

Multiple already realized and flying examples for sweep-morphing structures are available [41]. A change of the sweep angle of a wing by rotating the wing around the vertical axis of an aircraft also results in a change of span. Besides the mentioned *F-14 Tomcat* (cf. Figure 1-1), among other, the *Bell X-5*, the *F-111 Aardvark*, the *MIG-23*, the *Panavia Tornado* profit from enhanced performance through reduced drag and an increased flight envelope. Studies about the advances of a variable-sweep-wing aircraft regarding its RCS show the timeliness of this topic [22].
Isolated changes of the wing span shall improve the aerodynamic performance and can be used for aircraft control. An implementation for rotary wings is patented [81] and investigated by Gandhi [82]. The centrifugal-force-actuated elongation of their rotor blade bases on a spring mechanism that ensures the telescopic expansion of the rotor diameter in dependence of its current rotational speed. Fixed wing aircrafts like the *Makhonine MAK-123* with variable wing span are rare. Han et al. [83] developed such a variable-span wing for efficiently controlling wing-in-ground-effect vehicles.
A wing-twist mechanism for substituting conventional aircraft control surfaces is investigated by Guiler et al. [84]. The bending-twist coupling effect is utilized by Raither et al. [85] within a semi-passive morphing concept for twist control.

Summary of conventionally actuated morphing concepts

The previous section provides an overview of morphing structures that base on electric and fluidic actuation and describes the state of research in this field. The increasing amount of investigations on morphing concepts during the last years corresponds with the rising economic value of this topic. Leading edge concepts, like the *Droop Nose*, and trailing edge concepts, like the DARPA *Smart Wing* project, confirm the current capabilities to realize functional morphing structures. Both of these implementations are tested in the laboratory. With the MAW, a variable-camber wing is realized, which is examined in flight tests. Despite these realizations, morphing structures are still not state-of-

the-art. The benefits with the implementation of these structures in an industrial application are obvious but currently not sufficient to overcome the barriers for launching such a new technology. The search for alternative concepts, using non-conventional actuators and novel structural concepts is thus enforced. The aim of the research in the field of morphing structures is to expand the advantages of morphing structures for providing incentives for industrial application.

1.3.3 Smart-material-based actuation

The significance and thus the usage probability of a morphing concept strongly depends on the total performance of the substituting system. Besides energy source, morphing mechanism and periphery, the actuator has crucial influence on the efficiency of the concept (cf. chapter 1.2.1). In addition to different specific and energy-based parameters, smart materials compared to conventional actuators cover other regions of dimension-related amplitudes and forces. Energy converters as gearboxes can thus partially be avoided as well as the associated power dissipation. Piezoelectric materials made from lead-zirconate-titanate (PZT) and SMA are the dominant actuator types for morphing applications [86]. Shape-memory polymers (SMP), electrostrictive and magnetostrictive materials, moreover are used to enhance and also enable various morphing concepts. The following review summarizes concepts for shape-variable structures, which are driven by these so-called smart material actuators.

PZT

Although piezoelectric natural crystals, piezoelectric polymers and other polycrystalline piezoelectric ceramics are available, PZT ceramic compounds are the mainly used materials for actuator production [87]. In the following, PZT are regarded exclusively. The piezoelectric effect is utilized in three ways. The longitudinal piezoelectric or d_{33}-effect, can be observed, when an electric field is applied in parallel with the remanent electric polarisation of the PZT. In this case, the resulting strains in parallel direction are used for the actuation. For the transversal or d_{31}-effect, polarisation and electrical field are also orientated parallel to each other. The field orthogonal deformation thereby provides the actuation strains. A third variant, the shear or d_{51}-effect can be obtained, when the remanent polarisation and the electrical field are orientated perpendicular to each other. Performance values for PZT actuators are presented in Figure 1-5. In general, PZTs profit from high actuation frequency and power density but provide only low actuation strain.

The transition between conventional and smart material actuators can be experienced in the case of ultrasonic motors. These PZT-driven motors are used by Sanders et al. [72] and Bartley-Cho et al. [76] to power their *Eccentuator* concept for the morphing trailing edge that is realized in the *Smart Wing* project.

Due to the limited thickness of the PZT actuators of about 0.1 mm and a strain of less than 0.1 % [26], piezo stacks, a layer formation of single PZT plates that base on the longitudinal piezoelectric effect, are often used to increase the absolute travel. A variable-camber wind turbine blade is investigated by Dicker et al. [88]. The blade's deformation is controlled by an active truss structure, which is created by replacing all chord-perpendicular rods with PZT stack actuators. The functionality of aerofoil stiffening is thus expanded by the possibility to effect shape variations. A possibility to further increase the actuator's travel is the mechanical conversion of the actuation energy for lower forces and higher strains by a lever system. Computational tools for designing such PZT-driven compliant mechanisms to increase the translational strains are developed by Kota et al. [89]. A non-aeronautical application example from the manufacturing sector for these mechanisms is given by the smart device for active vibration suppression from Perner et al. [90]. A compliant-mechanism-amplified PZT stack actuator is thereby utilized to improve the quality of fibre-reinforced materials by increasing the accuracy of a fibre-placing robot arm.

The transversal piezoelectric effect can be used either directly for generating translational deformations or for causing bending. The shear-web-based actuation system is developed for

morphing a wing's camber by deforming the web of spars or ribs. Therefore Natterer et al. [91] used *Macro Fibre Composites* (MFC) to cause translational strains within the web. MFCs are ready to use PZTs, which are adhesively embedded between electrodes and a polymeric protective layer. The maximum displacement of $150\ \mu m$ is measured at the tip of the shear web and corresponds to the shear strain of 0.1875 %. A two directional morphing element named *Flexspar* is further designed to drive a missile flight control surface by bending. Therefore Barrett et al. [92] laminated PZT actuators on each side of a 0.08mm thick brass foil. The translational deformation is thus transferred in the bending of a beam that actuates the target structure with controllable amplitudes to cause the desired aerodynamic effects [34].

SMA

The solid-solid state transition from martensitic to austenitic crystal structure, which is triggered by heating a SMA above its transition temperature range, causes strains up to 8 % for nickel-titanium-alloys [93]. Figure 1-10, left, depicts an exemplary shape-memory coil spring that demonstrates the related effects with the two available sorts of SMA actuators. An SMA with martensitic crystal deforms due to a change of the crystal structure to an austenitic arrangement when heated up to the austenite transition temperature range. For a SMA with one-way effect a reversal of this deformation can be realized by cooling below the transition temperature range followed by the mechanical deformation to its initial shape. For the SMA with two-way effect, the pure temperature reduction is sufficient to cause inversely orientated deformations. In both cases the forces occurring from the martensitic to austenitic transformation are significantly higher than the forces that are caused by cooling or which have to be applied after cooling to recover the initial state of shape. Both types of SMA are utilized for actuating morphing structures.

In the DARPA *Smart Wing* project phase 1, SMA wires are used for the shape control of leading and trailing edge [94]. The wing twist is further controlled by SMA torque tubes with one-way effect. The resetting force is provided by an antagonistic arrangement of a first torque tube, which is connected concentrically with a second one. The maximum moment for the outer torque tube with $25.4\ mm$ of diameter and $1.5\ mm$ thickness is $224.8\ Nm$ and for the inner tube with $12.7\ mm$ of diameter and $1.3\ mm$ thickness it is $58.8\ Nm$ [95]. With the length of the torque tube the amplitude of distortion can be controlled. The VCCTEF wing, which is shown within a wind tunnel in Figure 1-7, right, is actuated with a similar SMA rotary actuator [96]. A spanwise-segmented morphing structure is thereby realized that allows for increased aerodynamic performance and an expanded flight envelope [97].

Figure 1-10, right, depicts a further concept for wing camber morphing that is based on SMA actuators. The cellular metal vertebrate structure, which is developed by Elzey et al. [35] controls the wing's state of shape and stiffens it against bending. The connection to the aircraft fuselage is problematic for this structure as well as for other morphing concepts, which rely on the substitution of the rigidly mountable wing spars.

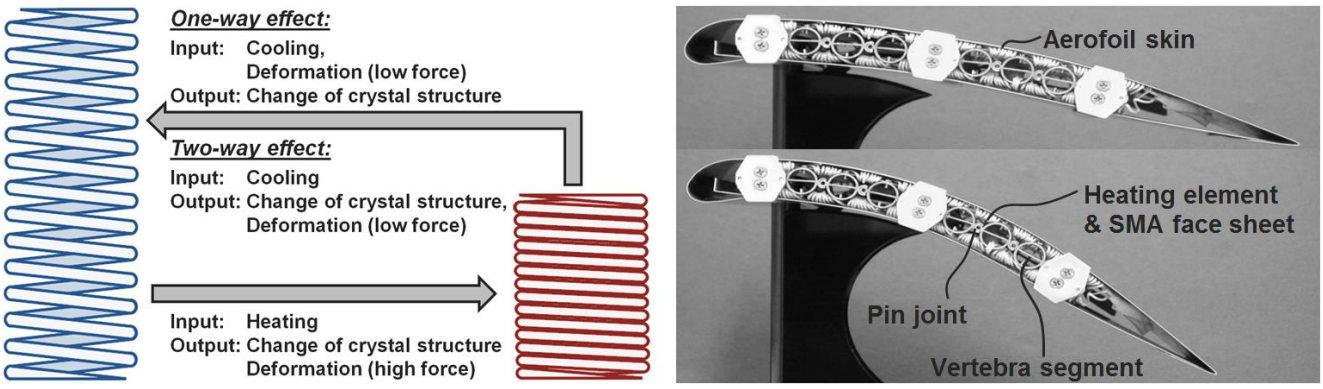

Figure 1-10: One-way and two-way shape-memory effect of SMA (l.) and application for vertebrate morphing structure (r.) [35]

Figure 1-11: Wind tunnel setup showing folding-wing aircraft with utilized SMP [98]

SMP, electrostrictive and magnetostrictive materials

Compared to PZTs and SMAs, the herein discussed SMPs, electrostrictive and magnetostrictive materials play a subordinate role in terms of smart materials for morphing structures. SMPs profit from actuation strains up to 1100 % that can be retrieved repeatedly [99]. Equally to SMAs the actuation is triggered by exceeding a temperature threshold. The actuation forces of SMPs depend on the *Young*'s modulus of the heated polymer. DARPA's *Morphing Aircraft Structures* (MAS) project demonstrates the potentials of SMPs for morphing structures. At the demonstrator structure of an UAV with foldable wings (see Figure 1-11) SMPs are used to cover the joint areas. The development of the morphing vehicle with respect to the SMP seamless skin is documented in [100]. Objectives like the improved distribution of wing root loads compared to sweep wing alternatives and increased mission radius are addressed with this morphing aircraft. The wind tunnel experiment [101] confirms the load carrying capacities of the folding mechanism and the SMP skin and verifies the numerically deduced outcomes for the aerodynamic efficiency [98]. A novel concept for morphing skins uses SMPs with integrated electrical heating to enable chordwise wing expansion. Reed et al. therefor investigate honeycomb core stiffened SMP skins, which tolerate large translational deformations [102].

Magnetostrictive and electrostrictive actuators are powered by applying a magnetic respectively an electric field. The magnetostrictive effect is used by Pelrine et al. [103] to realize linear actuators with muscle-like damping properties for driving walking robots. Research efforts on a concept for a variable-camber morphing structure that is driven by magnetostrictive actuators are made by Austin et al. [104]. Cho et al. [105] introduce a morphing concept that bases on electrostrictive polymers. It is used for driving the bio-inspired locomotion system of an inchworm-like robot for pipe inspection.

Summary of smart-material-based actuation of morphing concepts

Smart material actuators in the case of PZTs combine high power density (< 1e6 W/kg) and efficiency (< 0.99) with moderate or low actuation strains (< 0.1 %) and thus close a gap, which cannot be filled by conventional actuators. PZTs and SMAs are the primarily used actuator variants for morphing structures within the group of smart material actuators. Realizations using PZT stacks [90], as well as flat surface applications of single PZTs [92] can be found in the literature. SMAs provide a maximum power density of < 1.5e4, a limited efficiency of 0.02 and moderate actuation strains of up to 8.0 %. These actuators are successfully used for realizing the SMA rotary actuator of the VCCTEF wing [96]. SMP actuators are used because of their capability to cause high structural strains. Within the MAS project [98] this property is utilized for closing the hinge region of a folding wing (see Figure 1-11). PZT-driven morphing structures are already used in various industrial applications. However, their limitation to small actuation strains is not sufficient for many morphing concepts.

1.3.4 Structurally integrated fluidic actuation

The specific stresses and strains as well as the resolution of motion of fluidic actuators lead to a wide range of use and predestine it for aeronautical applications. The advantages regarding actuator strain and power density of pneumatic and hydraulic actuators compared with other drive systems can be obtained from Figure 1-5. The opportunity to integrally combine fluidic drive systems with a deformable structure provides the potential for a significant increase of material utilization and ultimately for weight saving. Discrete actuators, mounts, gearboxes and mechanisms become obsolete, when structurally integrated fluidic actuation is applied properly. The morphing concepts that are presented in the following are arranged for increasing integral design.

The *Pneumatic Artificial Muscle* (PAM) consists of a cylindrical and usually fibre-reinforced bladder, which contracts in axial direction when pressurized. The concept for PAMs is filed for patented by Pierce [106] in 1939. Due to its application for prosthetics by Joseph L. McKibben eight years later, which caused public interest, the concept is also called *McKibben Artificial Muscle*. Research activities utilizing PAMs are published in large numbers still today. Bubert uses PAMs for wing span morphing [107]. An artificial elephant trunk-like manipulator is realized by Kang et al. [108]. Woods et al. [109], [110] drive a variable-camber wing morphing structure, the *fishBAC*, that bases on the fish bone concept with PAMs. Energy conversion efficiency and weight savings are therein described as the major advantages of PAMs. The idea of integrated fluidic actuation is pushed forward by the utilization of PAMs for *Flexible Matrix Composites* (FMC) that are depicted in Figure 1-12, left. Shan et al. [111] and Kirn et al. [112] realized a morphing skin by combining multiple layers of unidirectional PAM tubes with an elastomeric potting. The applicability of FMCs for aerospace applications is evaluated by Feng et al. [113]. The shape-variable skin of their morphing-camber wing combines the functionalities of gapless translational deformation and actuation. Strains of $9.7\,\%$ and an output force of $12.3\,N$ are experimentally measured per PAM tube in the FMC compound.

Madsen et al. [17] realized the *Controllable Rubber Trailing Edge Flap* (CRTEF) for wind turbine blades by pressurizing cuboid-shaped voids within an elastomeric flap structure. Also without the fibre-reinforcement of the PAMs, a pressure of $0.8\,MPa$ is successfully applied to the structure. The lift coefficient of an experimental blade segment, could thus be altered by $20\,\%$, what leads to a reduction of dynamic loads by $50\,\%$. The concept is recently prepared for installation on a wind turbine test rig [114].
A specific category within the field of morphing structures is formed by soft robots. Basing on the functional principle of pressurized voids within elastomeric potting, grippers for handling fragile objects [115], compliant hands [116], locomotive soft robots [117] and a trunk-like manipulator for minimal invasive surgery are realized among others. Innovative pressure sources for soft robots are provided with the on-board chemical pressure generation that is investigated by Onal et al. [118] and the explosion-based concept by Shepherd [30]. The ease of manufacturing and the large design freedoms represent the main advantages of soft robots. The actuation forces however are limited due to the use of elastomeric material.
An increased material utilization that leads to weight savings is reached with thin-walled and cellular structures. Inflatable aircraft structures like the *Stingray* from *Prospective Concepts*, which is depicted in Figure 1-12, right, confirm the possibility to substitute even complete wings by pressure-stiffened structures. A similar approach for a thin-walled variable-camber wing is conceived by Reinhard et al. [119] in their further work on the *Stingray*. Additional pressure cushions in the aerodynamic skin allow reducing the run length of the profile unsymmetrically when pressurized. The resulting camber variations are sufficient to operate the UAV without additional control surfaces.
The idea of for pressure-driven adaptive cellular structures and in particular honeycomb structures is introduced by Dittrich [120] as the *Cellular Actuator Device* (CAcD). Barrett and Vos [121] further investigated this concept utilizing regular honeycombs with equilateral hexagonal unit cells. In 2010 their bio-inspired concept is filed for patent as the “Method and apparatus for pressure adaptive morphing structure” in Europe [122] and the USA [123].

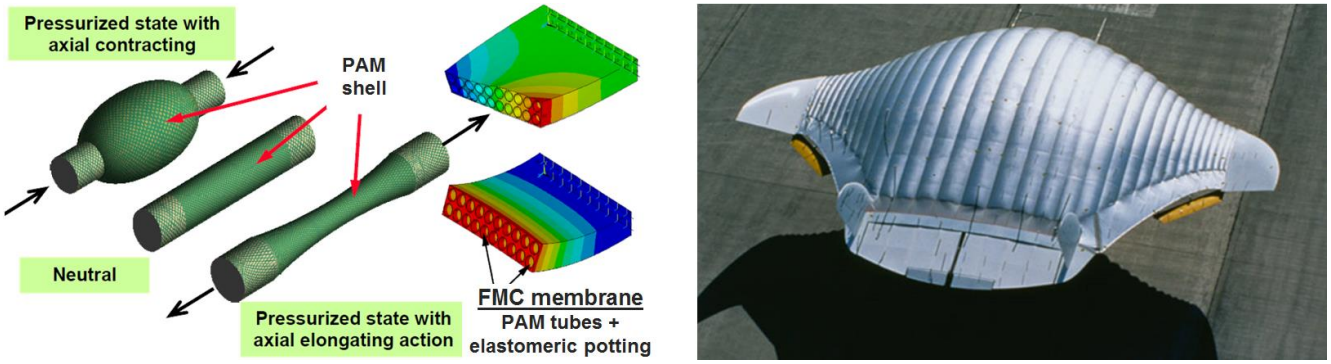

Figure 1-12: PAM actuated FMC membrane (l.) [124] and pressure-stiffened flying wing developed by *Prospective Concepts* (r.) [125]

Vos et al. [29] developed this initial idea to the PAH for substituting conventional leading and trailing edge flaps. These flaps autonomously change their shape in different flight altitudes by utilizing aerostatic pressure differences. Experimental investigations on a shape-variable PAH trailing edge in a wind tunnel validate the concept for cell-internal pressures of 0.00 MPa to 0.04 MPa [126]. Besides conceiving this actuation principle, Barrett et al. [15] showed that the positive behaviour of such a structure in case of micro-bursts during take-off or landing increases flight safety. Basing on these investigations, they developed an FAA-certifiable wing segment. An auxetic active honeycomb for morphing wingtips is numerically and experimentally examined by Sun et al. [127]. The effects of cyclic loading on the strength of a simplified pressurized honeycomb structure are thereby measured together with the associated deformational hysteresis.

An alternative cellular concept is conceived [128] and experimentally [129] validated by Luo et al.. The *Adaptive Pressure-Controlled Cellular Structure* is investigated numerically and could be realized successfully. The concept completely integrates pneumatic actuation in a polymeric structure for longitudinal extensions and allows for elongations of up to *35.0 %*. The approach of utilizing topology-optimization methods for computing the shape of the inflated cells is developed by Vasista et al. [130]. The morphing mechanism that is depicted in Figure 1-13, left, shows a simulation of the adaptive trailing edge flap that is actuated with a single cell row as well as a real-life demonstrator consisting of three cell rows.
Zhang et al. [131] theoretically investigate the mechanical behaviour of closed-liquid-cell materials with advanced *Finite Element Methods* (FEM) named the *Extended Multiscale FEM* (EMsFEM). Their further work indicated that the control of these pressurized unit cells, when successfully transferred to a cell compound, enables the creation of efficient morphing structures. After the generalization of the numerical approach for three-dimensional geometries by Zhang et al. [132], Lv et al. [133] implement a shape and topology optimization strategy basing on the EMsFEM. The adaption for consideration of geometrically highly nonlinear displacements allows computing complex fluidic cellular structures. The computational outcomes for the exemplary structure of a bending cantilever are shown in Figure 1-13, right. The proof of concept is shown at the numerical example of a Venus flytrap-like beam, which is able to deform similar to the plant's trapping leaves [134].

1.3.5 Pressure-actuated cellular structures

The working principle of the concept of PACS is illustrated before its advantages are presented. The classification within the research landscape and the thematic differentiation to related morphing concepts are further covered by this chapter. Previous achievements on the topic of PACS are summarized to show the underlying works. The benefits from a morphing concept like PACS are illustrated by summarizing the fields of application.

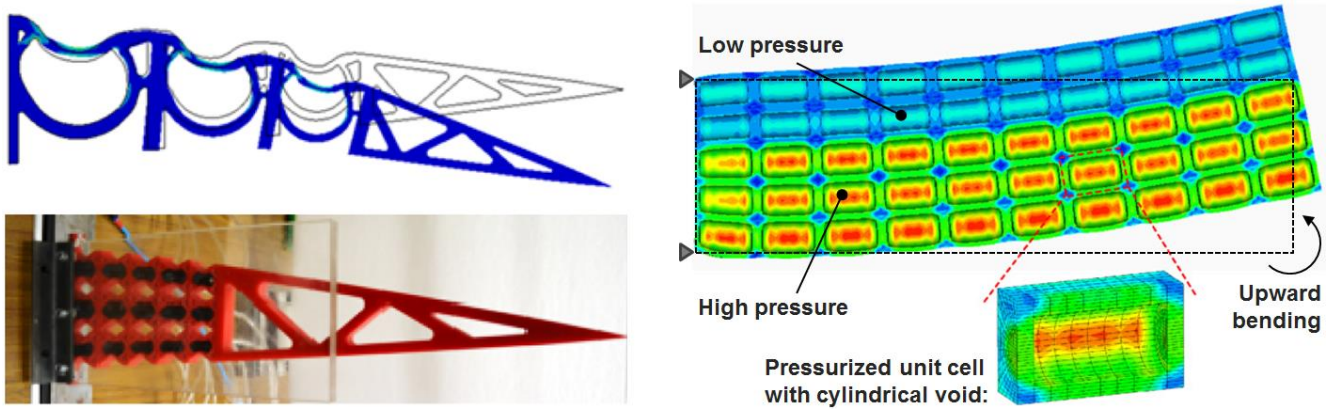

Figure 1-13: Topology-optimized cellular morphing trailing edge structure (l.) [37] and 3D nastic structure basing on closed-liquid-cells material [132]

A bio-inspired concept and its working principle

Biologically inspired technical solutions provide outstanding opportunities regarding the development and enhancement of materials, mechanisms, surfaces, sensors and structures [135]. With the immense variety of the evolutionary developed flora and fauna, an almost unlimited supply of well-tried ideas and technical concepts is available. Still, nature holds the capacities to deliver new insights in all areas of natural sciences [136]. A long-lasting, highly promising issue of aeronautical engineering, morphing structures, recently is vitalized by the concept of PACS, which is derived from the motional principle of the Venus flytrap, *Dionaea muscipula*.

The combination of integral fluidic actuation and a shape-variable structure, that determines the deformational reaction on the change of the fluid's pressure, is discovered at a special group of plants, the nastic plants. Representatives like the thigmonastic Cape sundew, *Drosera Capensis*, and the Venus flytrap, which use their touch sensing capabilities to trap small insects, are examples for a successful biological implementation of integral morphing structures.

The photography of the Venus flytrap that is given in Figure 1-14, left, shows the nastic plant with open leaves, ready to entrap its prey. Modern microscope technology allows having a look inside the cellular structure of the Venus flytrap. Figure 1-14, centre, illustrates one of the sensor hairs of the trapping leave. The sensor cells at its root perceive vibrations. The trapping mechanism is activated, when at least two stimulations are registered during 20 seconds at one and the same or at different trigger hairs. If the prey is caught successfully, the Venus flytrap activates its digestive glands which release their targeted nutrients. The essential functional element of the leave for the conception of the biologically inspired morphing structure is its movement apparatus.

Howard et al. [137] found that osmotic processes lead to cell sap pressures (symbolized by H_2O in Figure 1-14, right) of more than 8.0 MPa. Further investigations about the movement of nastic plants by Stahlberg et al. [138] indicate that different extensibilities of the leaves' inner and outer surface are one condition for the ability of the Venus flytrap to cause shape variations. The bending of the trapping leaves thus results from a different amount of strain within the inner and outer skin of the leave.

Following nature's example the motional principle of the Venus flytrap is abstracted and modified by Pagitz et al. [1] for the utilization in a technical application. Both principles, the fluidic actuation of a cellular structure and the differing extensibility of surface layers can be found in the concept of PACS, which shall be explained in the following.

In a first step, the idea of PACS can be observed at a two-dimensional consideration of a single polygonal cell that consists of flexibly connected rigid cell sides. Figure 1-15 shows a simple demonstrator that includes three symmetrical pentagonal single cells. It shall be used to illustrate the functional principle of PACS. The three cells differ by the lengths of the lowest two cell sides. Each of the cells is filled with plastic balls, which represent and function as an incompressible fluid.

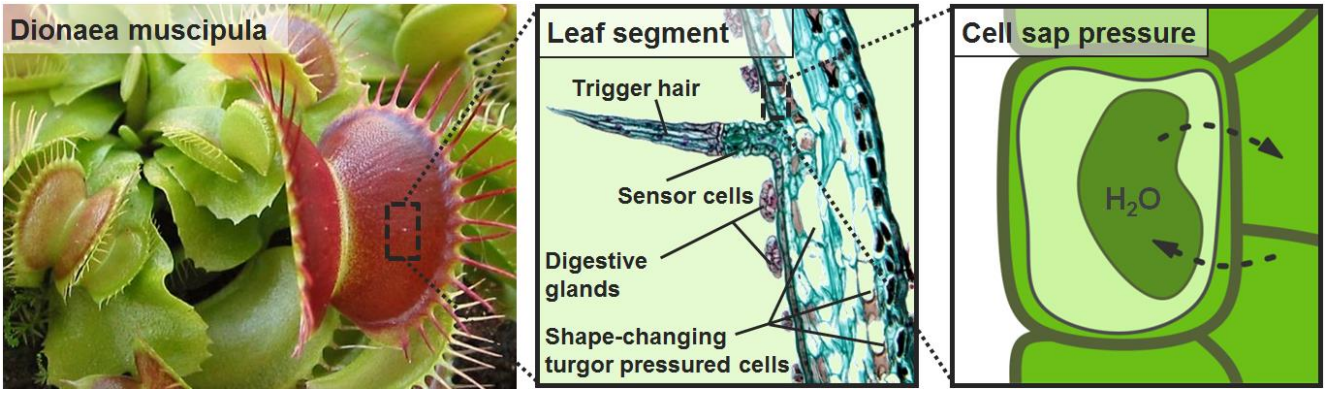

Figure 1-14: Venus flytrap, *Dionaea muscipula* (l.; by J. W. Webb) [139]; microscope slide of Venus flytrap (c.; by Carolina Biological Supply Company) [140], schematic drawing of the transfer of cell sap between adjacent cells (r.)

The cells' deformation can be read at the angle between the two levers, which are rigidly connected to the middle cell sides. The cell's hinges are assumed to be frictionless and without any bending stiffness. An infinitesimal amount of pressure is thus sufficient to cause the cell's deformation into a state of shape of maximum internal volume. Figure 1-15, b, shows the three cells I, II and III at their state of maximum cell-inherent volume V. The number of plastic balls within each cell consequently is maximal and the vertical position of the rod z_{Rod} is equal to zero for $V = V_{max}$. Due to the differing cell side lengths, the state of maximum volume varies. The related cell side angles u_{Vmax} differ between negative (I), zero (II) and positive (III). The demonstrator can be used to explain four substantial characteristics of a single PACS cell:

- The state of shape of maximum cell-inherent volume represents an energy minimum for the pressurized polygonal cell with flexibly connected rigid cell sides. This can be observed at the functional model by pushing the rod downwards for raising the fluid pressure (see Figure 1-15, b). The state of minimal potential energy thus occurs. Due to the maximization of the cell-inherent volume, therefore all hinge points lie on a circle [141].
- The state of shape, which provides the maximum cell-inherent volume, can be controlled by influencing the cell side lengths (cf. u_I to u_{III} in Figure 1-15, b).
- Each deformation that leads to another state of shape decreases the cell-inherent volume and thus raises the potential energy that is indicated by the vertical position of the rod ($z_{rod} > 0$, see Figure 1-15, a and c).
- The higher the cell-inherent pressure, the higher the stiffness against such deformations. The cells' deformation is completely prevented when the rod is clamped in its lowest position (see Figure 1-15, b).

The single PACS cell can be described as a blended actuator-structure device, which circumvents the structural dilemma that is described in chapter 1.2.3, by releasing the rotational DOFs at its vertices. Referring to Figure 1-5, it can be seen that the fluidic-pressure-driven PACS profits from high power density and efficiency. High actuation strains compared to piezoelectric or magnetostrictive actuators enable huge structural deformations without the need of lossy energy converters, like gearboxes or lever systems.

In similarity with the plants' mechanisms, a PACS with linearly aligned single cells and multiple cell rows can be described as a pressure-actuated structure with a non-extensible surface at one side and a flexible surface at its opposite. For the demonstrator shown in Figure 1-15 the non-extensible surface is represented by the top cell sides. The folding mechanism that is built by the lower cell sides however allows for an extension of the lower surface. A structure that is built of multiple of these single cells, which are arranged behind one another is able to bend upwards or downwards.

Figure 1-15: Illustration of the functional principle of PACS on the basis of three different pentagonal single PACS cells

A reproduction of the biological model for PACS is illustrated in Figure 1-16 for clarification. The depicted PACS is able to deform into the "Closed leaf"-shape for only the second cell row being pressurized and forms back to its "Open leaf"-shape for the pressurization of cell row one. The properties of the single cell keep valid for the cell compound. With individually controlled pressures for the cell rows one and two, a continuous motion between the two specified target shapes, open and closed leaf, can be achieved. An increased number of cell rows allows for the definition of more than two target shapes.

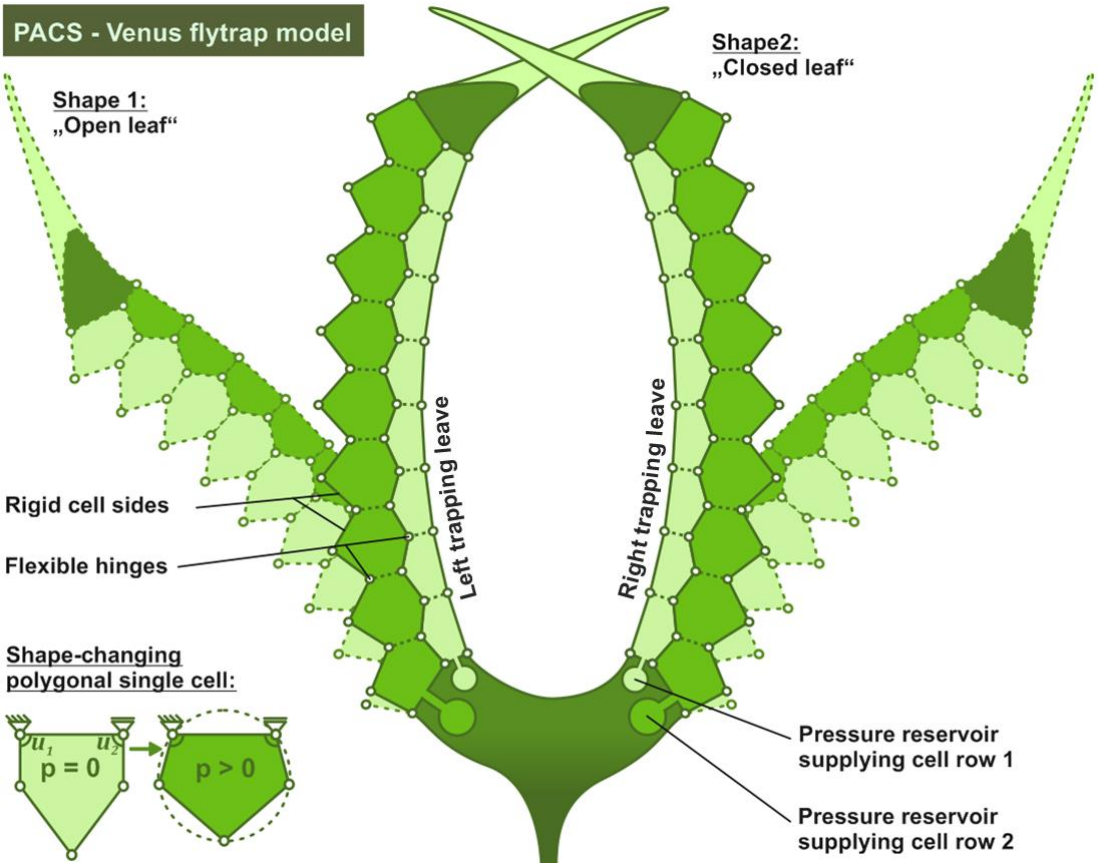

Figure 1-16: Principle of motion at the exemplary double-row PACS of the reproduction of the Venus flytrap, as the biological model for PACS

The change of curvature is kinematically limited by the cell size. The conceivable operating range regarding structural dimensions however can be varied from centimetres to meters without having any losses of functionality. A reduction of the cell size can thus be used to increase the maximum change of curvature. The lightweight potential of this morphing structure is based on its cellular design and the related large geometrical moment of inertia. Due to the hinge-based mechanism only single-curved structures can be realized.

Advantages of PACS

In contrast to competitive concepts, PACS provide a gapless upper surface, what enhances the aerodynamic characteristic of the morphing structure's surface and also avoids scattering of radar waves. With its blended actuator-structure design, additional gearboxes or energy converters are redundant. Excellent weight-saving potentials are thereby enabled. Fluidic actuators are identified to surpass others in terms of efficiency, maximum strain and power density (cf. Figure 1-5). As the concept of PACS bases on this type of actuation, high weight saving and efficiency potentials are expectable. The functional principle allows for the continuous deformation between multiple freely selectable target shapes.

Some promising alternative concepts, like the *fishBAC* [110], which is presented in chapter 1.3.4, are in need of huge actuation forces, as the stiffness of the basic load bearing structure has to be overcome to cause deformations. An increase of energy consumption is unavoidable. The increase of size and weight of the necessary actuator and the power converter disadvantages these concepts additionally. The PACS circumvents this structural dilemma (cf. chapter 1.2.3) by the release of rotational DOFs at hinge elements. The deformation and stiffening of the structure is achieved by controlling one and the same command signal. The concept of PACS thus profits from reduced control input, lower structural loads and increased actuation forces.

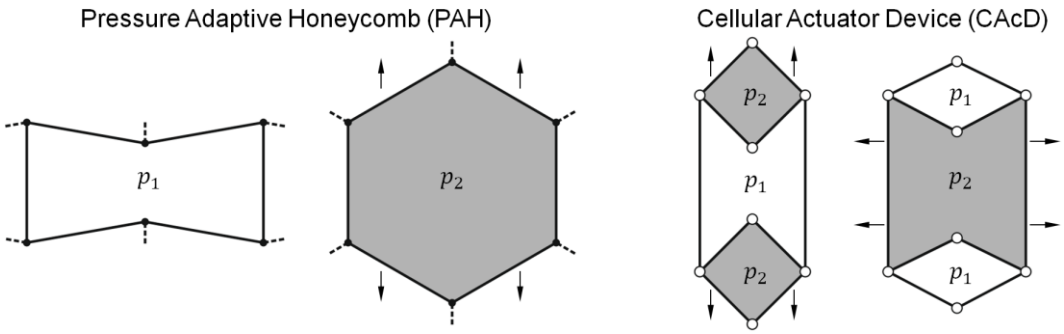

Figure 1-17: Unit cells of PACS-like concepts PAH (l.) and CAcD (r.)

Thematic differentiation

Two concepts for morphing structures, which also base on pressurized polygonal cells closely relate to PACS, the PAH, which is first investigated by Vos and Barrett [121], and the CAcD that is patented by Dittrich [120]. The differences between these concepts and PACS shall be described in the following.

The PAH structure consists of equilateral hexagonal unit cells (cf. Figure 1-17, left) that are interlinked to share a common pressure level, which is used to control deformations. The single cells are combined to a honeycomb structure that is made of single cells of equal size and constant cell side lengths. As presented by Vos et al. [142] and Scheepstra et al. [143], the deformation of the structure due to cell-internal and aerodynamic pressure is controlled by varying the shape and stiffness of the enclosing skin. Due to the uniform pressurization by aerostatic pressures ($p < 0.1\ MPa$), the structure internal cell sides do not have to withstand pressure-induced bending stresses and can be designed thin-walled. These thin-walled cell sides further allow for the deformation of the structure analogous to a flexure hinge, as separate pinned hinges are not provided.

The main distinction of PACS from the PAH lies in the discrete design of individual cells and cell rows. Due to the resulting antagonistic interaction of these cell rows, the PACS allow for the definitions of multiple target states of shape and for controlling the structural stiffness. The PAH whereas can be seen as a combination of a one-way actuator (pressurized cells) and a spring (elastic enclosing skin), which provides the necessary restoring forces. Cell side length modifications for controlling the pressure-induced deformation are not intended. The number of possible target shapes is thus limited. Due to the one-way principle of actuation, the structure can only bend in one direction. Without an antagonistic actuator, the pressure-induced stiffening of a PAH is only enabled for one deformational state, the state of maximum cell-inherent volume. The conception of PACS for pressures above $1.0\ MPa$ and the according increase of the bearable forces and the structural stiffness further distinguishes it from the PAH.

The CAcD of Dittrich consists of multiple polygonal cell tubes. The single cell is built of rigid cell sides, which are flexibly connected at its edges. Two types of cells are combined to effect antagonistic forces as it can be obtained from Figure 1-17, right. The cell compound is organized to share two different pressure levels, one for each of the cell types. Multiple target shapes can be reached by a variation of the differential pressure. The stiffness of the structure thereby depends on the magnitude of the applied pressure. The resulting cellular morphing structure is conceived to enable unidirectional or bi-directional translational deformations. As there are no realizations or further investigations published, the operational range regarding pressure values, cell size and deformation amplitudes is not yet investigated.

Despite the far-reaching accordance of the CAcD with the PACS, there are significant differences. The application of PACS allows a variation of curvature for single-curved structures. Target shapes are reached by bending about its surface and not by translational deformations. The two concepts hence affect different DOFs. In contrast to the CAcD, each of the PACS cells has to be individually shaped to provide the required performance. Due to its composition of multiple cell rows the PACS moreover enable to reach more than two individually definable target shapes.

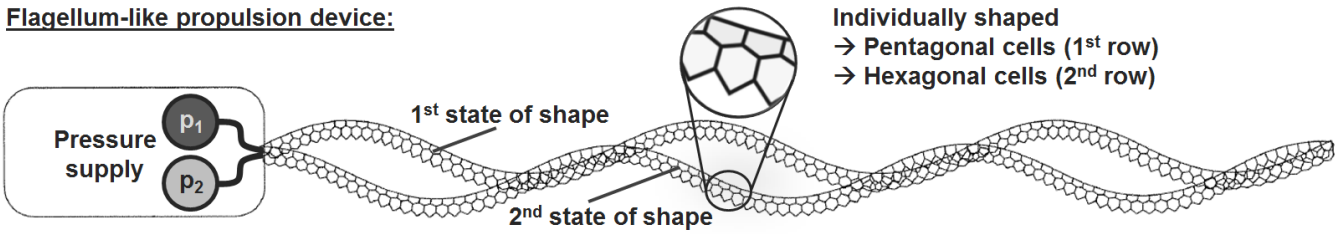

Figure 1-18: Example application for PACS - "Flagellum-like PACS propulsion device" [144]

Previous achievements

Pagitz et al. [1] transferred the physical principle behind the Venus flytrap's movement into a two-dimensional concept for fluidic-pressure-driven morphing structures. With a promising degree of deformation, high flexibility and sizeable characteristic, Pagitz et al. filed their idea for patent in 2012 [144]. As depicted in Figure 1-18, the PACS are initially conceived to consist of two antagonistic cell rows, with pentagonal-shaped cell tubes in the first row and hexagonal-shaped cells in the second cell row. In their further work, Pagitz et al. [1] showed theoretically how the deformation behaviour of such a structure can be controlled by optimizing the shape of each individual cell in terms of the cell side lengths. Although the flexible edges of the polygonal tubes are described as either pinned or flexure hinges, the computation of the cells' shape initially bases on frictionless joints with infinitesimal stiffness. The numerical approach they developed, bases on the computation of the inner energy U of the pressurized structure:

$$U = (p - p_\infty)V. \tag{1.1}$$

The information about the difference between the applied pressure p and the ambient pressure p_∞ together with the calculation formula for the enclosed volume V provide the necessary input. As the volume depends on the actual shape of the structure, a change of shape affects its inner energy. The equilibrium state of shape of a PACS is reached when U is minimal. For the computation of deformations, the unknown variables are given by the rotational DOFs of the hinges u. The cell side lengths are assumed to be constant throughout this computation. A gradient-based optimization algorithm is used to compute the energy minimum. The derivative of the inner energy with respect to the rotational degrees of freedom of the individual cell is

$$\frac{\partial U}{\partial u} = (p - p_\infty)\frac{\partial V}{\partial u} = 0 \tag{1.2}$$

and vanishes for an equilibrium state of shape. Basing on this equilibrium, the subsequent shape-optimization approach alters the cell side lengths until the equilibrium state for a given pressure load is identical with the target shape. Further details on this numerical implementation can be found in chapter 2.1.1. Together with Pagitz, Vos et al. [142] and Scheepstra et al. [143] developed a similar approach for computing the equilibrium state of shape of a PAH. As this concept bases on the utilization of regular hexagonal cells, shape optimization in terms of cell side length variation is not performed.

The publications about the gradient-based optimization algorithm, the theoretical proof of concept regarding the required pressures, the obtainable deformations, the preliminary analytical stress analysis for cell sides under the influence of single point loads and the idea of PACS itself represent the initial point for the herein presented research work.

In their further investigations, Pagitz et al. [145] expand the numerical approach of shape optimization for the consideration of more than two cell rows. An increase in the number of cell rows allows the specification of further target shapes. The mathematical integration of stiffness characteristics for flexure hinges moreover covers the demand for the shape optimization of compliant PACS. The efficiency of the numerical method is shown on the basis of a generic circular structure for different

hinge materials with varying *Young*'s moduli. The number of iterations, which is needed to find the equilibrium shape of a pressurized PACS and for the shape-optimization process, is taken as indicator. The influences of further simplifications, which result from model assumptions, are discussed in [146] and [147] on the basis of numerical investigations. Axial elongation of cell sides and eccentric hinges, which are necessary for the realisation of compliant PACS, are considered in the underlying computations. Depending on the stiffness of the used materials respectively the shape of the hinge eccentricity, deformational deviations of more than 40 % result for the initial calculations for compliant PACS compared to the more detailed approach. With this knowledge Pagitz [148] recently integrated the necessary approach for the physical description of both effects within his shape-optimization approach.
An investigation of the effects of changing the cells' size, pressures and materials on the structural weight and stiffness confirmed that PACS can be varied in size without suffering a loss of functionality. Pagitz et al. [146] found that for given target shapes and stiffness requirements, a cellular structure can either be made from a large number of small and highly pressurized cells that consist of a stiff material or from a small number of large and lightly pressurized cells that consist of a more elastic material. This predication will be discussed in the following chapters, as its validity is limited through manufacturing and geometrical boundary conditions. All of the underlying investigations are performed on the basis of a two-dimensional truss-model. Some of the initially made assumptions, like the infinitesimal stiffness of hinge, the neglection of the hinge eccentricities and the rigidity of cell sides, could be avoided during the development of the structural models, but others are neither avoided nor investigated for their influence on the results.
In their modular approach to adaptive structures Pagitz et al. [149] describe the advantages of additional structures within the PACS cell for enhanced shape control and cell side discharge. Cytoskeleton-like mechanisms are therefore integrated within the cell for connecting adjacent cell sides and to limit their DOFs through bearing pressure-induced lateral forces on the cell sides. The possibility of designing modular PACS that allow for reduced tooling and manufacturing costs is examined at the exemplary applications of a shape-variable leading edge, a trailing edge and an adaptive passenger seat.
The critical issue of a pressure-tight closure for sealing the cell structure is treated by Pagitz [147] in a first approach. A membrane-like concept for the pressure-tight sealing of the cell tubes is proposed. The presented tendon reinforced end caps are theoretically investigated for their necessary thickness and for the shape dependent energy consumption during deformation.

The structural model for morphing single-curved structures is further extended by Pagitz et al. [150] for realizing three-dimensional shape variations of shell-like structures. This reference is given for reasons of completeness, as it does not overlap with the contents of the herein presented work. Pagitz et al. uses pressurized prismatic cells with elastic cell walls and rigid edges in multiple layers to create a morphing structure which enables to control the shape of double-curved surfaces. The functionality of the mechanism is demonstrated theoretically by the computation of an axisymmetric shell that is able to deform between two states of shape, while changing its curvature between negative and positive.

Fields of application

The concept of PACS allows adapting the curvature of a structure. Arbitrary single-curved structural shapes can thus be reached, only limited by the maximum change of curvature which can be varied with the cell size. A continuous change between different states of shape is obtained by controlling the differential pressure of multiple cell rows. The functional principle of pressure-induced stiffening provides adaptive load bearing capabilities. These properties of PACS can be used beyond aeronautical applications. Rigid aircraft structures restrict existing systems in agility [72], efficiency [32], operating range [9] and load control [14]. Advantages regarding aerodynamic efficiency, functional integration and noise emission can be reached by substituting flaps, high-lift systems, spoilers, jet intakes or nozzles by shape-variable counterparts.

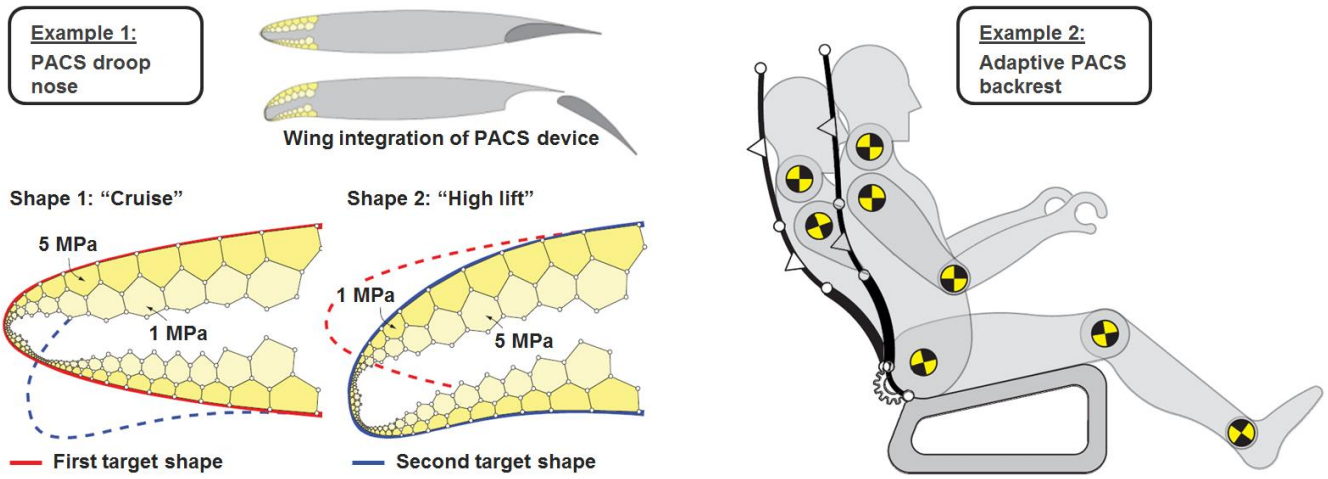

Figure 1-19: Shape-variable PACS droop nose (l.) [1] and adaptive PACS backrest (r.) [149]

A particular promising target structure, the morphing slat or droop nose, is investigated by Pagitz et al. [1]. PACS in this context offer the opportunity to substitute conventional high-lift systems, while optimizing the aerodynamic efficiency of the aerofoil. Figure 1-19, left, shows the shape-variable PACS droop nose for cruise flight as well as for take-off and landing conditions. The related investigations are performed theoretically on the basis of a two-dimensional truss model of the structure.

Besides the implementations for substituting conventional aircraft structures, automotive applications are also promising. Spoilers, sunroofs, cladding parts or even doors made of PACS are more than an interesting design feature. Using an already available on-board pressure supply, PACS can provide a lightweight alternative to rigid components. An adaptive backrest for a car seat or office chair is proposed by Pagitz et al. [149]. A modular PACS construction thereby allows for the adaption of the backrest for different sitting positions and body heights (see Figure 1-19, right) and is promising to simplify manufacturing.

For special groups of applications, which are predestined for the application of PACS, the shape-changing effects can be reached without external energy supply. Aerostatic effects for example are used for PAHs and investigated by Barrett et al. [15]. Hydrostatic forces and thermal expansion of gas or paraffin could be used in a similar way for the pressurization of PACS. Although the power density, frequency and the efficiency of thermal expansion actuators are moderate, an actuator which is heated by solar radiation can be preferential as it does not rely on on-board energy. With a volume extension of $1.14e-3\ K^{-1}$ [151], paraffin may be a suitable substance.

1.4 Objectives and outline

This chapter presents the major objectives with this work and provides an outline of the related fields of work. Beginning with the formulation of the research hypothesis, the methodology for approaching the underlying aims is presented and working hypotheses are deduced.

Research hypothesis

The research hypothesis includes the major objectives with the research work, describes a presumed circumstance and demands for its proof. For this contribution to the field of PACS, the following research hypothesis is formulated:

The division of the PACS in its basic functional subsystems leads to the improved system understanding that is needed for the identification of open conceptual issues, the proof of concept and its characterization. Together with the creation and iterated evaluation of design methods at an early stage of the investigations, the proposed procedure leads to increased flexibility and quality of results, allows for the implementation of a holistic design process and an effective realization of PACS.

The contents of the research hypothesis shall be explained briefly in the following paragraph, before the research methodology and the related fields of work are derived.
The preceding research on PACS (see chapter 1.3.5) addresses the theoretical investigation of the concept and provides methods for the simulation of deformations and for the shape optimization. The feasibility of this concept and the validity of the assumptions that underlie the theoretical investigations are not yet examined. The system of PACS shall first be completed by addressing open conceptual issues, before the numerical and experimental proof of concept and a reliable characterization of PACS is performed. Model uncertainties can thus be identified and eliminated. Therefore, the division of the PACS in its functional subsystems shall be performed where necessary. This division allows handling complexity, identifying open issues and finding particular solutions.
An exemplary and important subsystem is the cell closure. According to its major subtasks of bearing cell-axial loads, sealing and providing the interface to the cell body, further subdivisions are made. The identification of relations between the individual methods for solving the subsystems builds the fundament for the combination to the overall design process.
The evaluation of the underlying methods shall be initiated at an early stage of the investigations and realized by numerical computation and experimental tests. A progressive improvement process is to be implemented, which allows for the evaluation and enhancement of the subsystems and the related methods. The overall aim of creating a generic process for the holistic design of PACS on the basis of validated methods shall thus be achieved.

Research methodology

The research methodology, which is depicted in Figure 1-20, middle column, is based on the research hypothesis, provides the framework for the herein presented research results and shall be described in the following. Building on the underlying publications, open conceptual issues shall be identified and solved. With the top-down decomposition, a reasonable subdivision of the system is processed repeatedly and the according requirements are determined after the analysis of subsystems. The associated complexity management supports the identification of unresolved problems. In the reverse direction, suitable solutions are developed and investigated. After identifying solutions for each of the subsystems, a property analysis allows for their evaluation. The subsequent combination of solutions provides the input for the superior subsystem. This process is repeated until the highest system level is reached and a global solution for the design of PACS is found.
The accuracy of the resulting design methods is evaluated by experimental test or by validated simulation. The cell closure for example is experimentally tested with specific parameters. A thereby validated numerical model is used to identify the concept's sensitivity to various parameters and to determine their influence on the closure's efficiency. Design methods are identified as invalid when the properties of the therewith created structural subsystem are not consistent with the previously assumed properties. In this case, the true properties have to be reanalysed on the basis of the experimental outcomes. An alternative solution may be selected for this subsystem in case of a degradation of the concept. The necessity of the next step for creating valid design methods depends on the initial grade of knowledge about the respective subsystem. Experimental investigations may allow for the identification of issues, which are not recognised in the initial demand analysis but result in the rejection of the respective concept. A results-based extension of the demand analysis solves the problem of incomplete knowledge at an early stage of research by the integration of an additional control function.
An experimentally validated and successfully tested holistic design process for PACS (see Figure 1-20, right column) results from this methodology. The utilization of this design process for some selected applications demonstrates the functionality and flexibility of the design tool.

Working hypotheses and contents

The contents are organized in eight chapters. The already presented introductory section includes the problem definition, the motivation, the state-of-the-art, the objectives and approach to solution and the outline of this thesis. As depicted in Figure 1-20, left column, the holistic design process consists of

four essential elements, which are subsequently described in one main chapter each. These sections are followed by the experimental evaluation and application of the design process. The following working hypotheses (WH) are deduced from the primary objectives defined in the research hypothesis, correspond to the substantive chapters 2 to 7 and shall guide through this work:

WH-1: A numerical model for the shape optimization and characterization of PACS can be implemented on the basis of fundamental physical principles and under consideration of suitable assumptions.

WH-2: The methods for the transfer between the structural model and the cross-sectional design can be adjusted to consider the model assumptions in the form of boundary conditions such that deviations between model and real structure are minimal.

WH-3: A pressurization system for PACS can be implemented, which is able to bear the occurring cell-axial forces and allows for reliable pressure-tight sealing and sufficient deformability.

WH-4: Critical issues and boundary conditions from the manufacturing and assembly processes can be identified and considered at an early stage of the design process.

WH-5: Numerical and experimental investigations allow for the evaluation and enhancement of the implemented methods.

WH-6: The outcomes of the investigations can be used to implement an experimentally validated generic process for the holistic design of PACS, which can be used flexibly for a wide range of applications.

The computation of the truss geometry, from the determination of the structural model, the shape-optimization process to the simulation and characterization of PACS are discussed in chapter 2. Partial solutions are already described in the underlying literature, as presented in chapter 1.3.5. The methods for characterizing PACS, for simulating its load and parameter-dependent properties and for computing the resulting structural stresses are provided in full and expand the state of research.
The approach for deducing a cross-sectional design from the two-dimensional truss model considers the simulated structural loads for the geometrical sizing, the positioning and the orientating of hinges and cell sides. This fundamental step to the definition of the three-dimensional cell compound is presented in chapter 3.
A solution for realizing the closure of a shape-variable polygonal cell tube for differential pressures above 0.1 MPa is not available (cf. chapter 1.3.5) but essential for the implementation of PACS. A detailed demand analysis for the cell closure, appropriate concepts and the according characteristics of same are thus provided within chapter 4. Beyond, the method for generating the preferential concept, this section covers the investigation of solutions concerning sealing and fluid flow.
The process for the holistic design of PACS is completed with the examination of manufacturing and assembly issues that are summarized in chapter 5. Depending on the utilized materials and the size of the structure, the manufacturing boundary conditions lead to additional limitations for PACS, which cause repercussions on the design process. The outputs of this chapter allow for the first realization of a real-life PACS.

The subsequent evaluation of the concept and the related design methods are presented in chapter 6. The outcomes of the numerical methods are therein compared with FEM computations and experimental data. Measures are deduced, which enable the progressive improvement of the design process. Remaining inaccuracies of the final design methods are discussed in a critical evaluation.
In chapter 7, the design tool, which bases on the most accurate approach for the design of PACS, is first described in general before it is used for the design of some selected applications.
With the conclusion and outlook, which are presented in chapter 8, the major achievements are summarized and worthwhile objectives for future research on PACS are presented.

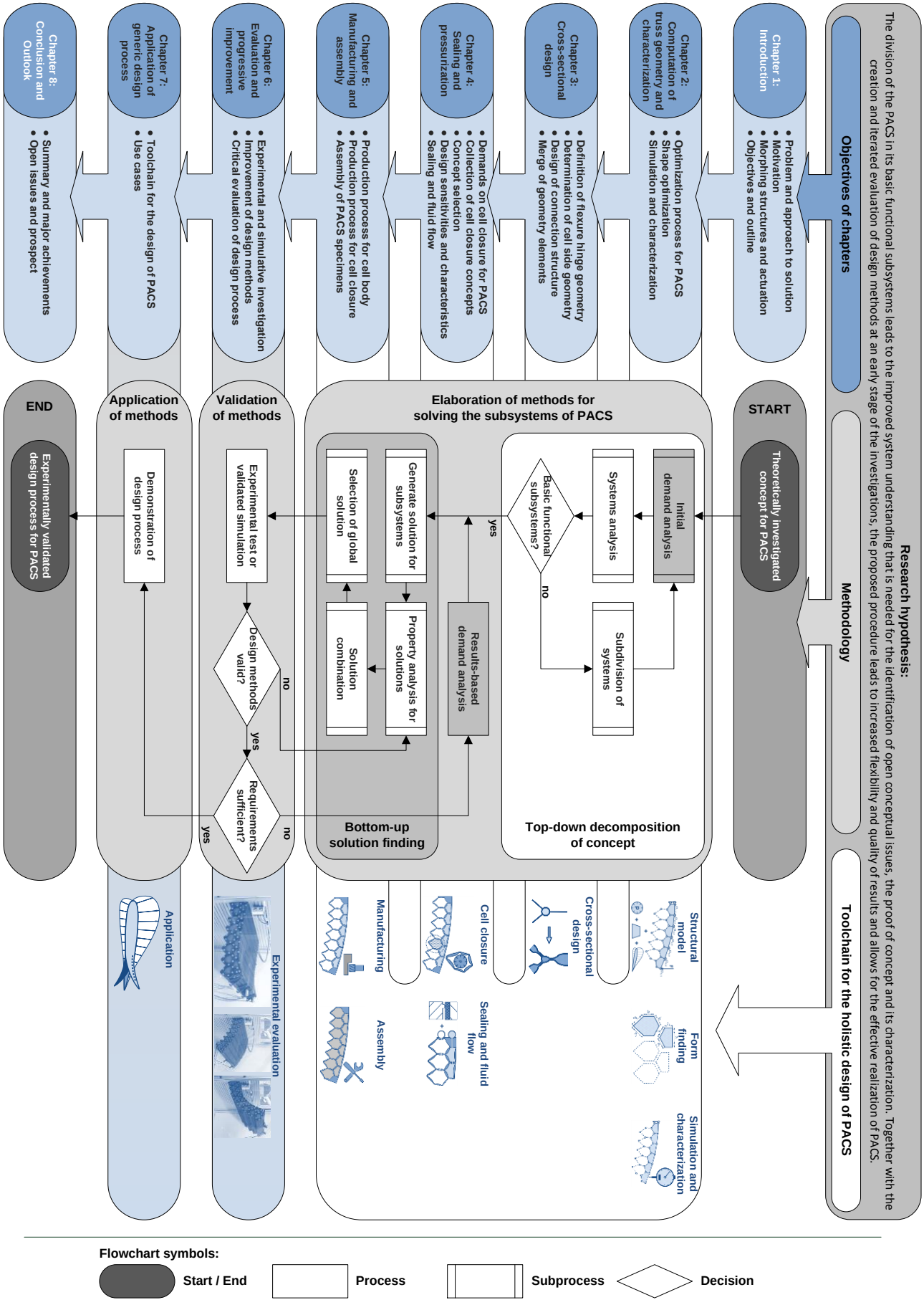

Figure 1-20: Outline of the thesis and flowchart for the conception, the evaluation and the progressive improvement of the design process for PACS

2 Computation of truss geometry and characterization

A PACS can be subdivided in the structural components cell body and cell closure. The herein presented initial design step is used to optimize the cell body structure such that it deforms between predefined target states for specific cell-inherent pressure loads. The shape of the PACS is computed on the basis of a two-dimensional truss-model, consisting of line elements representing the cell sides and point elements representing the flexure hinges, as depicted in Figure 1-16, Figure 1-18 and Figure 1-19. In addition to the shape optimization, structural loads and deformations shall be computed.

According to Eschenauer [152] each process of structural optimization, regardless of the underlying computational methods or target structures, can be organized in *Structural Model*, *Optimization Model*, and *Optimization Algorithm* (cf. Figure 2-1). The structural model includes numerical methods for describing the real structure and its physical behaviour mathematically. Depending on a given set of analysis variables, like DOFs or geometrical parameters, it is used for the computation of the optimization variables, like deformations, stresses, eigenfrequency or energy potential. The results of this computation are used to evaluate the optimization objectives.
The optimization algorithm solves the optimization problem and returns a set of modified design variables that are adapted with respect to the optimization objectives. A gradient-based method thereby calculates the sensitivity of the state variables in terms of a finite change of the design variables.
As part of the optimization model, the design model includes all of the necessary parameters to describe the structural system and provides the input for the structural model. Starting with an initial set of design variables it processes their iterative modification according to the results of the optimization model. The evaluation model forms the other part of the optimization model. It evaluates the outcomes of the structural model in terms of the optimization objectives for fulfilling target functions and boundary conditions and passes the state variables on the optimization algorithm. Figure 2-1 shows the *Three-Columns-Concept* by Eschenauer [152] and includes PACS-specific information.

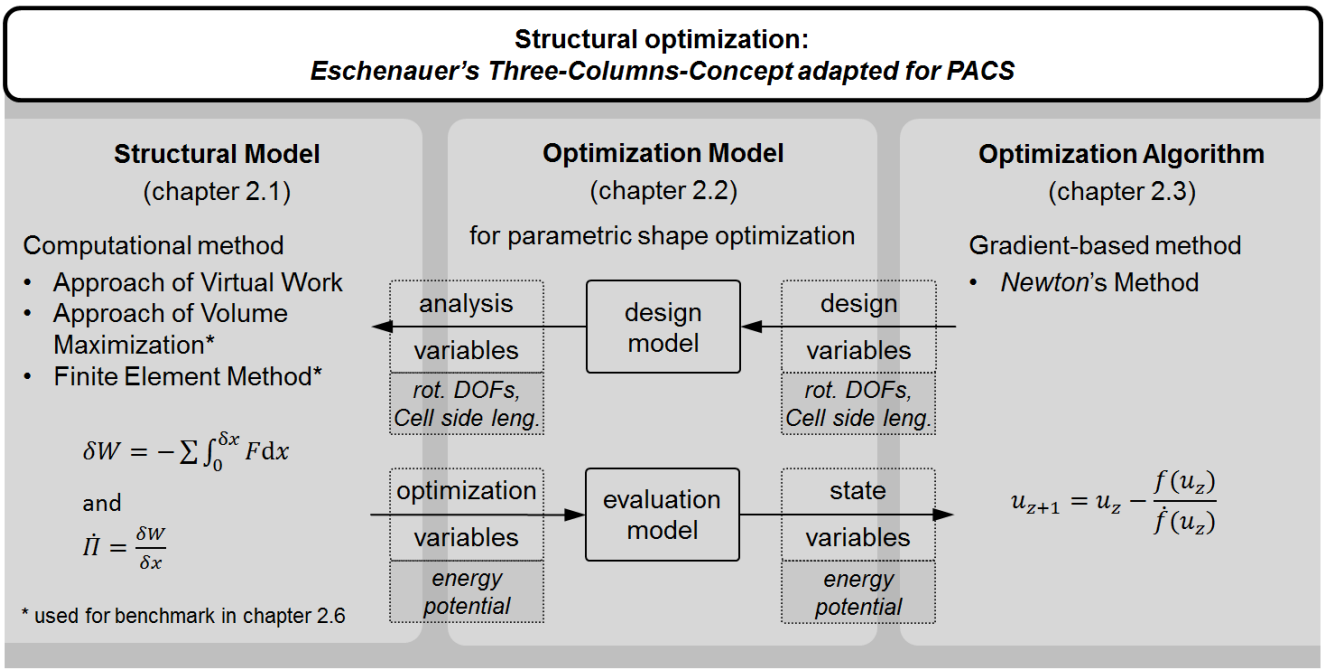

Figure 2-1: *Three-Columns-Concept* for structural optimization by Eschenauer [152] and adaption for the application of PACS

The optimization process is conceived for the computation of two substantial issues. First, the shape optimization shall allow for the determination of target equilibrium states of shape. Second, the equilibrium state of shape and thus the highly nonlinear deformations of the PACS shall be computed for design- and off-design load cases.
Both issues are covered by the optimization procedure that is presented in the following subsections. The structural model, the optimization model and the optimization algorithm are discussed in the chapters 2.1 to 2.3. Subsequently, the optimization procedures for the shape optimization (chapter 2.4) and for the simulation and characterization (chapter 2.5) of a PACS are described. Chapter 2.5 further provides an approach for computing structural loads for all states of shape what allows for the subsequent stress based design of PACS. The application of the underlying methods for the exemplary variable-camber wing structure (chapter 2.6) illustrates a typical optimization process. The outcomes of the optimization process are presented before the deformation and stress reactions of the structure for changing load conditions are simulated. The structural behaviour, by means of deformations and stresses, can thus be investigated for off-design load conditions.

2.1 Structural model

The first subsystem for the structural optimization is the structural model. It includes the numerical approach for describing the physical system. Basing on the input information including the model parameters, it is used to compute the optimization variables. Further, the structural model is used to calculate the structural stresses of the PACS for given load and boundary conditions (LBCs). For the herein developed optimization methods, an approach which is flexible against varying dimensions, levels of detail, changing load types and alternative boundary conditions is essential to meet the demand for generic formulation. Saving computational efforts is thereby advantageous but not of priority.
In the following, the FEM, the *approach of volume maximization* (AVM) and the *approach of virtual work* (AVW) are investigated for their suitability to describe the structural model for PACS. After its utilization for the computation of the optimization variables is described, the most advantageous approach is selected. Different levels of detail are further introduced, which allow reducing initial model assumptions. The influence of the material properties on the design of a PACS is examined and the integration of LBCs in the structural model is described.

2.1.1 Computational methods for describing the physical system of PACS

Three different numerical methods for describing the structural model of a PACS are presented in the following, which allow for the simulation of a PACS and the computation of the optimization objectives. At first, the working principle of the FEM is briefly introduced together with the capabilities of this approach, to give reasons for diverging from standard methods. The AVM is presented secondly. It is utilized by Pagitz et al. [1] for the shape optimization of PACS and to calculate deformations and structural stresses. It represents the only solution for the computation of PACS that is implemented and published prior to this work. An additional approach for describing and solving the physical system of PACS, the energy-potential-based AVW, is introduced. The subsequent comparison of the three methods in terms of the underlying objectives gives reasons for the efforts of investigating the additional approach.

Finite Element Method

The most widely used method for the computation of physical and in particular structural problems is the FEM. The basic method is explained at an exemplary beam structure in appendix A. In the following, its relation to the energy-potential-based approaches AVM and AVW and the simulation process for computing the deformations of a structure are presented in a brief manner.
The FEM is a displacement-based method that profits from the formulation of continuity conditions instead of equilibrium conditions. The straightforward combination of elements with predefined

characteristics by superpositioning its stiffness matrices at given DOFs is shown at the two-bar problem in appendix A. With the ability to map even huge and complex systems with finite elements and to compute also large nonlinear deformations, an enormous applicability results for the FEM that leads to its remarkable success [153]. The level of detail can be adjusted freely by the selection of appropriate elements and by the model resolution, which is controlled by the element size.
The solution process of the FEM is numerical and approximates the system with finite elements of known physical behaviour. Therefor the global stiffness matrix $\boldsymbol{K}$ is calculated, which relates the deformation $\boldsymbol{u}$ to the vector of internal or external forces $\boldsymbol{f}$:

$$\boldsymbol{f} = \boldsymbol{K}\boldsymbol{u} \overset{equil.}{=} 0. \tag{2.1}$$

For large deformations $\boldsymbol{u}$, which have to be considered for the simulation of the PACS, geometric nonlinear analysis are to be performed to take the associated change of the position and amount of internal and external forces into account. Therefore, an iterative approach is used, which optimizes $\boldsymbol{u}$ to find the equilibrium state of shape of the structure. According to equation (2.1) it is found, when the force vector $\boldsymbol{f}$ vanishes.
The most simplified FEM-model for PACS, which fulfils the requirements of the implementation of loads and the calculation of huge deformations, consists of one beam element per cell side and hinge region. Additional information about the kinematics of a PACS is redundant. A disadvantage of the FEM arises from the coupling of forces and displacements, as they cannot be regarded separately from each other. In the two-dimensional space each finite element considers at least three DOFs per beam end, consisting of one rotational DOF and two translational DOFs. The model of a single PACS cell with n edges is thereby described with at least $2n$ beam elements and $6n$ independent state variables. The subsequently presented approaches allow reducing the number of independent state variables substantially by including simplifying assumptions and kinematic constraints.

Approach of volume maximization (AVM)

For a polygonal single cell as well as for a cellular structure with multiple cell rows that consist of pentagonal and hexagonal cells, the equilibrium state can alternatively be found by utilizing the AVM. The behaviour of pressurized systems to deform into a state of maximum volume V is thereby utilized. This endeavour bases on the 2nd law of thermodynamics, which demands an increase of entropy S for any spontaneous change of state. For a closed thermodynamic system, the amount of substance n_m and the universal gas constant R_m are invariable. At a constant temperature T, a decline of inner energy $\Delta U < 0$ causes a raise of entropy $\mathcal{S}$ due to the reduction of the enthalpy ΔH:

$$\Delta \mathcal{S} = -\frac{\Delta H}{T}, \text{ with} \tag{2.2}$$

$$\Delta H = \Delta U + \underbrace{\Delta n_m R_m T}_{const}. \tag{2.3}$$

The relation between the inner energy and the change of the cell-inherent volume, which ultimately results in a change of the entropy $\Delta \mathcal{S}$ is given by

$$\Delta U = -\int \underbrace{(p(V) - p_\infty)}_{const}\, dV = (p - p_\infty)(V_1 - V_2). \tag{2.4}$$

Pagitz et al. [1] make use of this relation and formulate the equation for calculating the equilibrium state of a cellular structure to

$$\boldsymbol{f} = \sum \boldsymbol{f}_{Pent} + \sum \boldsymbol{f}_{Hex} = \sum p_{Pent} \frac{\partial V_{Pent}}{\partial \boldsymbol{u}_{Pent}} + \sum p_{Hex} \frac{\partial V_{Hex}}{\partial \boldsymbol{u}_{Hex}} \overset{equil.}{=} 0. \tag{2.5}$$

The global force vector $\boldsymbol{f}$ for all pentagonal cells with pressure p_{Pent} and volume V_{Pent} and hexagonal cells with pressure p_{Hex} and volume V_{Hex} vanishes in equilibrium. It is calculated as the sum of weighted derivatives of the cells' volumes V_{Pent} and V_{Hex} with respect to the vector of rotational degrees of freedom $\boldsymbol{u}_{Pent}$ and $\boldsymbol{u}_{Hex}$ of the pentagonal and hexagonal cells. The minimum number of independent state variables, which allows to completely describe the shape of a polygonal cell with n edges and thus to compute its volume V, is $n-3$ (cf. Figure 1-16). Compared to the FEM, the AVM thus significantly reduces the numerical efforts for both, the computation of deformations and the structural optimization. The optimization process for PACS that is used by Pagitz is presented in a more detailed description in appendix B.

Approach of virtual work (AVW)

The AVW is the most basic approach compared with the herein discussed variants for describing the structural model for PACS. Both, the FEM and the AVM can be derived from the AVW. Despite this hierarchical relationship, the three structural models are presented one after the other, in order to set the focus on their properties and the differences between them.

The AVW can be used to simulate structural systems consisting of rigid or elastic components. It is equal to an analysis of the energy potential for only conservative forces being considered. Forces are called conservative, when the performed work is independent of the pathway of the causing forces. For the optimization of PACS, sources for non-conservative forces, like friction and plasticity, are assumed to be negligible. The potential energy Π of a system that consists of multiple elements is thereby defined as the negative work W that is caused by the sum of all conservative forces F with related displacement x:

$$\Pi = -W = -\sum \int F dx. \tag{2.6}$$

Through the universal nature of this approach, it can be modified for the consideration of multiple force types. The basic method of the AVW can be understood as an analysis of the change of the potential energy $\partial\Pi$ due to infinitesimal structural deformations ∂u. The relation between the vector of energy potential $\dot{\boldsymbol{\Pi}}$, which is equal to the force vector $\boldsymbol{f}$, and the virtual work δW due to the vector of virtual displacement $\delta\boldsymbol{u}$ is

$$\dot{\boldsymbol{\Pi}} = \frac{\partial \Pi}{\partial \boldsymbol{u}} = -\frac{\delta W}{\delta \boldsymbol{u}} = \boldsymbol{f} \overset{equil.}{=} 0. \tag{2.7}$$

The equilibrium state of a structure is found for a vanishing vector of energy potentials $\dot{\boldsymbol{\Pi}}$, respectively a vanishing force vector $\boldsymbol{f}$. The energy potential $\dot{\Pi}$ represents the optimization variable for the subsequent shape optimization, the computation of deformations and stresses. Also for this approach, the length of the vector of independent state variables $\boldsymbol{u}$ for a polygonal cell with n edges is $n-2$.

A similar approach that also bases on the AVW is used by Vos et al. [142] for the computation of the equilibrium state of the PAH. The necessity to consider pressure-induced loads as well as single forces and momentums within the structural model, led to their decision of choosing the AVW as structural model for simulating the PAH.

Comparison of numerical methods and selection

Compared to the FEM, the AVM and the AVW significantly reduce the number of independent state variables. This is made possible by the implementation of constraints for the consideration of the closed-cell kinematics and by avoiding the coupling between forces and displacements. A further disadvantage of the FEM compared to the AVW is that it cannot be adapted for shape optimization as efficiently. Although an optimization algorithm utilizing *Newton*'s method is conceivable, it relies on the computation of cell side length dependent deformations. A plurality of geometrical nonlinear calculations is necessary to determine the respective sensitivity matrix, which relates the variation of cell side lengths to the change of deformations.

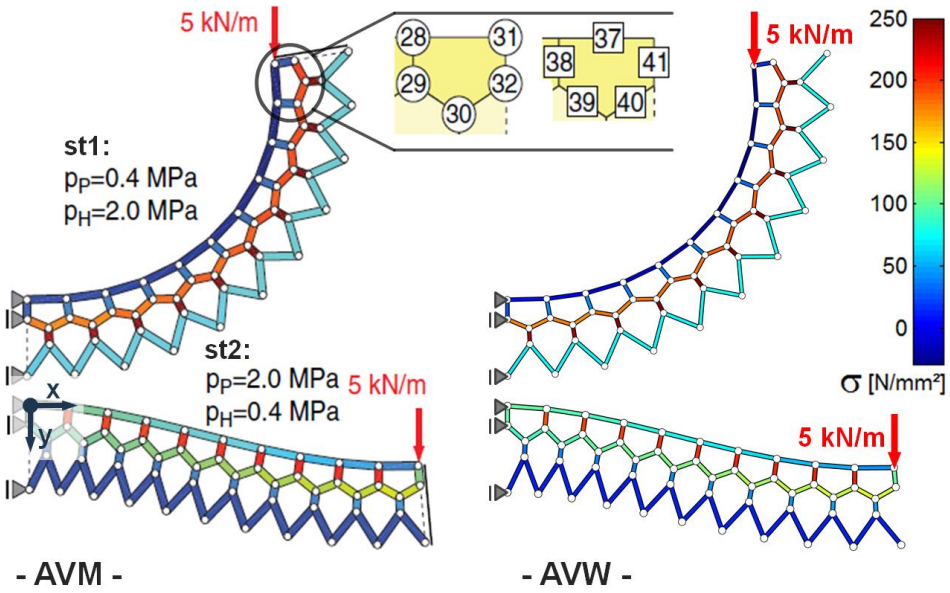

Figure 2-2: Visual comparison of deformational and stress results between the AVM (l.) [1] and the AVW (r.)

Both alternative solutions allow circumventing this additional numerical detour by reorganizing the vector of known and unknown variables to directly compute the sensitivity of the structural system to the change of cell side lengths (cf. chapter 2.4).
For the calculation of structural stresses and the determination of the highly nonlinear deformations, the FEM provides a suitable approach. For the shape optimization of PACS, the implementation of the specialised AVW and the AVM are more advantageous. As all of the three objectives are only reached with the alternative approaches in a sufficient manner, FEM computations with high level of detail are only used for evaluating the outcomes of the design process for PACS (cf. chapter 6).

With the initially presented AVM that is published by Pagitz et al. [145] and the herein utilized AVW equal results are achieved. Though both models base on significantly different mathematical formulations for the computation of the force vector $\boldsymbol{f}$, the equations for describing the equilibrium state of shape (2.5) and (2.7) are finally identical. To prove the accordance of both approaches, the deformation and stress results for a loaded cantilever that are calculated according to the AVW are compared with the ones that are published by Pagitz et al. [1] who use the AVM.
Figure 2-2 illustrates a truss model of the deformed double row PACS cantilever, which is used for the comparison. Cell side stresses for the AVM, left, and the AVW, right, are visualized. For the AVW the virtual rotation $\delta u = 2e\text{-}6$ is used. $Max\left|\dot{\boldsymbol{\Pi}}\right| < \eta_{\dot{\Pi}} = 1e-5$ is chosen as stop criterion for the iterative process. The mathematical representation is further implemented according to modelling variant 1, which is introduced and described in detail in 2.1.2. The underlying information about geometry and LBCs are given in appendix C.

The following listing provides a quantitative comparison of the computational outcomes. Table 2-1 and Table 2-2 include the hinge positions and cell side longitudinal stresses for the rightmost pentagonal cell of the depicted cantilever. The two states of shape, which result from different pressurization conditions, are identified with $st1$ and $st2$. The nomenclature for hinge points and cell sides can be obtained from Figure 2-2. The maximum relative deviations of $\eta_{xy,max} = \max(\eta_x, \eta_y) = 2.18e\text{-}5$, with $\eta_x = x_{AVW}/x_{AVM}$ and $\eta_y = y_{AVW}/y_{AVM}$, for hinge coordinates and of $\eta_{\sigma,max} = \max(\eta_\sigma) = 1.12\text{e-}5$, with $\eta_\sigma = \sigma_{AVW}/\sigma_{AVM}$, for stresses result and verify the accordance of both approaches. Both approaches ultimately base on the minimization of the potential energy of the structure. The quality of results that can be achieved with bot structural models is thus comparably high.

Table 2-1: Hinge coordinates at equilibrium state resulting from the AVW and relative deviation from the outcomes of the AVM

Hinge position	28	29	30	31	32
$x_{st1,AVW}$ [mm]	634.7526	684.7465	706.0382	628.0246	677.3419
$\eta_{st1,x}$ [mm]	**1.66E-05**	**1.53E-05**	**1.72E-05**	**2.18E-05**	**2.06E-05**
$y_{st1,AVW}$ [mm]	-497.7714	-496.9911	-553.0862	-597.5448	-605.7789
$\eta_{st1,y}$ [mm]	**-1.47E-05**	**-1.76E-05**	**-1.72E-05**	**-1.19E-05**	**-1.43E-05**
$x_{st2,AVW}$ [mm]	884.3754	884.3366	937.0098	984.3712	989.0498
$\eta_{st2,x}$ [mm]	**-1.05E-06**	**-1.32E-06**	**-1.45E-06**	**-1.00E-06**	**-1.20E-06**
$y_{st2,AVW}$ [mm]	157.5725	207.5725	236.3046	156.6603	206.4409
$\eta_{st2,y}$ [mm]	**8.35E-06**	**5.78E-06**	**5.91E-06**	**1.12E-05**	**8.61E-06**

Table 2-2: Cell-side-longitudinal stresses at equilibrium state for the AVW and relative deviation from the outcomes of the AVM

Cell side	37	38	39	40	41
$\sigma_{st1,AVW}$ [MPa]	-29.4297	33.7916	192.5066	193.2167	17.8446
$\eta_{st1,\sigma}$ [MPa]	**1.21E-06**	**1.64E-06**	**2.04E-06**	**1.09E-06**	**-9.41E-06**
$\sigma_{st2,AVW}$ [MPa]	42.7882	204.0865	133.5502	131.7478	98.2794
$\eta_{st2,\sigma}$ [MPa]	**-2.96E-06**	**1.42E-06**	**1.29E-06**	**1.37E-06**	**-1.34E-07**

In contrast to the computation of the local energy potential by including the forces that act on each single structural element, the AVM summarizes the pressure-dependent forces of a complete cell by simply multiplying the volume of a cell with the cell-internal pressure value. The major advantage with the AVM is thus the related reduction of the computational efforts for each iteration step. Condensing the potential energy of all structural elements of a cell to a single equation accelerates the computation of stresses, deformations and of the structural shape. However, this model is optimized to consider the cell internal pressure loads and not arbitrary external forces. The utilization of the AVM for the computation of deformations and for structural optimization is explained in appendix B.
For the purpose of including the rotational stiffness of compliant hinges, external point, line and areal loads, the flexibility of the AVW provides decisive advantages. All of these load types can be included without an adaption of the underlying structural model (see chapter 2.1.4). Also geometrical changes in terms of boundary conditions or the number of cell sides of single or multiple cells may be made. Regarding the demand on the structural model to allow for ongoing model enhancements, the flexibility of the AVW, is highly appreciated. A novel approach for the optimization of the PACS further allows for a significant reduction of computational efforts (cf. chapter 2.4) by reducing the necessary number of iterations for minimizing the energy potential $\dot{\Pi}$.

2.1.2 Levels of detail and corresponding assumptions

At first, different levels of detail are discussed, which distinguish themselves in terms of complexity and accuracy. The assumptions for the most simplified implementation are listed and reduced for increasing modelling accuracy. Following this, the design differences between the implemented modelling variants and the respective reasons for the further development are described. A comparison with FEM-based results allows to analyse the achieved accuracy and thus to evaluate the increased computational efforts.
For the conceptual idea of PACS multiple polygonal single cells, which consist of rigid cell sides that are connected by flexible hinges, are combined to a cell compound. The low bending stiffness of the flexure hinges compared to that of cell sides, together with the applied loads lead to the PACS's pressure-dependent deformation behaviour. The cell body geometry and the applied loads are assumed not to change in depth direction.

Table 2-3: Cell elements and associated stiffness and hinge eccentricity assumptions for five different modelling variants

Structural model	**Variant 1**	**Variant 2**	**Variant 3**	**Variant 4**	**Variant 5**
Cell side stiffness [EI, EA]	[∞, ∞]	[∞, ∞]	[∞, ∞]	[EI, ∞]	[EI, EA]
Hinge stiffness [EI, EA]	[0, ∞]	[EI,∞]	[EI,∞]	[EI, ∞]	[EI, EA]
Hinge eccentricity [ζ]	[0]	[0]	[ζ]	[ζ]	[ζ]
Illustration	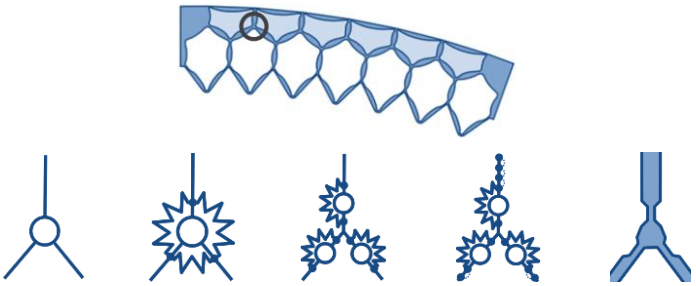				
Complexity / Accuracy					
Status	Implemented with AVW	| Prospect |	FEM		

A two-dimensional cross-sectional model is thus used for all levels of detail to save computation time. The simplest implementation (variant 1) that is able to differentiate between the two structural elements and to reproduce the deformation behaviour of the structure consists of rigid line elements for cell sides, which are interlinked by flexible point elements representing the hinges. Basing on this reduced level of detail, which is used for the initial computation of a PACS structure, the investigation of the concept's potentials is processed. In order to enhance the quality of the structural model and to eliminate sources for variances, it is expanded and supplemented by additional structural mechanisms. Depending on the underlying assumptions behind the calculations and the according level of detail that is used for the modelling of the structure, five possible variants are deduced and specified in Table 2-3. The variants 1 to 3 are part of the following chapters and implemented with the AVW (see chapter 2.1.1), variant 4 is exemplary and gives a prospect to the future work and variant 5 is covered by FEM computations. Already the lowest level of accuracy, variant 1, provides the possibility for shape optimization and to compute deformations and stresses. In this case, both the cell side bending (EI) and its longitudinal stiffness (EA) are assumed to be infinite. The hinges possess infinitesimal bending stiffness and concentrate locally at the crossover of cell sides. The bending stiffness of the related flexure hinges is implemented in variant 2. Variant 3 additionally includes the eccentricity of the hinge elements, which is inevitable for the herein investigated PACS with flexure hinges. The illustrations within Table 2-3 show a symbolic representation of the structural model. The thickness distribution for hinges and cell sides that is shown for variant 5 is exemplary and only illustrates the necessary difference of hinge and cell side thicknesses for ensuring the flexure hinges' functionality. Dynamic loads and the dynamic structural response on a change of loads are not considered in any of the herein presented computations. The properties of each implemented design variant are discussed in the following. The evaluation of the accuracy of the different modelling types is presented subsequently.

Variant 1: Infinitesimal hinge stiffness

The most simplified model for describing PACS bases on a two-dimensional representation that consists of rigid cell sides and articulated joints at the cell side's crossovers. The rotational stiffness of the hinges is assumed to be infinitesimal for this modelling variant. The resulting properties for the hinge thus correspond to a conventional hinge. Figure 2-3 shows a representative section of this structural model. Although this type of model allows simulating the deformational behaviour of PACS, the accuracy of results for the herein investigated compliant structure suffers from this simplification.

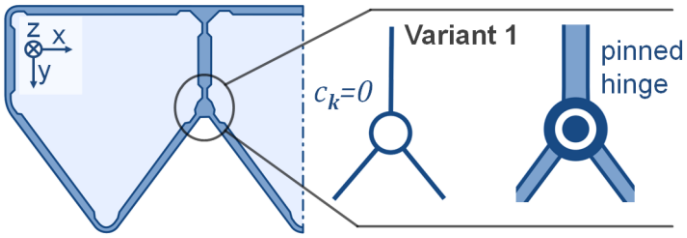

Figure 2-3: Hinge joint with infinitesimal rotational stiffness, cross-section of target structure (l.), implementation in structural model (m.) and structural equivalent (r.)

As depicted in Figure 2-4, the cell side perpendicular forces $F(x)$ at the position x due to the pressure load p on the cell side a of a pentagonal PACS cell induces the given distribution of cell side axial forces $N(x)$ and transverse forces $Q(x)$. The resulting moments $M(x)$ are responsible for the rotational deformation of hinges and thus the variation of the cell's shape.

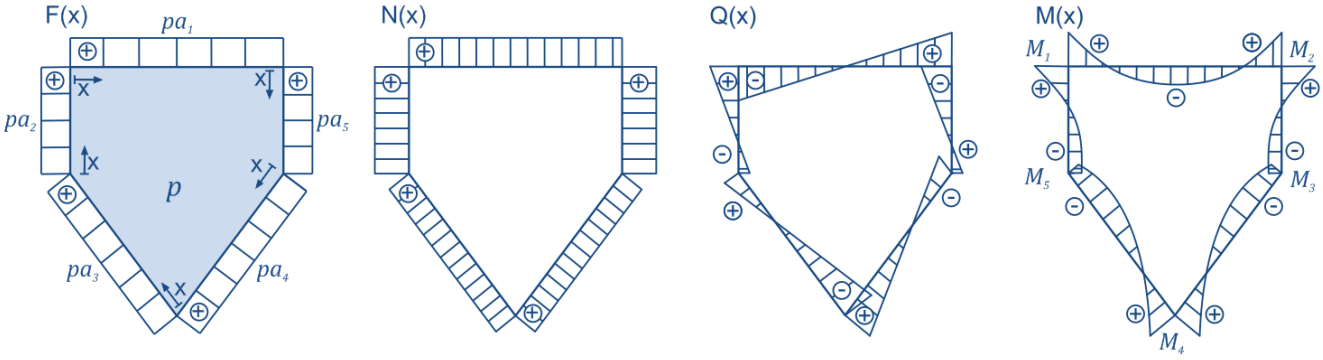

Figure 2-4: Qualitative presentation of forces F(x) that result from the cell inherent pressure p, and the resulting axial loads N(x), transverse loads Q(x) and moments M(x) within an exemplary PACS cell

The assumptions that reduce the real structure to variant 1 of the structural model are summarized in Table 2-4. For infinitesimal hinge stiffness the equilibrium state of shape is not reached until all hinge moments M_k at hinge k vanish. Infinite as well as infinitesimal pressures are leading to residual moments M_k at any state of shape, which does not provide the maximum cell-inherent volume.

Table 2-4: Assumptions of modelling variant 1

	Label	Description
Hinge	A-H1	Hinge bending stiffness neglected
	A-H2	Hinge longitudinal stiffness neglected
	A-H3	Hinge eccentricity neglected
	A-H4	Concentrated one-dimensional hinges
	A-H5	Thickness transition hinge - cell side neglected
	A-H6	Nonlinear material behaviour neglected
	A-H7	Transversal contraction in depth direction neglected
Cell side	A-CS1	Cell side bending neglected
	A-CS2	Cell-side-longitudinal elongation neglected
	A-CS3	Nonlinear material behaviour neglected
Cell closure	A-CC1	Structural cell closure stiffness neglected
	A-CC2	Pressure-induced forces on cell body neglected
	A-CC3	Influence of cross-sectional variance at edge region neglected
Pressure supply	A-PS1	Non-uniform pressure load over cell side lengths neglected
	A-PS2	Influence of cross-sectional variance for fluid channels neglected

Hence, considering modelling variant 1, the state of shape of a single PACS cell does not depend on the amount of pressure. Due to the implemented stiffness properties of cell sides and hinges an elongation of the respective elements cannot be taken into account. Also the consideration of cell side bending, the eccentric design of hinges at cell side crossovers and the geometrical transition area between hinges and cell sides is omitted. The effects of the cell closure with its pressure-dependent influence on the global structural stiffness are neglected. Also deviations from the constant pressurization over the cell side lengths are neglected in this model but may be relevant for a real-life PACS.

Although the basic behaviour of a PACS can be computed by modelling variant 1, the related assumptions result in deformational deviations and variations that concern structural stresses. At the example of a double row PACS the magnitude of deviations compared to the FEM approach is quantified for the model variants 1 to 3 in the following. The results are visualized in Figure 2-8.

Variant 2: Finite hinge stiffness

In contrary to the implementation of variant 1, the cells of the herein dimensioned compliant PACS are not modelled with discrete hinges of infinitesimal stiffness. In common with the functional principle of pressure-actuated nastic plant, as nature's equivalent, modelling variant 2 considers the bending stiffness of flexure hinges. Though a PACS that utilizes pinned hinge joints is conceivable, compliant mechanisms hold two essential advantages. According to the plant cell a compliant PACS cell can be manufactured with gas-tight cell walls without any auxiliary structure. Beyond that, the integral design of a compliant PACS saves weight and substitutes the respective assembly process. For the calculation of the equilibrium state of shape, the computation of structural loads and for the shape optimization, the integration of the finite hinge stiffness in the numerical model enhances the accuracy of results. Most of the assumptions of Table 2-4 are still valid. This section extends the presented model variant 1 by dropping the assumption A-H1 by the implementation of finite hinge stiffness.
The flexural stiffness c for a compliant hinge joint, which leads to a rotational deformation Δu due to a moment M, can be approximated by calculating the bending stiffness of a beam with the second moment of inertia I_z, the length s, the thickness t and the depth d (see Figure 2-5). For a material with a *Young*'s modulus E it results in

$$c = \frac{M}{\Delta u} = \frac{EI_z}{s} = E\frac{dt^3}{12s}. \tag{2.8}$$

As depicted in Figure 2-5, the eccentric hinges at the positions $[\boldsymbol{k}, 1]$ and $[\mathbf{k}, 2]$ are combined to locally concentrated one-dimensional hinge elements. The vector $\boldsymbol{k}$ identifies the hinge position within the PACS cell compound. It is described after the selection of the structural model variant in chapter 2.1.3.

The cumulative hinge stiffness $c_{\boldsymbol{k}}$ is calculated by evaluating

$$c_{\boldsymbol{k}} = \frac{1}{1/c_{\boldsymbol{k},1} + 1/c_{\boldsymbol{k},2}}. \tag{2.9}$$

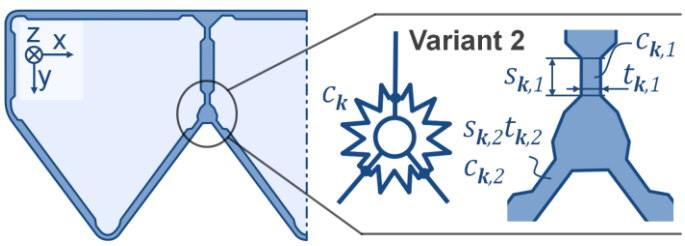

Figure 2-5: Compliant hinge elements with wall thickness t_k and length s_k and resulting bending stiffness c_k, cross-section of target structure (l.), implementation in structural model (m.) and structural equivalent (r.)

The hinge stiffness can thus be considered in the AVW by evaluating the related potential energy due to bending. The number of necessary input variables is increased. However, the effects on the computation time are negligible. The hinge stiffness is assumed constant and the hinge angles are known for each state of shape. The AVW thus allows this enhancement of the model without involving additional DOFs and with approximately constant computational efforts. However, an important increase of the quality of results can be achieved (cf. Figure 2-8).

Variant 3: Eccentric compliant hinges

Without a novel element description variant 3, provides a remedy for the assumption of neglected hinge eccentricity A-H3. In a real-life PACS structure the hinge length varies between about five and twenty percent of the cell size. As the centre of a flexure hinge cannot coincide with the intersection point of linked cell sides, the dislocation of the hinge position is on the same scale. Figure 2-6, right, shows the crossover of cell sides for a cell compound made of GFRP (for further detail, see chapter 6.1.3) with a cell width of fifty millimetres and gives an example for the need for hinge eccentricity.
The implementation of eccentric flexure hinge elements results in an increase of DOFs but leads to a more detailed and realistic model. In order to consider the computation efforts the number of additional DOFs has to be kept small. The eccentric hinge is thus modelled as rigid triangle with fixed side lengths and only one rotational DOF $u_{\zeta,\boldsymbol{k}}$ that describes its orientation about the z-axis. A suitable way to describe this triangle is depicted in Figure 2-6, left. The eccentricity $\zeta_{\boldsymbol{k}}$ at hinge $\boldsymbol{k}$ defines the geometry of the element in the structural model.

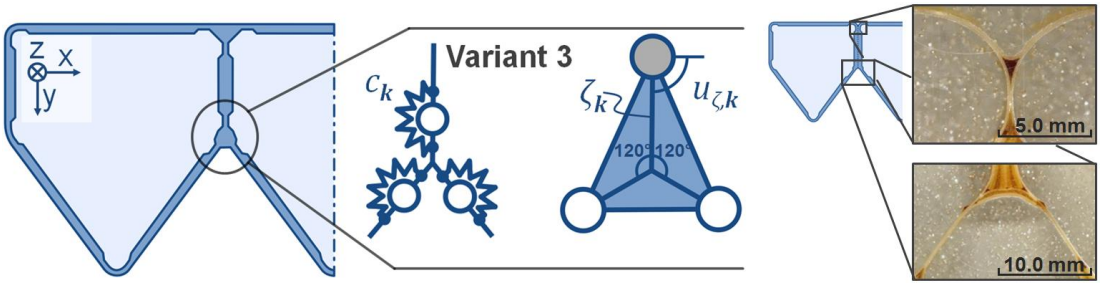

Figure 2-6: Definition and notation of eccentric compliant hinge element, cross-section of target structure (l.), implementation in structural model and necessary parameters (m.) and exemplary realization of eccentric compliant hinges at crossing points of adjacent cells (r.)

The equations for calculating the energy potential for a PACS are still valid. The risen number of DOFs however increases the necessary computations for determining the equilibrium state. The profitability of this approach under consideration of the computational accuracy and the related additional computational effort is evaluated in the following.

Accuracy of modelling variants and selection

Differences in accuracy of the three presented implementations utilizing the AVW are illustrated in this exemplary comparison. The outcomes summarize the presented work on the numerical computation of compliant PACS and assess the quality of the obtained results according to the concomitant efforts.
The target structure is a double row PACS cantilever. It consists of six equally shaped pentagonal cells in the first row and five identical hexagonal cells plus two boundary cells in the second row. The structure is designed to deform from an initially straight manufacturing shape into a shape in which the surface cell sides describe a circular arc with variable curvature. Due to the equality of the cells' geometry, each cell contributes similarly to the deformation. For the evaluation of the deformation accuracy, it is thus applicable to analyse the angle $\Delta\beta$ which cumulates all deformations between the left support and the rightmost cell. The angle $\Delta\beta$ is measured at the first cell side of the sixth pentagonal cell (see Figure 2-8). Compared to the evaluation of a translational value, the angular value is independent of the structure's dimensions.

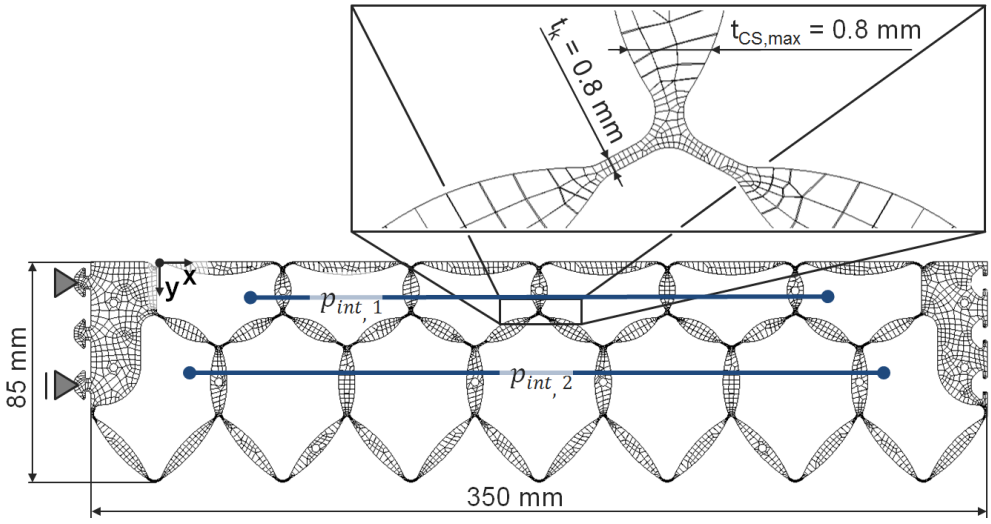

Figure 2-7: FEM model of the investigated double row PACS cantilever

Another reasonable value for this comparison would be given by the root mean square (RMS) value of all surface angles. As this value equally is of cumulative nature, an increased expressiveness compared to the angle $\Delta\beta$ is not given. For reasons of transparency and straightforwardness, the angle $\Delta\beta$ is used for this and all similar investigations.

The length of the cantilever is $350\ mm$ and it consists of a polyamide material with an assumed linear-elastic stiffness behaviour and a *Young*'s modulus of $E = 2.0\ GPa$. The pressure values are chosen to cover both, a state of shape near the deformational convergence (cf. chapter 2.5.4), which results from the high pressure $\boldsymbol{p}_{int,I} = [0.05, 0.5]\ MPa$, and another, for the lower pressure $\boldsymbol{p}_{int,II} = [0.1, 0.01]\ MPa$. The low pressure state is examined additionally due to the increased sensitivity of deformations to variances of internal and external forces and especially to deviations that are caused by model assumption.

The PACS structure, which is shown in Figure 2-7, is additionally calculated with the FEM tool *Ansys* (variant 5) in order to provide the reference values for the comparison. As it can be seen in the enlarged section the herein used cross-sectional geometry differs from the schematic sketch within Figure 2-6. At this state of research, load-based design process was not yet available. The depicted structure thus represents the results of an early design approach which aimed at limiting peak stresses by manually smoothing the transition between hinge and cell side elements. Two separate regions are defined to create the mesh of the structure. The cell side elements are determined to have an element edge length of $2\ mm$, hinge regions are modelled with a refined average edged length of $0.3\ mm$. The three-dimensional structural FEM model is built of linear *Solid186* elements. The deformational outcomes of this FEM-based approach are used as a baseline.

Table 2-5 comprises the quantitative values for the rotational deformation $\Delta\beta$ as well as the percentage variance in relation to the FEM-based results η_{FEM}. An improvement of accuracy from $\eta_{Var1,FEM,I} = \Delta\beta_{Var1,I}/\Delta\beta_{FEM,I} - 1 = 37.14\ \%$ to $\eta_{Var3,FEM,I} = 9.47\ \%$ for the first pressure setting and from $\eta_{Var1,FEM,II} = 85.88\ \%$ to $\eta_{Var3,FEM,II} = 0.59\ \%$ for the second one, clearly confirms the benefit of increased modelling complexity. Comparing the resulting values $\Delta\beta_I$ and $\Delta\beta_{II}$ for different model variants, it can be seen that the consideration of the hinge bending stiffness (*Var1* to *Var2*) reduces deformation. The implementation of eccentric hinges (*Var2* to *Var3*) results in decreased deformations for state *I* and increased deformations for state *II*. The effects are thus case-dependent.

Especially in low pressure regions, which are characterized by a non-converged deformation, the modelling methods including infinite hinge stiffness provide superior results. This can be explained by the stiffening of the overall structure and a decreasing sensitivity against hinge-stiffness-induced forces with rising cell pressures. The eccentricity of the hinge points directly affects the pressure-related energy potential of the pressurized cellular structure. The significance of the impact on the accuracy of computational results is quantified. In Figure 2-8 the deformational results for the loaded structure are visualized for the different modelling variants in an overlapped illustration to simplify the comparison.

Table 2-5: Rotational deformation at cell side one of the sixth pentagonal cell for the three presented modelling variants and deviations from FEM-based results

		Variant 1	Variant 2	Variant 3	Variant 5
$\Delta\beta_I$	[°]	35.04	29.80	27.97	25.55
$\eta_{FEM,I}$	[%]	+37.14	+16.63	+9.47	-
$\Delta\beta_{II}$	[°]	6.32	2.86	3.42	3.40
$\eta_{FEM,II}$	[%]	+85.88	-15.88	+0.59	-

The conception, implementation, extension and evaluation of the structural model for describing the PACS are performed. The computational results from the most accurate AVW-based model, variant 3, differ by $\eta_{Var3,FEM,I} = 9.47\ \%$ and $\eta_{Var3,FEM,II} = 0.59\ \%$ compared to the FEM-based outcomes. An increase of the model accuracy may be demanded within the future work on PACS. For the herein presented research, these values are sufficient. Variant 3 is thus selected for further use within the holistic design process for PACS.

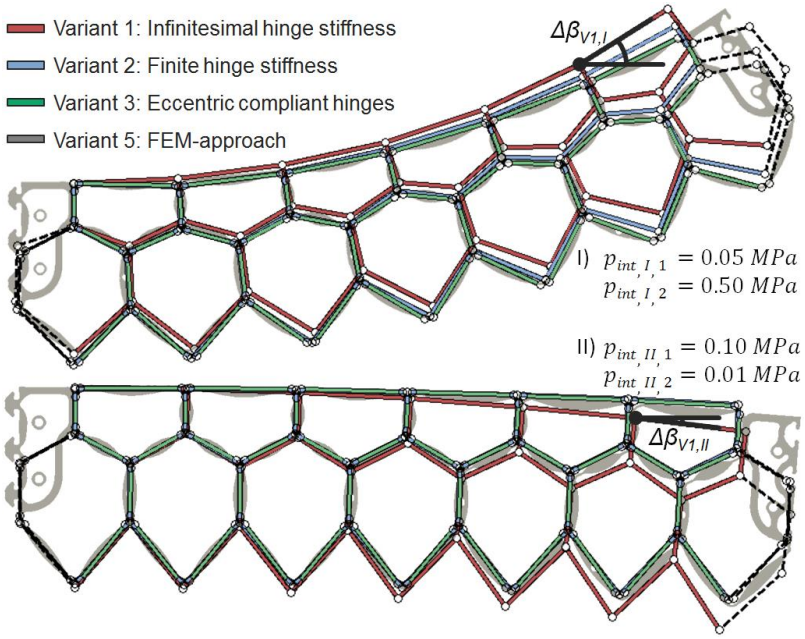

Figure 2-8: Deformations resulting from the different model variants for two pressure settings

2.1.3 Notation for model parameters

For the selected structural model variant, which includes the finite stiffness of flexure hinges and their geometrical eccentricity, the relevant model parameters are identified and labelled in Figure 2-9. The therein presented configuration of PACS consists of two cell rows, pentagonal cells in the first and hexagonal cells in the second cell row and is used throughout this work. The cell side angles u_H, the cell side lengths a_{CS} and the cell side crossover angles u_ζ, which is defined with respect to the x-axis, completely define the shape of the single cells and of the cell compound. The hinge stiffness c_H and the hinge angles u_c are labelled within the cells of the second cell row. These parameters hold the additional information that is necessary to describe the bending stiffness and the curvature of the flexure hinges. The hinge coordinates $\boldsymbol{x}$ entirely depend on the parameters that are shown in the first cell row but are needed for the computation of the structure's energy potential according to chapter 2.1.4 and are thus also listed. All of the individual hinge and cell side related parameters are identified with the position vector $\boldsymbol{k} = [h, i, j]$. It is assembled from the number of the individual cell element j, the number of the cell i that includes this element, with $i = 1$ for the leftmost cell, and the number of the respective cell row h, with $h = 1$ for the topmost cell row.

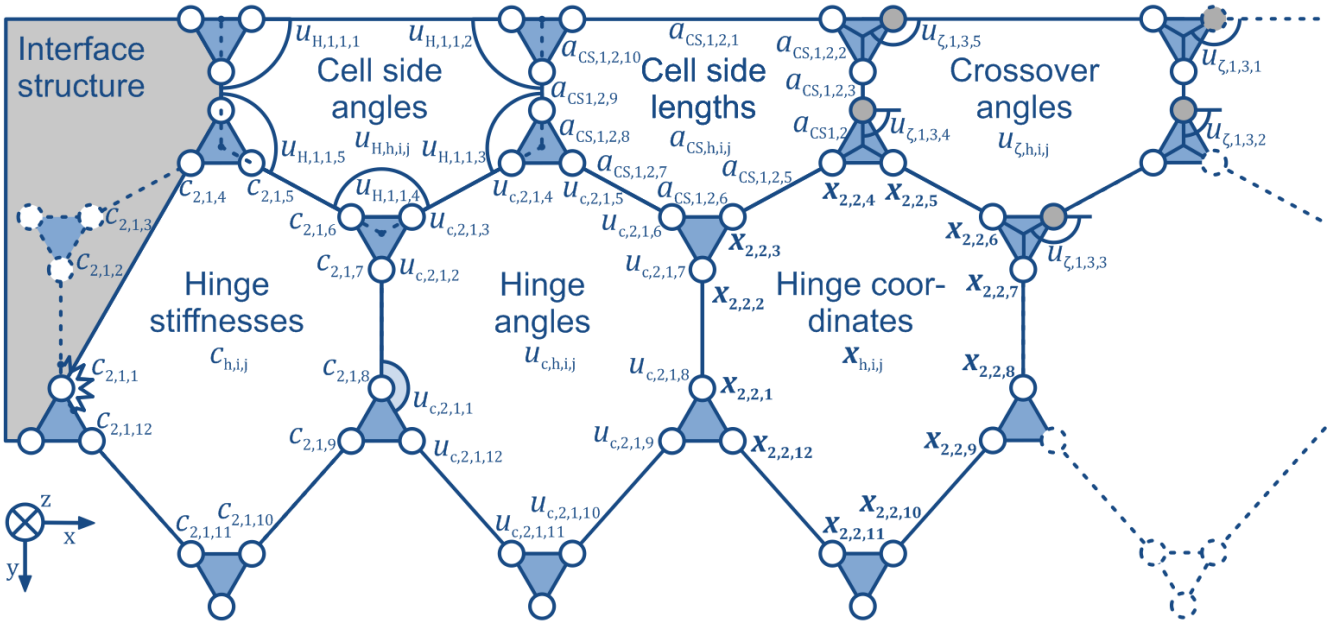

Figure 2-9: Notation for cell side angles u_H, cell side lengths a_{CS}, cell side crossover angles u_ζ, hinge stiffness c, hinge angles u_c and hinge coordinates x

The vector $\boldsymbol{k}$ is exemplarily given in Figure 2-9 for all model parameters that are needed to describe the double-row PACS.
In the following, the herein given notation for the selected model variant 3 is used to describe the formulation of load and boundary conditions, the definition of design and optimization variables, as well as for the analysis of computational results.

2.1.4 Load and boundary conditions within the structural model

The main purpose for each structure and also for PACS is to withstand and bear loads. The extent of the herein described LBCs allows adapting the presented structural model for its utilization for a variety of applications and thus fulfils the requirement for a generic design approach. After a description of the specific load type, its origin and its preparation for computational use, as well as the integration into the numerical approach for the shape-optimization process are presented.

Boundary conditions
The boundary conditions have to be defined according to the requirements of the respective application and are used to describe kinematical constraints like supports. The integration of boundary conditions in the AVW is realized by controlling the vector of independent state variables $\boldsymbol{u}$. Further information about the composition of $\boldsymbol{u}$ is given together with the description of the optimization model in chapter 2.2. The individual independent state variables, which are determined by the definition of a boundary condition, are kept constant, according to

$$u_{\boldsymbol{k}} = const., \tag{2.10}$$

or depend on other independent state variables:

$$u_{\boldsymbol{k}} = funct(\boldsymbol{u}). \tag{2.11}$$

The size of the vector of independent state variable is thus reduced. Due to the decreased number of optimization variables, the calculation effort is reduced for an increasing number of boundary conditions.

The double row structure, which is shown in Figure 2-9, is clamped at its left connection structure. The independent state variables of the first cell row are thereby not affected. For the first cell of the second cell row, however, the number of independent state variables is decreased and the hexagonal cells that are defined by three rotational DOFs are kinematically reduced to pentagonal ones with two rotational DOFs. Also the combination of the first and second cell row leads to a reduction of independent state variables due to the kinematical coupling. In this case, one of the independent state variables of each hexagonal cell is replaced by a dependent state variable, which relates to one or more independent state variables. Figure 2-10 illustrates the typical support and boundary conditions for a double-row PACS and holds the information about the remaining independent state variables that have to be determined within the optimization model.

Distributed cell-side-perpendicular loads

Distributed loads, given as force value per unit length, can be applied to any cell side. The resultant force that acts on the respective cell side is orientated in cell-side-perpendicular direction and depends on the length of the cell side. The distributed load is assumed to be constant over the cell side length. Non-constant distributions can be modelled by defining nodal forces, which are presented afterwards.
Two representatives of such distributed cell-side-perpendicular loads are introduced to be used in the optimization process. As its operating principle bases on the pressurization of polygonal cells, the first and inevitable load type for PACS is defined by the cell-internal fluidic pressure. The second load type is used to describe external pressure loads. The consideration of an aerodynamic pressure distribution that acts on the structure's surface allows designing PACS for aerodynamic applications.
Pressure loads acting on cell sides represent the driving force for deformations and further affect the overall structural stiffness. For the optimization of the PACS the internal cell pressure p_{int} is a necessary input and thus considered as known. With the cell side lengths $\boldsymbol{a}$, the vector of pressure forces results in

$$\boldsymbol{f}_p = p_{int}\boldsymbol{a}d. \tag{2.12}$$

The energy potential can be computed as the derivative of virtual work ∂W at a change of the independent state variable u, with the cell side-perpendicular displacement $\delta r_{p,\boldsymbol{k}}$ at the cell side $\boldsymbol{k}$ and the virtual rotational displacement δu to

$$\dot{\Pi}_p = -\frac{\partial W_p}{\partial u} = -\frac{\sum_{\boldsymbol{k}} f_{p,\boldsymbol{k}}\delta r_{p,\boldsymbol{k}}}{\delta u}. \tag{2.13}$$

External pressure loads, like the herein presented aerodynamic loads, may have critical influence on the resulting deformations of a PACS. A PACS that is used to adjust the shape of a surface in an aerodynamic application for example could not be controlled adequately when the operational loads would not be considered in the structural model. Consequently the deformation and ultimately the aerodynamic reaction on a change of cell internal pressure would be unknown. In the following, the structural model is thus extended for the consideration of the external aerodynamic pressure loads.
Similar to the cell-internal pressure, the aerodynamic pressure load is applied to the surface cell sides of the upper cell row. The related force vector and energy potential are given with

$$\boldsymbol{f}_{ad} = p_{ad}\boldsymbol{a}d \text{ and} \tag{2.14}$$

$$\dot{\Pi}_{ad,e} = -\frac{\partial W_{ad}}{\partial u} = -\frac{\sum_{\boldsymbol{k}} f_{ad,\boldsymbol{k}}\delta r_{ad,\boldsymbol{k}}}{\delta u}. \tag{2.15}$$

Due to the inclusion of aerodynamic forces in the process of shape optimization, additional computations for coupling the aerodynamic reactions on structural deformations are redundant. With this, the target shape of the PACS is controlled in presence of aerodynamic forces.

Moments

For the dimensioning of compliant PACS according to modelling variant 3 (and variant 2), the consideration of the flexure hinge stiffness is essential. A PACS of infinitesimal hinge stiffness would reach its equilibrium state already at an infinitesimal cell pressure. The pressure-dependent deformation behaviour of the PACS is thus highly influenced by the rotational hinge stiffness, which is therefore to be considered in the structural model. The related moment that act on each compliant hinge is determined in dependency of the local hinge deformation $\Delta u_{c,\boldsymbol{k}}$. The computation of the related energy potential is described in the following.

For a constant thickness $t_{\boldsymbol{k}}$ along the flexure hinge, the stiffness $c_{\boldsymbol{k}}$ at hinge $\boldsymbol{k}$ can be calculated according to equation (2.8). For the investigation of the two-dimensional model, the depth $d = 1e3\ mm$ is used. The hinge stiffness can be considered in the structural model by the force vector $\boldsymbol{f}_c$, which depends on the local hinge bending $\Delta \boldsymbol{u}_c$:

$$\boldsymbol{f}_c = -\boldsymbol{c}\Delta \boldsymbol{u}_c. \tag{2.16}$$

The hinge moments are considered in the computation of the energy potential by

$$\dot{\Pi}_c = -\frac{\partial W_c}{\partial u} = -\frac{\sum_{\boldsymbol{k}} f_{c,\boldsymbol{k}} \delta u}{\delta u}. \tag{2.17}$$

As it can be obtained from equation (2.16) the hinge moment $\boldsymbol{f}_c$ counteracts any deformations from the manufacturing state of the structure and is thus negative in the local rotational coordinate system. The subsequently presented loads effect these deformations.

Forces

Forces can be applied in the form of vectors with constant orientation and value to each node respectively hinge. A modular PACS structure is connected at both of its ends and transfers loads. The ability to introduce loads at these ends is thus necessary. The possibility to apply discrete forces also within the structure further allows for the loading of the PACS surface. The applicability of the design process for PACS can thus be expanded for implementations like adaptive seats, lifting mechanisms or gripping tools, as loads are thereby introduced at the structure's surface and at its ends.

Point loads $\boldsymbol{f}_{pl}$ are applied to the model at hinge points, $\boldsymbol{f}_{pl} = \boldsymbol{f}_{pl,\boldsymbol{k}}$, or at additional external points, $\boldsymbol{f}_{pl} = \boldsymbol{f}_{pl,ext,o}$, which are connected rigidly to two hinge points. The related cumulative force vector is

$$\boldsymbol{f}_{pl} = [\boldsymbol{f}_{pl,\boldsymbol{k}} \quad \boldsymbol{f}_{pl,ext,o}]. \tag{2.18}$$

The energy potential is calculated with the force-parallel virtual displacement $\delta r_{pl,\boldsymbol{k}}$, respectively $\delta r_{pl,ext,o}$ resulting from δu, to

$$\dot{\Pi}_{pl} = -\frac{\partial W_{pl}}{\partial u} = -\left(\frac{\sum_{\boldsymbol{k}} f_{pl,\boldsymbol{k}} \delta r_{pl,\boldsymbol{k}}}{\delta u} + \frac{\sum_{\boldsymbol{k}} f_{pl,ext,o} \delta r_{pl,ext,o}}{\delta u}\right). \tag{2.19}$$

A further type of force vector is additionally defined to allow for including forces of inertia. Depending on the acceleration of the structure, the inertial force act in constant direction. It is calculated with knowledge of the applied material's density ρ, the cross-sectional area $A_{\boldsymbol{k}}$ of cell side $\boldsymbol{k}$, the gravitational acceleration $\ddot{x} = g$ and its angular orientation θ in the xy-plane. The resultant force vector is computed by

$$\boldsymbol{f}_{in} = \rho \boldsymbol{A} d \ddot{x} \begin{bmatrix} \cos(\theta) \\ \sin(\theta) \end{bmatrix}. \tag{2.20}$$

Density and acceleration can be identified previously to the shape-optimization process. The cross-sectional area of the PACS in contrast depends on the individual cell-side-length and thickness distribution, which are determined after the shape-optimization procedure. As the inertial forces in turn

affect the resulting truss geometry, an iterative process is used to approach the target state of shape. This process is described in chapter 2.6.2 and exemplary results are given for the variable-camber wing application in chapter 2.6.3. The energy potential is calculated with the inertial-force-parallel component of the virtual displacement $\delta r_{in,\boldsymbol{k}}$, due to a change of the independent state variable u, by

$$\dot{\Pi}_{in} = -\frac{\partial W_{in}}{\partial u} = -\frac{\sum_{\boldsymbol{k}} f_{in,\boldsymbol{k}} \delta r_{in,\boldsymbol{k}}}{\partial u}. \tag{2.21}$$

Assembly to global energy potential

The integration of the essential forces that act on the PACS allows designing a shape-variable structure that moves between predefined form functions in presence of internal and external forces. As determined in Figure 2-1, the necessary output is the global energy potential of the PACS. It is assembled as the sum of all energy potentials:

$$\dot{\Pi} = \dot{\Pi}_p + \dot{\Pi}_{ad} + \dot{\Pi}_c + \dot{\Pi}_{pl} + \dot{\Pi}_{in}. \tag{2.22}$$

With the utilization of the AVW for the consideration of different load types, the presentation of the structural model that is used to describe the physical structure numerically is completed. The evaluation of the energy potential in terms of the optimization objective is performed within the subsequently described optimization model.

2.2 Optimization model

The optimization model can be subdivided in the design model and the evaluation model (cf. Figure 2-1). The design model provides the necessary input parameters that are used to completely describe the physical model in the form of analysis variables. Within the evaluation model, the optimization variables, as the output of the structural model, are evaluated in terms of the optimization objective.

2.2.1 Design model

According to the description of the structural model in chapter 2.1, the necessary parameters for building and evaluating the structural model are to be defined. Cell side angles, cell side lengths and crossover angles (cf. Figure 2-9) have to be defined to describe the initial shape of the structure as starting point for the optimization process. LBCs are further determined. For the definition of the hinge stiffness, the utilized materials are to be specified with regard to their *Young*'s moduli and strength values. With this information, the analysis variables as an input for the structural model are defined.

Cell arrangement and related analysis variables

Figure 2-10 visualizes the selected cell arrangement that is examined in the following. It specifies the boundary conditions in terms of the kinematical connection of neighboured cells and of the connection structure at the PACS's left and right ends. This exemplary cell arrangement that is used in the following to describe the design process for PACS can be characterized by

- two cell rows,
- pentagonal cells in first and hexagonal cells in second cell row and
- a connection structure that demands for one more cell in the second than in the first cell row and fixes specific rotational DOFs at both sides of the second cell row.

In the following, the analysis variables are defined. In addition to the constant LBSs that are introduced in chapter 2.1.4, it comprise of the vector of independent state variables $\boldsymbol{u}$ that describe the rotational DOFs and the vector of cell side lengths $\boldsymbol{a}$, which is used to control the structures deformation behaviour.

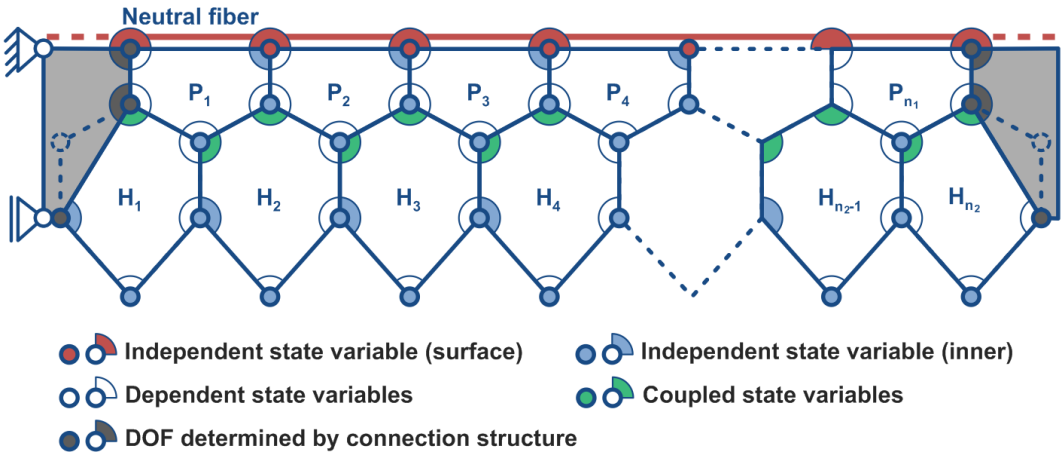

Figure 2-10: Exemplary cell arrangement of PACS and related independent, dependent, coupled and fixed state variables

As the vector of independent state variables $\boldsymbol{u}$ includes surface $\boldsymbol{u}_0$ as well as inner state variables $\boldsymbol{u}_1$, it comprises of

$$\boldsymbol{u} = \begin{bmatrix} \boldsymbol{u}_0 \\ \boldsymbol{u}_1 \end{bmatrix}. \tag{2.23}$$

For given cell side lengths $\boldsymbol{a}$, the outer shape of a PACS can be defined by the independent surface state variables $\boldsymbol{u}_0$, as illustrated in Figure 2-10. Therefore, one cell side angle per pentagonal cell plus one cell side angle for controlling the angle between the neutral fibre and the right hand connection structure are needed. For the application of modelling variant 3, the description of the eccentric hinge elements expands the number of independent state variables by the rotational DOF of the rigid crossing triangle u_ζ (cf. Figure 2-6 and Figure 2-9). The vector of independent surface variables $\boldsymbol{u}_0$ is complemented by one independent angle per pentagonal cell for the orientation of the crossover minus one for the last cell:

$$\boldsymbol{u}_0 = \begin{bmatrix} 2\pi - \frac{\pi}{2} - u_{H,1,1,1}, 2\pi - u_{H,1,1,2} - u_{H,1,2,1}, \dots, 2\pi - u_{H,1,n_1-1,2} - u_{H,1,n_1,1}, 2\pi - \\ u_{H,1,n_1,2} - \frac{\pi}{2}, \\ u_{\zeta,1,1,1}, \dots, u_{\zeta,1,n_1-1,1} \end{bmatrix}. \tag{2.24}$$

For the illustrated double row cantilever the number of independent surface state variables sums up to $2n_1$. The number of cells per cell row h is n_h. The vector of independent inner state variables is $\boldsymbol{u}_1$. It consists of one cell side angle per pentagonal cell and one cell side angle per hexagonal cell minus two fixed ones due to the bearing. It can be seen that one rotational DOF of the first and last cell of the second cell row are determined by the herein utilized design of the connection structure. Additional independent inner state variables are used to describe the orientation of the crossing triangles. Two angles per pentagonal cell and two per hexagonal cell minus two fixed angles have to be defined to specify the shape of a structure, according to Figure 2-10. The length of the vector of independent inner state variables sums up to $3n_1 + 3n_2 - 4$ per state of shape. With $n_2 = n_1 + 1$ for the given cell compound, the length of $\boldsymbol{u}_1$ is $6n_1 - 1$. It is calculated by

$$\boldsymbol{u}_1 = \begin{bmatrix} u_{H,1,1,2}, \dots, u_{H,1,n_1-1,2}, \\ u_{H,2,1,1}, \dots, u_{H,2,n_2-1,1}, \\ u_{\zeta,1,1,2}, u_{\zeta,1,1,3}, \dots, u_{\zeta,1,n_1-1,2}, u_{\zeta,1,n_1-1,3}, \\ u_{\zeta,1,n_1,3}, u_{\zeta,1,1,2}, u_{\zeta,1,1,3}, \dots, u_{\zeta,1,n_1-1,2}, u_{\zeta,1,n_1-1,3}, u_{\zeta,1,n_1,3} \end{bmatrix}. \tag{2.25}$$

In accordance with the division of the rotational DOFs in surface and inner state variables, the vector of cell side lengths $\boldsymbol{a}$ comprises of surface cell side lengths $\boldsymbol{a}_0$, with length n_1, and inner cell side lengths $\boldsymbol{a}_1$, with length $3n_1 + 3n_2 + 2 = 6n_1 + 5$. The vector of cell side lengths is

$$\boldsymbol{a} = \begin{bmatrix} \boldsymbol{a}_0 \\ \boldsymbol{a}_1 \end{bmatrix}. \tag{2.26}$$

The surface cell side lengths are considered as invariable in the shape-optimization procedure. The vector of surface cell side lengths $\boldsymbol{a}_0$ is defined by

$$\boldsymbol{a}_0 = \left[a_{CS,1,1,1}, \dots, a_{CS,1,n_1,1} \right]. \tag{2.27}$$

The overall surface length of the PACS is thus not influenced in the optimization process. An alternative approach that allows for a modification of these parameters could be advantageous but is not examined in more detail.
For facilitating the subsequent formulations the surface cell side lengths have to be distinguishable from the inner ones. A further division of the inner cell side lengths allows organizing the cell sides according to their utilization for reaching the respective target state of shape. The cells within each particular cell row are modified in the shape-optimization step to cause one specific target shape under consideration of the related load state. Thus, the two vectors $\boldsymbol{a}_{1,1}$ and $\boldsymbol{a}_{1,2}$ that contain the inner cell side lengths of the first and the second cell row are utilized for controlling the first and the second target state of shape. It are defined by

$$\boldsymbol{a}_{1,1} = \left[\begin{matrix} a_{CS,1,1,3}, a_{CS,1,1,5}, a_{CS,1,1,7}, a_{CS,1,1,9}, \\ a_{CS,1,2,3}, a_{CS,1,2,5}, a_{CS,1,2,7}, \dots, a_{CS,1,n_1,3}, a_{CS,1,n_1,5}, a_{CS,1,n_1,7} \end{matrix} \right] \text{ and} \tag{2.28}$$

$$\boldsymbol{a}_{1,2} = \left[\begin{matrix} a_{CS,2,1,7}, a_{CS,2,1,9}, a_{CS,2,1,11}, a_{CS,2,1,1}, \\ a_{CS,2,2,7}, a_{CS,2,2,9}, a_{CS,2,2,11}, \dots, a_{CS,2,n_2,7}, a_{CS,2,n_2,9}, a_{CS,2,n_2,11} \end{matrix} \right]. \tag{2.29}$$

The length of $\boldsymbol{a}_{1,1}$ is $3n_1 + 1$ and that of $\boldsymbol{a}_{1,2}$ is $3n_2 + 1 = 3n_1 + 4$. The vector of inner cell side lengths $\boldsymbol{a_1}$ is assembled to

$$\boldsymbol{a_1} = \begin{bmatrix} \boldsymbol{a}_{1,1} \\ \boldsymbol{a}_{1,2} \end{bmatrix}. \tag{2.30}$$

With defining the composition of the analysis variables, the necessary input information for the structural model can now be described.

Initial analysis variables and LBCs

Prior to the optimization process initial values have to be defined to determine the input for the structural model. Therefore all independent state variables $\boldsymbol{u}$ and the cell side lengths $\boldsymbol{a}$ are needed. As the number of independent surface state variables $\boldsymbol{u}_0$ is less than the number of inner cell side lengths $\boldsymbol{a}_1$, which are used to control the shape variation, the solution of the optimization process is not unique. The definition of the initial model parameters thus influences the optimization results. The effects of different initial parameters on the optimization procedure and its outcomes are investigated in chapter 2.4.3 at an exemplary structure.

As described in chapter 2.1.4, boundary conditions are defined by the determination of constant or dependent instead of independent state variables. The boundary conditions that are shown in Figure 2-10 are used in the following and allow for a distributed load introduction. The connection structure and the geometrical arrangement of both cell rows among themselves have to be considered within the definition of the state variables. In comparison with a connection variant that only includes the first cell row, this geometrical arrangement profits from an additional load path. The increased design

height further reduces forces due to bending moments at the bearing. Reduced stresses and increased stiffness result. The possibility of integrating the fluid supply in the rigid connection structure is a further advantage of this design. In contrast, an increase of weight comes along with the size of the connection structure. To constrain the model in the two-dimensional space, the structure is fixed at its left connection structure. As the rotations of the hinges at both ends of the PACS are restricted by the connection structure, additionally the angles $u_{c,\boldsymbol{k}}$ with $\in$ [1,1,9; 1,1,10; $1, n_1, 3$; $1, n_1, 4$; 2,1,1; 2,1,2; $2, n_2, 5$; $2, n_2, 5$; $2, n_2, 6$; $2, n_2, 7$; $2, n_2, 8$], have to be kept constant in the numerical computations. For the herein used cell arrangement the definition of the vectors of independent state variables is given within equation (2.24) and (2.25). For changing boundary conditions, these vectors have to be adjusted.
The definition of internal and external loads according to chapter 2.1.4 can be made separately for each target state of shape. A change in the loading of the structure due to the shape variation can thus be considered in the optimization.

Influence of material selection on the performance of PACS
The selection of materials substantially influences the stiffness and strength of the PACS and thus defines its functional envelope. Due to the importance of the material parameters for the performance of the PACS, this section introduces the methods for evaluating the quality of various materials for their application for PACS. The performance of a PACS depends on its deformation capability and stiffness characteristic. The selection of materials thus aims on the reduction of the deformation- and pressure-induced material utilization in terms of stresses.
As the cell side thickness can be varied in wide range and exceeds the hinge thickness many times over, critical bending and axial stresses concentrate at hinge elements. For the load-based material selection it is thus valid to consider only hinge stresses. The optimal hinge thickness t_{opt}, which allows for the maximum cell pressure p_{max} is analysed for different material classes in the following.
The hinge deformations and pressure-induced stresses are computed analytically for a single cell, as the related detailed analysis of a complete PACS is part of the subsequent chapters. Nevertheless, the herein presented relations keep valid for the cell compound.

In contrast to rigid structures and the majority of alternative morphing concepts, the PACS rely on the cell's pressurization for providing the required stiffness against external forces. These conceptually necessary internal loads lead to prestresses in the structure that have to be borne additionally to external loads. A cell with internal pressure p and a diameter D of a circular arc that includes each edge of the cell (cf. Figure 1-16, bottom left) is considered. The normal force for hinge elements can thus be calculated according to the pipe formula to

$$F_n = \frac{pdD}{2}. \tag{2.31}$$

The related normal stresses within the flexure hinges result in

$$\sigma_n = \frac{F_n}{dt}. \tag{2.32}$$

The usage of flexure hinges for the realization of cell side joints further causes bending stresses that locate at the hinges' extreme fibre and are due to the rotational deformation Δu_c. The analytical equations for calculating the bending stresses are obtained from the substitute model of a beam with thickness t, length s and depth d that represents the flexure hinge. The longitudinal and bending stresses at each hinge element are assumed to be constant over its length. This is valid for a flexure hinge with an optimal orientation and curvature that align the hinge in parallel with the resultant forces that act on the hinge. The moment M, which depends on the bending stiffness c and the hinge bending Δu_c, is calculated according to equation (2.8). The bending stress at the extreme fibre of a compliant hinge is

$$\sigma_b = \frac{6|M|}{dt^2} = \frac{tE|\Delta u_c|}{2s}. \tag{2.33}$$

The maximum stresses can be calculated by

$$\sigma_{max} = \sigma_n + \sigma_b = \frac{pD}{2t} + \frac{tE|\Delta u_c|}{2s}. \tag{2.34}$$

The minimum wall thickness t_{min} for a hinge of length s, the diameter of the cell's circumcircle D, change of the hinge angle Δu_c, *Young*'s modulus E, yield strength R and the applied pressure p, results in

$$t_{min} = \frac{sR+\sqrt{(sR)^2-sDpE|\Delta u_c|}}{E|\Delta u_c|}. \tag{2.35}$$

The possibility to raise the strength of a hinge by increasing its wall thickness is limited through the fact that, for a given angular distortion, the bending stresses increase with the thickness (cf. equation (2.33)). The following equations provide the solution for the optimum thickness t_{opt}, which allows applying the maximum pressure p_{max} to a given PACS cell. This optimum hinge thickness is calculated with

$$p(t) = \left(\mathrm{R} - \frac{tE|\Delta u_c|}{2s}\right)\frac{2t}{D} \text{ and} \tag{2.36}$$

$$\frac{\partial p(t)}{\partial t} = \left(\mathrm{R} - \frac{tE|\Delta u_c|}{s}\right)\frac{2}{D} \overset{t=t_{opt}}{=} 0, \text{ to} \tag{2.37}$$

$$t_{opt} = \frac{Rs}{E|\Delta u_c|}. \tag{2.38}$$

Combining equation (2.36) and (2.38) yields the maximum pressure load p_{max} that can be borne for the given change of the hinge angle, hinge length, diameter of the cell's circumcircle and for the material dependent parameters *Young*'s modulus and yield strength. For $t = t_{opt}$ the maximum tolerable internal pressure is limited to

$$p_{max} = \frac{R^2 s}{ED|\Delta u_c|}. \tag{2.39}$$

This analytical equation does not consider stress concentrations at thickness transients or due to bending inhomogeneity. As the further design steps allow keeping these effects in tolerable regions, this equation is used for the selection of materials by reference to the target structure.
It can be obtained, that a reduction of the cell size or an increase of the hinge length would unload the hinges and result in an increase of the maximum pressure load. Currently less appropriate materials could thus be taken into consideration. However, the hinge length is limited to about one tenth of the cell diameter. Larger values cannot be realized with flexure hinges due to the space requirements of the hinge eccentricities. A high ratio of D/s further lowers deviations between a real-life PACS and the related truss model, as flexure hinges are approximated with one-dimensional elements. An increased accuracy thus results for the presented modelling variants 1 to 3.

In the following, static datasheet values are used to reduce the pool of potential materials. Fatigue issues have to be treated by strength reduction. Sun et al. [154] investigated composite mechanics and pose that static load and appropriate material characteristics can only provide limited results. As stated in their work, for a fatigue designing of FRP structures the estimated number of $1e5$ load cycles within a full component life leads to a significant reduction of material strength. For a unidirectional CFRP lamina a strength loss of about 30% is given in transverse direction.

Table 2-6: Material data and resulting optimal hinge thickness t_{opt} and maximum cell pressure p_{max} for a cell circumcircle diameter of 50 mm a hinge length of 5 mm and 20° of hinge bending

Class	Material	$E, E_{\|\|}$ [GPa]	$R, R_{\|\|}$ [MPa]	R^2/E [MPa]	t_{opt} [mm]	p_{max} [MPa]
Ceramics	Silicon nitride	290	500	**0.86**	0.02	0.25
	Silicon carbide	450	650	**0.94**	0.02	0.27
	Zirconium oxide	175	500	**1.43**	0.04	0.41
Plastics	PA2200	1.50	40	**1.07**	0.38	0.31
	PA12	1.30	40	**1.23**	0.44	0.35
	ULTEM 1010	2.77	81	**2.37**	0.42	0.68
	PEEK	3.70	100	**2.70**	0.39	0.77
Metals	AlMgSi0,5	70	200	**0.57**	0.04	0.16
	EN-AW-7075	72	480	**3.20**	0.10	0.92
	Ti6Al4V	114	850	**6.33**	0.11	1.82
	EN-GJS-1400-1	165	1100	**7.33**	0.10	2.10
Elastomers	Hytrel 7246	0.525	50	**4.76**	1.36	1.36
	Elastollan 1160	0.20	50	**12.50**	3.58	3.58
	TPU-92A	0.029	20	**12.84**	9.88	3.95
	Elastollan 1195	0.060	55	**50.42**	13.13	14.44
CFRP-fabric	T800+MTM49-3	70	950	**12.89**	0.19	3.69
GFRP-UD	HexPly913	42	1200	**34.29**	0.41	9.82
CFRP-UD	T800+M21	160	3000	**56.25**	0.27	16.11

In this work exclusively static values are used in order to show the functionality of the concept and to compare static design values with static experimental loads. Table 2-6 summarizes the suitability of five material groups, FRPs, elastomers, metals, plastics and ceramics for their performance potential for PACS. The preselection of three to four materials per class allows focusing on the most promising representatives. According to the stress-based criterion that is formulated in equation (2.39) and the given initial PACS geometry, the optimum performance is provided by the unidirectional CFRP material T800+M21 as it holds the maximum ratio of

$$R^2/E. \tag{2.40}$$

For an exemplary PACS cell with a maximum hinge bending angle of $\Delta u_c = 20°$, a cell diameter of $D = 50\,mm$ and a uniform hinge length of $s = 5\,mm$ the resulting values for optimal thickness and maximum pressure are given in Table 2-6 and point the use-case-specific limitations for the respective materials. The most suitable material for the application of PACS is the one with the highest ratio of R^2/E.
For a given hinge distortion, hinge length and diameter of the cell's circumcircle, this ratio leads to the maximum pressure value and thus determines the design envelope. The illustration, given in Figure 2-11, depicts this envelope for typical hinge distortions between 0.5° and 20°. The unidirectional CFRP T800+M21 material describes the upper boundary of the graph.

In addition to the mechanical aspects, two further requirements influence the material selection. Manufacturing issues are discussed in chapter 5, but can be estimated already with the information about the optimum hinge thickness from Table 2-6. A ceramic structure with a wall thickness below $0.05\,mm$, which has to be kept constant over a cell depth of more than half a meter, leads to huge manufacturing challenges. Also a hinge thickness of more than $10\,mm$ at a cell diameter of $50\,mm$ for elastomeric materials is not realistic.

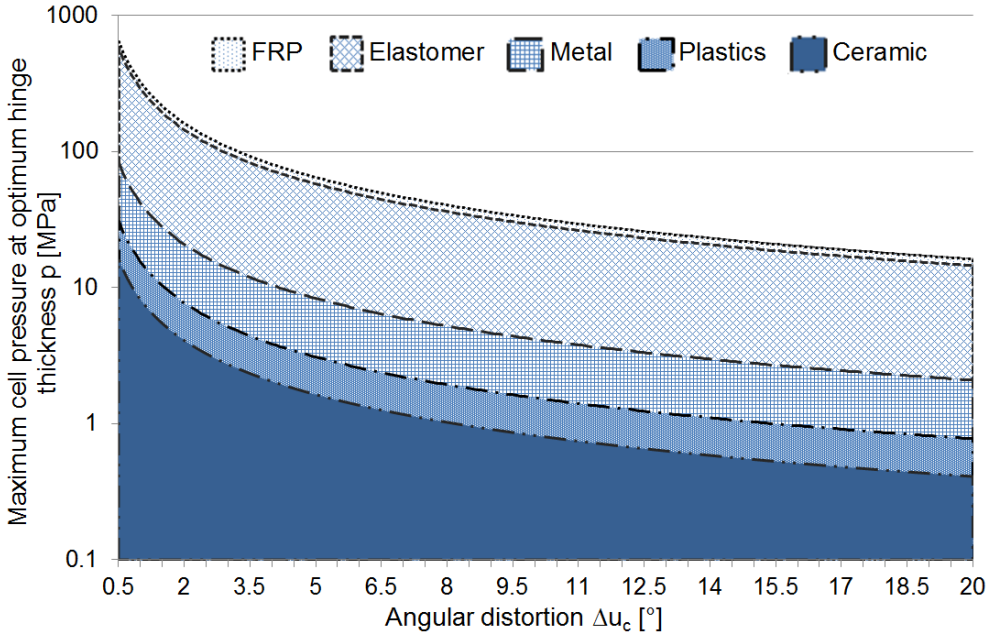

Figure 2-11: Design envelope for different material groups, for a cell with a circumcircle diameter of 50 mm and a hinge length of 5 mm

Pagitz et al. [146] further investigated the influence of the *Young*'s modulus on the accuracy of the shape-optimization process. They found that the smaller the *Young*'s modulus, the higher the variance between target and resultant shape. The reason for this is the elongation of cell sides, which currently is not considered in their shape-optimization strategy and in the herein presented approach. For $E = 1\ GPa$ a total deformational error of about $\eta_{\Delta\beta} \approx 40\ \%$ due to cell side strains is described in the underlying literature for an exemplary circular PACS geometry. For $E > 20\ GPa$ the error reduces to $\eta < 10\ \%$. The actual shape-optimization methods for controlling target deformations are accurate for such stiff materials and inadequate regarding elastomers or plastics. Further investigations may allow including the extensional deformation of cell sides and thus improve the accuracy for all groups of materials.

2.2.2 Evaluation model and optimization variables

The evaluation model is used to evaluate the current energy potential $\dot{\boldsymbol{\Pi}}$ of the structure, which provides the optimization variables, in terms of the target value. Depending on the evaluation result, the optimization process is thereupon either continued or stopped. The optimization objective is approximated in the form of a stop criterion. Within a numerical approach, the stop criterion allows quantifying the limit value for the tolerable variance of the optimization variables in terms of the optimization objective.
For both computation variants, the structural optimization and the computation of deformations, the optimization variables are given by the vector of energy potentials $\dot{\boldsymbol{\Pi}}$. According to equation (2.7), the equilibrium state of shape for the current shape of the structure is found, when the optimization objective of $\dot{\boldsymbol{\Pi}} = 0$ is reached. Therefore, the energy potential that relate to each of the independent state variables must become infinitesimal in the numerical approach. In the evaluation model the maximum value of $\dot{\boldsymbol{\Pi}}$ is thus investigated and has to fall below the limit value for the energy potential $\eta_{\dot{\Pi}}$:

$$max\left|\dot{\boldsymbol{\Pi}}\right| < \eta_{\dot{\Pi}}. \tag{2.41}$$

This stop criterion should be adapted to the size of the PACS cells. The energy potential due to the internal cell pressure for example increases by the square of the cell size. An adaption of $\eta_{\dot{\Pi}}$ is thus

reasonable in order to provide a constant optimization quality in terms of the resulting independent surface state variables respectively surface cell side lengths. The underlying stop criterion for each of the herein presented example structures is thus given together with the model description.

2.3 Optimization algorithm

According to the *Three-Columns-Concept* (see Figure 2-1), that is proposed by Eschenauer for the subdivision of an optimization process, the optimization algorithm represents the third subsystem.
For approaching the optimization objective of minimizing the vector of energy potentials, the optimization algorithm modifies the design variables. Due to the continuity of the optimization problem, a gradient-based method, can be used. The solution is thereby approached iteratively.
The gradient-based *Newton*'s method provides quadratic convergence and thus efficient approach. The vector of design variables for the shape-optimization process $\boldsymbol{w}_{z+1}$ for the iteration step $z+1$ is

$$\boldsymbol{w}_{z+1} = \boldsymbol{w}_z - \frac{\dot{\Pi}}{\partial \dot{\Pi}/\partial \boldsymbol{w}}. \tag{2.42}$$

The modification of the inner cell side lengths allows for solving the issue of shape optimization. In terms of calculating the structural deformations of a given PACS with specific LBCs, the independent state variables $\boldsymbol{u}$ are modified according to

$$\boldsymbol{u}_{z+1} = \boldsymbol{u}_z - \frac{\dot{\Pi}}{\partial \dot{\Pi}/\partial \boldsymbol{u}}. \tag{2.43}$$

The implementation of both optimization variants for PACS is described in the following sections.

2.4 Shape optimization

The shape-optimization process enables to compute the geometry of a PACS such that it moves between predefined target states of shape under consideration of internal and external loads and geometrical boundary conditions (cf. chapter 2.1.4). It is implemented according to the *Three-Columns-Concept* and composed of the previously defined subsystems structural model, optimization model and optimization algorithm. The underlying methods are presented in the following and illustrated and evaluated at the exemplary structures of a beam pendulum and a generic double row PACS.

2.4.1 Implementation of the shape-optimization procedure for PACS

In the following, the model parameters that define the initial starting point for the shape optimization are determined and the analysis, the optimization, the state and the design variables are specified. The iterative process for approaching the optimization objective is further explained on the basis of the flowchart that is presented in Figure 2-12.

The initial model parameters which are needed at the beginning of the optimization process include the information about the independent state variables, the cell side lengths, the LBCs and the material characteristics for hinges and cell sides. The number of target states of shape, which have to be determined additionally to the initial model parameters, is equal to the number of cell rows h. As presented in chapter 2.2.1, the target states are therefore described by the vector of independent surface state variables $\boldsymbol{u}_0$ for the given surface cell side lengths $\boldsymbol{a}_0$. The shape-optimization procedure, which allows for the optimization of the inner cell side lengths $\boldsymbol{a}_1$, can be divided in two loops that are executed in succession. The vector of independent surface state variables $\boldsymbol{u}_0$ and the vector of surface cell side lengths $\boldsymbol{a}_0$ are kept constant during both optimization sections. The shape of the upper surface of PACS is thus always identical with the target shape.

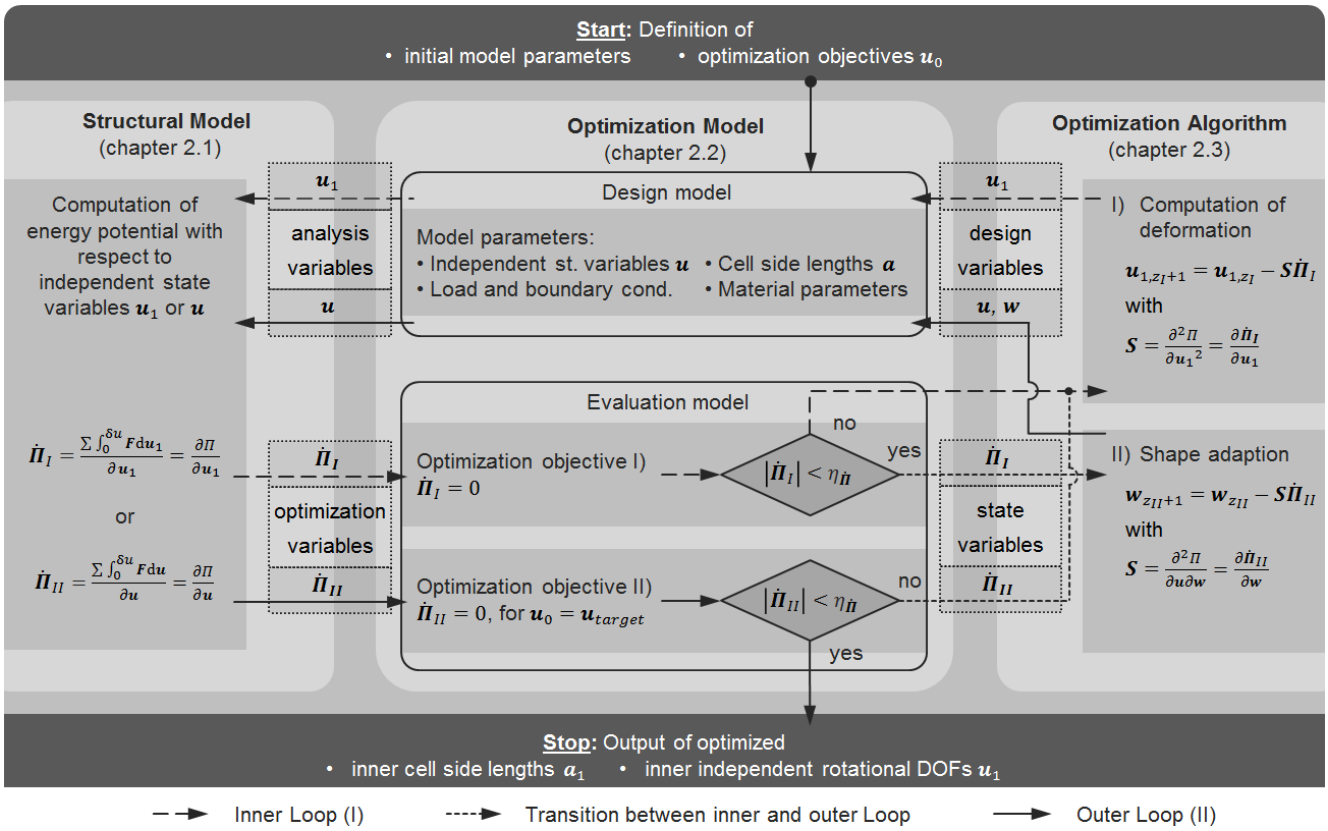

Figure 2-12: Flowchart describing the shape optimization for PACS

The optimization objective is reached when a geometrical shape in terms of the independent inner state variables $\boldsymbol{u}_1$ and inner cell side lengths $\boldsymbol{a}_1$ is found, which leads to an equilibrium of energy potentials for this enforced surface shape. Within the first loop the equilibrium state of shape in terms of the inner independent state variables $\boldsymbol{u}_1$ is calculated. For a double row structure two different target states of shape can be determined by defining $\boldsymbol{u}_{0,st1}$ and $\boldsymbol{u}_{0,st2}$. Similar to the geometrical definition also two sets of LBCs have to be defined. The difference between the internal pressures $\boldsymbol{p}_{int,st1}$ and $\boldsymbol{p}_{int,st2}$ primarily causes the energy potential that allows for the deformation between the two target states of shape. These values are decisive for the existence of a solution for the optimization process.

The vector of energy potentials of the first loop $\dot{\boldsymbol{\Pi}}_I$ that represents the optimization variables and relates the change of the energy of both target states of shape Π_{st1} and Π_{st2} to the change of the inner state variables $\boldsymbol{u}_1$ is

$$\dot{\boldsymbol{\Pi}}_I = \frac{\partial \Pi}{\partial \boldsymbol{u}_1} = \begin{bmatrix} \frac{\partial \Pi_{st1}}{\partial \boldsymbol{u}_1} \\ \hline \frac{\partial \Pi_{st2}}{\partial \boldsymbol{u}_1} \end{bmatrix} = \left[\begin{array}{ccc} \frac{\partial \Pi_{st1}}{\partial u_{1,1}} & \cdots & \frac{\partial \Pi_{st1}}{\partial u_{1,6n_1-1}} \\ \hline \frac{\partial \Pi_{st2}}{\partial u_{1,1}} & \cdots & \frac{\partial \Pi_{st2}}{\partial u_{1,6n_1-1}} \end{array}\right]^{equil.} = 0. \tag{2.44}$$

In accordance with equation (2.43), the equilibrium state of the structure for the inner independent state variables $\boldsymbol{u}_1$, is calculated. The vector $\boldsymbol{u}_1$ is modified according to

$$\boldsymbol{u}_{1,z+1} = \boldsymbol{u}_{1,z} - \frac{\dot{\Pi}_I}{\partial \dot{\Pi}_I / \partial \boldsymbol{u}_1}, \tag{2.45}$$

until the maximum absolute value of the vector of energy potentials $max|\dot{\boldsymbol{\Pi}}_I|$ falls below $\eta_{\dot{\Pi}}$.

The actual optimization of the inner cell side lengths $\boldsymbol{a}_1$, which allows influencing the global equilibrium state of shape, is approached next. The energy potential of the second loop $\dot{\boldsymbol{\Pi}}_{II}$ for all independent state variables $\boldsymbol{u}$, which represents the analysis variables, has to vanish, to achieve the equilibrium state of shape for the global structure. The optimization objective is thus defined by

$$\dot{\boldsymbol{\Pi}}_{II} = \frac{\partial \Pi}{\partial \boldsymbol{u}} = \begin{bmatrix} \frac{\partial \Pi_{st1}}{\partial \boldsymbol{u}} \\ \hline \frac{\partial \Pi_{st2}}{\partial \boldsymbol{u}} \end{bmatrix} = \left[\begin{array}{ccccccc} \frac{\partial \Pi_{st1}}{\partial u_{0,1}} & \cdots & \frac{\partial \Pi_{st1}}{\partial u_{0,2n_1}} & \frac{\partial \Pi_{st1}}{\partial u_{1,1}} & \cdots & \frac{\partial \Pi_{st1}}{\partial u_{1,6n_1-1}} \\ \hline \frac{\partial \Pi_{st2}}{\partial u_{0,1}} & \cdots & \frac{\partial \Pi_{st2}}{\partial u_{0,2n_1}} & \frac{\partial \Pi_{st2}}{\partial u_{1,1}} & \cdots & \frac{\partial \Pi_{st2}}{\partial u_{1,6n_1-1}} \end{array}\right] \overset{equil.}{=} 0. \tag{2.46}$$

The energy potential $\dot{\boldsymbol{\Pi}}_{II}$ is adapted in the optimization process by the computation of the design variables $\boldsymbol{w}$. The vector of design variables $\boldsymbol{w}$ consists of the rotational DOFs $\boldsymbol{u}_1$ as well as of the cell side lengths $\boldsymbol{a}_1$. Coupling the change of independent inner state variables $\boldsymbol{u}_1$ to the change of cell side lengths $\boldsymbol{a}_1$ is essential. An exclusion of this dependency within the computation of the gradient for the utilized *Newton*'s method would result in an optimization, which cycles in an infinite loop. The mixed vector of design variables $\boldsymbol{w}$ for the shape optimization is defined by

$$\boldsymbol{w} = \begin{bmatrix} \boldsymbol{w}_{st1} \\ \hline \boldsymbol{w}_{st2} \end{bmatrix} = \begin{bmatrix} \boldsymbol{u}_{1,st1} \\ \boldsymbol{a}_{1,1} \\ \hline \boldsymbol{u}_{1,st2} \\ \boldsymbol{a}_{1,2} \end{bmatrix}. \tag{2.47}$$

Pagitz et al. [1] presented a method for the shape optimization of PACS, which only relates the change of the independent rotational surface DOFs to the change of cell side lengths. 2,000 to 20,000 iterations are necessary to find the shape of an optimized structure with an accuracy of about 0.01° related to the target values [145]. The lasting error as well as a the significantly high number of necessary iteration steps, which disagrees with the quadratic convergence of *Newton*'s method, can be explained by the negligence of the coupled unknown state variables $\boldsymbol{a}_1$ and $\boldsymbol{u}_1$ (cf. appendix B).

Similar to equation (2.42) the mixed vector of unknown design variables $\boldsymbol{w}$ for the iteration step $z+1$ is thus computed by

$$\boldsymbol{w}_{z+1} = \boldsymbol{w}_z - \frac{\dot{\boldsymbol{\Pi}}_{II}}{\partial \dot{\boldsymbol{\Pi}}_{II}/\partial \boldsymbol{w}} = \boldsymbol{w}_z - \boldsymbol{S}^{-1}(\boldsymbol{u}, \boldsymbol{w}_z)\dot{\boldsymbol{\Pi}}_{II}(\boldsymbol{u}, \boldsymbol{w}_z). \tag{2.48}$$

After each iteration step of the second loop, the first loop is initiated and allows for minimizing the energy potential $\dot{\boldsymbol{\Pi}}_I$. The sensitivity matrix $\boldsymbol{S}$ for a double row PACS results in

$$\boldsymbol{S} = \frac{\partial^2 \boldsymbol{\Pi}}{\partial \boldsymbol{u} \partial \boldsymbol{w}} = \frac{\partial \dot{\boldsymbol{\Pi}}}{\partial \boldsymbol{w}} = \left[\begin{array}{ccccccc} \frac{\partial \dot{\Pi}_{st1,1}}{\partial u_{1,1}} & \cdots & \frac{\partial \dot{\Pi}_{st1,1}}{\partial u_{1,6n_1-1}} & \frac{\partial \dot{\Pi}_{st1,1}}{\partial a_1} & \cdots & \frac{\partial \dot{\Pi}_{st1,1}}{\partial a_{3n_1+1}} \\ \frac{\partial \dot{\Pi}_{st1,2}}{\partial u_{1,1}} & & \frac{\partial \dot{\Pi}_{st1,2}}{\partial u_{1,6n_1-1}} & \frac{\partial \dot{\Pi}_{st1,2}}{\partial a_1} & & \frac{\partial \dot{\Pi}_{st1,2}}{\partial a_{3n_1+1}} \\ \vdots & \ddots & \vdots & & \ddots & \vdots \\ \frac{\partial \dot{\Pi}_{st1,8n_1-1}}{\partial u_{1,1}} & \cdots & \frac{\partial \dot{\Pi}_{st1,8n_1-1}}{\partial u_{1,6n_1-1}} & \frac{\partial \dot{\Pi}_{st1,8n_1-1}}{\partial a_1} & \cdots & \frac{\partial \dot{\Pi}_{st1,8n_1-1}}{\partial a_{3n_1+1}} \\ \hline \frac{\partial \dot{\Pi}_{st2,1}}{\partial u_{1,1}} & \cdots & \frac{\partial \dot{\Pi}_{st2,1}}{\partial u_{1,6n_1-1}} & \frac{\partial \dot{\Pi}_{st2,1}}{\partial a_1} & \cdots & \frac{\partial \dot{\Pi}_{st2,1}}{\partial a_{3n_1+4}} \\ \frac{\partial \dot{\Pi}_{st2,1}}{\partial u_{1,1}} & & \frac{\partial \dot{\Pi}_{st2,2}}{\partial u_{1,6n_1-1}} & \frac{\partial \dot{\Pi}_{st2,2}}{\partial a_1} & & \frac{\partial \dot{\Pi}_{st2,2}}{\partial a_{3n_1+4}} \\ \vdots & \ddots & \vdots & & \ddots & \vdots \\ \frac{\partial \dot{\Pi}_{st2,8n_1-1}}{\partial u_{1,1}} & \cdots & \frac{\partial \dot{\Pi}_{st2,8n_1-1}}{\partial u_{1,6n_1-1}} & \frac{\partial \dot{\Pi}_{st2,8n_1-1}}{\partial a_1} & \cdots & \frac{\partial \dot{\Pi}_{st2,8n_1-1}}{\partial a_{3n_1+4}} \end{array}\right]. \tag{2.49}$$

The inverse of the sensitivity matrix is computed according to the *Moore-Penrose* method. For the present case of a non-quadratic matrix, this approach minimizes the 2-norm of the increment for the mixed vector of unknown state variables $\boldsymbol{S}^{-1}\dot{\boldsymbol{\Pi}}$. The iterative process of the second loop and of the overall shape optimization procedure is continued until the maximum energy potential $\dot{\boldsymbol{\Pi}}_{II}$ falls below $\eta_{\dot{\Pi}}$. For all results that are presented in the following, a virtual rotation of $\delta u = 2e - 6$ is used to compute the energy potentials and its gradients.

The number of equations, which result from equation (2.48) is defined by the length of the vector of energy potential $\dot{\boldsymbol{\Pi}}_{II}$, that is equal to the length of the vector of independent rotational DOFs $\boldsymbol{u}$ and sums up to $8n_1 - 1$ per state of shape. The size of the vector of unknown design variables for the first target state of shape $\boldsymbol{w}_{st1}$ is $9n_1$ and for the second state of shape $\boldsymbol{w}_{st2}$ it is $9n_1 + 3$. It can be seen that in both cases, the number of unknown variables is higher than the number of equations. The solution for a PACS which deforms into the given states of shape at a given pressure set is thus not unique. Additional boundary conditions, which are not covered by this thesis, could thus be integrated in the optimization procedure to consider end stops, manufacturing requirements or structural stresses. Also an optimization of the number of cells, which is given as constant at the moment, may provide advantages. Due to the discontinuity of the energy potential the gradient-based optimization algorithm would then be inappropriate.

For this iterative process, the surface cell side lengths $\boldsymbol{a}_0$ and the independent surface state variables $\boldsymbol{u}_0$ that are used to define the target states of shape are kept constant. The vector of energy potentials $\dot{\boldsymbol{\Pi}}_{II}$ is minimized in the optimization process with respect to all independent state variables $\boldsymbol{u}$ by the variation of the inner cell side lengths $\boldsymbol{a}_1$ and the inner independent state variables $\boldsymbol{u}_1$. A shape optimization procedure for PACS is thus found which includes the sensitivity of the energy potential $\dot{\boldsymbol{\Pi}}_{II}$ on both, the inner cell side lengths $\boldsymbol{a}_1$ and the inner independent state variables $\boldsymbol{u}_1$.
In the following, the shape optimization process is demonstrated at the exemplary structure of a beam pendulum first, before a generic double row PACS is optimized to deform between specified surface geometries.

2.4.2 Shape optimization of a beam pendulum

The theory about the optimization of the shape of a PACS is introduced and shall now be illustrated at a simple mechanical problem. Figure 2-13 shows two different flexible mounted rigid beam models. The length of the beams a shall be optimized such that the angle α_B takes a specific value.

Beam pendulum with line load and point mass

The first structure (a) is loaded with a beam perpendicular line load q_B and a weight force due to the point mass m_B. The shape of this structure can be determined analytically. The second beam model (b) shows an increased similarity to the implementation of a PACS in terms of geometry and LBCs, and is examined subsequently.
For the computation of the energy potential $\dot{\Pi}_B$ of the beam the shape-optimization procedure that is described in chapter 2.4.1 is applied. The virtual work δW is calculated according to equation (2.6) as the sum of all integrals of forces F over their displacement δx. In similarity to the kinematic of the PACS the angle α_B describes the deformation of the structure and the beam length a is used to control the target deformation. An equilibrium state is found for this kinematic system when the energy potential $\dot{\Pi}_B$ vanishes:

$$\dot{\Pi}_B = \frac{\delta W_B}{\delta \alpha_B} = \frac{m_B g a \sin(\alpha_B)\delta\alpha_B - \frac{1}{2} q_B a^2 \sin(\pi/2)\delta\alpha_B}{\delta\alpha_B} \overset{equil.}{=} 0. \tag{2.50}$$

An analytical solution can be derived for this equation, which allows to compute the beam length a that results in the beam deflection α_B. The beam length a has to fulfil

$$a = \frac{2 m_B g}{q_B} \sin\left(\alpha_{B,t}\right). \tag{2.51}$$

The analytical solution is substituted by an iterative process for the complex kinematical system of a PACS. In order to evaluate the approach that is described in chapter 2.4.1, the iterative process is compared with the analytical one by listing the intermediate results from the computational sub steps.

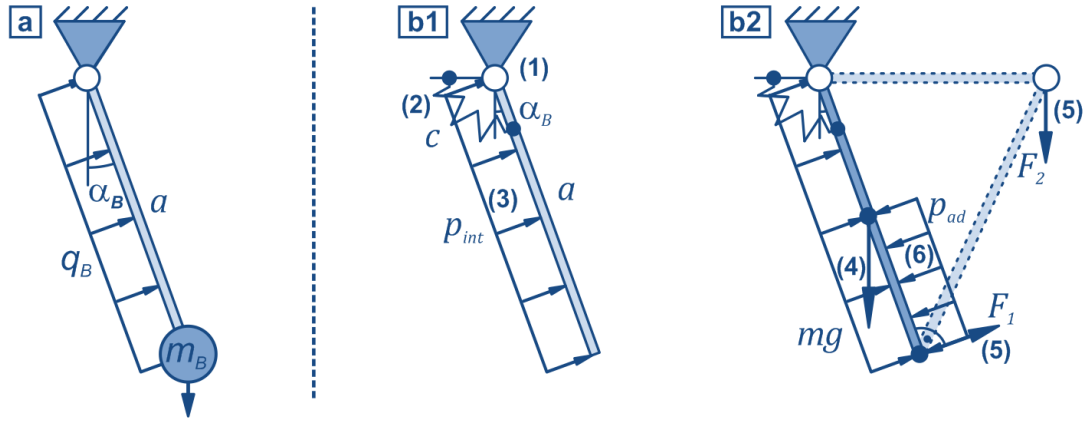

Figure 2-13: Beam pendulum model for the illustration of the shape-optimization process: a) model with line load and point mass, b) basic model for describing a PACS with extended load introduction

In contrast to the optimization procedure that is illustrated in Figure 2-12, the vector of independent state variables $\boldsymbol{u}$ is identical with the vector of independent surface state variables $\boldsymbol{u}_0$ and the length of $\boldsymbol{u}_1$ is zero. This simplified example can thus be computed without consideration of the first iteration loop for minimizing the energy potential $\dot{\Pi}_I$ that only depends on $\boldsymbol{u}_1$. The necessary parameters of the beam pendulum are given in Table 2-7.
With the analytical approach the target beam length is calculated to $a_t = 69.3672$ mm. The initial value $a_0 = 250\,mm$ is determined. The potential energy for the numerical approach can be deduced from equation (2.48). The derivative of the potential energy after the beam length is

$$\frac{\partial \dot{\Pi}_{II,B}}{\partial \boldsymbol{w}_B} = \frac{\partial \dot{\Pi}_{II,B}}{\partial a_B} = m_B g sin(\alpha_B) - q_B a sin(\pi/2). \tag{2.52}$$

The beam length $a_{B,z+1}$ for the iteration step $z+1$ is calculated by

$$a_{z+1} = a_z - \frac{m_B g a_z sin(\alpha_B) - \frac{1}{2} q_B a_z^2}{m_B g sin(\alpha_B) - q_B a_z}. \tag{2.53}$$

The computational outcomes are listed in Table 2-8. Due to the quadratic convergence of *Newton*'s method the energy potential $\dot{\Pi}_B$ falls below the limit value of $\eta_{\dot{\Pi}} = 1e-5\,J/rad$ after six iterations. The deviation $\eta_{B,z}$ of the current beam length compared to the analytical result is reduced accordingly.

Table 2-7: Parameters for the definition of the beam pendulum model

Parameter	Unit	Value
a_0	[mm]	250
a_t	[mm]	69.3672
$\alpha_{B,t}$	[°]	45.0
q_B	$[N/mm]$	1.0
m_B	$[t]$	5.0e-3
g	$[mm/s^2]$	9.81e3

Table 2-8: Numerical results for the shape optimization process after z iterations

Iteration step z	Beam length a_z [mm]	Energy pot. $\dot{\Pi}_B$ $[J/rad]$	Deviation $\eta_{B,z}$ [%]
1	145.1352	2.26e+1	1.09e+2
2	95.3550	5.50e+0	3.75e+1
3	74.9330	1.24e+0	8.02e+0
4	69.7520	2.09e-1	5.55e-1
5	69.3693	1.34e-2	3.04e-3
6	69.3672	7.32e-5	9.26e-8
7	69.3672	2.23e-9	0

The implementation of the previously described optimization process is illustrated at the exemplary structure of a beam pendulum. The approach is verified by comparing analytically and numerically obtained results. The application of the optimization process for a beam model with increased similarity to the PACS provides deepened insight in the approach, before it is utilized for PACS.

Beam pendulum with extended load introduction

With the example of a beam pendulum with extended load introduction, a further simplified mechanical problem is used to describe the implementation of the discussed loads in the shape-optimization approach for PACS. The pendulum is depicted in Figure 2-13, (b), for two load cases. Starting with a reduced model in a first step, the increased diversity of load types according to chapter 2.1.4 is considered in a second step. Figure 2-13, (b1), shows the beam pendulum with a hinged bearing (1), a rotational spring (2), which represents the stiffness of the flexure hinge c, and an internal pressure load p_{int} (3). It is assumed that the rotational spring is without preloads for $\alpha_B = 0°$, what defines the initial shape of the structure.

Similar to the previous example, the equilibrium state of the beam pendulum shall be reached at a specific hinge deflection α_B. Therefore, the beam length a shall be determined. The virtual work and the energy potential for this kinematic system and for the depth d is given by

$$\delta W = \underbrace{\frac{1}{2} p_{int} a^2 d \delta\alpha_B}_{\text{(internal pressure)}} - \underbrace{c\left(\alpha_B \delta\alpha_B + \frac{1}{2}\delta{\alpha_B}^2\right)}_{\text{(hinge stiffness)}}. \tag{2.54}$$

The energy potential is calculated with

$$\dot{\Pi}_B = -\frac{\delta W}{\delta\alpha_B} = \dot{\Pi}_{B,p} + \dot{\Pi}_{B,c} = -\frac{1}{2} p_{int} a^2 d + c\left(\alpha_B + \frac{1}{2}\underbrace{\delta\alpha_B}_{\approx 0}\right) = 0. \tag{2.55}$$

As presented in chapter 2.3, the system of equations for a complete PACS structure is to be computed numerically. For this example, however, an analytical solution can still be derived. The resulting beam length is

$$a = \sqrt{\frac{2c\alpha_B}{p_{int} d}} = \sqrt{\frac{E t_k^3 \alpha_B}{6 s_k p_{int}}}. \tag{2.56}$$

As it can be seen, for a beam pendulum with a flexure hinge of stiffness c, the equilibrium state is independent from the depth d. In order to complete the mechanical model for the consideration of inertial forces (4), point loads (5) and external aerodynamic pressure loads (6) the beam pendulum example according to Figure 2-13, (b2). The virtual work therefore is calculated by

$$\begin{aligned}\delta W = {} & \underbrace{\frac{1}{2} p_{int} a^2 d \delta\alpha_B}_{\text{(internal pressure)}} + \underbrace{\frac{3}{8} p_{ad} a^2 d \delta\alpha_B}_{\text{(aerodynamic pressure)}} - \underbrace{c\left(\alpha_B \delta\alpha_B + \frac{1}{2}\delta\alpha_B^2\right)}_{\text{(hinge stiffness)}} + \underbrace{\left(F_1 - \frac{3}{2}F_2\right) a \delta\alpha_B}_{\text{(point loads)}} + \\ & + \underbrace{\frac{1}{2} mgsin(\alpha_B) a \delta\alpha_B}_{\text{(inertial forces)}}.\end{aligned} \tag{2.57}$$

The necessary beam length for adjusting the equilibrium state at the angle α_B results from

$$\begin{aligned}\dot{\Pi}_B = {} & \dot{\Pi}_{B,p} + \dot{\Pi}_{B,ad} + \dot{\Pi}_{B,c} + \dot{\Pi}_{B,pl} + \dot{\Pi}_{B,in} = \\ & \left[\frac{1}{2} p_{int} - \frac{3}{8} p_{ad}\right] a^2 d + \left[\frac{1}{2} mgsin(\alpha_B) + F_1 - \frac{3}{2} F_2\right] a - c\alpha_B = 0.\end{aligned} \tag{2.58}$$

The implementation of LBCs according to chapter 2.1.4 is described and specified at the example of a beam pendulum with extended load introduction. The optimization approach shall be applied for the shape optimization of a generic double row PACS in the following.

2.4.3 Shape optimization of a generic double row PACS

An exemplary double row PACS is optimized to investigate the convergence behaviour of the shape-optimization process. Three different hinge materials with a Young's modulus of $E_0 = 0.0\,GPa$, $E_1 = 10.0\,GPa$ and $E_2 = 20.0\,GPa$ and three starting geometries define the initial model parameters. Each of the investigated structures consists of $n_1 = 5$ cells in the first and $n_2 = 6$ cells in the second cell row. The pressure loads $\boldsymbol{p}_{int,st1} = [1.0, 0.0]\,MPa$ and $\boldsymbol{p}_{int,st2} = [0.1, 1.0]\,MPa$ provide the necessary forces for reaching the target deformation of $\Delta u_{0,st1} = 5°$ and $\Delta u_{0,st2} = -5°$ per cell. The baseline geometry Geo_0 is modified to better comply with the optimization objective and labelled Geo_+. With the third alternative initial geometry Geo_- also a poorly chosen starting geometry is optimized, in order to evaluate the robustness of the process. Detailed information about the input parameters for the structural model is given in appendix D.

The optimization process is performed according to chapter 2.4.1 and follows the flow chart that is presented in Figure 2-12. The logarithmic representation of the convergence behaviour over the wall-clock time t_{WT} in dependency of different initial geometries and *Young*'s moduli is shown in Figure 2-14. The computation is implemented in *Matlab R2011a* and executed on a *Windows 7* workstation with an *Intel Xeon E5-2643* processor with 3.30 GHz. The stop criterion of $\eta_{\dot{\Pi}} = 1e-5\,J/rad$ leads to a maximum angular deviation in terms of the target geometry of $\eta_{u_0,max} = 1.90e\text{-}7°$.
Depending on the initial geometry the energy potential falls below the stop criterion after $z_{II} = 7 \ldots 10$ iterations. The necessary number of iterations z_I for the intermediate step of optimizing the inner independent state variables $\boldsymbol{u}_1$ is given in Figure 2-14 for Geo_+ and Geo_-.

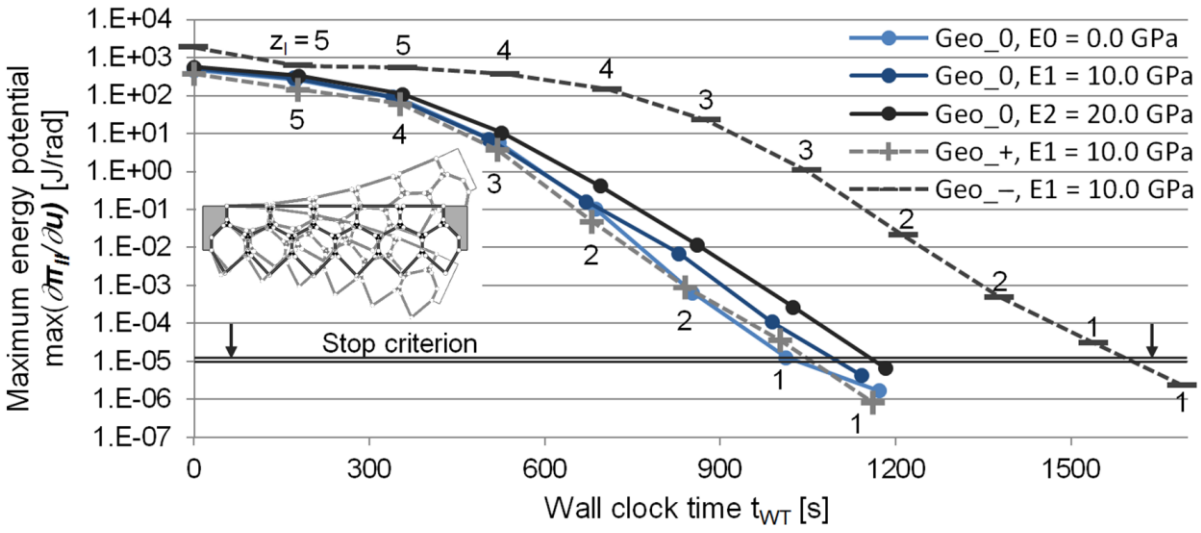

Figure 2-14: Convergence curve for exemplary structure extracted from the shape-optimization procedure for infinitesimal and finite hinge stiffness

It can be seen that the speed of the shape-optimization procedure depends on the definition of suitable initial model parameters. The optimization objective is reached for each set of initial parameters. As multiple solutions exist, which lead to the targeted deformation behaviour, the resulting PACS structures are not identical. In this investigation all of the different sets of initial model parameters lead to valid results. However, the optimization objective cannot be reached, if

- the forces that are provided by the internal cell pressure or by external loads are not sufficient to allow for the desired deformation and to overcome the structural stiffness,
- the initial model parameters lead to an invalid design of the cell compound, or if
- the change of the vector of design variables for shape optimization $\boldsymbol{w}$ results in an invalid design of the cell compound.

An invalid design is for example given when the length of one cell side of a pentagonal cell exceeds the sum of the remaining cell side lengths. No matter of the cell side angles the pentagonal cell can thus not be formed.
The fundamental equations of the shape-optimization process for PACS are described. With the optimization of a generic double row cantilever structure, it is shown for different initial model parameters in terms of *Young*'s moduli and starting geometries that the gradient-based optimization method converges rapidly and reliably. The related equations remain valid for an increased number of cell rows and can also be utilized to conceive PACS that are able to deform between more than two target shapes.

2.5 Simulation and characterization

Within the shape optimization, the geometry of the PACS is determined to provide the capability of deforming from an initial manufacturing state of shape into a given number of target shapes that is equal to the number of cell rows h. For these states of shape and the underlying LBCs the deformations of the PACS are known. The effects of a change of internal or external loads on the equilibrium state of the structure are not analysed so far. Within this section, the simulation of the shape-optimized structure is described and allows to examine the PACS for changing LBCs and thus to investigate its pressure-dependent deformation and stiffness characteristics. Further, the approach of virtual work is used to compute the structural stresses within the cell side and hinge elements.

2.5.1 Computation of the equilibrium state of shape

The difference between optimizing the equilibrium state of shape for a given geometry and computing the geometry of a structure for causing a desired shape variation lies in the definition of the design variables (cf. Figure 2-12 and Figure 2-15). In both cases the optimization objective is defined by the minimization of the vector of energy potentials $\dot{\boldsymbol{\Pi}}$ and thus the computation of the equilibrium state of shape. In the shape-optimization process, the vector of design variables $\boldsymbol{w}$ is used to control the energy potential for the given target shapes. For the computation of the deformations of a given PACS due to a specific load case, this vector is replaced by the vector of independent state variables $\boldsymbol{u}$.

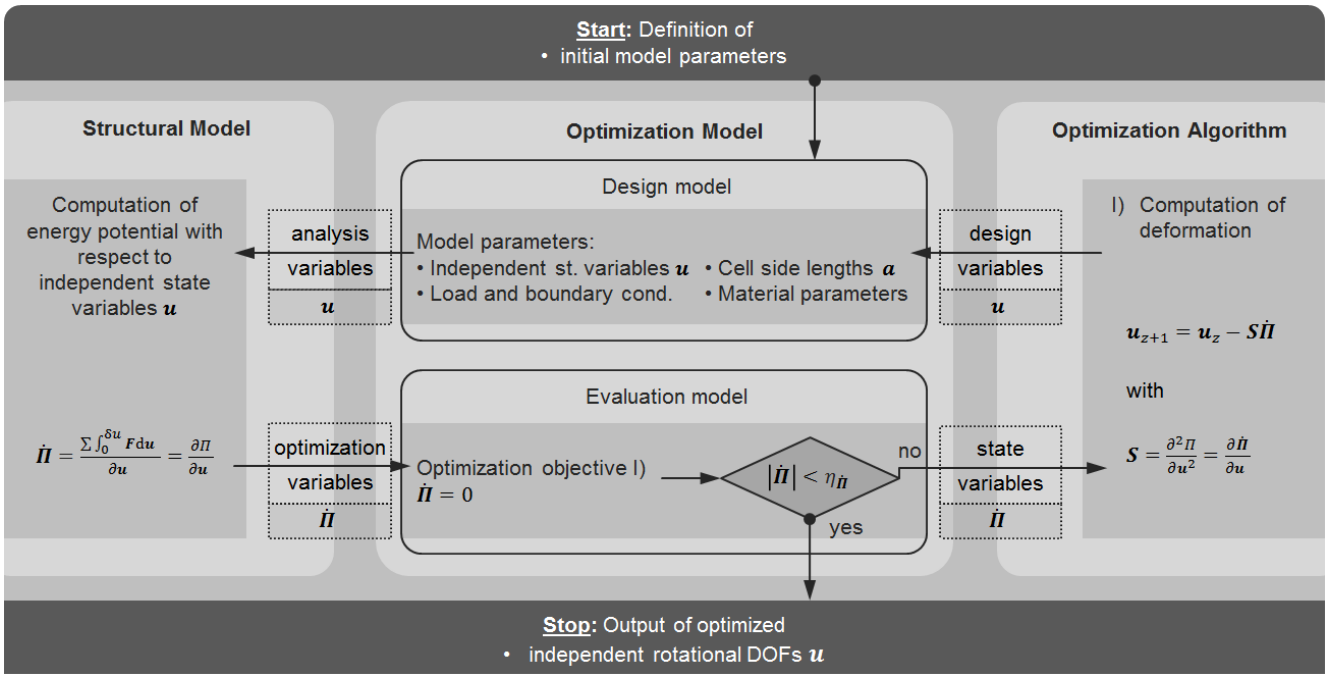

Figure 2-15: Flowchart describing the simulation of a PACS in terms of the optimization of the independent state variables $\boldsymbol{u}$

The adaption of the so far presented optimization process for the calculation of the equilibrium state of shape of a PACS with respect to the applied LBCs is given in the following. Figure 2-15 illustrates the simulation process, which shall be understood as an optimization of the independent state variables $\boldsymbol{u}$. The application of LBCs is described in chapter 2.1. The optimization approach according to the gradient-based Newton's method is given with equation (2.43).

The deformations of the shape-variable structure can be described as the difference between the equilibrium state of shape and the manufacturing state of shape. A variation of forces that act on the structure causes a change of the equilibrium. Analogically to equation (2.46), the vector of energy potentials $\dot{\boldsymbol{\Pi}}$ can be calculated by

$$\dot{\boldsymbol{\Pi}} = \frac{\partial \Pi}{\partial \boldsymbol{u}} = \left[\frac{\partial \Pi}{\partial u_{0,1}} \quad \dots \quad \frac{\partial \Pi}{\partial u_{0,2n_1}} \quad \frac{\partial \Pi}{\partial u_{1,1}} \quad \dots \quad \frac{\partial \Pi}{\partial u_{1,6n_1-1}}\right]. \tag{2.59}$$

For structural systems with a small number of DOFs the equilibrium state can be found by calculating $\boldsymbol{u}$ in a closed solution. For the structural model of a PACS, with a large number of optimization variables, the current state variable $\boldsymbol{u}_{z+1}$ for the iteration step $z+1$ is calculated iteratively by

$$\boldsymbol{u}_{z+1} = \boldsymbol{u}_z - \frac{\dot{\boldsymbol{\Pi}}}{\partial \dot{\boldsymbol{\Pi}}/\partial \boldsymbol{u}} = \boldsymbol{u}_z - \dot{\boldsymbol{\Pi}}(\boldsymbol{u}_z)\boldsymbol{K}^{-1}(\boldsymbol{u}_z). \tag{2.60}$$

The calculation of the second derivative of the potential energy after the independent state variables $\boldsymbol{u}$ leads to the stiffness matrix $\boldsymbol{K}$. The size of $\boldsymbol{K}$ is $[8n_1 - 1 \times 8n_1 - 1]$ for the herein considered double row PACS (cf. Figure 2-10). The stiffness matrix is calculated by

$$\boldsymbol{K} = \frac{\partial^2 \Pi}{\partial \boldsymbol{u}^2} = \frac{\partial \dot{\boldsymbol{\Pi}}}{\partial \boldsymbol{u}} = \begin{bmatrix} \frac{\partial \dot{\Pi}_1}{\partial u_1} & \frac{\partial \dot{\Pi}_1}{\partial u_2} & \dots & \frac{\partial \dot{\Pi}_1}{\partial u_{8n_1-1}} \\ \frac{\partial \dot{\Pi}_2}{\partial u_1} & \frac{\partial \dot{\Pi}_2}{\partial u_2} & & \frac{\partial \dot{\Pi}_2}{\partial u_{8n_1-1}} \\ \vdots & & \ddots & \vdots \\ \frac{\partial \dot{\Pi}_{8n_1-1}}{\partial u_1} & \frac{\partial \dot{\Pi}_{8n_1-1}}{\partial u_2} & \dots & \frac{\partial \dot{\Pi}_{8n_1-1}}{\partial u_{8n_1-1}} \end{bmatrix}. \tag{2.61}$$

The necessary input for the numerical computation of the equilibrium state of a double-row PACS is completed. In accordance with the shape optimization, this approach can be extended by the consideration of more than two cell rows by adapting the vector of independent rotational DOFs.

2.5.2 Computation of cell side and hinge stresses

The computation of structural stresses on the basis of model variant 3 provides essential information for the selection of materials, the design of cell sides and the orientation and dimensioning of flexure hinges. Preliminary strength analysis can thus be performed for cell side and hinge elements. Bending moments at hinge elements are computed analytically with knowledge of the local structural deformations. Methods for the computation of cell side longitudinal forces for each state of shape are presented in the following.

The computation of stresses is processed by using the AVW. Analogically to the virtual displacement δu the virtual cell-side-elongation δa causes the virtual work δW. The quotient of virtual work and virtual displacement in this case yields the scalar potential respectively force value f within the observed cell side:

$$\dot{\Pi} = -\frac{\delta W}{\delta a} = -\frac{\sum \int_0^{\delta a} F \mathrm{d}a}{\delta a} = -f. \tag{2.62}$$

With a size of $7n_1 + 5$, the vector of energy potentials, which yields the normal load within each cell side of the double row PACS that is depicted in Figure 2-10, is calculated to

$$\dot{\boldsymbol{\Pi}} = \frac{\partial \Pi}{\partial \boldsymbol{a}} = \left[\frac{\partial \Pi}{\partial a_1} \quad \cdots \quad \frac{\partial \Pi}{\partial a_{7n_1+5}}\right] = \boldsymbol{f}_{CS,n}. \tag{2.63}$$

It is equal to the vector of cell side normal forces $\boldsymbol{f}_{CS,n}$. Depending on the respective cell side wall thickness $t_{CS,\boldsymbol{k}}$, the cell side normal stresses for a PACS of depth d are

$$\sigma_{CS,n,\boldsymbol{k}} = \frac{f_{CS,n,\boldsymbol{k}}}{dt_{CS,\boldsymbol{k}}}. \tag{2.64}$$

A constant global cell side thickness of $t_{CS} = 1\,mm$ is underlying all of the illustrations that are presented in the following. Additionally to the normal forces, the lateral force and the moment distribution is needed for the sizing of cell sides. An illustration of the involved loads and an exemplary force and moment distribution over the cell side length is shown in Figure 2-16.

The total surface load $p_{tot,\boldsymbol{k}}$ can be extracted from the present load set and comprises of internal and external aerodynamic pressure loads. According to equation (2.8), the hinge moments $M_{\boldsymbol{k}^-}$ and $M_{\boldsymbol{k}^+}$ at the left hinge $\boldsymbol{k}^- = (h, i, j)$ and at the right hinge $\boldsymbol{k}^+ = (h, i, j+1)$ can be calculated from the known hinge stiffnesses $c_{\boldsymbol{k}}$ and bending angles $\Delta u_{c,\boldsymbol{k}}$. The transverse force distribution results in

$$Q_{\boldsymbol{k}}(x) = F_{l,\boldsymbol{k}^-} - \frac{1}{2} p_{tot,\boldsymbol{k}} a_{\boldsymbol{k}} d + p_{tot,\boldsymbol{k}} dx. \tag{2.65}$$

The distribution of moments can be calculated by

$$M_{CS,\boldsymbol{k}}(x) = M_{\boldsymbol{k}^-} + \left(F_{l,\boldsymbol{k}^-} - \frac{1}{2} p_{tot,\boldsymbol{k}} a_{\boldsymbol{k}} d\right) x + \frac{1}{2} p_{tot,\boldsymbol{k}} dx^2. \tag{2.66}$$

Both lateral forces $F_{l,\boldsymbol{k}^-}$ and $F_{l,\boldsymbol{k}^+}$ on the left and right side of the examined cell side can be calculated with knowledge of the given hinge moments. Using the boundary condition of $M_{CS,\boldsymbol{k}}(x = a_{\boldsymbol{k}}) + M_{\boldsymbol{k}^+} = 0$ with equation (2.66) yields

$$F_{l,\boldsymbol{k}^-} = -\frac{M_{\boldsymbol{k}^-} + M_{\boldsymbol{k}^+}}{a_{\boldsymbol{k}}}. \tag{2.67}$$

With $Q_{\boldsymbol{k}}(x = a_{\boldsymbol{k}}) + F_{l,\boldsymbol{k}^+} - \frac{1}{2} p_{tot,\boldsymbol{k}} a_{\boldsymbol{k}} d = 0$ and equation (2.65), the second transverse force is

$$F_{l,\boldsymbol{k}^+} = \frac{M_{\boldsymbol{k}^-} + M_{\boldsymbol{k}^+}}{a_{\boldsymbol{k}}} = -F_{l,\boldsymbol{k}^-}. \tag{2.68}$$

The transverse forces at both sides of the cell side elements can be calculated by superposing the moment- and pressure-based load components according to

$$f_{CS,l,\boldsymbol{k}^-} = F_{l,\boldsymbol{k}^-} - \frac{1}{2} p_{tot,\boldsymbol{k}} a_{\boldsymbol{k}} d \text{ and} \tag{2.69}$$

$$f_{CS,l,\boldsymbol{k}^+} = F_{l,\boldsymbol{k}^+} - \frac{1}{2} p_{tot,\boldsymbol{k}} a_{\boldsymbol{k}} d. \tag{2.70}$$

Compared to the hinge stresses, the cell side stresses are subordinate and thus influence the sizing of the PACS only slightly. However, the related forces are needed for computing the stresses within the hinge elements. As the hinge elements are conceived to avoid transversal forces (cf. chapter 3), only bending moments and normal forces should have to be borne.
With knowledge of the support reactions of the cell side elements, the resultant forces at hinge $\boldsymbol{k}$ can be computed by evaluating

$$f_{H,\boldsymbol{k}} = \sqrt{\left(f_{CS,n,\boldsymbol{k}}\right)^2 + \left(f_{CS,l,\boldsymbol{k}}\right)^2}. \tag{2.71}$$

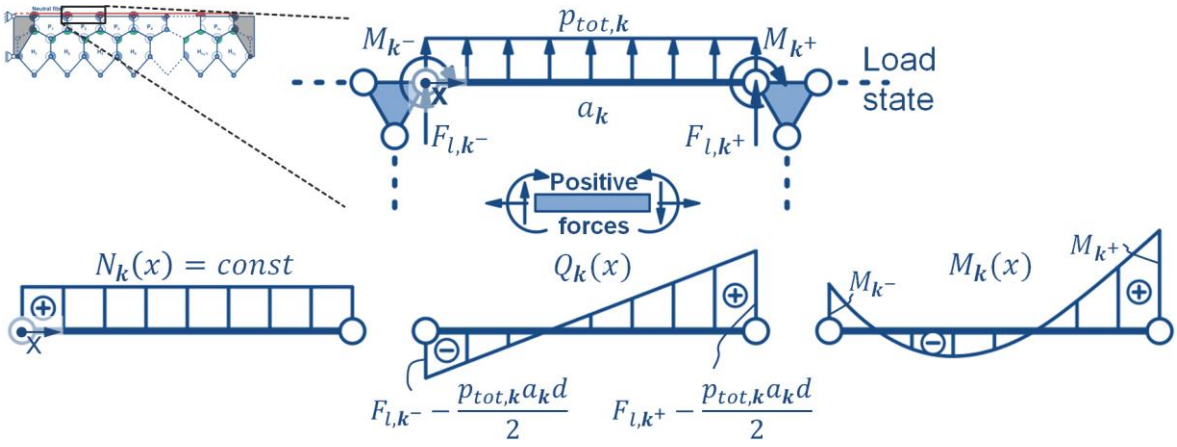

Figure 2-16: Exemplary normal force, transverse force and moment distribution for the cell side element of a compliant PACS

The global vector of hinge normal forces $\boldsymbol{f}_H$ can thus be assembled. The stresses in the extreme fibre of the hinge element is calculated by superpositioning the normal stresses with the maximum bending stresses. The maximum hinge stress $\sigma_{H,\boldsymbol{k}}$ for a hinge with the thickness $t_{H,\boldsymbol{k}}$ is

$$\sigma_{H,\boldsymbol{k}} = \frac{f_{H,n,\boldsymbol{k}}}{dt_{H,\boldsymbol{k}}} + 6\frac{c_{\boldsymbol{k}}\Delta u_{c,\boldsymbol{k}}}{dt_{H,\boldsymbol{k}}^2}. \tag{2.72}$$

The ability to compute the structural loads for each equilibrium state of shape of a given PACS geometry allows for the analysation of stresses and the load-based design of cell side and hinge elements. Stress results from these calculations do not include local maxima. Stress peaks appear for example at transition zones between cell sides and hinges for a compliant hinge that is not optimally aligned in terms of forces. FEM-based analysis are thus to be processed subsequently to this preliminary examination to ensure not to exceed the material strength.

2.5.3 Simulation of a beam pendulum

The presented methods for the computation of cell side stresses and deformations shall be applied for the simple mechanical problem of the beam pendulum. The example that is shown in Figure 2-13 (a) and described in chapter 2.4.2 is reused to evaluate the given formulations.
The equilibrium state of this kinematic system is found when the potential energy vanishes. According to equation (2.7) the respective angle α_B can be calculated analytically with

$$\delta W_{B,equil.} = m_B g a sin(\alpha_B)\delta\alpha_B - \frac{1}{2}q_B a^2 sin(\pi/2)\delta\alpha_B, \text{ to} \tag{2.73}$$

$$\alpha_B = \sin^{-1}\left(\frac{q_B a}{2m_B g}\right). \tag{2.74}$$

For the given beam pendulum more than one solution for the beam angle α_B can be found, which leads to an equilibrium state of shape.

The beam longitudinal stresses can be computed according to equation (2.63) and (2.64). The AVW thereby simplifies the evaluation of the integral $\int_0^{\delta a} F\mathrm{d}a$, as it allows to obtain the virtual work by calculating the product of the force and the force-parallel local displacement. For the given example the virtual work is computed by

$$\delta W_{B,\sigma} = m_B g cos(\alpha_B)\delta a + \frac{1}{2}q_B a cos(\pi/2)\delta a. \tag{2.75}$$

For a beam of thickness t_B and depth d_B the beam-longitudinal stress is thus

$$\sigma_B = \frac{1}{t_B d_B}\frac{\delta W_B}{\delta a} = \frac{m_B g}{t_B d_B} cos(\alpha_B). \tag{2.76}$$

The presented methods are applied for a single PACS cell in the following.

2.5.4 Simulation and characteristics of a single PACS cell

The pressure-dependent deformation behaviour of an exemplary pentagonal single PACS cell is computed according to chapter 2.5.1 and visualized in Figure 2-17. The geometry of the examined structure is given in the centre depiction. The rotational deformation of the independent DOF $u_{H,1,1,1}$ holds an asymptotic pathway between zero deformation at zero internal pressure and its predefined limit value of $\Delta u_1 = 15°$ for an infinite amount of pressure. The deformation course of a PACS over the internal pressure can be divided into three phases. Within the *Deformation* phase (I) the cell distorts from the unstressed manufacturing shape into a geometrical state that approaches 80 % of the asymptotic state of shape. This phase is responsible for most of the deformation of the structure, yet it does not provide the required stiffness towards external forces. The *Transition* phase (II) represents the interim between phase I and III, where minor distortions (80…95 %) still occur and the stiffening of the cell is already initiated. In the *Stiffening* phase (III) the remaining deformation potential of the structure of 5 % is minimal. A rise of pressure primarily leads to an increased stiffness.
The hinge stiffness $c/d = 10.94\ N/rad$ is calculated according to equation (2.8) and used for each hinge element. It bases on the hinge length of $s_C = 5\ mm$, the thickness of $t_C = 0.25\ mm$ and the *Young*'s modulus of the GFRP material HexPly913 of $E = 42\ GPa$. The deformation pathway over the pressure is additionally given for half and double of the stiffness value c in order to illustrate the influence of this parameter on the structural characteristics. As an increase of the stiffness delays the deformations to higher cell pressures, a decrease of the hinge stiffness leads to faster convergence with the deformational asymptote.

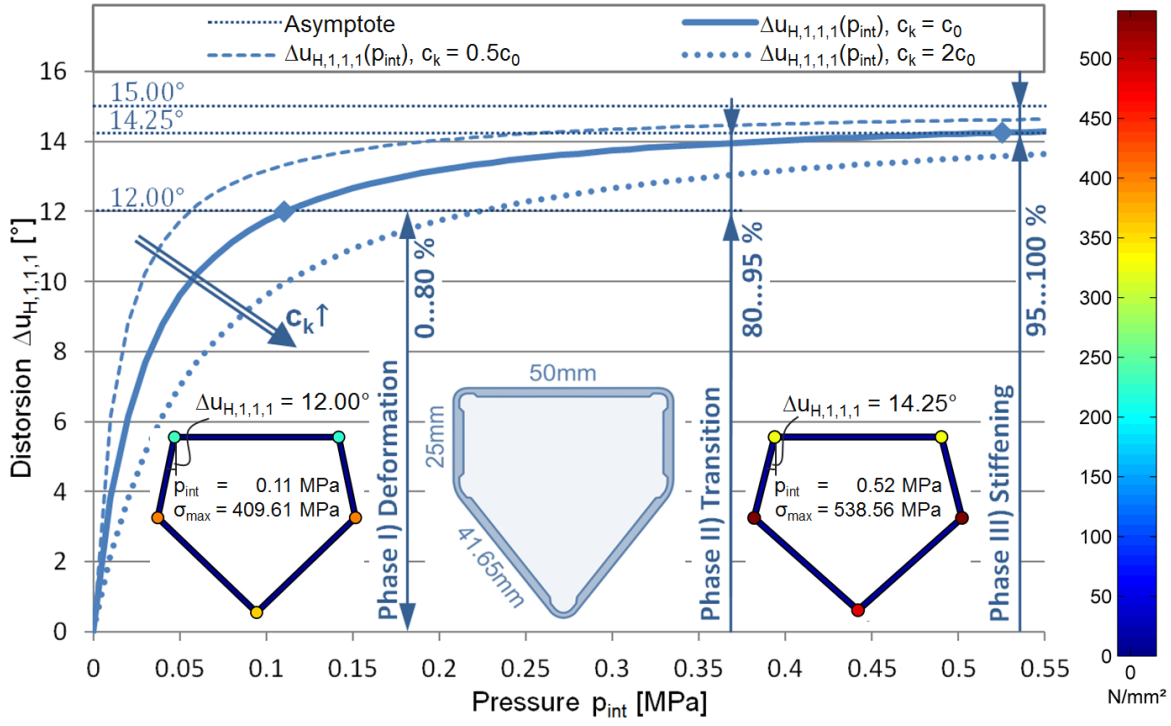

Figure 2-17: Pressure-dependent deformation $\Delta u_{H,1,1,1}$ of the first hinge of a symmetrical single cell, with an asymptotic distortion of $\Delta u_{H,1,1,1} = 15°$

Figure 2-17 also visualizes the structural stresses within the hinge and cell side elements of the PACS cell for two pressure loads and the resulting states of shape. The internal pressure values $p_{int} = 0.11\ MPa$ and $p_{int} = 0.52\ MPa$ are chosen to cause 80 % and 95 % of the asymptotic deformation. The two depicted states of shape of the single cell describe the lower and upper limit of the *Transition* phase. It can be seen that the structural stresses concentrate at the flexure hinges. For these load cases the maximum stresses of $\sigma_{max} = 409.61\ MPa$ and $\sigma_{max} = 538.56\ MPa$ are examined. They appear at the hinge elements and consist of normal and bending stresses according to equation (2.72).

With the exemplary structure of the single PACS cell the optimization process for the computation of deformations could be described. Moreover the characteristic deformation course of the single PACS cell is divided in three significant sections. These sections differentiate by their contribution to the deformation and stiffening of the structure. The dominance of hinge stresses over cell side stresses is verified. In the following, the methods for shape optimization, simulation and characterization are used to design a double row PACS for an aeronautical application.

2.6 Shape optimization and characterization of the variable-chamber wing PACS

The concept of PACS shall be used to provide a solution for the variable-camber wing. It allows for the adaption of the wing's profile according to the actual flight condition. Thill et al. [43] summarizes the possible advantages of such a variable-camber wing to:

- the expansion of the flight envelope and the increase of flight performance,
- the improved stealth characteristics,
- the reduction of drag and vibration and
- the improved properties regarding flutter.

Barrett et al. [15] moreover describes the advantageous effects of flexible flaps on the flight safety in case of microbursts during take-off and landing. Thereby, a decreased stiffness for the high lift configuration is preferential as it lowers lift peaks, which result from a changing air speed.
The exemplary aeronautical application is described first, before the shape-variable structure is designed. The respective PACS is optimized according to chapter 2.4 and its deformation behaviour and the related structural loads are investigated as described in chapter 2.5. The herein presented PACS device for realizing the variable-camber wing is further used in the subsequent chapters as a demonstrative example to illustrate the overall design process.

2.6.1 Description of target application

The general methods for the shape optimization, simulation and characterization of a PACS, which base on a two-dimensional structural truss model, are presented in the chapters 2.1 to 2.5. Its application for a double row PACS according to Figure 2-10, which is used for the implementation of the variable-camber wing, are discussed in the following.
The variable-camber wing PACS device is to be designed for a subsonic aircraft. Following the blended wing body configuration of *SAGITTA* [155], the symmetrical NACA 0012 aerofoil is chosen as the baseline configuration. Possible arrangements of the PACS within the wing profile can be obtained from Figure 2-18. The utilization of PACS for the variable-camber wing allows conceiving multiple implementations, each with particular boundary conditions. The illustrated substitute models show three possible concepts: (1) a double-sided PACS device with closed surface (cf. *Flettner Flap* or servo tab), (2) a split aerofoil and (3) a single-sided device with extending surface.

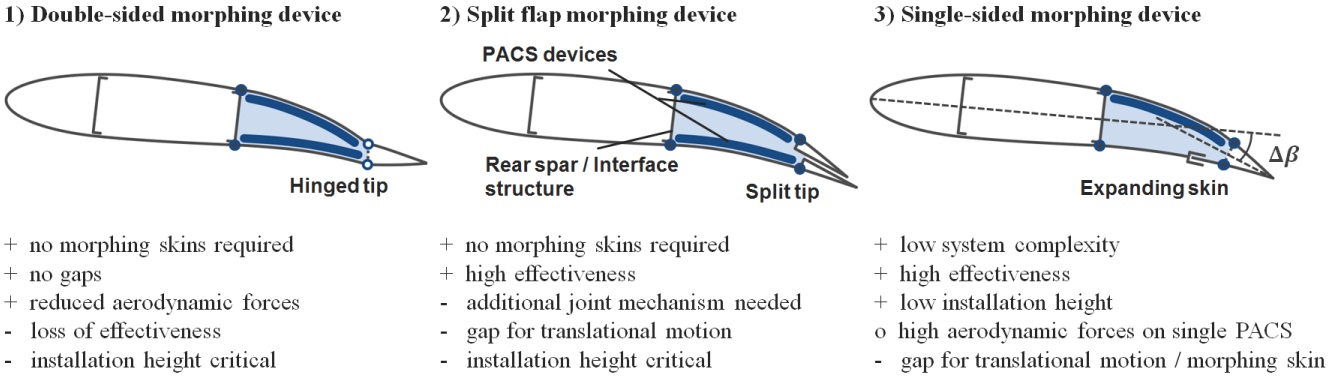

Figure 2-18: Possibilities for the integration of PACS in a morphing aerofoil and their advantages and disadvantages

The according advantages and disadvantages are listed below of each depiction. Due to its advantages regarding the system complexity, the aerodynamic effectiveness and the required installation space, the single-sided morphing device (3) is chosen for this application of PACS. The increased moments and forces that come along with this design concept further allow demonstrating the load-carrying capabilities of the PACS. The positioning of the active system on the upper side avoids step changes of curvature at the fluid mechanically more sensitive low pressure regions.

2.6.2 Load and boundary conditions for the variable-camber wing PACS

The herein presented PACS device consists of two cell rows and is built of $n_1 = 5$ pentagonal cells in the first and $n_2 = 6$ hexagonal cells in the second cell row. It provides a maximum trailing edge deflection of $\Delta\beta = 15°$ for achieving an aerofoil shape with considerable positive camber. The LBCs, which also include the aerodynamic boundary conditions and the related changes of the aerodynamic pressure distribution due to shape variations, are discussed in the following subsections. The input information for the structural model of the variable-camber wing PACS is summarized in appendix E.

Bearing

The PACS is conceived to substitute the conventional wing from 0.6 to 0.9 of the chord length c_{CL}. The shape of the underlying aerodynamic profile NACA 0012 that is used for this application can be described analytically with the definition of the length-dependent thickness

$$t_{NACA\_0012}(x) = 0.6 * (0.2969x^{0.5} - 0.1260x - 0.3516x^2 + 0.2843x^3 - 0.1015x^4). \quad (2.77)$$

The bearing conditions for the PACS are primarily given by the selected integration concept. The single-sided implementation (3) that is shown in Figure 2-18 defines the boundary conditions for the introduction of loads. The boundary conditions within the cell compound, which are defined in chapter 2.2.1 and illustrated in Figure 2-10, are used for this application. It allows to connect the PACS rigidly with the wing's front and rear section and thus to transfer forces and moments between both ends of the structure.

Internal pressure

The necessary internal pressure influences the stiffness of the structure. It thus has to be adjusted to the applied loads. The internal pressure further causes structural stresses in the cell side and hinge elements. These stresses increase linearly with the applied pressure load and usually are considerably lower than the bending induced hinge stresses. The analytical equations that are presented in chapter 2.2.1 for the selection of suitable materials for PACS provide an approach for the preliminary computation of the maximum internal pressure in terms of material strength. For the application of the variable-camber wing, the maximum internal pressure is given with $p_{int,max} = 1.0\ MPa$.

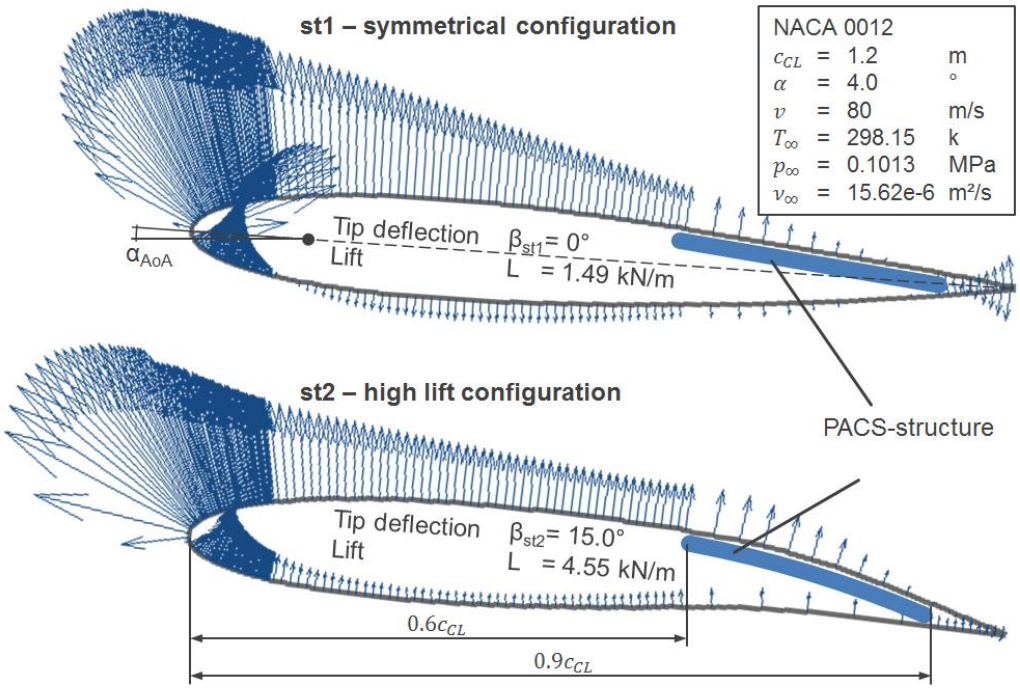

Figure 2-19: Utilization of PACS for realizing the variable-chamber wing and resulting aerodynamic forces

Aerodynamic pressure loads

For the computation results that are presented in the following, the chord length c_{CL}, the flight velocity v_∞, the ambient temperature T_∞ and pressure p_∞ and the kinematic viscosity ν_∞ are given in Figure 2-19. It can be seen that the moderate deflection of $\Delta\beta = 15°$, what means 3° per cell of the first cell row, is sufficient to cause an increase of lift force by the factor 2.52 to $L = 4.55\,kN$ per meter wing span. For the assumed *Reynolds number* of $Re = 6.15e6$ an increase of the lift-to-drag ratio from $C_L/C_D = 69.50$ to $C_L/C_D = 117.48$ results from the variation of the aerofoil shape.

For the realization of a gapless trailing edge flap, the panel-method-based software *XFOIL* is used to compute the two-dimensional aerodynamic pressure distribution on the undeformed and deformed NACA 0012 profile. The results from the aerodynamic computations are visualized in Figure 2-19.

The quality of the aerodynamic pressure distribution that can be achieved using *XFOIL* is evaluated by Madsen H.A. et al. [156] for the sub-sonic application of a wind turbine blade. The computational outcomes for five differing aerofoils are compared with the results of two other software programs and in addition with experimental data. The accuracy of the resulting pressure distribution is specified to lie within ± 10 % for all converged solutions below stall. Only the maximum lift coefficient came up to be overvalued by about 15 %. These values are sufficient for the herein presented investigations.

The resulting pressure distribution is considered in the computation of energy potentials according to equation (2.15). Additional forces and moments due to the aerodynamic pressure on the lower skin of the aerofoil and on its trailing edge have to be included in the optimization and are described as discrete point loads in the following.

Flexure hinges

The influence of the design of the flexure hinges on its stiffness c_k, in terms of the length s_k and thickness t_k, is described within equation (2.8). The length of the flexure hinges is limited to about one tenth of the cell diameter to ensure the concept's functionality. The thickness of the flexure hinge also has to be chosen carefully. In addition to its effects on the structural stiffness, the resulting stresses due to bending are substantially influenced by the hinge thickness. As shown within chapter 2.2.1, for the selected material HexPly913 with the *Young*'s modulus $E = 42\,GPa$ and the strength $R = 1200\,MPa$, an optimum hinge thickness can be found under consideration of internal and external loads.

The hinge stiffness of $c_k/d = 12.42\ N/rad$ is used for the variables-camber wing PACS. Detailed information about the initial geometry of the variable-camber wing PACS is provided in appendix E.

Discrete point loads

As it can be obtained from Figure 2-19, the single-sided concept for the variable-camber wing leads to additional forces and moments at the trailing edge side of the PACS. Surface-perpendicular pressure loads at the rigid trailing edge and the lower skin of the aerodynamic profile are supported by the PACS and have to be applied to the structural model. Besides the subsequently introduced aerodynamic forces, which act on the surface of the PACS, these external bearing forces are introduced at the connection to the rigid trailing edge.
The lower aerodynamic skin has to allow extensional deformations and simultaneously shall prevent from bending. Linear bearings or shear-flexible morphing skins, which are investigated by da Rocha et al. [157], could be used to realize the necessary mechanism. Additional loads due to the structural strain of the morphing skin may result from such a mechanism and can be considered in the form of point loads. As the further design of this substructure is not part of this work, also the related loads are not included in this optimization.

Inertial forces

The magnitudes of the inertial forces depend on the acceleration of the structure, the density of the applied material and the cross-sectional area of the cell body structure (see equation (2.20)). Thus, the mass of a PACS cannot be extracted from the herein used truss model. The transfer between truss model and two-dimensional model is done in a subsequent process that is described in chapter 3. The change of the structural masses and the according change of the inertial forces are calculated in an iterative process to provide relief. For the exemplary structure of the variable-camber wing PACS, the initial overall mass of $m_0 = \rho A d = 10.0\ kg$ results from the assumed cross-sectional area of $A_0 = 5.56e3\ mm^2$, the density of HexPly913 of $\rho_{HexPly913} = 1.80e\text{-}6\ \frac{kg}{mm^3}$ and the depth $d = 1e3\ mm$. Figure 2-20 shows the flowchart that illustrates the iterative process, which is utilized to update the cross-sectional area (CSA), the depending PACS geometry and the related structural mass. The change of the CSA after each iteration step η_A is calculated to

$$\eta_A = \left|\frac{A_{z+1} - A_z}{A_z}\right|. \tag{2.78}$$

The course of this value over the iteration steps as well as the course of the change of the structural mass $m/d = \rho A$ are presented in the next subsection (cf. Figure 2-22) for the given variable-camber wing example.

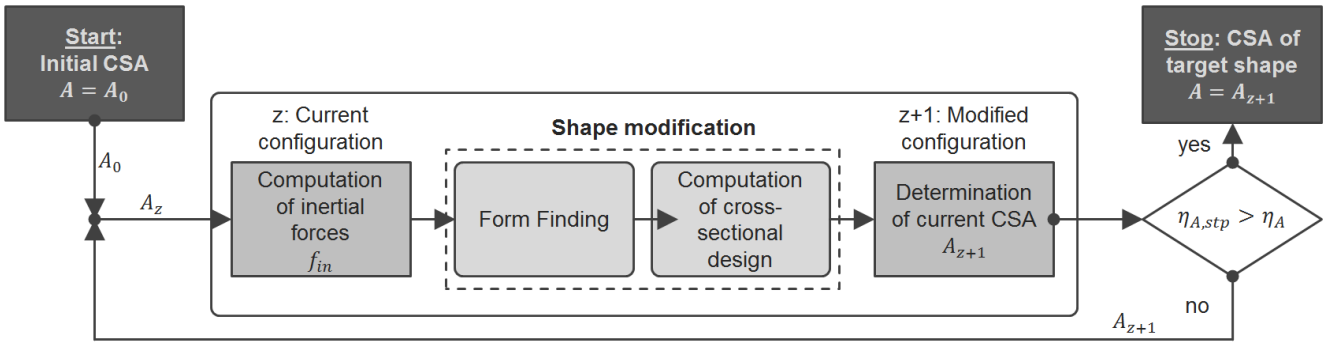

Figure 2-20: Flow chart for the iterative computation of the structure's CSA

2.6.3 Shape optimization of variable-chamber wing structure

For the application of the variable-camber wing, the double-row PACS structure is conceived to move between two target shapes $st1$ and $st2$. The variable-camber wing PACS device replaces the rigid aerofoil between 0.6 and 0.9 of the chord length (see Figure 2-19). The first state $st1$ that shall be achieved is given by the undeformed NACA 0012 profile. The second target shape $st2$ superimposes the initial geometry with the constant curvature of 3° per cell of the upper cell row. A total deflection of $\Delta\beta = 15°$ compared to the first shape is thus achieved. Moreover, the determination of the initial state of shape $st0$ yields the potential to lower bending-based hinge stresses or to satisfy manufacturing needs. For this use case, the initial state of shape is defined to be identical with the first target shape. In case of system failure, the structural stiffness of the PACS causes the deformational resetting to the symmetrical NACA profile.

Figure 2-21 shows the structural model for both target states of shape and thus visualizes the initial model parameters for the shape optimization. In addition to the LBCs, the independent surface state variables $\boldsymbol{u}_0$ and the surface cell side lengths $\boldsymbol{a}_0$, the initial values for the vector of design variables $\boldsymbol{w}$ are therefore provided. A summary of this information as the input for the shape optimization is given in appendix E.
The cell side and hinge stresses are calculated according to chapter 2.5.2. Figure 2-21 shows the initial design of the truss structure before the first optimization step is processed ($z = 0$). The stress results for hinge and cell side elements are given for the undeformed and deformed but apart from that unloaded structures. The hinge bending stresses can thus be estimated prior to the shape optimization. Basing on these results, design parameters like hinge length and cell size can be modified in order to reduce the structural stresses. As the first target shape $st1$ is identical with the initial state $st0$, the bending-induced stresses vanish. For the second target shape $st2$, the maximum hinge bending of $\Delta u_{st2,max} = 7.34°$ can be examined. The global maximum stress results in $\sigma_{st2,max} = 197.24\ MPa$ for the deformational state $st2$ at hinge $\boldsymbol{k} = [2,2,10]$.
The applied inertial forces depend on the shape of the PACS. In order to consider this dependency within the shape optimization process an iterative process is implemented that allows updating the structural mass, as illustrated in Figure 2-20. After the completion of the shape-optimization process according to chapter 2.4.1, the CSA is computed as described in chapter 3.

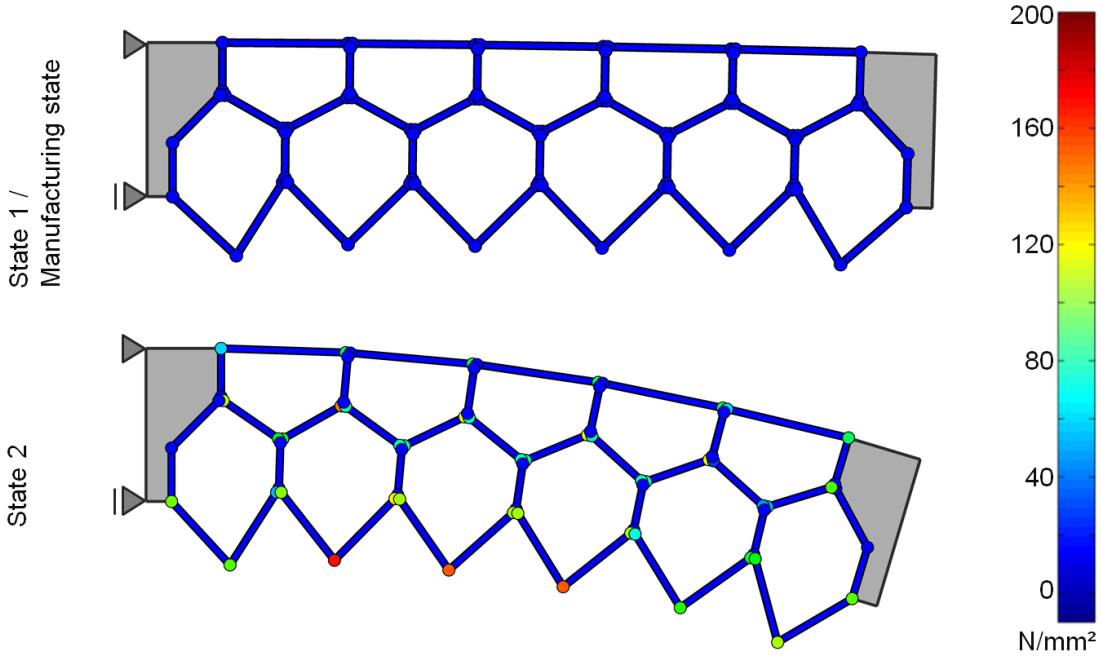

Figure 2-21: Initial configuration for shape-optimization process in variable-camber wing application and deformation-based stresses

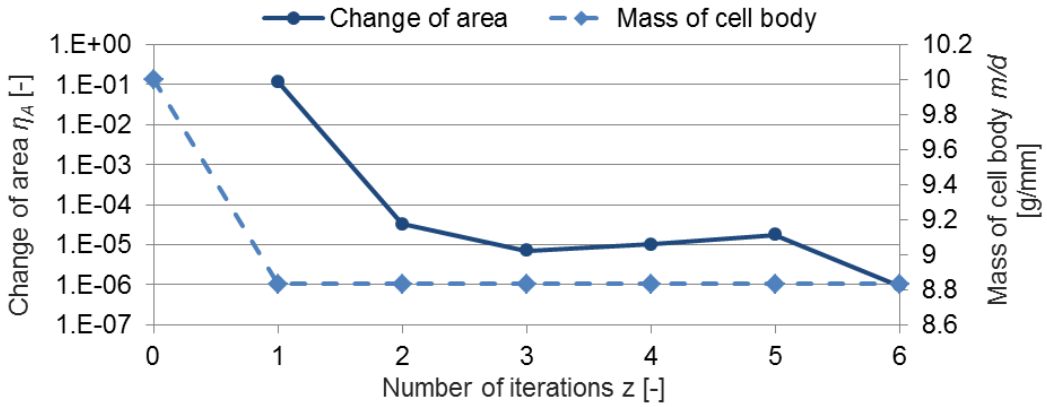

Figure 2-22: Change of weight during iterations of shape optimization

With the information about the CSA, the volume and mass of the PACS can be calculated and the inertial forces are updated. Subsequently, the next shape-optimization process is launched until the change of the cross-sectional area is less than the stop criterion $\eta_{A,stp} = 1e\text{-}6$. For the variable-camber wing PACS the change of the CSA falls below this value after six iterations. Figure 2-22 visualizes the change of the CSA and the absolute mass of the PACS in dependency of its depth m/d. The change of the structural mass between iteration five and six is $\Delta|m/d| = 9.82e\text{-}5\ g/mm$.

The shape optimization for the variable-camber wing PACS device is performed and the results are illustrated in Figure 2-23. Aerodynamic loads, point loads and inertial forces are shown relatively to each other and with their orientation. The internal pressure in each cell row is determined to $\boldsymbol{p}_{int,st1} = [0.1, 1.0]\ MPa$ for the first and to $\boldsymbol{p}_{int,st2} = [1.0, 0.1]\ MPa$ for the second target state of shape.

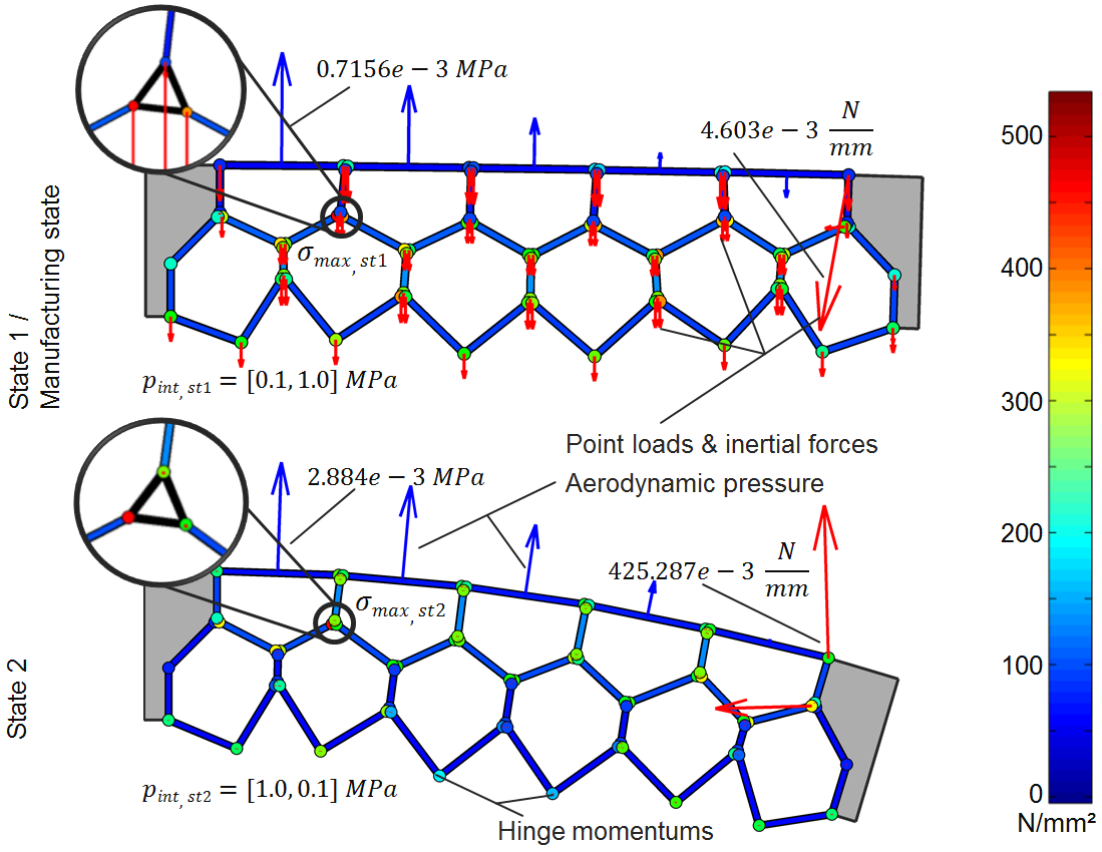

Figure 2-23: Resulting truss geometry and structural stresses after shape optimization of variable-camber wing PACS

Deformations and structural stresses are given with consideration of the target-state-dependent LBCs. A comparison of the unloaded initial structure (cf. Figure 2-21) with the loaded target structure (Figure 2-23) visualizes the modification of the cell side lengths, which results from the optimization process. It also illustrates the proportion of structural stresses that is due to deformations. The superposition of bending and normal stresses within the hinge elements leads to a maximum stress of $\sigma_{st2,max} = 536.17\ MPa$ for the second state of shape at hinge $\boldsymbol{k} = [1,1,4]$. Basing on the material data that is presented in Table 2-6, the strength utilization of the GFRP material HexPly913 is 44.7 % in the most highly stressed hinge element.

The methods for the shape optimization of PACS are applied for the use-case of the variable-camber wing. With this, the first step of the holistic design of PACS, the shape optimization is fully described and demonstrated.

2.6.4 Structural behaviour of PACS and design sensitivities

The computation of the geometry for PACS on the basis of a two-dimensional truss model is described and provides the input for the herein presented simulation and characterization. The deformational reaction on changing internal or external forces for an arbitrary state of shape in general and for the initial and target states of shape in particular, is presently unknown. This means that the deformational shape of the structure is only known for the specified LBCs, which lead to the target states of shape. Any change of these LBCs leads to an unknown deformation. Based on the two-dimensional structural model, the effects of a variation of external and internal loads on the deformations, or in other words the stiffness of the structure, are investigated in this section.
The methods for the computation of the equilibrium state of shape for arbitrary loads allow investigating the load-dependent deformation behaviour. As an expansion of the investigations on the single PACS cell in chapter 2.5.4, the categorization of the deformation phases is transferred to the double row PACS. The calculation of the respective structural stresses is described subsequently.
A summary of design sensitivities, which influence the structural characteristics, is provided as a result of these investigations.

The deformational reaction on changing external forces and in particular on an alternating aerodynamic pressure distribution on the wing is unknown and exceeds the present information about the structure for three specific pressure and load states. A change in flight velocity, angle of attack or cell pressure consequently would lead to an unknown wing shape. The deformations and stresses in dependency of these loads can be investigated according to chapter 2.5. The presented results are exemplarily given for the aeronautical device but are transferable for arbitrary applications. In similarity with the pressure-dependent deformation behaviour of the single cell that is described in chapter 2.5.1, the deformation behaviour of the cell compound can also be divided in the three phases, *Deformation* (I), *Transition* (II) and S*tiffening* (III). These phases of deformation can be found for single pressurized cell rows and for a constant ratio of pressure between different cell rows. The boundaries of the phases are marked in Figure 2-24 for the variable-camber wing PACS.
The rotation $\Delta\beta$ corresponds to the orientation of the upper cell side of the last cell in the first cell row ($\boldsymbol{k} = [1,5,1]$). It depends on the behaviour of all intermediate cells between this cell and the bearing and thus provides a cumulative representation of the local deformation values. The rotation $\Delta\beta$ over the pressure factor PF is depicted for the three different pressure ratios that are given in the legend. External forces are neglected for this investigation. It can be seen that for a pressure factor of $PF = 1.5$, which is multiplied with the pressure values, the rotational angle $\Delta\beta$ can be adjusted between $-1.0°$ and $28.7°$ by controlling the pressure ratio $p_{int,1}/p_{int,2}$. Analogically, the control of both, the pressure factor and the pressure ratio, allows reaching each point of the area that is enclosed by the upper and lower deformation courses.

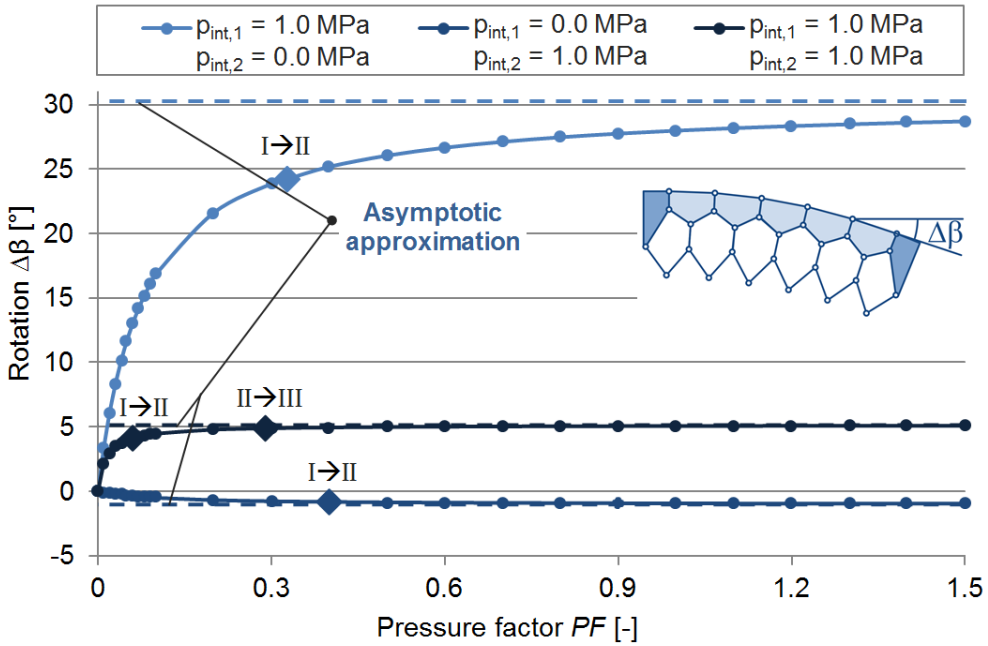

Figure 2-24: Pressure-dependent deformation and stiffening behaviour for separated and combined pressurization

Besides the investigation of the deformational characteristics of PACS, the stiffness and strength properties are evaluated. Figure 2-25 depicts the rotational deformation together with the maximum stress σ_{max} for the target pressure ratios $\boldsymbol{p}_{int,st1} = [0.1, 1.0]\ MPa$ and $\boldsymbol{p}_{int,st2} = [1.0, 0.1]\ MPa$ that are defined for causing the target shapes. Regarding the second load state, the black double line in Figure 2-25, bottom, marks the minimum pressure factor that is sufficient to bear the current loads. A further reduction of the pressure factor or an increase of the applied forces would lead to a step in the deformation course due to instability. The gradient-based computation of the equilibrium state does not converge. The different states of shape that result from these varying pressures are presented in appendix E and illustrate the effects of the cell pressure on the structural stiffness. Five main conclusions, which condense the included information, can be deduced from these graphs.

- A PACS structure loaded with external forces may collapse for low internal pressures. An increase of the hinge stiffness and the cell pressure prevent from excessive deformations.
- The structural stresses do not imperatively rise with increasing external forces. Depending on their orientation, with respect to the actual deformations, external forces may also reduce the maximum total stress of a PACS by counteracting local deformation and hinge bending.
- The convergence of the asymptotic deformation for a finite pressure factor (cf. Figure 2-24 and Figure 2-25) is counteracted by increasing hinge stiffness and external forces.
- The greater the distance between target state of shape and asymptote, the greater is the pressure-induced energy potential and thus the impact of changing cell pressure factors on this state of shape.
- The stiffness against external forces is different for each pressure ratio. The effects of external loads on the structural deformation have to be computed for each relevant load case.

The possibility of influencing the structural stiffness allows controlling the structural reaction on a variation of loads. Besides the pressure input, the concept of PACS provides additional opportunities to influence the structural behaviour. Advantages result in particular for the variable-camber wing application. The symmetrical wing profile configuration is intentionally adjusted for the pressure ratio $\boldsymbol{p}_{int,st1}$.

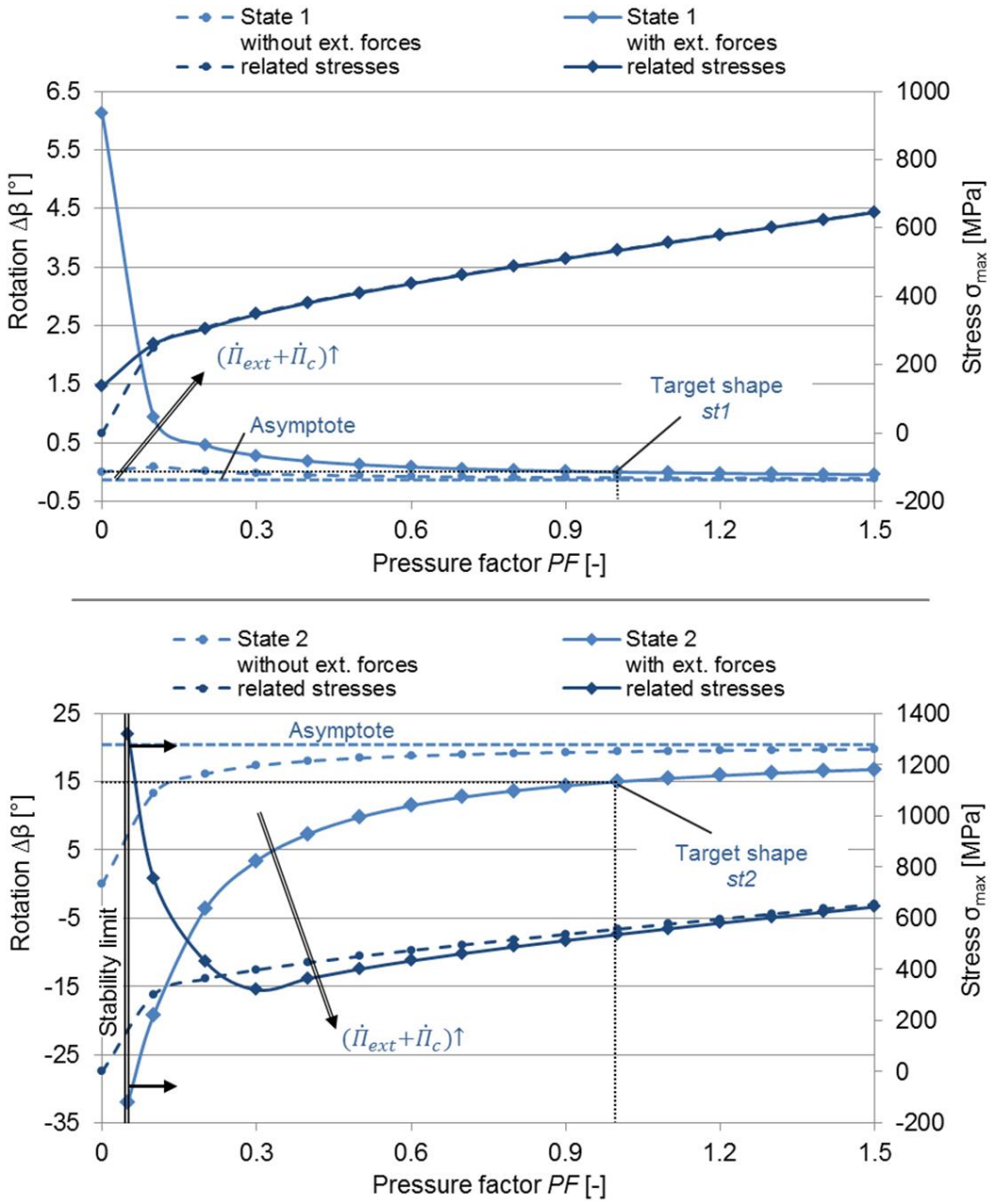

Figure 2-25: Pressure-dependent deformation and structural stresses for the design pressure states, with and without the related external forces of the variable-camber wing application

In this case, the second cell row is pressurized more intensively than the first one. Due to the large distance of the cells of the second row to the neutral fibre and thus the longer lever arm, the stiffness of the PACS at shape $st1$ exceeds the one of $st2$, which is mainly defined by pressure forces on the first cell row. An increase of the aerofoil stiffness prevents from flutter and unfavourable dynamic lift effects. The stiffer state of shape is thus chosen to form the symmetrical aerofoil, which is conceived as cruising, or high speed configuration.

The most important design parameters, which determine the structural strength, its deformation potential, the stiffness against external forces, the deformability and manufacturability, are summarized in Table 2-9 and described in the following:

- The shape of the polygonal cell tubes and the method of their combination to the cell compound define the kinematics of the PACS. Together with the cell size, the geometrical input for calculating the structure's energy potential according to equation (2.7) is given. As the essential influence parameter for controlling the structural stiffness and deformation, the cell geometry substantially affects the efficiency of the PACS.

Table 2-9: Design sensitivities and their influence on the characteristics of PACS

Field	Design parameter	Influenced characteristics
Cell geometry	Cell shape	Global stiffness, stresses, deformability
	Size	Global stiffness, stresses, deformability, manufacturability
Hinge geometry	Length	Hinge stiffness, deformation behaviour, stresses
	Thickness	Hinge stiffness, deformation behaviour, stresses, manufacturability
	Transition	Hinge stiffness, deformation behaviour, stresses
Cell side geometry	Thickness	Stresses, deformation behaviour
	Transition	
Material	Stiffness	Stresses, deformation behaviour
	Strength	Global stiffness, loadability, deformability
	Processability	Manufacturability
States of shape	Initial shape	Deformation behaviour, stresses
	Target shape	
Loads	Pressure	Global stiffness, stresses, deformations behaviour
	External loads	Stresses, deformation behaviour

- Hinge length, wall thickness and geometrical transition between hinges and cell sides influence the hinge stiffness, as stated in equation (2.8). These design parameters affect the deformational behaviour and the resulting stresses in the hinge elements. For the subsequently presented transfer of the truss model to the cross-sectional design, the orientation and curvature of the compliant hinges provide additional factors of influence.
- The cell side length is determined in the truss model and results from the shape optimization. As investigated by Pagitz et al. [146] the cell side longitudinal stiffness, which is controlled by the cell side length, wall thickness and transition geometry clearly affects the resulting deformations. Deformational deviations and cell side stresses can be reduced by an increase of the respective wall thickness.
- From equation (2.34) it can be seen that the *Young*'s modulus of the applied material influences the appearing stresses for a given load state and geometry. As the stiffness of hinges and cell sides is also affected (cf. equation (2.8)), the deformational behaviour depends on the material stiffness. By limiting the pressure level, the material strength is responsible for the maximum structural stiffness, and restricts its loadability and deformability. The manufacturing process and the according achievable accuracy depend on the characteristics of the selected material.
- With the determination of the target shape of a PACS, only the geometry of the neutral fibre is specified. An advanced optimization procedure that allows considering structural stresses and deformation courses could be implemented in the future work on PACS. As the solution for the initial state of shape is not unique, a *Pareto*-optimal geometry can theoretically be computed which reduces the global maximum stresses and optimizes the pressure-dependent deformation course.
- Internal pressure loads and external forces affect the stresses of the structure and influence its deformation behaviour. Due to the functional principle of PACS, the global structural stiffness is primarily caused by the cell-inherent pressure.

The characterization of the variable-camber wing PACS and the identification of influence factors on this characteristics is completed. With knowledge of the structural behaviour, the transfer of the truss model to a cross-sectional design for PACS can be approached in the next step of the design process.

3 Cross-sectional design

The structural model that is used within the shape-optimization process reduces the PACS to its functional components of point and line elements for saving calculation time and to diminish initial design efforts. This chapter describes the methods for the transfer of the abstracted truss model, according to model variant 3, to the geometry of an equivalent cross-sectional area. The major objectives are to reduce the resulting stresses under consideration of deformations and loads and to reproduce the stiffness characteristics of the shape-optimized model. The kinematic characteristic of the structure, which is determined by the local hinge position and stiffness, shall match with that of the truss model to fulfil the assumptions of modelling variant 3 (cf. chapter 2.1.2) and to cause the desired deformation behaviour.

The herein presented methods allow designing the PACS cross-sectional area for one single load state, which is designated as the design point (DP). The load state that causes the highest structural stresses should be used as the DP, as the load-based design allows reducing these stresses. The maximum pressure load of 1.0 MPa in both cell rows ($\boldsymbol{p}_{int,DP} = [1.0, 1.0]\ MPa$) is assumed to fulfil this demand and is determined as the DP for the herein presented investigations.

The variable-camber wing PACS (cf. Figure 2-23) is used to illustrate the approach. The methods for the design of the eccentric flexure hinges with prescribed stiffness, the rigid cell sides and the connection structure are introduced in the following subchapters. The design approach for the merge of these structural sub-elements to an overall cross-sectional design is presented subsequently. Figure 3-1 visualizes the resulting cross-section of the PACS, points out the underlying design variables and gives an overview of the subsequent chapters, which include the description of the related design methods.

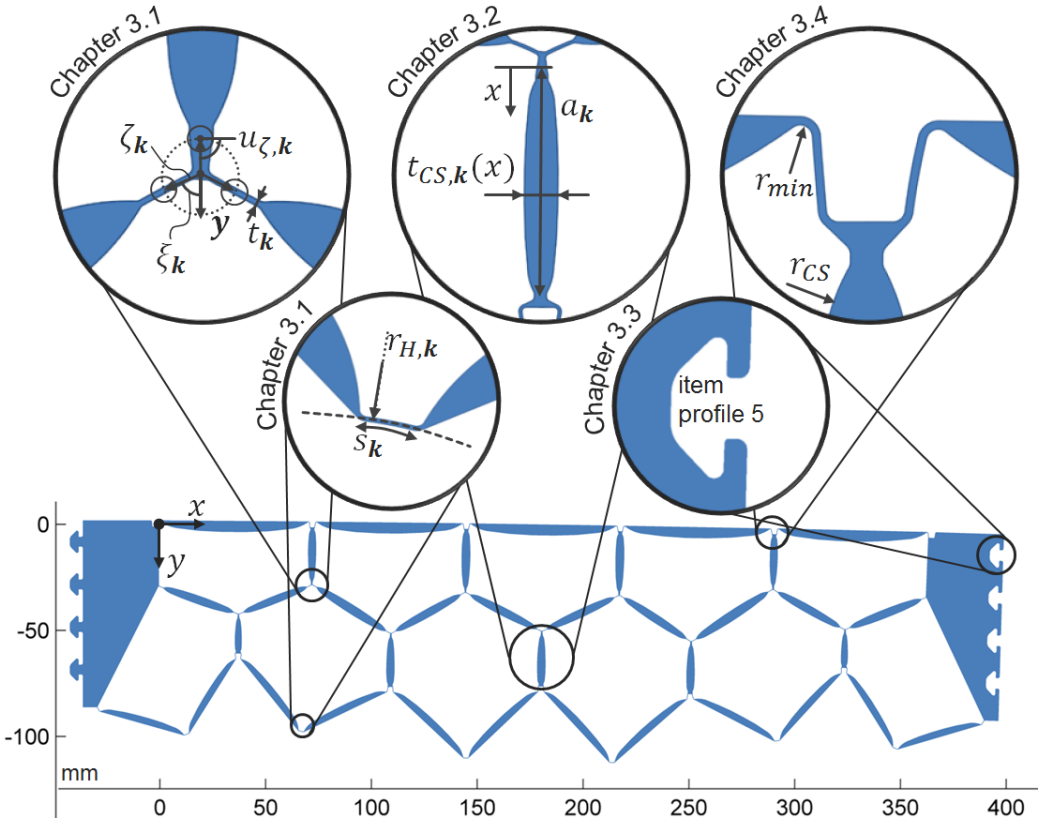

Figure 3-1: Resulting cross section for the variable-camber wing PACS device and respective design parameters

3.1 Flexure hinge geometry

In the truss model, hinges are assumed to be concentrated to a single point and possess a constant rotational stiffness. The resulting demands on the cross-section geometry for an eccentric flexure hinge of finite length with specific orientation and curvature are discussed subsequently. The following criteria must be met with the two-dimensional hinge design:

- Structural stresses due to deformations and loads that are defined for the DP and concentrate at hinge elements shall be reduced. A homogeneous stress distribution over the hinge length shall be achieved, which does optimally not surpass the analytically calculated stresses that consist of only normal and bending stresses.
- The flexure hinges have to be aligned parallel to the resultant forces that act on its endpoints to avoid transverse forces and the resulting additional stresses.
- The appropriate dimensioning of the hinge's curvature avoids a further potential source for bending stresses due to transverse forces. For an optimal stress distribution, also the change of curvature due to bending between initial state and DP has to be considered (cf. Figure 3-2).
- The position of the flexure hinges in the cross-sectional design shall correspond to its location in the truss model. This is a non-trivial issue as the location of the rotational deformation of a flexure hinge is not concentrated at a single point and distributes over its length. An effective hinge position is to be found and should be defined relatively to the position of the hinge endpoints. The effective position of the deformed hinge under consideration of the DP conditions has to be transferred to determine the hinge position for the initial state of shape.
- Length and wall thickness define the stiffness of the flexure hinge according to equation (2.8). The objective to match the rotational stiffness, which is used in the truss model for the shape-optimization procedure, shall be reached. Moreover, length and thickness can be modified in order to reduce the hinge length or to optimize its thickness following equation (2.38). The radius of the hinge eccentricity $\zeta_{\boldsymbol{k}}$ limits the hinge length $s_{\boldsymbol{k}}$, as an intersection of adjacent hinges must be avoided for ensuring their functionality and stiffness characteristics. The need for high longitudinal stiffness to prevent hinge strains is subordinate to the stiffness and strength requirements.

Stresses at the extreme fibre of a hinge element due to normal forces and bending cannot be avoided. Each change of shape causes deformations that concentrate at flexure hinges and result in bending stresses. The analytical relation between rotational deformations and bending stresses is given in equation (2.72). In addition to bending, a hinge element is loaded by forces, which are introduced at its endpoints and result from the underlying LBCs. An optimal hinge design considers the direction of the resultant force for the alignment of a flexure hinge. Local stress peaks due to lateral forces can be avoided by a hinge direction that is parallel to the orientation of the resultant force.
The necessary information about the hinge forces at the DP can be extracted from the structural model as described in chapter 2.5.2. The orientation $\xi_{\boldsymbol{k}}$ of the hinge intersection with radius $\zeta_{\boldsymbol{k}}$ is thus defined to minimize stresses for the specific DP. Figure 3-1 shows the cross section of the variable-camber wing PACS that is designed according to the herein presented methods. On the basis of the shape-optimization results and an internal pressure load of $\boldsymbol{p}_{int,DP} = [1.0, 1.0]\ MPa$, the deformations and forces at the structure's sub-elements, the hinges and cell sides, are analysed and provide the input for the design of the cross-sectional area. Additional external forces are neglected for this example.
The hinge design is optimized for longitudinal tension and bending loads. Stability criteria for the hinge elements in case of compressive and lateral forces are not implemented. The cell-internal pressure loads have to be determined to prevent from stability failure.

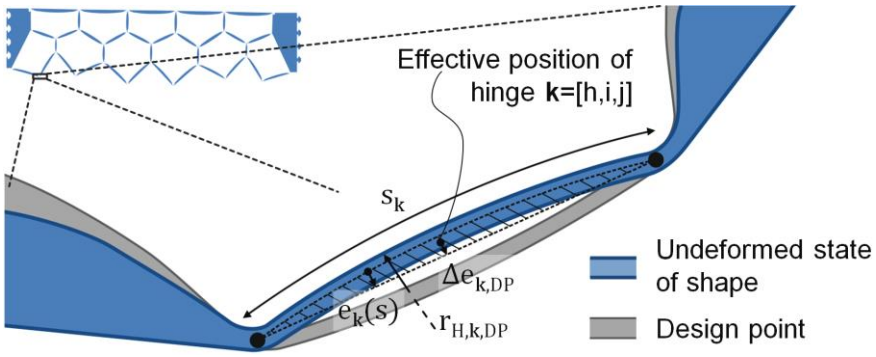

Figure 3-2: Distance between hinge chord and effective position of flexure hinge

The hinge direction shall be calculated for the undeformed state $st0$ of the PACS. The change of its orientation due to the structural deformation between undeformed and design state has to be considered. The hinges' orientation parallel to the resultant hinge force vector $\boldsymbol{f}_{H,\boldsymbol{k}}$ is calculated for the design state first. As each hinge is rigidly connected to at least one cell side, the hinge orientation for the undeformed state can be found by evaluating the local cell side rotation $\Delta u_{CS,\boldsymbol{k},DP}$ at the DP. The cell side orientation angle $\xi_{\boldsymbol{k},st0}$ results in

$$\xi_{\boldsymbol{k},st0} = \measuredangle\left(\boldsymbol{f}_{H,\boldsymbol{k}}, [1,0]\right) - \Delta u_{CS,\boldsymbol{k},DP} = \operatorname{acos}\frac{\boldsymbol{f}_{H,\boldsymbol{k}} * [1,0]}{|\boldsymbol{f}_{H,\boldsymbol{k}}|} - \Delta u_{CS,\boldsymbol{k},DP}. \tag{3.1}$$

Equally to the hinge direction, the curvature of the hinge is designed on the basis of the actual loads of the DP. Besides the eliminated lateral bearing forces $f_{H,l,\boldsymbol{k}}$, the dimensioning of the optimal hinge thickness $t_{\boldsymbol{k},opt}$ according to equation (2.38) does not include bending stresses due to improper curvature. The optimal curvature $\kappa_{\boldsymbol{k},DP}$ at the DP for a flexure hinge of length $s_{\boldsymbol{k}}$ that is loaded with the pressure $p_{\boldsymbol{k}}$ and the resultant hinge force $f_{H,\boldsymbol{k}}$ avoids stress peaks due to lateral forces and is given by

$$\kappa_{\boldsymbol{k},DP} = \frac{1}{r_{H,\boldsymbol{k},DP}} = \frac{dt_{\boldsymbol{k}} p_{\boldsymbol{k}}}{f_{H,\boldsymbol{k}} t_{\boldsymbol{k}}} = \frac{dp_{\boldsymbol{k}}}{f_{H,\boldsymbol{k}}}, \text{ with} \tag{3.2}$$

$$\frac{1}{\kappa} = \frac{\sigma t}{p}. \tag{3.3}$$

The pipe formula that is given with equation (3.3) is used herein to calculate the curvature of the pretensioned and pressure-loaded flexure hinge. The hinge curvature $\kappa_{\boldsymbol{k},st0}$ for the manufacturing state $st0$ is adjusted in order to consider the local hinge rotation $\Delta u_{\zeta,\boldsymbol{k},DP}$ and is calculated by

$$\kappa_{\boldsymbol{k},st0} = \kappa_{\boldsymbol{k},DP} - \frac{\Delta u_{\zeta,\boldsymbol{k},DP}}{s_{\boldsymbol{k}}}. \tag{3.4}$$

For a straight flexure hinge of finite length $s_{\boldsymbol{k}}$ the concentrated or effective hinge position can be assumed to be located at the centre of the hinge line. As the hinges are not designed to be straight in their manufacturing state, the effective hinge position doesn't lie on the hinge line. The distance of the effective hinge point from the hinge's chord line $\Delta e_{\boldsymbol{k},DP}$ is calculated by integrating the distance between hinge and chord line $e_{\boldsymbol{k}}(s)$ over the hinge length $s_{\boldsymbol{k}}$ (see Figure 3-2). It is used in the design process to consider the effective hinge position for the DP. The distance of the effective hinge point from the hinge's chord line $\Delta e_{\boldsymbol{k},DP}$ is calculated with

$$e_{\boldsymbol{k}}(s) = r_{H,\boldsymbol{k},DP}\left(\cos\left(\frac{s_{\boldsymbol{k}}}{r_{H,\boldsymbol{k},DP}}\right) - \cos\left(\frac{s_{\boldsymbol{k}}}{2r_{H,\boldsymbol{k},DP}}\right)\right), \text{ to} \tag{3.5}$$

$$\Delta e_{\boldsymbol{k},DP} = \frac{1}{s_{\boldsymbol{k}}}\int_{-\frac{s_{\boldsymbol{k}}}{2}}^{\frac{s_{\boldsymbol{k}}}{2}} e_{\boldsymbol{k}}(s)\,ds_{\boldsymbol{k}} = \frac{2r_{H,\boldsymbol{k},DP}^2}{s_{\boldsymbol{k}}}\left(\sin\left(\frac{s_{\boldsymbol{k}}}{2r_{H,\boldsymbol{k},DP}}\right) - \frac{s_{\boldsymbol{k}}}{2r_{H,\boldsymbol{k},DP}}\cos\left(\frac{s_{\boldsymbol{k}}}{2r_{H,\boldsymbol{k},DP}}\right)\right). \tag{3.6}$$

The accurate position of the hinge is essential for the deformational characteristic of the PACS. The distance between the hinge chord and the effective hinge position at the DP $\Delta e_{\boldsymbol{k},DP}$, which bases on the curvature $\kappa_{\boldsymbol{k},DP}$, is adjusted in the manufacturing state of shape as an initial chord-perpendicular offset. As illustrated in Figure 3-2, this initial offset is given by $\Delta e_{\boldsymbol{k},DP}$.

3.2 Cell side geometry

In the truss model, cell sides are considered as rigid line elements with infinite longitudinal and bending stiffness. For the dimensioning of cell sides the main objectives are to approach the assumption of rigidity and to satisfy the demand for structural strength. The following requirements shall be fulfilled within this sizing process of the cell side elements:

- Cell side stresses shall be controlled by the adjustment of the local wall thickness. The thickness distribution over the cell side length has to be determined with consideration of the applied loads to utilize the respective material strength and save weight.
- Bending and longitudinal stiffness have to be increased to fulfil the demand for rigidity. With increasing the wall thickness, the stiffness of cell sides can be enhanced and stresses are reduced, but at the cost of additional weight.
- The first cell sides of the first cell row form the outer skin of the PACS. Especially for applications for which the PACS are used as an aerodynamic surface, the shape of these structural elements has to be controlled to suit the related needs.

With knowledge of the local cell side loads for the DP, which are calculated according to chapter 2.5.2, the cell side thickness is determined to suffice the desire for constant extreme fibre stresses. The analytical equations for calculating the appearing longitudinal and bending stresses are provided in the following, before the concept for the load-dependent design of the cell side elements is presented.
Constant normal stresses due to an axial cell side force $f_{CS,n,\boldsymbol{k}}$ are calculated according to equation (2.64). The thickness-dependent normal stress within a cell side is

$$\sigma_{CS,n,\boldsymbol{k}}(x_{\boldsymbol{k}}) = \frac{f_{CS,n,\boldsymbol{k}}}{dt_{CS,\boldsymbol{k}}(x)}. \tag{3.7}$$

The cell side elements are additionally loaded with cell-side-perpendicular loads, which cause bending. The resulting bending stresses at the extreme fibre of a beam depend on the local cell side moment $M_{CS,\boldsymbol{k}}(x)$, the according wall thickness $t_{CS,\boldsymbol{k}}(x)$ and the second moment of inertia in the out-of-plane respectively z-direction $I_{CS,z,\boldsymbol{k}}(x)$. It can be calculated by evaluating

$$\sigma_{CS,b,\boldsymbol{k}}(x) = \frac{M_{CS,\boldsymbol{k}}(x)t_{CS,\boldsymbol{k}}(x)}{2I_{CS,z,\boldsymbol{k}}(x)}. \tag{3.8}$$

The computation of the cell side moment $M_{CS,\boldsymbol{k}}(x)$ is described by equation (2.66). The second moment of inertia in z-direction is

$$I_{CS,z,\boldsymbol{k}} = \int_0^{t_{CS,\boldsymbol{k}}(x)/2} t^2 dydz = \frac{dt_{CS,\boldsymbol{k}}^3(x)}{12}. \tag{3.9}$$

The total stress at the most highly loaded extreme fibre $\sigma_{CS,tot,\boldsymbol{k}}$, which depend on the position x of the cell side, result from the superposition of axial and bending stresses according to

$$\sigma_{CS,tot,\boldsymbol{k}} = \sigma_{CS,n,\boldsymbol{k}} + \sigma_{CS,b,\boldsymbol{k}} = \left|\frac{f_{CS,n,\boldsymbol{k}}}{dt_{CS,\boldsymbol{k}}(x)}\right| + \left|\frac{M_{CS,\boldsymbol{k}}(x)t_{CS,\boldsymbol{k}}(x)}{2I_{CS,z,\boldsymbol{k}}(x)}\right| < \frac{R}{SF_{CS}}. \tag{3.10}$$

For ensuring structural integrity, the total cell side stresses have to be smaller than the strength value of the applied material under consideration of the cell side safety factor SF_{CS}. This stress limitation is used to determine the minimum cell side wall thickness at position x.

$$t_{CS,min,k}(x) = \frac{f_{CS,n,k} + \sqrt{f_{CS,n,k}^2 + 24Rd/SF_{CS}|M_{CS,k}(x)|}}{2Rd/SF_{CS}}. \quad (3.11)$$

For the PACS structure that is depicted in Figure 3-1, this stress criterion is used to compute the minimum thickness of the cell sides.

As described in the second objective, the stiffness of cell sides impacts the accuracy of the computations according to the structural optimization model. The increase of the bending and the longitudinal stiffness, results in the improved conformity of the structural model, which bases on rigid cell side elements. The longitudinal stiffness of a rectangular beam with *Young*'s modulus E, depth d, cell side length a_k and varying thickness $t_{CS,k}(x)$ is

$$c_{CS,n,k} = \frac{Ed \int_0^{a_k} t_{CS,k}(x)dx}{a_k^2}. \quad (3.12)$$

The bending stiffness c_k can be calculated based on equation (2.8), to

$$c_{CS,k} = \frac{EI_{CS,z,k}}{s_k} = \frac{Edt_{CS,k}^3(x)}{12s_k}. \quad (3.13)$$

According to the equations (3.12) and (3.13), a raise of wall thickness increases the longitudinal cell side stiffness linearly and the bending stiffness with the third power. For consideration of the assumption of rigid cell side elements, an increased safety factor is used to improve the cross sectional design regarding the deformation accuracy. For the use case of the variable-camber wing, a large safety factor in terms of cell side stresses of $SF_{CS} = 8$ is chosen and allows for the increase of the cell sides' longitudinal and bending stiffness.

3.3 Connection structure

The last component of a PACS, which completes the compilation of structural sub-elements, is the connection structure. As an interface between the cell body and a conventional rigid structure or further modular PACS devices, the connection structure fulfils the boundary conditions that are determined in the design model. It has to fulfil the following major functionalities:

- The connection structure transfers loads between the PACS's truss structure and the peripheral structure. Deformations, within the linkage or due to material strains have to be avoided to fulfil the assumption of rigidity. Due to the large design freedoms for sizing and topology variations, structural stresses can be controlled to be uncritical.
- The bearing conditions that are provided by the connection structure have to comply with the specifications of the truss model, as they control the position and orientation of the PACS. The design of the connection structure has to fulfil the specifications of the optimization model in terms of the constrained DOFs (cf. Figure 2-10).
- The weight-based performance values of the PACS, like power density and specific actuation stress, have to be enhanced by the light-weight design of the connection structure.
- Depending on the actual use case, the connection structure shall allow for a combination of modular PACS devices, to allow for economic development and production.
- For the usage of the PACS as a shape-variable aerodynamic surface, the connection structure, as part of this surface, has to fulfil the respective shape requirements.
- As the pressure supply is positioned outside the shape-variable structure, the connection has to enable the fluid transfer.
- In case of defects or for maintenance, the connection has to be detachable.

For the variable-camber wing device, the demands on the interface to the peripheral structure are satisfied by a form-locking tongue and groove profile. The selected geometry is inspired by the connection concepts that are used by the *item industrial technology* [158] company to assembly aluminium profiles. Figure 3-1 visualizes this interface structure, the intermediate rigid geometry, which is utilized for implementing the fluid supply, and the linkage to the truss structure. An approach for the optimization of connection structure under consideration of stiffness, stresses and functional areas is not investigated, but would allow reducing the material usage and thus lower weight.

3.4 Transition geometry for the connection of structural sub-elements

The methods for the dimensioning of the individual elements, for the cross-sectional design of a PACS, are presented. The necessary methods for the combination of hinges in the crossover areas, the transition between hinges and cell sides and the linkage between truss and connection structure are presented in this chapter. The combination to the PACS's cross-sectional area is subject to the following requirements:

- Stress peaks at the transition of hinges, cell sides and the connection structures shall be avoided.
- Both for the subsequent integration of the cell closure concept and for the consideration of manufacturing boundary conditions, the design process for the transition geometry has to take geometrical limitations into account.
- Transition areas shall not influence the deformation behaviour of the PACS, are treated as rigid and have to be designed accordingly.

The merge of the structural sub elements is illustrated in Figure 3-3 for the most substantial transition areas at hinge crossovers (I) and between hinges and cell sides (II). The eccentric hinges are introduced in variant 3 to model flexure hinges at cell side crossovers accurately. The intersection of three hinge elements represents the most frequent transition variant. As illustrated in Figure 3-3, left, each transition is implemented by two circular arcs that are interlinked by one straight line. In order to prevent stress peaks and to consider manufacturing limitations, the radius r_{min} is used therefore. Trigonometric calculations allow for an arrangement that provides tangentially constant transitions, which are marked as black dots, between these lines and the hinge elements. The tangential continuity allows for avoiding notches. The two variants that are used for defining the transition geometry differ in terms of the directions of curvature and are labelled with a and b. Depending on the hinge length s_k and thickness t_k only a sufficient hinge eccentricity ζ_k allocates the required space for the transition structure and the related minimum radius r_{min}. For complying with manufacturing boundary conditions and for avoiding stress concentrations due to the notch effect, the minimum radius r_{min} has to be determined for the transition geometry to suit the actual circumstances in terms of geometries and structural loads.

The connection between hinge and cell side elements represents the second variant of transitions. The linkage between a hinge and a boundary cell side is depicted in Figure 3-3, right. In contrary to an inboard cell side, the illustrated external variant possesses a non-symmetric thickness distribution and requires two different transition geometries. A circular arc with radius r_{min} connects tangentially with the hinge structure. The outer surface of the PACS is closed by a straight line, which links the circular arc and the cell side tangentially. The internal surface of this cell side is completed by a second circular arc with radius r_{CS}. It establishes the transition to the analytically calculated stress-based thickness distribution according to equation (3.11). For each internal cell side, this transition variant is applied to both edges of the cell side. The cell side radius r_{CS} has to be determined to allow for the integration of the cell closure structure that is introduced in the next chapter.

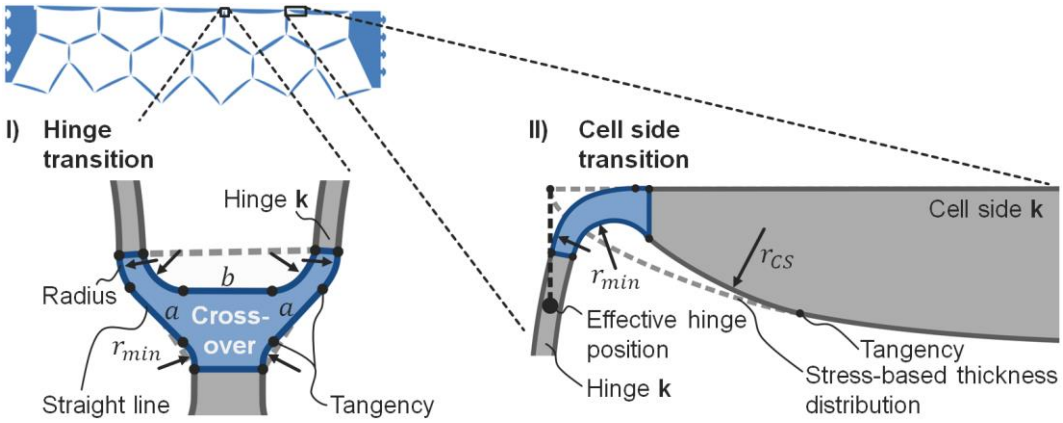

Figure 3-3: Transition geometry between hinges at a crossover (l.) and between hinge and boundary cell side (r.)

The influence of the transition structure on the effective stiffness of the flexure hinges is not investigated. Due to the smooth transition and the only gradual increase of wall thickness, a decrease of hinge stiffness is expected. The deformation behaviour of a PACS, which is sized according to the herein described methods, is examined in chapter 6.1.8 by simulation and experimental test.
It should also be noticed that for load states, varying from the DP, the hinge cell side geometry is not optimal. An optimization potential is identified for the selection of the DP. An optimal DP is chosen to cause the maximum stresses in the PACS. Thus, structural stresses are reduced for this most critical load case. Such an optimization exceeds the contents of this work but points the way for further investigations.

The application of the presented approach for translating an entire PACS truss model into a cross-sectional area is illustrated in Figure 3-1 at the example of the variable-camber wing structure. The assumptions for hinge elements within structural model variant 3 are thereby implemented in the cross-sectional design. The advances in terms of stress reduction due to the force and deformation-based two-dimensional design are investigated and can be confirmed in the subsequent evaluation (see chapter 6.1.6).
With the areal information, the three-dimensional cell body can be formed by extrusion. This dimensioning process completes the two-dimensional draft design for the realization of PACS.

4 Sealing and pressurization

The PACS's cell body is designed and dimensioned to bear loads in the plane of motion. The application of internal pressure loads causes forces in cell-axial direction. For the realization of a functional PACS, a closure concept for the pressure-tight sealing of the shape-variable polygonal cell tubes is needed as well as a lightweight solution for bearing the resultant forces. A holistic design for covering the cells' ends includes a structural concept for the aerial closure of the cell openings (chapter 4.1 to 4.4) and also an assembly concept for the pressure-tight connection between closure and cell structure (chapter 4.5). The demand analysis for cell closure structure is followed by the collection of concepts. The requirements-based selection of the best solution and its simulative characterization are presented subsequently. This chapter completes with the description of the pressure-tight connection of closure and cell body and the design of the fluid flow.

4.1 Demands on the cell closure for PACS

The main challenge in developing a suitable closure for shape-variable cross sections is to combine the conflicting aims of structural strength, such that it withstands out-of-plane (pressure) and deformation-induced loads, and of flexibility, with respect to the in-plane strain. Two-dimensional considerations for designing and characterising the PACS cell body are given in chapter 2 and 3. The therein determined global mechanical behaviour of the structure may significantly be influenced by an inadequately designed closure concept. Therefore, the conception, implementation, and characterization of an efficient cell closure solution shall allow for high performance and accuracy of the assembled cellular structure. The following chapter analysis and discusses the requirements on shape-variable end caps for PACS, which are illustrated in Figure 4-1.

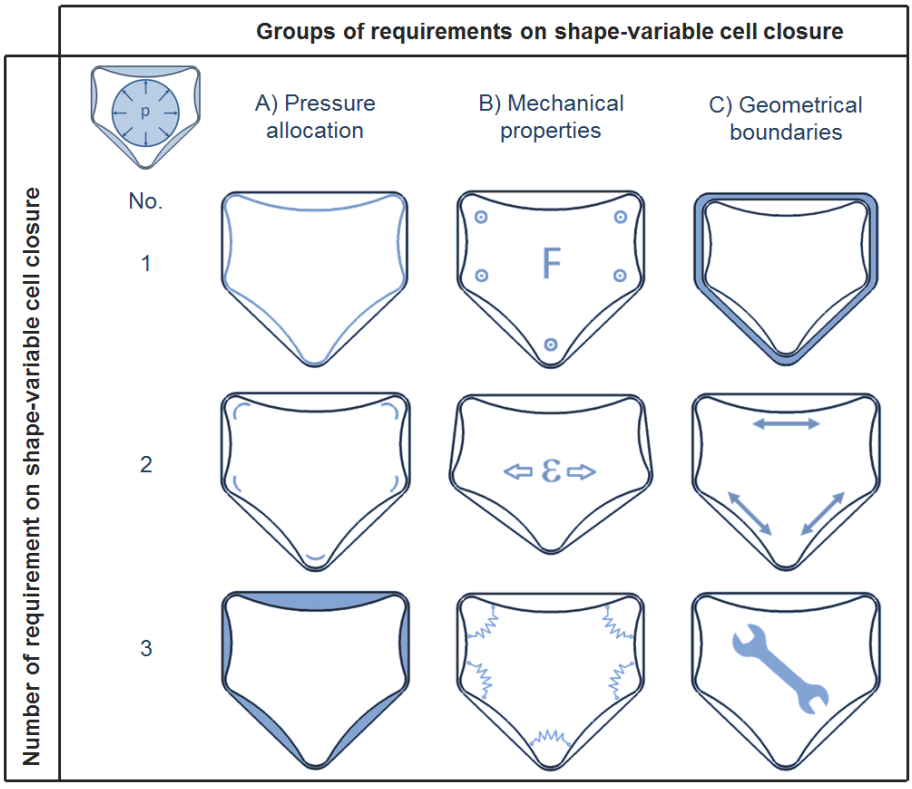

Figure 4-1: Demands on concepts for the shape-variable cell closure, exemplarily shown for a single pentagonal PACS cell

The concept for the cell closure has to ensure the constant pressurization of the complete cell compound, at cell sides, hinges and edge regions (A). It has to bear significant axial forces and simultaneously has to permit cross-sectional deformations, whilst avoiding to influence the PACS structural stiffness (B). Solving conflicting goals regarding stiffness and strength is further complicated by geometrical boundary conditions from neighboured cells and the individual design of the cells' cross sections (C). A classification into pressure allocation, mechanical properties and geometrical boundaries is thus given.

A) Pressure allocation

For analysing the pressure-allocation capabilities of the closure concept, the pressurized areas are divided into the cell side areas (requirement A1 for cell closure concept according to Figure 4-1: $R_{CC}A1$), the narrow areas at the flexure hinges ($R_{CC}A2$) and the front surface ($R_{CC}A3$) that has to be closed. An optimal concept would allow for a constant pressurization of all three zones. A simple elastomeric bladder for example is well suited for the pressurization of the cell sides, but shows disadvantages regarding $R_{CC}A2$, as the inherent stiffness of the bladder prevents the pressurization of sharp corners. A cell closure solution which requires much space in cell-axial direction may disturb the constant pressure distribution near the end of the cell tubes. The requirement $R_{CC}A3$ would thus not be fulfilled sufficiently. Losses of performance and deviations from the numerically determined structural behaviour shall be avoided by demanding these requirements.

B) Mechanical properties

The main deformations of the cell body concentrate at the flexure hinges. In addition to the irregular distribution of in-plane deformations that result from the cells' kinematics, the varying thickness of cell side and hinge elements leads to the concentration of in-plane strains at the narrows of the cross-section near the flexure hinges. Increased stresses thus have to be borne in areas with high space restrictions. These locally concentrated loads due to deformations are superimposed by pressure-induced stresses. An essential mechanical requirement for the end cap thus addresses its structural strength against cell axial loads ($R_{CC}B1$) and in plane deformations ($R_{CC}B2$).
In contradiction to an exclusively strength-focused design, the demand for a high grade of deformability and an infinitesimal counteraction ($R_{CC}B3$) limits the tolerable in-plane stiffness of the closure. An appropriate concept has to provide a compromise solution that considers all of these demands.

C) Geometrical boundaries

The design freedom is further limited by geometrical boundary conditions. As the cellular compound consists of multiple adjacent cell tubes, the installation space is restricted to half of a wall thickness ($R_{CC}C1$), as depicted in Figure 4-1. Depending on the applied cell material and the manufacturing boundaries, the hinge thickness usually ranges between $0.2\ mm$ and $1.0\ mm$. The hinge thickness thus limits the size of the end cap as well as the sealing area substantially.
The need for adaptability to different cell side lengths and cell sizes is based on the concept of PACS ($R_{CC}C2$), as the shape-optimization process results in an individual geometry for each cell. Only a geometrically flexible closure structure that can be used for all cells of a PACS or at least for a huge range of different cell geometries, allows keeping design and manufacturing efforts low.
In case of failure or for maintenance work, the closure preferably has to be easily accessible and exchangeable. The assembly concept for the closure further should not require a modification of the cross-sectional design, if this modification results in increased weight or a variation of stiffness ($R_{CC}C3$).

The demands on the cell closure concept for PACS allow to examine state-of-the-art implementations for their suitability and to develop customized solutions. These demands are further used for the subsequent evaluation of concepts.

4.2 Collection of cell closure concepts

Different concepts are investigated, which fulfil the particular requirements for PACS closures with varying quality. After an overview of conventional sealing solutions from literature, a collection of six relevant concepts is presented. The emphasis of this chapter lays on the implementation of the shape-optimization methods for the isotensoid and deformation supportive end caps (DSEC).

4.2.1 State-of-the-art solutions

An evolutionary conception profits from the existing solutions and tries to adapt them to the current needs. As the pressure-tight sealing of openings with limited shape variations does not imperatively exceed the state-of-the-art solutions, this chapter focusses on the investigation of existing sealing concepts. Available representatives are investigated in order to summarize the state-of-the-art and to provide the ground work for novel concepts (cf. Figure 4-2).

The partitioning of neighbouring volumes by separating the contained fluids with similar or differing pressure is the main function of seals. Dynamic seals allow relative motions, in contrary to static seals that are used to connect adjoining partners, which do not move relative to each other [159]. Static seals, like gaskets and sealing rings, which can be used for pressure gradients above $100\,MPa$, are maintenance-free and wear-resistant. Due to the cross-sectional in-plane deformation, their application is limited to cell-axial implementations. A solution for the mechanical requirement for allowing large translational strains in the plane of deformation cannot be deduced from static seals.
The advantages of dynamic seals for the application of PACS are the ability to allow limited translational and rotational displacements as well as the capacity to compensate gap variations perpendicular to the sealing surface. While in contact with the inner cell surface, the touch contacted dynamic seal is not able to close openings, which are multiples of the seal's profile height in size. Attaching the seal in cell-axial direction would solve the problem but requires a static sealing partner at both ends of the PACS structure. Such an implementation, which encloses the shape-variable structure between two glass plates, is realized by Vasista et al. [37] (cf. Figure 1-13, right). Nonetheless, this solution is not feasible for outside of the laboratory.
Special types of seals extend the potential scope of conventional closure concepts for PACS. Compression seals are conceived to compensate large deformations perpendicular to the contact plane. Sealing high pressures over large areas with compression seals requires a huge wall thickness to provide the necessary bending stiffness. Coincidently the in-plane stiffness shall be kept small. Vos et al. [121] thus preferred to use airtight plastic bladders, which are evaluated by experiment for a cell differential pressure of $0.04\,MPa$. Bellows similarly handle huge displacements, but are not suited to bear loads perpendicular to the cross-sectional plane of the PACS structure. An additional load path for bearing cell-axial forces is necessary with this concept. Inflatable seals are complex, in need of a separate pressure supply and influence the cell's deformation behaviour. The geometric flexibility and the similar functional principle compared to the PACS are beneficial.

Figure 4-2: Conventional sealing concepts (from l. to r.): gasket, O-ring, rotary shaft seal, V-ring, compression seal, bellow and inflatable seal

Regarding the state of research, four concepts that allow for the pressurization of shape-variable cell-like structures are of interest for this examination. The PAMs are already presented in chapter 1.3.4 and used for the actuation of pressurized flexible matrix composites [124]. Disadvantages like the axial

contraction, the additional structure and thus weight reduce the value of this concept for its utilization for PACS. As such tube-based concepts allow for the application of pressures up to 8.0 MPa, they are still of high relevance for closing PACS cells. Investigations on the adaption of the concept of PAMs for their utilization for PACS are presented in chapter 4.2.3.
Non-reinforced plastic tubes are used by Vos et al. [121] and enabled to apply maximum pressures of 0.04 MPa to the PAH. For the pressurization of PACS this value is not sufficient.
The concept of Vasista et al. [37], which is shown in Figure 1-13 bases on an elastic bladder. Two glass plates at each side of the cells are used to support the bladder and bear cell-axial forces. Thus, the stiffness of the closure material could be reduced significantly. The need for an additional external structure and the experimentally proven applicability for only 0.1 MPa cannot satisfy the demands on a cell closure for PACS.
A common solution for closing rigid tubular structures like pressure vessels is given by isotensoid closure structures. The load-based design of the closure's geometry allows reducing the necessary wall thickness for bearing the pressure loads and thus to decrease the weight of the structure. For the use-case of PACS, such a concept also profits from the thickness-related reduction of the in-plane stiffness. Pagitz et al. [147] theoretically investigated isotensoid and tendon-reinforced isotensoid end caps for closing single PACS cells. Although the results could not be validated by experiment, the simulative outcomes for pressures up to 2.0 MPa are promising. Isotensoid structures are investigated in chapter 4.2.5.

The demands on shape-variable closures for PACS exceed the performance of conventional solutions. Available state of research concepts are either heavy and hardly applicable for PACS, not suitable for pressures of more than $0.04\ MPa$, in need of additional supporting structures, or only investigated theoretically. The subsequently presented examination of cell closure solutions for PACS is performed to provide more appropriate concepts.

4.2.2 Flat plate cell closure

The simplest way of sealing the cells' ends is given by a flat plate. The advantages of this concept are the optimal wetting capabilities, its adaptability to arbitrary cell geometries and the straightforward manufacturing. The possibility of casting one complete end of a cell compound in a single manufacturing step significantly reduces production and assembly expense, compared to a multi-part structure. The deformability can be ensured by considering the required elasticity during the selection of materials. Necessary fracture strains of more than 25 % predestine elastomers for these applications. Radial σ_r and tangential σ_t stresses are maximal at the flat plate's edge and can be estimated analytically according to the plate theory of Timoshenko [160] for a uniformly-loaded circular plate with clamped edges with

$$\sigma_{fp,r,max} = \frac{3pD^2}{16t^2} \text{ and} \tag{4.1}$$

$$\sigma_{fp,t,max} = \frac{3pD^2}{16t^2}\nu. \tag{4.2}$$

The minimum plate thickness should further be controlled to limit the out-of-plane deflection. This deformation leads to additional space requirements in cell-axial direction and in consequence avoids the pressurization of the edge region, what results in a loss of the energy potential that is needed for the deformation of the PACS (cf. $R_{CC}A3$). The maximum deflection w_{max} is calculated by

$$w_{max} = \frac{3pD^4(1-\nu^2)}{256Et^3}. \tag{4.3}$$

The required plate thickness in case of a predefined maximum deflection w_{max} is thus

$$t_{fp,min,w} = \sqrt[3]{\frac{3pD^4(1-\nu^2)}{256Ew_{max}}}. \quad (4.4)$$

Assuming a circular plate with the diameter $D = 50\,mm$ that is loaded with the pressure $p = 0.5\,MPa$ and made of the thermoplastic material PA12 with the *Young*'s modulus $E = 1300\,MPa$, the *Poisson*'s ratio of $\nu = 0.5$ and the strength $R = 40\,MPa$, a minimum stress-based plate thickness of $t_{fp,min,\sigma} = 2.42\,mm$ is required and results in a deflection of $w_{max} = 1.49\,mm$. The resulting in-plane stiffness is responsible for the amount of energy, which is necessary to deform the cell closure. An additional mechanical issue can occur in the form of leakage. The higher the forces that are needed to deform the seal, the higher are the loads on the connection between cell structure and closure. Leakage and overstressing occur at this connection region, especially at the thin-walled flexure hinges as observed in chapter 6.2.1.
Summarizing the flat plate concept, it should be noted that a flexible membrane requires large cell-axial space due to high deformations and thus cannot ensure the pressurization of the edge region, what causes a loss of energy potential. Stiff plates whereas require a similar amount of energy potential for deformation. Additionally the related forces that have to be transferred between cell body and closure lead to leakage.

In order to increase the ratio between bending and axial stiffness and thus to reduce stresses and deflections, a sandwich construction is investigated. Figure 4-13, left, shows the trial structure of an aramid honeycomb sandwich with elastomer skin, which provides the desired low in-plane stiffness. The unevenly distributed appearance of wrinkles indicates stress concentrations and causes delamination. Face sheet wrinkling could be avoided by pretensioning the skin material.
Both types of flat plate cell closure concepts are characterized and evaluated in chapter 4.3 before the best solution is selected.

4.2.3 Tube solutions

Thin elastic tubes, as shown in Figure 4-4, (1), can be used to seal small gaps with only a few millimetres in diameter at limited pressures. Fibre-reinforced tubes, like depicted in Figure 4-4, (2), allow bearing considerable higher pressures without additional load bearing structures. Both types of tubes and the related clamping concepts are investigated in this section.
Regarding the equations (4.1), (4.2) and (4.3) the necessary thickness of a cell closure that fulfils the limitations regarding deflection and stresses, can be diminished by a reduction of the plate diameter. This relation is utilized in the concept of the elastic tube, which is supplemented by a rigid structure at both ends of the cells to reduce the cross-sectional area that has to be covered. As the deformational envelope of the cells can be extracted from the numerical investigations, an area within the cells' cross-section can be determined, which is not intersected by the cell structure for any state of shape. This area can be filled by a rigid structure, which relieves the elastic tube without increasing the in-plane stiffness of the PACS cell significantly. The maximum diameter of the residual non-reinforced area (NRA) depends on the cells' kinematics but clearly falls below the original NRA. The rigid structure can further be conceived to clamp the elastic tube in a fluid-tight conical press fit and to provide a pressure port. Figure 4-3 illustrates the portion of the sealing area that can be closed by a rigid structure.

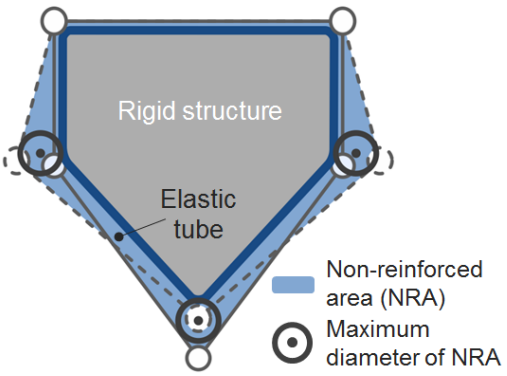

Figure 4-3: Reduction of effective plate diameter by tube solution with rigid clamping

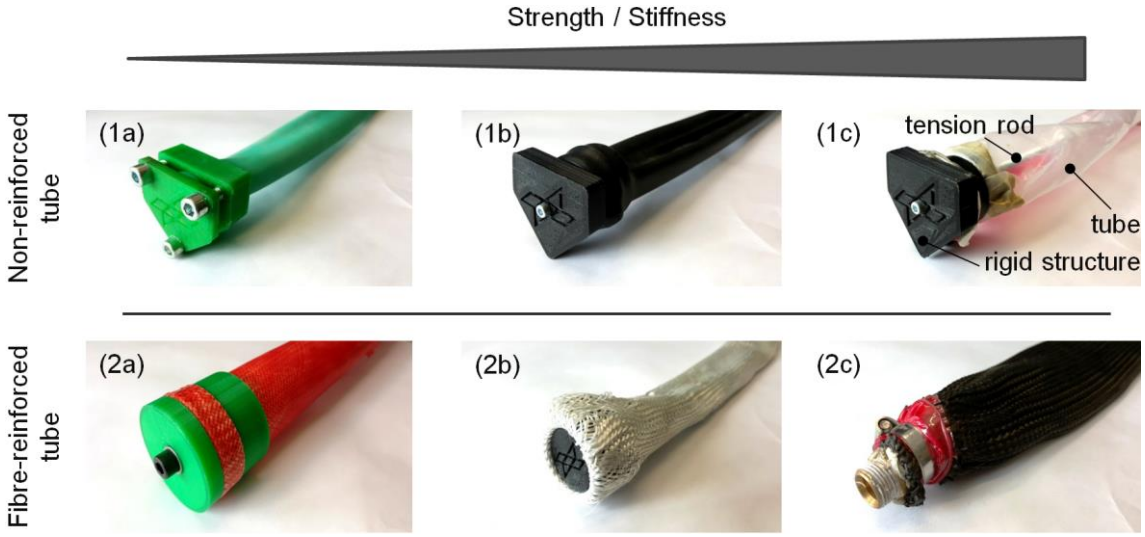

Figure 4-4: Examined tube concepts without (1) and with fibre reinforcement (2) with different realizations for the connection between tube and pressure port

The low stiffness in the plane of deformation, the straightforward assembly and sealing as well as the exchangeability and maintainability of this closed-system solution are beneficial. The adaptability for varying cell geometries avoids the necessity for an individual closure design for each cell. Disadvantages like external fluid flow and additional weight due to structural redundancies have to be accepted. A further issue is the inherent stiffness of the elastic tube. Stiff tube implementations avoid the pressurization of edge regions according to requirement $R_{CC}A2$, whereas elastic variants strongly restrict the maximum applicable pressure. Three variants with different tube stiffness, which are made from latex (1a), butyl rubber (1b) and polyethylene (1c) are realized and shown in Figure 4-4. Each concept consists of a rigid clamping structure, an elastic tube and a central tension rod (see Figure 4-4, 1c), which combines both rigid structures. The tube solutions (1a-2c) are shown with different rigid structures and clamping concepts, as multiple design variants are investigated for finding an appropriate solution for each tube. For reasons of strength increase, fibre-reinforced elastomers are investigated for realizing the thin-walled tubes (2a-c). The resulting concept combines high tensional stiffness for bearing pressure loads with shear and bending flexibility, which allow for cross-sectional shape variations. The rigid end section and the additional secondary load path are redundant, as both are replaced by the reinforcing fabric. The advantages of the non-reinforced tubes can thus be extended by the ability to bear high pressure loads. The resulting concept is similar to that of the PAM actuator [109], which is commercially distributed by *Festo AG & Co KG* for pressure loads up to $0.8\,MPa$ [161]. Their axial contraction due to pressurization leads to the desired deformation, when used as actuators. For the application for PACS, this behaviour is unfavourable and ultimately limits the tolerable change of the cell geometry for a fibre-reinforced tube of given diameter. Disadvantages like the increased manufacturing effort compared to a non-reinforced solution, wear due to axial contraction and fatigue have to be considered in the concept selection. The investigated fibre-reinforced concepts are depicted in Figure 4-4. The best performance is provided by the variant with glass-fibre-reinforced elastomeric matrix (2a). (2b) and (2c) show two non-infiltrated glass- and carbon-fibre-reinforced variants.

The latex-based realization is utilized for the investigation of a single row GFRP PACS structure (cf. chapter 6.1.3). Compared to the alternative tube solutions, it represents the most appropriate tube solution and allowed to reach a maximum pressure of $0.35\,MPa$ [162].

The utilization of non-reinforced and fibre-reinforced tubes for the pressurization of PACS cells improves the flat plate concept due to the reduction of the NRA. Due to the therewith enabled thickness reduction, a significant decrease of the in-plane stiffness results and yields an increase of the PACS's performance. The necessity of an additional load path in cell axial direction, which is realized by the tension rod, increases the weight of the closure concept and thus reduces its specific performance. Manufacturing efforts, pressure limitations and wear are further critical disadvantages.

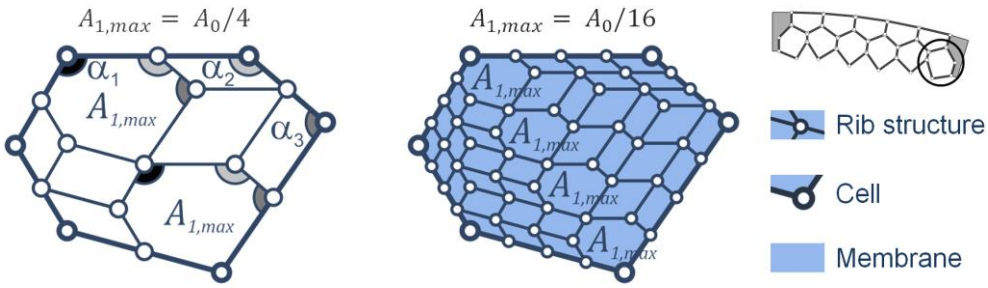

Figure 4-5: Design principle of the CRC for division of initial area by four and sixteen and position of independent hinge angles α_1, α_2, and α_3

4.2.4 Compliant Rib Cap (CRC)

The herein presented approach shall illustrate the possibility to release specific DOFs that are necessary to allow for the deformation of the cell, whilst constraining those DOFs, which are needed to bear the pressure-induced loads.
The basic idea of the CRC is to combine a shear-flexible and bending stiff mechanism with an elastic fluid-tight skin. In contrast to the regular honeycomb core that is introduced in chapter 4.2.2, a mechanism, which is adapted to the cells' kinematic, allows for evenly distributed deformations and reduces the closure's in-plane stiffness. The resulting structure bears out-of-plane pressure loads primarily by its rib structure, which profits from configurable bending strength and stiffness. The elastomeric skin undertakes the task of sealing. The functions of load bearing and sealing are thus separated according to the main structural elements hinged rib structure and thin elastomeric skin.

Figure 4-5 shows the design principle for the sample geometry of an irregular hexagonal PACS cell. Similar geometries can be found within a PACS for each cell of the second cell row. Due to the individual design of each PACS cell, the investigation of the herein presented mechanism for only regular polygons would not be sufficient. The kinematic design of the rib structure ensures that each hinge is connected to at least three neighbouring hinges. Each node of the mechanism is thus fully constrained by the surrounding cell structure, respectively by its independent hinge angles. Comparable to the divisibility of a parallelogram, the kinematics of the CRC consists only of such beam orientations and ratios of cell side lengths, which are already used by the surrounding polygon. This strategy of dividing the pressurized area into multiple fragments is applicable to arbitrary convex polygons and can theoretically be applied for any resolution.
An important property of this CRC concept is that the halving of cell sides results in a division of the original cross-sectional area A_0, such that the largest newly formed subarea $A_{1,max}$ is $A_0/4$. As for all convex polygons the largest newly formed cross section is equal to the initial geometry except for its scale, this relation is valid. The recurrence of independent hinge angles illustrates the equality. Regarding the equations (4.1), (4.2) and (4.4), the following relationships can be obtained:

$$t_{min,w} \sim D^{4/3} \text{ and} \tag{4.5}$$

$$t_{min,\sigma} \sim D. \tag{4.6}$$

With this, the quartering of cell sides allows for the reduction of the thickness of the sealing plate to $t_{CRC,min,\sigma} = 0.605\,mm$. The CRC skin thickness and in-plane stiffness are thereby decreased to $t_{CRC,min,\sigma}/t_{fp,min,\sigma} = 25.0\,\%$, compared to that of the flat plate. Overlaps due to the finite dimension of the rib elements and hinges as well as the manufacturability limit the scalability. A real-life implementation of this mechanism is depicted in Figure 4-13.

4.2.5 Isotensoid cell closure

Out-of-plane forces cannot be borne efficiently by a monolithic two-dimensional structure, as large deformations in the cell's longitudinal direction and huge bending-induced stresses arise. The CRC solves this issue by introducing a shear-flexible mechanism that allows for the release of in-plane DOFs whilst providing sizeable bending stiffness for bearing out-of-plane forces. A solution that is not in need of this separation reduces complexity due to integral manufacturing. The concept that is presented in the following further allows distributing structural loads homogeneously and with large utilization of the deployed material and thus holds the potentials to reduce the in-plane stiffness and save weight. In the following, the procedure of generating an isotensoid seal geometry is introduced before the adaption of this concept for the application of PACS is presented and its particular properties are analysed.
Bletzinger et al. [163] and Wüchner et al. [164] investigated the *Updated Reference Strategy* (URS), as an iterative approach for the shape optimization of minimal surfaces and prestressed isotensoid membranes. After each iteration step of their AVW-based method, the reference geometry of the membrane structure is updated. Following this substantial idea of the URS, an implementation using common FEM software is realized. After the description of the approach for the shape-optimization of minimal surfaces, it is verified by an analytically solvable sample problem. The implementation for calculating minimal surfaces is subsequently extended by a strategy, which allows for the computation of isotensoid pressure-loaded membranes that are controllable in size.

Minimal surface
The minimal surface shall be computed for an arbitrary reference geometry using FEM. The approach for solving this issue is illustrated in Figure 4-6 (I). The minimal surface of a membrane structure is calculated in an iterative solution process. Basing on the initial shape of the membrane, a homogenous preload is applied. In the FEM model, this preload is determined in the form of an initial strain ε_{init}. In similarity with a soap bubble with isotensoid shape, the pretensioning of the membrane allows to reduce the structure's surface. After each iteration step, the geometry is updated, what means that the model is transformed into its deformed shape and structural stresses are deleted. The surface is thus minimized iteratively.
Due to the property of minimal surfaces to show a constant respectively isotensoid stress distribution for the given load conditions, the stress-based stop criterion $\left|\sigma_{z,max}/\sigma_{z,min} - 1\right| < \eta_\sigma$ for the iteration step z is used to terminate the iterative process. Figure 4-6 (I) shows the initial and target shapes for a membrane which is supported by two identical concentric circles. This exemplary geometry of a catenoid with initially cylindrical shape, radius $r_{cat,0} = 1$ and height $h_{cat,0} = 1.2$ (cf. Figure 4-8) is used to demonstrate the accuracy and convergence behaviour of the shape-optimization process for minimal surfaces as its resulting envelop surface can be described analytically by

$$r_{cat}(h_{cat}) = r_{cat,t}\cosh\left(\frac{h_{cat} - h_{cat,0}/2}{r_{cat,t}}\right). \tag{4.7}$$

The FEM model is implemented in *Ansys* with twenty-five four-node shell elements (Shell181) over the height. For the initial configuration a cylinder with radius $r_{isot,0} = r_{cat,0}$ and height $h_{isot,0} = h_{cat,0}$ is used. A strain of $\varepsilon_{init} = -0.999$ is applied. The solver is set to consider nonlinear geometrical deformations. Analogue to the URS the computed deformations are used to modify the affected elements and thus the geometry of the membrane.
The quality of the FEM-based results is evaluated with respect to the analytical description of the catenoid. A deviation of less than 0.01 of the catenoid's radius $\Delta r_{isot,z}/r_{cat}$ at $h_{cat} = h_{cat,0}/2$ compared to the analytical solution results already after two iterations (see Figure 4-8, top right).

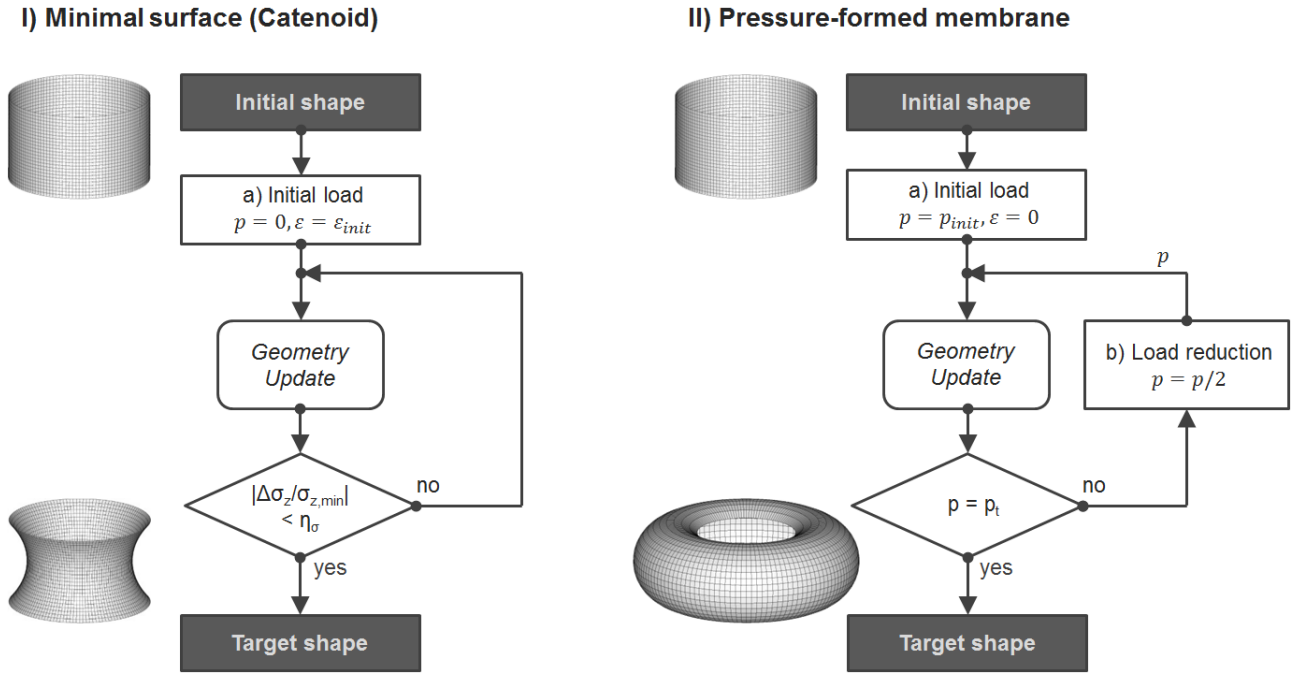

Figure 4-6: Flow charts for the shape modification of an initially cylindrical membrane with the objectives of creating I) a minimal surface and a II) a pressure-formed membrane

Pressure-formed membrane

The minimal surface only shows a uniform stress distribution for homogeneous and surface-tangential loads. The resulting shape of the structure is not optimized for bearing surface-normal loads and it is equal to the flat plate for the two-dimensional target contour of a PACS cell. An outlook for the adaptability of the URS for the shape optimization of pressure-loaded isotensoid structures is given by Bletzinger et al. in [163] with the example of an inflated bubble. Similarly to the example from literature, the pressure intensity is herein controlled to start at a high value, which causes large deformations, and is halved after each iteration step until the target pressure is reached. The initial pressure is thus $p_{init} = 2^{(z_{max}-1)} p_t$. Figure 4-6 (II) illustrates the respective procedure as well as the computational outcomes for the pressure-formed membrane with initially cylindrical shape.

Two problems occur using this strategy. First, the resulting membrane structure is not stressed uniformly. The stress distribution $\Delta\sigma_z/\sigma_{z,min} = \sigma_{z,max}/\sigma_{z,min} - 1$ varies by about 30 % as depicted in Figure 4-8, bottom-right chart. The geometry that results from this approach is not isotensoid. The reason for this is the missing convergent shape of the geometry. The pressure forces cause an extension of the membrane and the reference geometry is set to the deformed state after each iteration step. As the difference between undeformed and deformed state only depends on the magnitude of the applied forces, which are always oriented to induce positive strains, the geometry cannot converge to a certain shape. For a non-converging geometry, the desired isotensoid shape changes after each iteration step. A remaining stress deviation is the result.

Beyond that, the size of the bulge cannot be regulated as it depends on the initial pressure set. As it is responsible for the ensuing stress level, the size of the inflated membrane is crucial for the shape optimization of the cell closure. In addition to the general demand for stress reduction, the height of the end cap reduces the pressurized length of a PACS cell (cf. $R_{CC}A3$), what causes a loss of performance. A non-controllable bulge is thus not desired for the present application. The necessity for the advancement of this approach is thus given.

Extension-regulated isotensoid

With the extension regulation a solution is found and described subsequently, which widens the previous approach for the task of generating a geometry that causes a uniform stress distribution at a specific target pressure and is controllable in size.

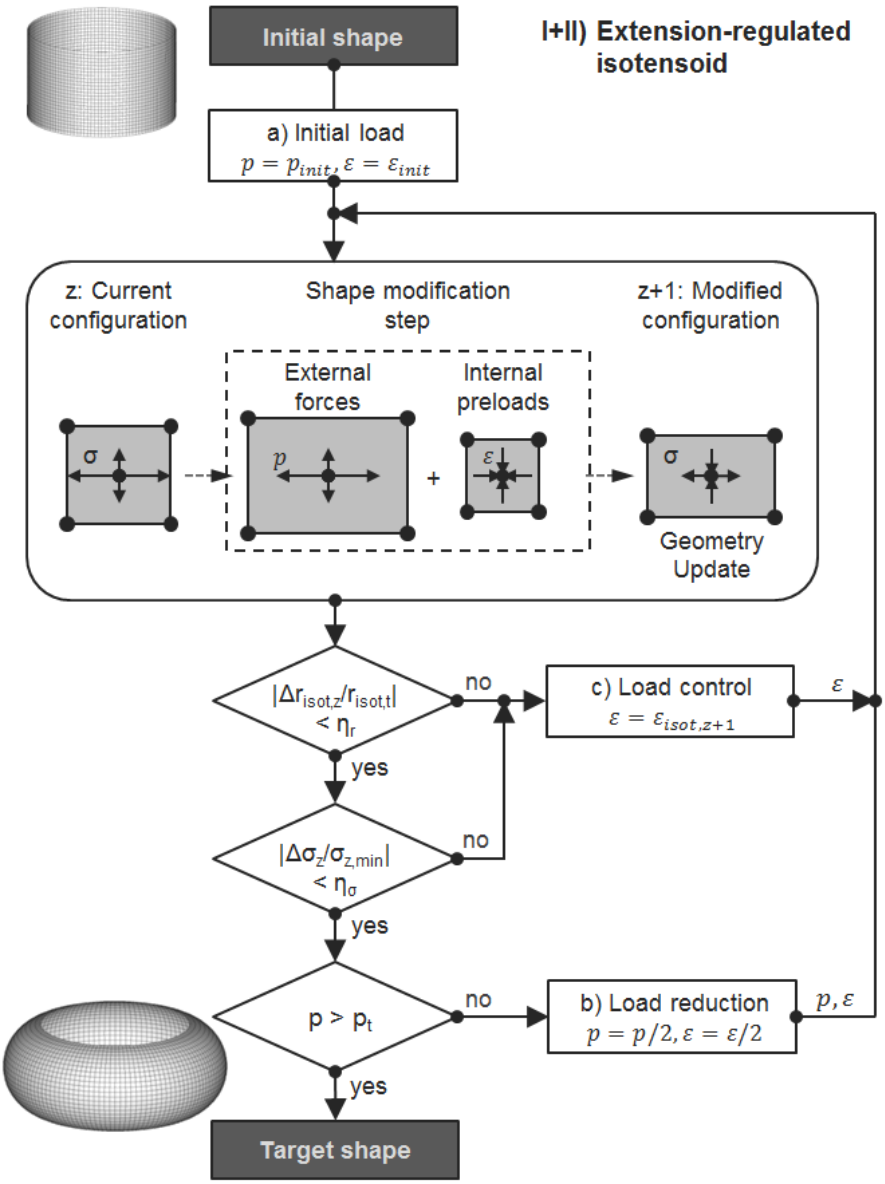

Figure 4-7: Flow chart for the process of shape modification for creating the ERI

The strategy for generating minimal surfaces (I) allows to preload membranes uniformly, whereas the method for creating pressure-formed membranes (II) includes also loads that are not tangential to the surface (cf. Figure 4-6). The combination of these two approaches leads to an approach for creating the extension-regulated isotensoid (ERI). The basic idea with the ERI is to modify the shape of the elements according to their strains and thus to form the structure according to the principle stresses that are caused by external forces.

The flow chart, given in Figure 4-7, visualizes the principle procedure. Considering the mentioned example, an initial cylindrical geometry with radius $r_{isot,0}$ is therein used as reference to calculate an isotensoid structure with target radius $r_{isot,t}$ for a given pressure load p. According to the catenoid example, the target radius is extracted as the distance between cylinder axis and membrane element node at $h_{isot} = h_{isot,0}/2$. In each iteration step, strains due to the pressure load are calculated. The strains are superimposed with a uniform internal strain, which is adjusted to the residual geometrical extension $\Delta r_{isot,z} = r_{isot,z} - r_{isot,t}$. The extension of the membrane structure is thus regulated by controlling this internal strain. Figure 4-7, middle, shows how the shape of the single elements is altered during the procedure for calculating the ERI. The iteration step is repeated until the variance compared to the target shape is less than η_r and the deviation of stresses falls below η_σ.

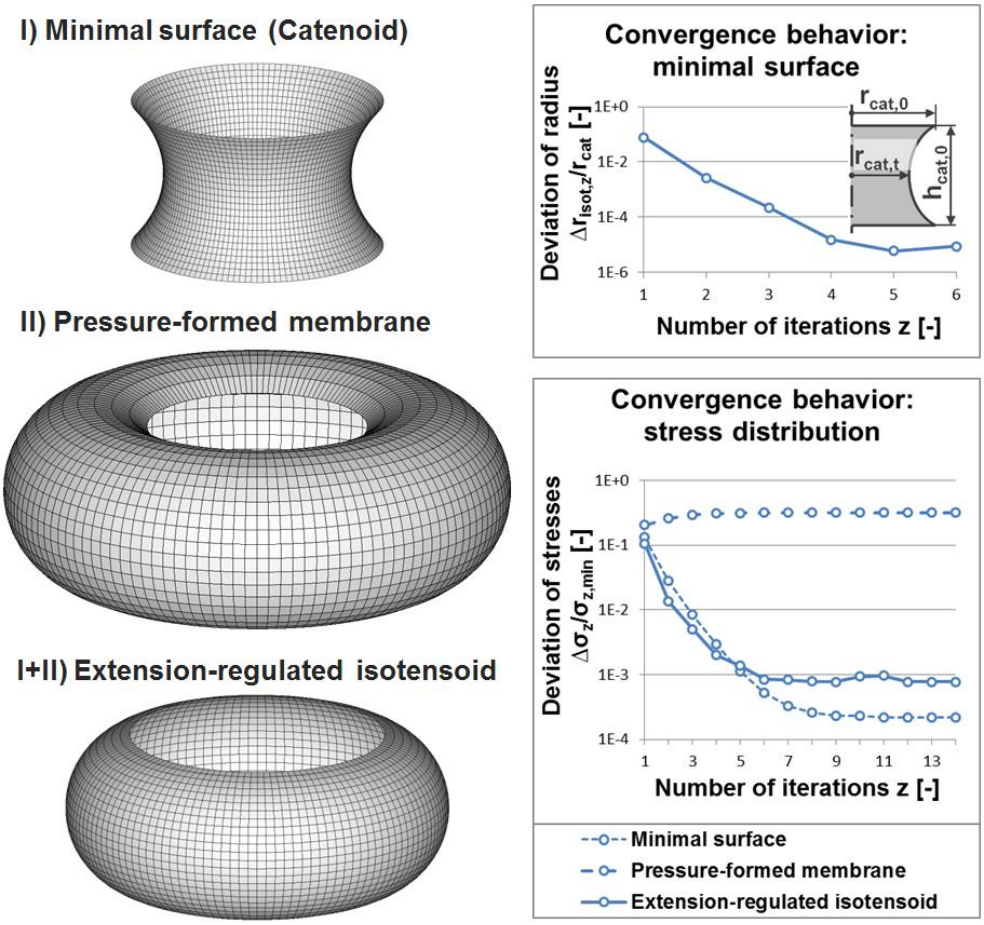

Figure 4-8: FEM-based shape optimization for minimal surfaces (I), pressure-formed membranes (II), and extension-regulated isotensoid (I+II)

The shape of the exemplary cylindrical structure is thus optimized and provides the geometry of the ERI. The membrane structure is thereby computed to show a homogeneous stress distribution for the target pressure load $p_t = 0.5\,MPa$, and the target radius $r_{isot,t} = 1.5 r_{isot,0}$ at $h_{isot} = h_{isot,0}/2$ (see Figure 4-8, I+II). The lower chart of Figure 4-8 shows a deviation of stresses $\left|\Delta\sigma_z/\sigma_{z,min}\right|$ of less than $1e-3$ after $z = 14$ iterations. A final geometrical variance of $\eta_r = 8.7e-8$ compared to the target radius is examined.

A gradient method is used to regulate the radius r_{isot}. The control element, see Figure 4-7 (c), with access to the internal strain $\varepsilon_{isot,z+1}$ for the iteration step $z+1$ is governed by the following equation:

$$\varepsilon_{isot,z+1} = \varepsilon_{isot,z} - \left(2r_{isot,z} - r_{isot,z-1} - r_{isot,t}\right)\frac{(\varepsilon_{isot,z} - \varepsilon_{isot,z-1})}{\Delta r_{isot,z} - \Delta r_{isot,z-1}}. \tag{4.8}$$

Figure 4-8 summarizes the investigations on the convergence behaviour of the three presented methods for the shape optimization of membrane structures. The computational results for the minimal surface (I), the pressure-formed membrane (II) and the extension-regulated isotensoid (I+II) are illustrated. An isotensoid end cap with a cylindrical base contour could also be calculated analytically as [165] shows for linear elastic isotropic materials. Due to the geometrical flexibility of the strategy for computing the ERI, it can be adjusted for the closure of a PACS cell by simply changing the base contour of the initial configuration and the corresponding boundary conditions in the structural model. Figure 4-9 depicts the shaded isotensoid sealing cap and the related deviation of the *von Mises* stresses $\left|\Delta\sigma_{vM}/\sigma_{vM,min}\right|$ for a pressure load of $p = 0.5\,MPa$ and a constant membrane thickness of $t = 0.1\,mm$. Three-node shell elements (Shell181) with an element edge length of 1 mm are therefore used. Further information about the structural model, the method for considering geometrical restrictions according to requirement $R_{CC}C1$, the related LBCs and the optimization process are presented in appendix F.

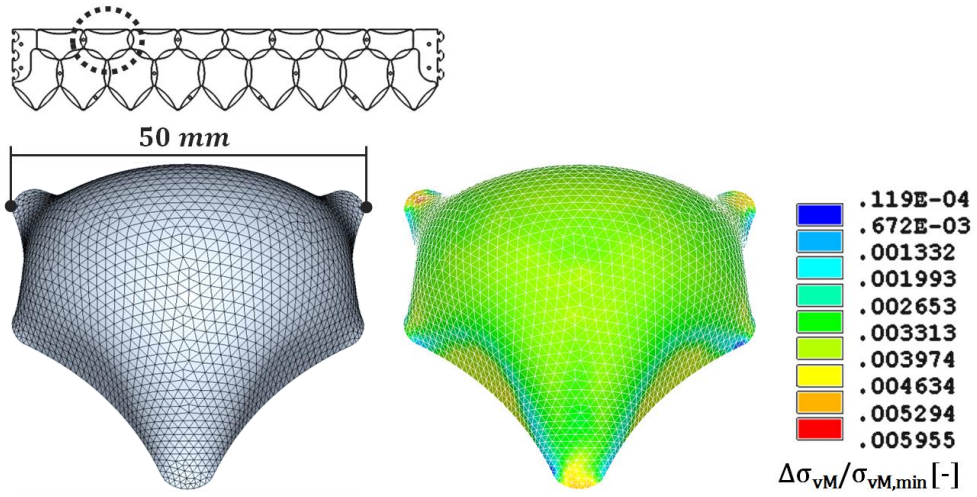

Figure 4-9: Shaded isotensoid cell closure (l.) and *von Mises* stress distribution (r.) for the pressure load p = 0.5 MPa and a membrane thickness of t = 0.1 mm

Convergence is reached after $z = 14$ iteration steps. The geometrical deviation of $\left|\Delta r_{isot,z}/r_{isot,t}\right| = 4.72\text{e}-8$ related to the target closure height of $r_{isot,t} = 25\,mm$ and a residual stress divergence of $\left|\Delta\sigma_{vM}/\sigma_{vM,min}\right| = 6.02\text{e}-3$ compared to the minimum *von Mises* stress of $\sigma_{vM,min} = 50.488\,MPa$ are suitable values within the context of PACS.
According to the pipe formula (see equ. (2.31) and (2.32)) the analytically calculated stress value is $\sigma_{isot,ana} = 62.5\,MPa$ for a cell's outer diameter of $D = 50\,mm$. Basing on the computational results for the minimum *von Mises* stress, the effective diameter of the cell closure thus has to lie at approximately $D_{isot} \approx 40.39\,mm$ for this example. Regarding the design criteria that are described in chapter 4.2.2, a wall thickness of $t_{isot,min,\sigma} = 0.127\,mm$ would be sufficient to bear the pressure loads. A reduction of the stress-based membrane thickness to $t_{isot,min,\sigma}/t_{fp,min,\sigma} = 5.25\,\%$, compared to the flat plate concept is thus achieved.

Based on the example of the complex edge contour of the pentagonal PACS cell's cross section, it can be assumed that the computational approach that is used to calculate the geometry of the ERI is stable for arbitrary initial configurations. The functional principle is adaptable to other shape-optimization problems. As the shape modification is driven by structural strains, other external forces beyond pressure loads are conceivable. As it could be interesting for components built of fibre reinforced polymers [166], a follow up work should address anisotropic materials.

4.2.6 Isotensoid Rib Cap (IRC)

Equally to the flat plate the necessary wall thickness of the isotensoid end cap depends on the cell size. The combination of isotensoid and CRC is thus obvious and allows for further thickness reductions. Reinforcing the isotensoid membrane with the shear-flexible load-bearing rib structure provides the possibility to decrease the pressure-induced membrane stresses. Similar to the CRC the IRC benefits from a reduced NRA of the segmented sealing surfaces. Dividing the cell sides by four also reduces the sealing stresses or the necessary membrane thickness by four. The minimum thickness of the IRC results in $t_{IRC,min,\sigma} = t_{isot,min,\sigma}/4 = 0.032\,mm$. Compared to the flat plate, this corresponds to a thickness reduction to $t_{IRC,min,\sigma}/t_{fp,min,\sigma} = 1.31\,\%$. The related reduction of the in-plane stiffness of such an end cap is significant.
Two demonstrators for the isotensoid rib cap are realized and shown in Figure 4-13. On the top of the right column, an IRC is depicted with a division of the cell side lengths by two. The illustration below shows the possibility of a compliant implementation to reduce manufacturing efforts. A division of the cell side lengths by six underlies this demonstrator.

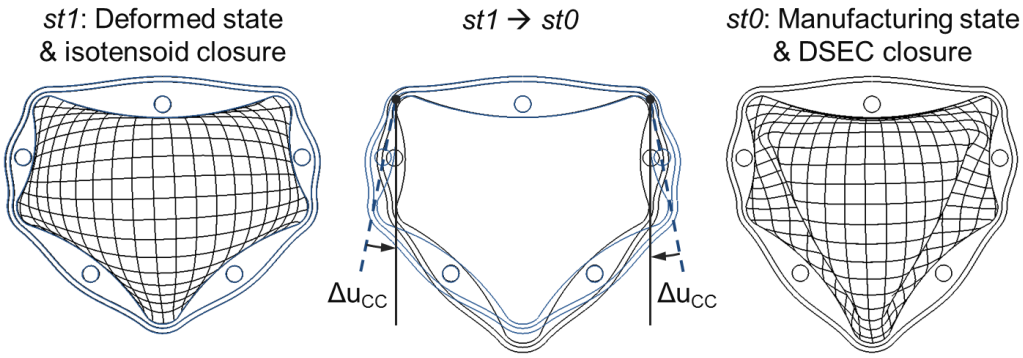

Figure 4-10: Shape-optimization strategy for DSEC

4.2.7 Deformation Supportive End Cap (DSEC)

Regarding the initial requirements for a sealing solution, the so far presented concepts satisfy the pressure-allocation capabilities and the geometrical boundaries. Furthermore, different possibilities to reduce membrane stresses and respectively to lower the membrane thickness are shown. Mechanical demands concerning strength and minimized structural stiffness were in the foreground. For reasons of simplification and comparability, the considered structural loads are limited to internal pressure forces.
The influence of pressure-induced stiffness is not yet considered, but assumed to significantly affect the PACS's deformation behaviour. Deformation-induced stresses that are passed on from the PACS structure should further be considered in the dimensioning of the cell closure. An extension of the introduced shape-optimization strategy for the isotensoid cell closure (cf. chapter 4.2.5) is needed, which allows for the consideration of cross-sectional deformations. In addition, the isotensoid state of the cell closure should not be designed for the undeformed cell contour. If possible, it should appear at a deformed state of shape, where the maximum pressure loads act on the cell body and the cell closure. Thus the material utilization can be enhanced and the closure concept ultimately profits from reduced deformational stiffness.

Referring to the initially presented conventional seals, the DSEC can be understood as a combination of gasket, bellow and inflatable seal. The herein realized idea for a shape-variable sealing concept, which uses the cell-inherent pressure to compensate the necessary deformation energy, is implied in [162] and published in detail in [167]. The feasibility investigations and the conceptual development are part of this article and presented below.
Pressure-induced membrane stresses can be borne efficiently by isotensoid-shaped structures. For the state of maximum pressure load, which shall be equal to the deformed state of the PACS $st1$, the membrane should take an isotensoid shape. Thus, the deformations between manufacturing $st0$ and deformed state $st1$ have to be considered in the shape optimization. The procedure, which allows generating this pre-deformed closure geometry is presented exemplarily for the pentagonal single cell and illustrated in Figure 4-10.
The basic idea is to generate the isotensoid membrane for $st1$ and subsequently deform it into the manufacturing state $st0$. As the deformations of the cell's cross-sectional area are known from the two-dimensional calculations of the pressured cell's equilibrium with neglected sealing membrane, the deformation vectors of the contour nodes can be used to deform the closure membrane. According to the requirements on geometrical boundaries, a contact condition is additionally implemented. It prevents the structure from intersecting with neighbouring membranes. The bounding area is built by extruding of the end cap's base contour in cell-axial direction. The contact condition is implemented to provide frictionless gliding. The structural model that is utilized for the computation of the isotensoid cell closure and described in appendix F is therefore reused.
The determination of the shell thickness t_{DSEC} has significant influence on the resulting structural shape. Depending on the ratio between extensional stiffness and bending stiffness, the realized sealing structure with shape $st0$ can be controlled to prefer extensional or bending deformations to reach state

$st1$. The comparison of the structural stiffness that results from compression and bending leads to the deformation mechanism, which should be preferred. The following investigation allows for the analytical approximation of the preferable deformation mechanism on the basis of a beam model, before the results are verified for the three-dimensional closure structure (cf. chapter 4.4).
The computation of the energy potential is used to examine the stiffness of the structure. At the simplified example of an axial-stressed beam, the stiffness against translational deformations in terms of compression and bending is investigated for different geometrical boundary conditions. For its cross sectional area A, initial length $l_{B,0}$ and stiffness E, the energy potential for a longitudinal compressed beam $\dot{\Pi}_{B,ax}$ is calculated as the derivative of the virtual work δW_{ax} in axial direction after the virtual displacement δl_B. It results in

$$\dot{\Pi}_{B,ax} = \frac{\delta W_{ax}}{\delta l_B} = \frac{EA}{2l_{B,0}} \frac{\delta(l_B^2)}{\delta l_B} = \frac{EA}{l_{B,0}} \delta l_B. \tag{4.9}$$

Assuming a pre-curved beam with an initial chord length $l_{B,0}$ and the degree of curvature φ, the energetic potential $\dot{\Pi}_{B,b}$, which is needed to reduce $l_{B,0}$ by bending with constant moment (see Figure 4-11), is calculated by

$$\dot{\Pi}_{B,b} = \frac{\delta W_b}{\delta \varphi} = \frac{EI}{2s} \frac{\delta(\varphi^2)}{\delta \varphi} = \frac{EI}{s} \delta \varphi = \frac{EI}{s} \frac{\delta \varphi}{\delta l_B} \delta l_B, \text{ with} \tag{4.10}$$

$$\frac{\delta \varphi}{\delta l_B} = \frac{\varphi^2}{s(\varphi cos\frac{\varphi}{2} - 2sin\frac{\varphi}{2})}, \text{ derived from} \tag{4.11}$$

$$l_B = \frac{2s}{\varphi} sin\frac{\varphi}{2}. \tag{4.12}$$

For a better comparability of the potentials $\dot{\Pi}_{B,ax}$ and $\dot{\Pi}_{B,b}$, the substitution of the moment of inertia I and the arc length s leads to

$$\dot{\Pi}_{B,b} = \underbrace{\frac{EA}{l_{B,0}} \delta l_B}_{=\dot{\Pi}_{B,ax}} * \underbrace{\frac{t^2}{l_{B,0}} \frac{sin\frac{\varphi}{2} \tan\frac{\varphi}{2}}{3(\varphi - 2tan\frac{\varphi}{2})}}_{potential\ factor\ \Phi}, \text{ with} \tag{4.13}$$

$$s = \frac{\varphi l_B}{2sin\frac{\varphi}{2}}. \tag{4.14}$$

The potential factor represents the ratio between the bending- and extension-based energy potential $\Phi = \dot{\Pi}_{B,b} / \dot{\Pi}_{B,ax}$ that is needed to deform a beam with chord length $l_{B,0}$, wall thickness t and degree of curvature φ. Figure 4-11 illustrates the potential factor Φ for a range of representative values regarding the PACS closure structure. As Φ is less than one for the vast majority of the investigated geometrical parameters, Figure 4-11 shows that bending is the energetically less expensive deformation mechanism for the relevant geometrical boundary conditions that can be found with a cell closure for PACS.

The differences between the beam and the sealing cap lay in the more complex-shaped geometry, a non-constant curvature and in the unevenly-distributed load introduction. The compression and bending of a beam represents the extreme cases of deformation. For the DSEC seal, both variants occur in combination. Nevertheless, equation (4.13) can be used to explain the performance-enhancing effects due to the stiffness reduction by shifting the prior deformation mechanism towards bending. For the shape optimization of the DSEC, this means that the wall thickness of the cell closure structure has to be set to give preference to bending deformations. The validity of this assumption that bases on the transferability of equation (4.13) to the three-dimensional PACS closure structure is verified by simulation in chapter 4.4 and experimentally validated in chapter 6.1.4.

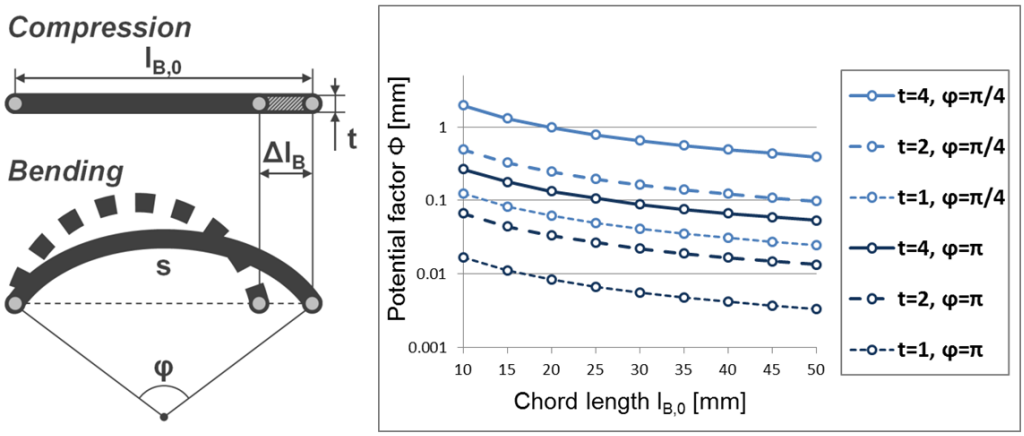

Figure 4-11: Notation and exemplary potential factors Φ for compression- and bending-induced deformation

By reducing the wall thickness t, the only influenceable parameter of equation (4.13) is modified. The lower the thickness of the closure, the higher the ratio between bending and extensional deformation and consequently the more bending-induced folds appear during the shape optimization.
The results for two different thickness values in the shape-optimization step t_{SO} are depicted in Figure 4-12 for a hexagonal PACS cell with a realistic cross-section. These more complex edge contours occur for optimized hinge orientations and include the load dependent hinge orientations and curvatures according to chapter 3. The cell closure on the right side is formed with half the thickness of the geometry on the left. Notice that the folding of the two sealing cap configurations significantly differs. The influence of a varying initial wall thickness on the resulting shape of the cell closure and the related pressure-dependent deformation characteristics is investigated in chapter 4.4.

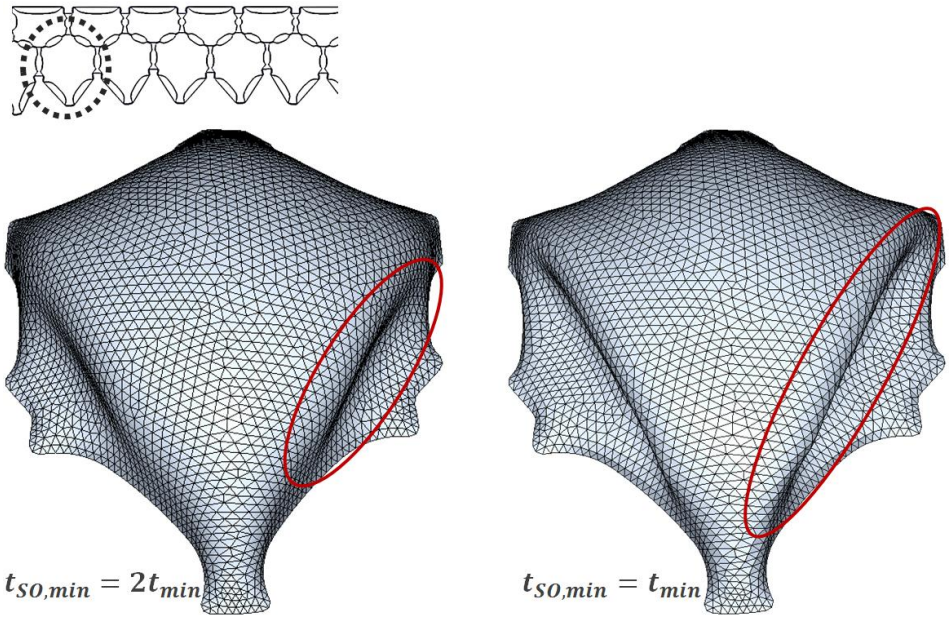

Figure 4-12: Effects of the wall thickness for shape optimization t_{SO} on the resulting cell closure shape

The DSEC is conceived to utilize the cell-inherent pressure to cause deformations equally to the underlying cell. It is further designed to provide a nearly isotensoid shape in the state of maximum pressure-induced deformation. With its preferential deformation mechanism of bending, the DSEC provides reduced stiffness against the underlying cell's deformation. Figure 4-12 illustrates that the presented shape-optimization strategy is also applicable for the geometrically complex base contours, which result from the cross-sectional design for PACS.

4.3 Concept selection

The introduced closure concepts are rated in consideration of the demand analysis in chapter 4.1 and on the basis of their characteristics, which are presented in the following. The rating matrix that is given in Table 4-1 summarizes the advantages and disadvantages of the different concepts. Weighting factors are not used, as each of the requirements is essential for the functionality of the cell closure.

State-of-the-art solutions provide good wetting capability and exchangeability. The investigated off-the-shelf sealing concepts turned out to be not capable of compensating strains larger than 25 %. State of research solutions are either hardly applicable for PACS, do not allow for pressures higher than 0.1 MPa or are so far only investigated theoretically.
The flat plate allows casting a complete PACS segment in a single production step, benefits from good wetting capabilities and an excellent adaptability to various cell geometries. The high in-plane stiffness and the difficulties with maintenance and repair are distinct disadvantages (cf. Figure 4-13, left).
Geometrical requirements, which limit the design room for the cell closure and cause the demand for the flexibility for various cell shapes, are fulfilled by the tube solutions. The stand-alone design allows for accessibility in case of maintenance and repair. The beneficial low stiffness of the tube concepts against deformation is accompanied by an insufficient quality of pressure allocation. The deficient potential for bearing increased pressure loads represents the critical disadvantage.
The CRC improves the load bearing and stiffness characteristics of the flat plate closure. Since each cell shape requires an individual kinematic, the design, realization and assembly of this concept is expensive. A hinge-based prototype structure for the CRC is shown in Figure 4-13, middle.
Conceived to optimize the stress distribution within the sealing material, the shape-optimized isotensoid seal is well suited for pressure-induced loads. The pressurization of the edge region is not ensured. As the isotensoid shape constitutes the energetic minimum of a pressured cell closure, the deformation is hindered for increasing pressures.
With a higher conceptual complexity and the problem of intersecting hinges of neighbouring cells, the IRC is less suitable than the isotensoid cell closure. Figure 4-13, right, shows a hinge-based and a compliant prototype of the IRC.
Regarding the pressurization of cell sides and hinge regions, the DSEC seal shows as good performance as other concepts. The pressurization of the cells' edge region profits from the shape of the folded cap. The isotensoid geometry, which represents an energetic minimum as it includes the maximum volume, is calculated for the deformed state $st1$ of the cell. For increasing pressures the enclosed volume enlarges during deformation due to the smoothing of wrinkles and the closure's base contour deforms into the predefined target shape. Low stiffness against the cells' deformation results, as the target shapes of cell and closure are identical. A high grade of contour deformation can further be realized without a violation of geometrical boundaries.

Table 4-1: Characterization of sealing concepts regarding the requirements listed in Figure 4-1

\Demand Concept	$R_{cc}A1$	$R_{cc}A2$	$R_{cc}A3$	$R_{cc}B1$	$R_{cc}B2$	$R_{cc}B3$	$R_{cc}C1$	$R_{cc}C2$	$R_{cc}C3$	SUM
DSEC	+	+	+	+	+	+	+	0	0	*+7*
Tube solution	+	0	0	-	0	+	+	+	+	*+4*
Isotensoid	+	+	-	+	0	0	+	0	0	*+3*
Flat plate	+	+	+	0	0	-	+	+	-	*+3*
CRC	+	+	+	+	0	0	-	0	-	*+2*
IRC	+	+	-	+	0	0	-	0	0	*+1*
State-of-the-art	+	+	0	0	-	0	0	-	+	*+1*

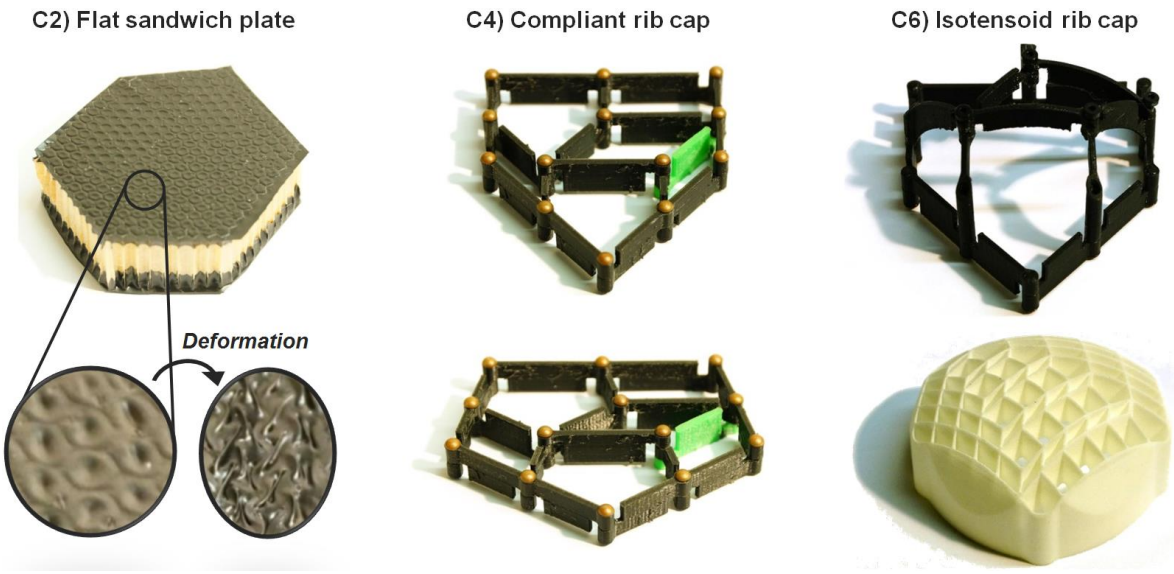

Figure 4-13: Realization of sandwich-stiffened flat plate (l.), CRC (m.) and IRC (r.)

The DSEC closure is selected as the preferential cell closure concept for PACS. The flat plate, as the simplest concept in terms of design and manufacturing, and the isotensoid seal, as suggested by Pagitz et al. [147], are considered as reference in the conceptual evaluation that is presented subsequently.

4.4 Design sensitivities and characteristics

The stiffness and pressure-dependent deformation behaviour of the DSEC relies on three essential design parameters:

- the wall thickness for shape optimization t_{SO},
- the cell closure height r_{isot}, and
- the closure material with *Young*'s modulus E and yield strength R.

It is shown analytically at the exemplary structure of a beam in chapter 4.2.7 that the more efficient deformation mechanism in terms of the necessary energy, compared with extension is bending. As the wall thickness t_{SO} can be used to promote the preferred deformation mechanism, the effects of varying wall thicknesses during the shape-optimization process are investigated first. Due to the ability of setting arbitrary end cap heights r_{isot} in the shape-optimization strategy, the cap dimensions that yield the favoured solution with respect to the overall system's performance are analysed subsequently. The effects of the utilized material and the related wall thicknesses t_{DSEC}, which is determined in terms of strength requirements, on the performance of the cell closure are further examined. The best performance is reached with a closure solution, which leads to the lowest influence on the cells' deformation and thus on the global pressure-dependent behaviour of a PACS.

The investigation of the effects of different design parameters on the performance of the DSEC bases on the comparison of its pressure-dependent deformation behaviour with that of the PACS cell. For this comparison the energy potential of both structures provides the key value. As shown in Figure 4-14 it can be extracted from the FEM simulation in the form of the totalized cell side moment M_{CC} that is needed to deform the closure respectively the PACS cell by the angle Δu_{CC}. The positive moment M_{CC} is orientated to cause a positive deformation Δu_{CC}. The energy potential of the cell closure can thus be contrasted with the energy potential of the underlying cell with the same size $d = r_{isot}$. The resulting differential moment $\Delta M_{CC} = M_{CC} - M_{cell}$ is oriented according to the closure moment. Ultimately, the necessary energy potential, which has to be provided by the cell structure to cause the cell closure's deformation, can be calculated for a range deformation angles Δu_{CC}. The DSEC solution is further compared with an isotensoid-shaped seal and the flat plate concept.

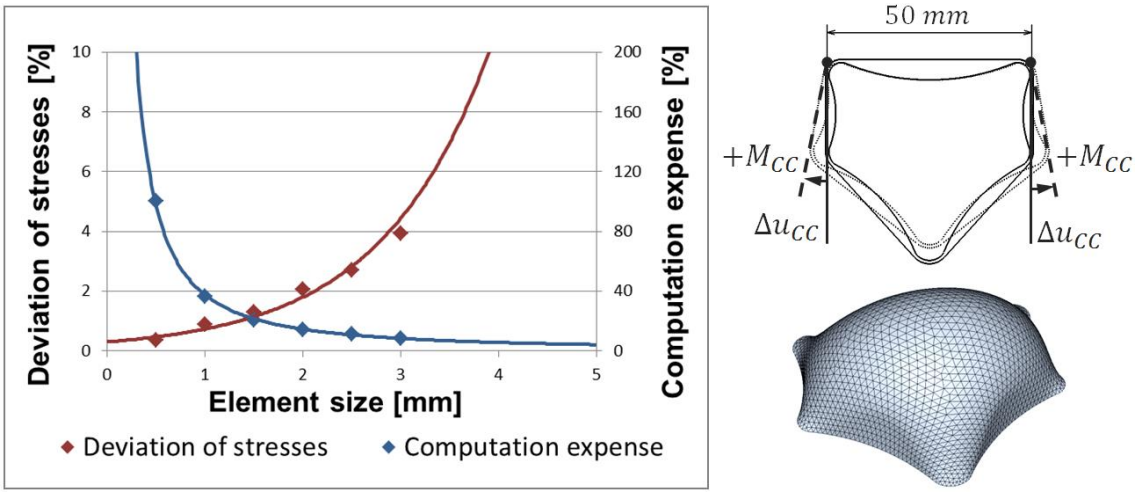

Figure 4-14: Sensitivity analysis and computation expense for isotensoid geometry

For this purpose the exemplary pentagonal cell geometry, which is shown in Figure 4-14, top right, is used and determined to show a target deformation respectively convergence angle of $\Delta u_{CC} = 8.5°$. With the assumed diameter of $D = 50\,mm$, the cell contour is representative for the application of a double-row PACS, like the variable-camber wing structure. As the subsequently presented investigations of the cell closure characteristic are based on FEM computations, a sensitivity analysis is processed to find a suitable discretization for the DSEC geometry. For the closure height of $r_{isot} = 25\,mm$, the sensitivity curve and the related computation time, compared to the most expensive variant, are illustrated in Figure 4-14, left. With a deviation from the isotensoid stress distribution of less than 1 % and a tolerable computational expense, an element edge length of 1.0 mm is chosen for the subsequently presented examinations.

The minimum applicable shell thickness for the shape optimization, which results in a stable computation process, is $t_{SO,min} = 0.01(D/2)$. For thinner sealing structures, the implicit solver may not converge for the described model as the investigations of Tempel [168] show. Analogues to equation (4.13) however, it is found that the *Young*'s modulus of isotropic materials does not affect this reaction and the resulting DSEC seal's shape. The reason for the thickness limitation lies in the snap through of folds. It is observed, that for increasing deformation and thicknesses below $t_{SO,min}$, compression-loaded areas of the cell closure structure abruptly change their wrinkling pattern. Although further investigations on such thin-walled DSEC structures may lead to more efficient cell closures, they exceed the scope of this work.
Three different closure shapes that are generated by using the shell thicknesses for the shape-optimization process $t_{SO} = t_{SO,min}$, $t_{SO} = 5t_{SO,min}$ and $t_{SO} = 10t_{SO,min}$ are shown together with their deformation-dependent behaviour. For the characterization of the resulting structures, the thickness $t_{DSEC} = t_{SO,min}$ is used for all solutions after the shape-optimization process to provide the necessary comparability. The total closure moment M_{CC} is shown in Figure 4-15, left. The highest moments are provided by the closure with the lowest wall thickness. The point of zero moment determines the equilibrium state of shape of only the cell closure. The comparison of the related angle $\Delta u_{CC,equil.}$ with the convergence angle of the underlying cell allows for the evaluation of the cell closure variant.
The right graph shows the differential moment between closure and unimpaired cell structure of the same height and compares the pressure-induced deformation of the seal with that of the individual PACS cell. The most relevant section of this graph is again near the convergence angle. It can be seen, that the differential momentum, which has to be provided by the cell to deform the closure at this angle is minimal for the closure variant with $t_{SO} = t_{SO,min}$.
In accordance with equation (4.13), the design with deep folds, which facilitates bending deformations and results from the minimum shell thickness $t_{SO} = t_{SO,min}$, yields the highest momentum respectively energy potential and the smallest deviation compared to the deformation of the undisturbed PACS cell.

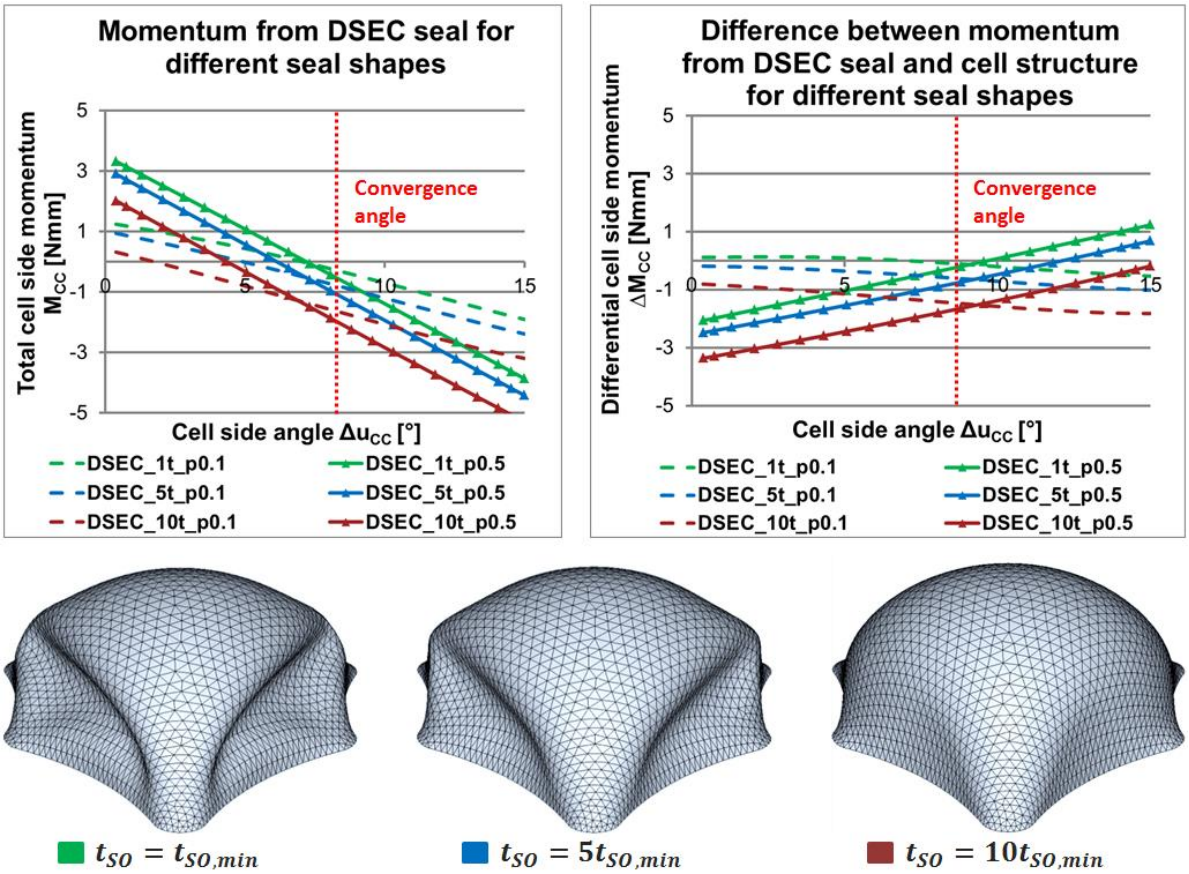

Figure 4-15: Effects of the shell thickness for shape optimization t_{SO} on the shape of the DSEC and on the pressure-induced moments

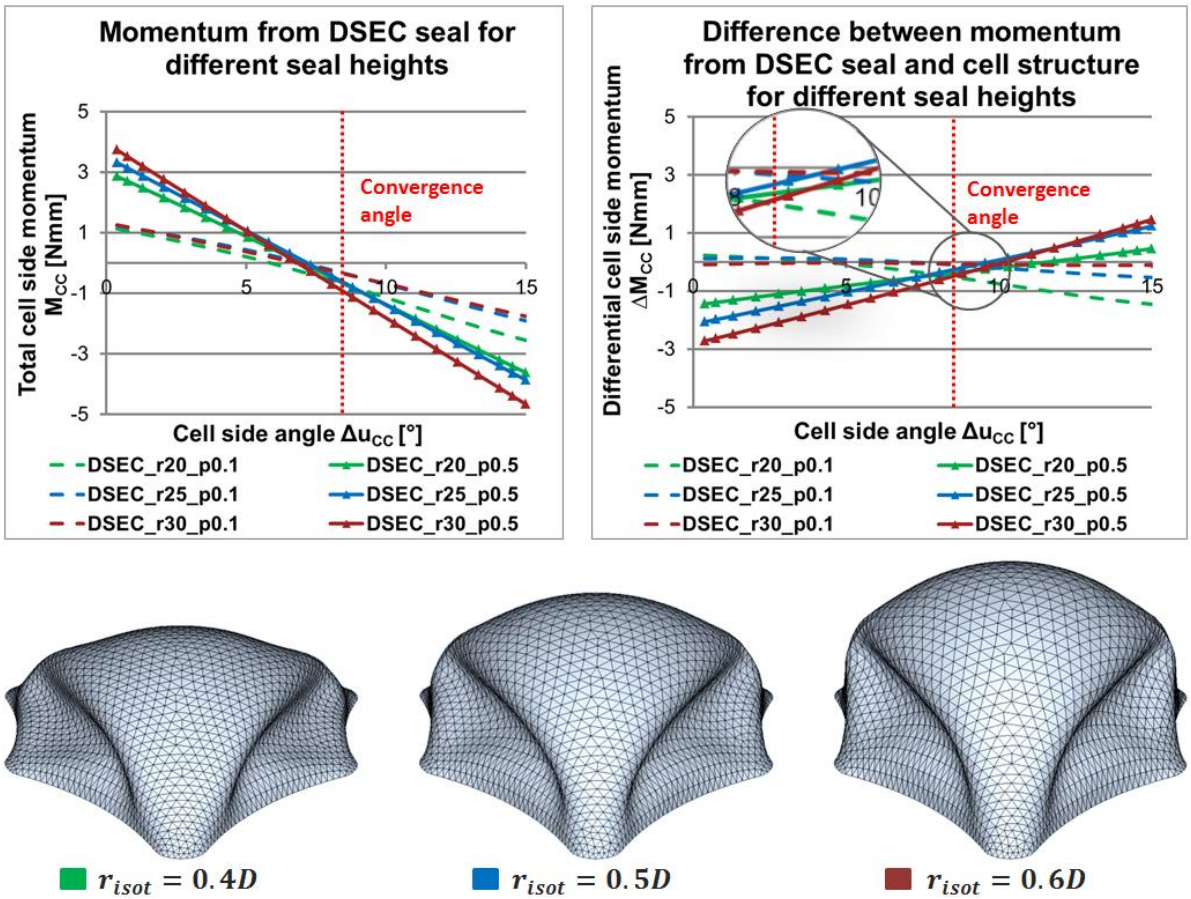

Figure 4-16: Effects of DSEC height r_{isot} on the pressure-induced moments

The height of the cell closure is the second significant design parameter for the DSEC that is to be investigated. The effect of the cell closure height on the performance of PACS is analysed to find enhancement potentials concerning the end cap dimensions. Therefore three DSEC geometries are computed with the heights of $r_{isot,1} = 20\,mm$, $r_{isot,2} = 25\,mm$ and $r_{isot,3} = 30\,mm$ and a shell thickness of $t_{SO} = t_{SO,min} = t_{DSEC}$. Figure 4-16 shows that the largest seal shape provides the highest initial moments. However, for the convergence angle the closure with $r_{isot,2}$ shows the smallest moments.
As the length of the cell body structure has to be reduced by the same amount as the cap is extended, the initial advantage of a large end cap is further reduced. The DSEC with the height $r_{isot} = 0.5D$ shows the best performance as it leads to the highest pressure-induced deformation and shows the slightest deviations in terms of the cell's moments, for the convergence angle (cf. Figure 4-16, right).
With the wall thickness for the shape optimization $t_{SO} = t_{SO,min}$, and the size of the structure $r_{isot} = 0.5D$, the three-dimensional shape of the DSEC is determined. These values are used for the further investigations.

The third variable that shall be investigated for its influence on the characteristics of the cell closure is the closure material. Depending on its yield strength R, the maximum pressure $p = 0.5\,MPa$ and a cell diameter of $D = 50\,mm$, the wall thickness t_{DSEC} is determined by

$$t_{DSEC} = \frac{pD}{4R}. \tag{4.15}$$

The *Young*'s modulus and the yield strength of the applied materials are listed in Table 4-2 together with the related wall thickness for the closure structure. The selection of materials in Table 4-2 is limited to elastomers. For materials with higher stiffness and increased yield stress, which allows for thinner wall thicknesses, an increased deformational performance may be found. In similarity to the shape-optimization process, however, dynamic deformations due to the existence of multistable states result for thin structures. This is validated in Figure 4-17 by showing two stable states of shape for an unloaded DSEC that is made of the material PA2200 with a thickness of $t_{DSEC} = 0.5\,mm$. As this unsteady deformation mechanism yields unknown dynamic stresses, no further investigations are done in this area. For the holistic design of PACS, only materials are considered for the cell closure, which lead to a steady deformation behaviour.

Table 4-2: Exemplary materials for the DSEC and related *Young*'s modulus, yield strength and closure thickness

Nr.	Material	*Young*'s modulus E [MPa]	Yield strength R [MPa]	Thickness t_{DSEC} [mm]
1	**TPU-92A**	29.08	4.76	1.313
2	**Arnitel PL420-H**	100	5.3	1.179
3	**Arnitel PB582-H**	300	16.5	0.379

The results of the simulation are summarized in Figure 4-18. A thin membrane-like cell closure represents the most efficient implementation. The DSEC variant with the lowest thickness provides the highest moments due to its low structural stiffness. The difference between the pressure-dependent behaviour of cell structure and closure is also minimal for Arnitel PB582-H.

A comparison of the DSEC seal with previously established solutions, i.e. the isotensoid and the flat plate, is performed to evaluate the improvements that come along with the selected DSEC concept. Figure 4-19 visualizes the performance advance. Notice that the moments for the flat plate are plotted at the secondary y-axis, as they exceed the values of the isotensoid and the DSEC closure significantly.

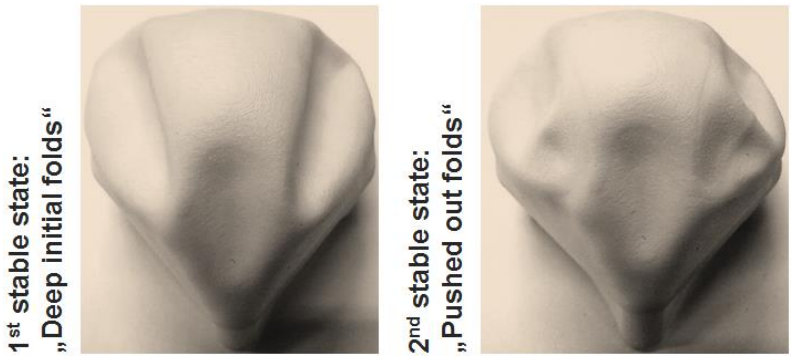

Figure 4-17: Two stable states of shape for DSEC sealing made of the material PA2200

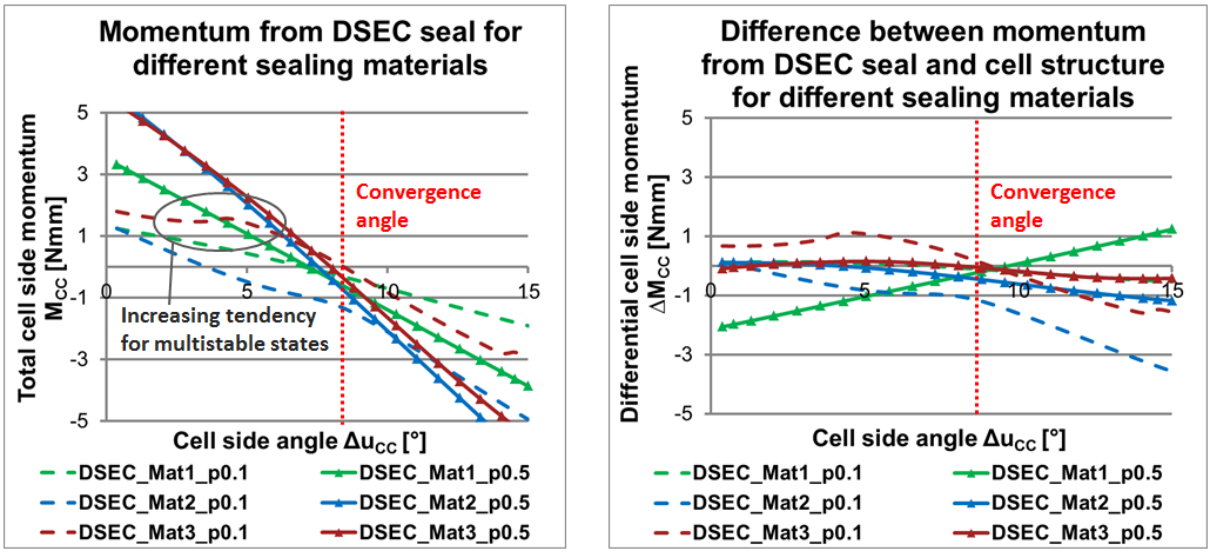

Figure 4-18: Effects of the applied material and the related wall thickness on the pressure-induced moments

The differential cell side moment that is needed to deform the pressurized isotensoid seal near the convergence angle at $p = 0.5\ MPa$ is reduced to $\Delta M_{CC,DSEC}/\Delta M_{CC,isot} = 8.57\ \%$ for the DSEC. The differential moments from the flat plate are two orders of magnitude higher than the moments which are needed to deform the DSEC. A decreased to $\Delta M_{CC,DSEC}/\Delta M_{CC,fp} = 0.85\ \%$ is deduced.

The deformation of the DSEC seal is further compared with the pressure-dependent distortion of the PACS cell in Figure 4-20. This comparison yields a summary about the deformation characteristics of the DSEC. The cell is modelled with rigid cell sides and flexible hinges with a thickness of $t_H = 0.5\ mm$ and consists of PA12. It can be seen that the curves show similar trends. Especially near the convergence angle of the cell, the DSEC closure cannot completely follow the underlying structure.
As it can be observed in Figure 4-20, the deformations of the PACS cell and the DSEC diverge for increasing pressures. Following the initial idea that a pressurized DSEC seal deforms into the isotensoid shape, allows for the argumentation that a variation of this state $st1$ causes a modification of the resulting deformation behaviour. So far this state $st1$ is chosen to coincide with the convergence state of shape of the undisturbed cell. The divergence between pressure-dependent behaviour of cell and seal can be reduced by adjusting the deformation Δu_{CC} of the state $st1$. Figure 4-20 thus additionally shows the results for an overdriven DSEC closure (DSEC_OV) with an initial state $st1$ that shows a deformation of $\Delta u_{CC,OV} = 1.25 \Delta u_{CC}$. The increased deformation for pressures above $0.1\ MPa$ can be utilized to enhance the deformation accuracy for the cell compound.

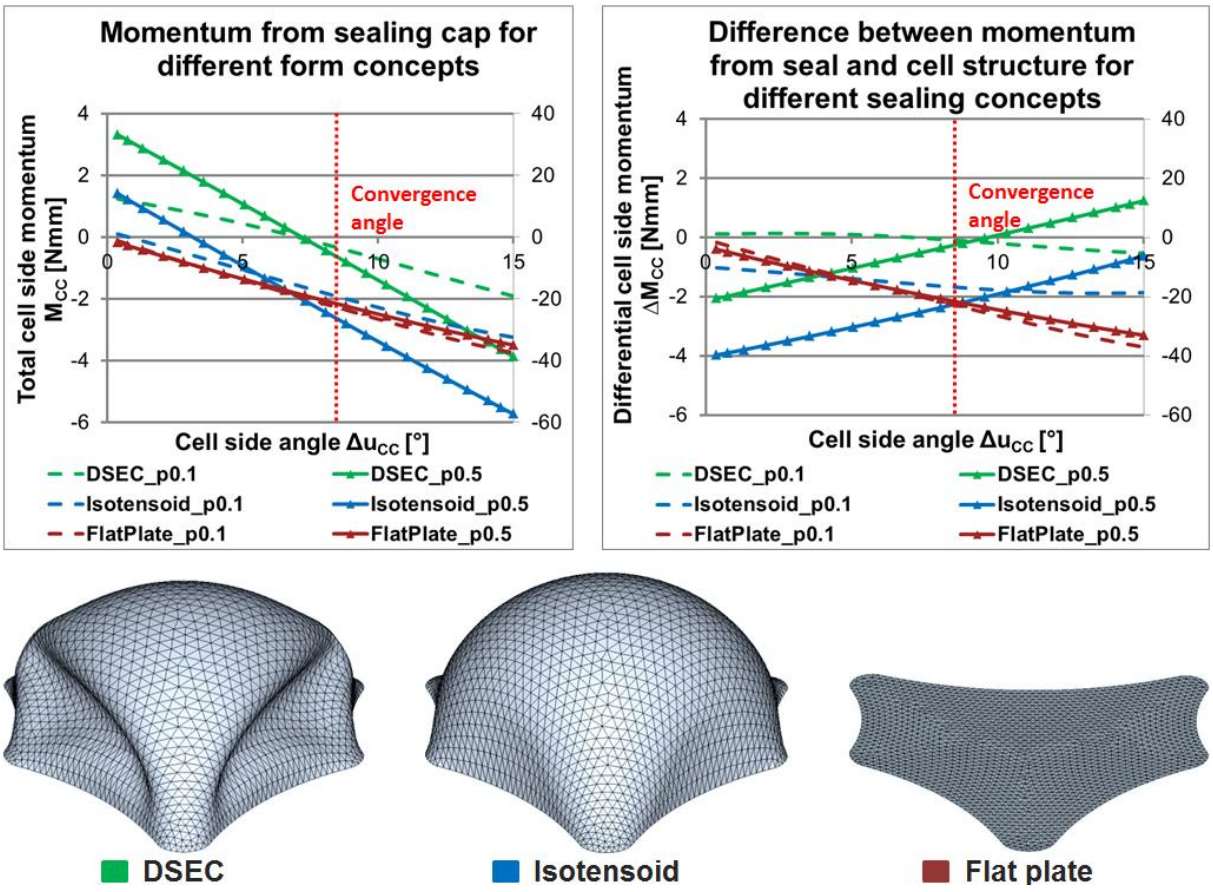

Figure 4-19: Comparison of the sealing concepts DSEC, isotensoid and flat plate

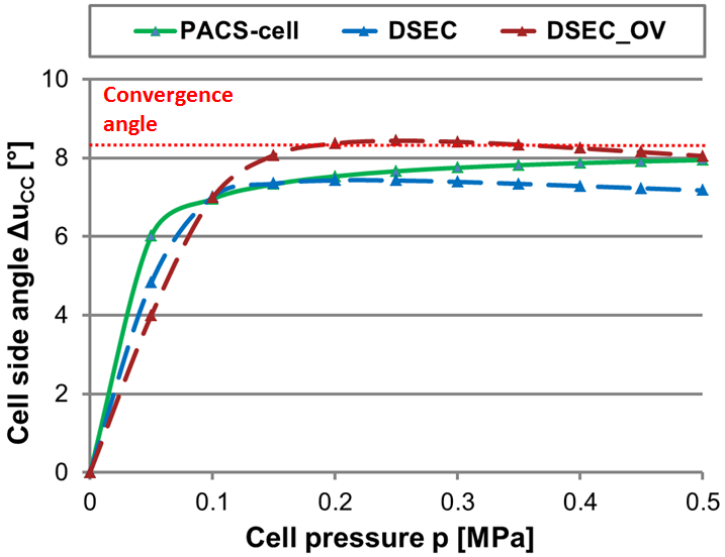

Figure 4-20: Pressure-dependent deformation behaviour $\Delta u_{CC}(p)$ for cell and seal

The undeformed and pressure-loaded deformed shape of the overdriven DSEC specimen, which is made of *TPU92-A* and experimentally tested in chapter 6.1.4, are shown in Figure 4-21 as a result of FEM-based simulation. The resulting stress distribution is not isotensoid for the overdriven and the conventional DSEC. Due to local concentration of bending and extensional strain stress gradients appear especially near folds. The maximum *von Mises* stresses of the loaded overdriven DSEC is $\sigma_{DSEC,max} = 3.366\,MPa$. It exceeds the stresses of the ideal isotensoid shape of $\sigma_{isot,max} = 2.806\,MPa$ by 19.96 %.

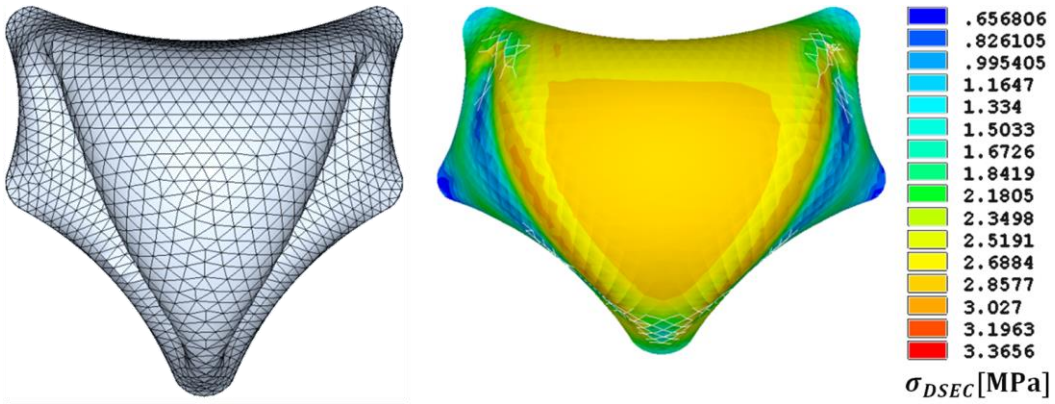

Figure 4-21: FEM model of the DSEC_OV and simulated deformation results for p = 0.5 MPa and t_{DSEC} = 2.0 mm and according stress distribution

For the subsequent utilization as a shape-variable cell closure for PACS, the DSEC is used as the best solution. Regarding the initial requirements, the major topics of deformability, stiffness reduction and strength outweigh the minor disadvantages regarding geometrical adaptability for different cell geometries, maintainability and of non-uniform stress distribution. Further design improvements could compensate the stress deviations through wall thickness regulations or shape control.

4.5 Sealing and fluid flow

Although an integral production of cell and closure is conceivable, due to the selection of different materials, the herein presented PACS device is designed for differentially-manufactured components. It consists of the structural elements cell body and cell closure. The concept for the assembly of these components and the required geometrical changes for the pressure-tight sealing and the fluid flow completes this chapter about the sealing and pressurization for PACS.

Three assembly concepts are identified to be convenient for the application of PACS [169]. Welding of cell body and closure leads to a pressure-tight connection with minor or without additional material and mass. The welding compatibility of cell compound and closure material is premise for this connection method. Transitions between thin hinge regions and cell closures with increased wall thickness together with a small joining surface disadvantages the butt joint compared to the lap joint (see Figure 4-22). The lap joint whereas yields the disadvantage of hinge stiffening and poor accessibility.
The possibility of connecting components made from different materials is given by the bonding process. The joint stresses [170] can be calculated for the lap joint by

$$\tau_{C,max}^{*} = \sigma_{ax}\sqrt{\frac{G_C t_1}{E_1 t_C(1+\psi)}}, \text{ with} \tag{4.16}$$

$$\psi = \frac{E_1 t_1}{E_2 t_2} < 1. \tag{4.17}$$

$\tau_{C,max}^{*}$ is the maximum shear stress within a bonded joint due to the joint partner stresses σ_{ax} in cell axial direction. The shear stiffness of the cohesive film is G_C, its thickness is t_C. E_1 and E_2 are the *Young*'s moduli and t_1 and t_2 the wall thicknesses of the joint partners that are used to compute the ratio of longitudinal stiffness ψ. The load bearing flange length for bonded joints l^* is computed by

$$l^* = 5\sqrt{\frac{E_1 t_1 t_C}{G_C(1+\psi)}}. \tag{4.18}$$

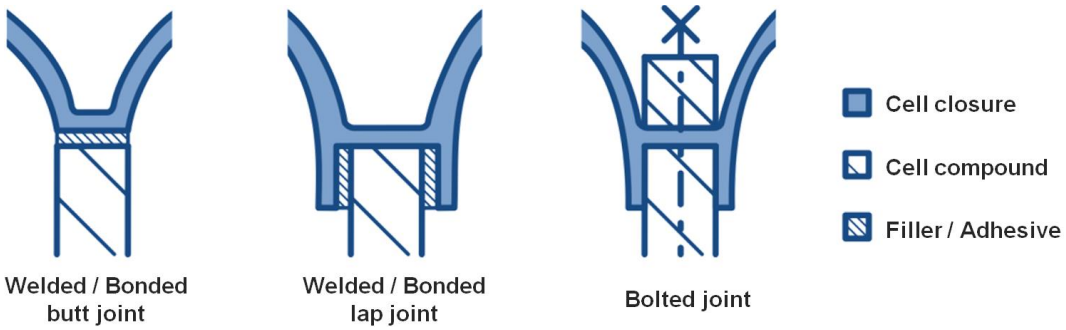

Figure 4-22: Assembly and sealing concepts for connecting cell compound and cell closure

The *Young*'s moduli and the thickness of the joint partners significantly influence this load-bearing length and the strength of the connection. The stiffer the respective joint partners, the higher the applicable loads. For the use of elastomeric material, bonded joints are thus less appropriate.

In contrast to welded and bonded joints, the utilization of bolted joints does not limit the material selection for the joint partners. Bolting provides axial forces for the clamping of the DSEC so as to ensure pressure tightness between mounting frame and cell structure. For this fluid-tight connection between DSEC closure and PACS cell, the end cap is extended by a gasket seam. Figure 4-23 shows that closure and gasket are designed as an integrated membrane. Apart from hinge areas and thin-walled cell sides, leakage occurred in preliminary experimental investigations at regions, where the required contact pressure could not be applied. Especially the bore holes for bolts are found to be a source for loss of fluid and therefor pressure. For this reason the gasket concept is enhanced by a sealing bead along the contour of each cell. Figure 5-5 illustrates the resulting design which increases the local clamping force equally to an O-ring seal and thus leads to a complete pressure-proof solution.

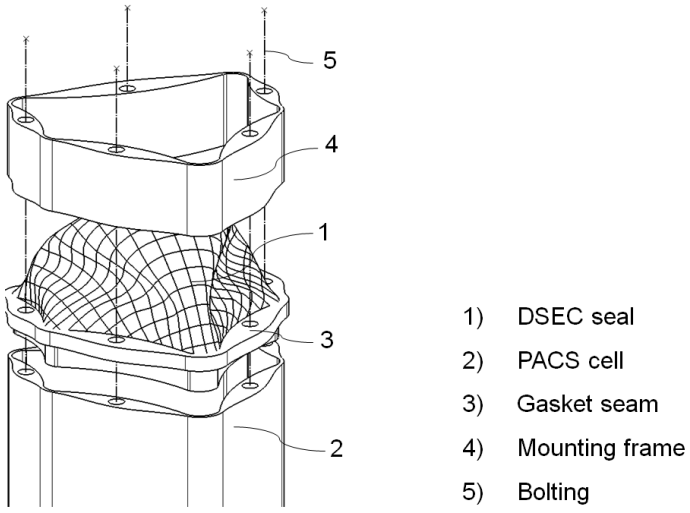

Figure 4-23: Sealing concept for the connection between cell body structure and DSEC for a single PACS cell

The disadvantage about this variant is that an additional structure, the mounting frame, is needed to distribute local attachment forces. The clamping of the gasket is realized by this further component, which shows the same cross section as the cell body. In addition to pressure-induced forces, the bolted joint thus has to bear forces that are required to achieve the sealing effect. The necessary diameter D_{Bolt} of the bolts [159] can be calculated according to

$$D_{Bolt} = \sqrt{\frac{A_{Bolt}}{\pi}} = \sqrt{\frac{(F_{cl}+F_{op})k_A\kappa}{\pi R_{Bolt}}}. \tag{4.19}$$

The clamping force F_{cl} and the operating force F_{op} have to be borne by a bolt of strength R_{Bolt} for a tightening factor k_A and the friction-based reduction factor κ_A. As depicted in Figure 4-23 it can be seen that the wall thickness of the cell sides may have to be increased according to the resulting bolt size, to enable this connection. The shape of the DSEC and the assembly concept are covered by patent application [171].

With the sealing and pressurization, the structural design for PACS is elaborated to a fully functional three-dimensional model. The necessary preparations for the realization of a PACS for experimental investigations are thus made.

5 Manufacturing and assembly

Although different production processes are used for the iteratively developed PACS structures, the manufacturing issues focus on the realization of the load-based cell body design that is presented in chapter 3 and the DSEC cell closure and sealing concept that is suggested in chapter 4. The three-dimensional geometries for the PACS cell body, the closure membrane and the appropriated mounting frame are defined within the related design steps. The manufacturing and assembly processes for these parts are non-trivial and have repercussions on the design, which shall be determined. Processes for single-part production are in the foreground, as the major objective of this chapter is to describe their use for the realization of PACS specimens for conceptual evaluation.
After analysing the demands on the production processes an overview and valuation of suitable production techniques is presented. Hereafter, the processes, which are qualified and used for the different realizations of PACS, are characterized. This section is completed with the description of the assembly process that relates to these realizations.

5.1 Manufacturing processes for cell body structure

The main requirements on the production process for the cell body structure, which are defined in the demand analysis, are applicable for integral and segmented design. The objective of this chapter, in addition to the presentation, assessment and selection of suitable manufacturing techniques is to point out the application limits with these processes and to provide a description of the essential process parameters.

5.1.1 Demands on production processes

The demands on the manufacturing processes for the PACS's cell body structure can be divided into cross-sectional in-plane ($R_{CB}1$ to $R_{CB}2$), out-of-plane ($R_{CB}3$ to $R_{CB}7$) and quantity ($R_{CB}8$ to $R_{CB}9$) issues. Requirements on the highly loaded hinge elements (requirement 1 for production process of cell body: $R_{CB}1$) concern the geometrical accuracy, which influences the stiffness and strength properties of PACS and the joint strength for connecting hinges and cell sides. Regarding equation (2.8), a change in thickness affects the hinge stiffness with the third power. A deviation η_{thk} of more than 10 % shall thus not be exceeded. Although the asymptotic deformation of the cell compound is not influenced by varying hinge stiffness values, the deformation phase is affected considerably (cf. Figure 2-17). The effects of doubling or halving of the hinge stiffness are presented in chapter 2.6.3. Stress maxima due to local changes of the wall thickness t_H also have to be avoided. Demands on the manufacturing of cell sides ($R_{CB}2$) are subordinate. The geometrical accuracy at cell side regions is less critical for deformational behaviour and due to the freely selectable cell side safety factor SF_{CS}, for stress considerations.
Huge thickness ratios between hinges and cell sides, which result from the cross-sectional design (cf. chapter 5.1.1), are problematic for production techniques like casting due to chemical or thermal shrinkage. Out-of-plane issues are given by such production-induced deformations, the cell compound dimensions, and the processible materials. Production-induced deformation ($R_{CB}3$) results in local geometrical inaccuracy but also in global deviations. In the xy-plane it causes variations towards the targeted structural deformation behaviour and affects the cross-sectional as well as the three-dimensional geometry. A curvature of the hinges in the cell-axial direction could lead to malfunction of the whole structure. The dimensions of the PACS ($R_{CB}4$) in the cross-sectional plane and in depth direction, which are below $d = 1e3\,mm$ for the first realizations, may exceed manufacturing limitations. Besides the depth of the cell compound, the flexibility of the resulting structure yields difficulties particularly for cutting processes. To realize a span of several meters, a longitudinal

segmentation for the variable-camber wing PACS device is possible but expensive. Regarding system weight and complexity, segmentation is thus unfavourable. Moreover, a manufacturing process is only suitable for a group of materials ($R_{CB}5$). For the selection of this process, the conceived material thus has to be considered. The manufacturing process is rated according to the relevance of the processible materials for PACS (see Table 2-6). Depending on the purpose of the realization the following requirements may be optional or substantial. The tightness of the cell body ($R_{CB}6$) should optimally be given without rework or additional sealing elements. The fluid ducts ($R_{CB}7$), which cause undercuts, are preferably integrated without additional manufacturing steps.
The necessary efforts and costs regarding the manufacturing preparation and the production of a single PACS demonstrator ($R_{CB}8$) or of a large number of cell structures ($R_{CB}9$) is a critical criterion for the selection of a convenient process. The requirements for the manufacturing of the cell compound structure are summarized in Table 5-1.

Table 5-1: Requirements on manufacturing process for cell body structure

Label	Description
$R_{CB}1$	Geometrical accuracy of hinge elements
$R_{CB}2$	Geometrical accuracy of cell side elements
$R_{CB}3$	Avoidance of manufacturing-induced deformations
$R_{CB}4$	Manufacturing dimensions
$R_{CB}5$	Quality of processible materials
$R_{CB}6$	Pressure tightness of component
$R_{CB}7$	Integral manufacturing of fluid ducts
$R_{CB}8$	Suitability for single-item production
$R_{CB}9$	Suitability for series production

5.1.2 Relevant processes and valuation

A selection of suitable manufacturing processes and their evaluation with respect to the demand analysis for the application for PACS is given in Table 5-2. For the underlined manufacturing processes, which can be found in [172] and [173], either prototypes are built or experiences by manufacturing simulations are made. The processes are rated on the basis of the demand analysis and with the information that is collected during production trials and presented in the following. The rating value 2 means that the particular requirement is completely fulfilled -2 stands for non-fulfilment. Weighting factors are applied in terms of the specific needs of the single-part production of test specimens that are used for the evaluation of the design process. Table G-1 provides the underlying comparison of requirements that is needed to determine the weighting factors.
In order to reduce the number of the herein presented manufacturing techniques for the PACS cell body, the most suitable processes are first identified. For gaining the necessary information about the adequacy of these production processes in terms of PACS production trials and simulations are performed. The FRP prepreg, the water-cutting and the SLS process are identified as the three top-rated manufacturing techniques for PACS, regarding the underlying requirements. The FRP prepreg process is used to manufacture the first realization of a PACS [162]. The excellent mechanical properties of the processible materials, is decisive for the high classification of the FRP prepreg process. Water cutting allows for the processing of large components and widely selectable materials. Manufacturing-induced deformations can be excluded as the raw material is processed in cured condition. The SLS process profits from fast and efficient single item production. The disadvantage of inferior materials like PA2200 (cf. Figure 2-6), which can be processed in the SLS, is accepted for the implementation of prototypes. Due to the possibility of integral manufacturing of the fluid duct, the SLS process is assessed slightly better than wire-cut EDM.
The examination results about the manufacturing processes, which are investigated for this selection but discarded due to the current weighting of requirements, are summarized in appendix H.

Table 5-2: Evaluation of manufacturing processes for the cell compound according to the demand analysis for single-part production (EDM: Electrical discharge machining; SLM: Selective laser melting; SLA: Stereolithography; FDM: Fused deposition modelling)

No.	Manufacturing process	Performance w.r.t. requirements									
		$R_{CB}1$	$R_{CB}2$	$R_{CB}3$	$R_{CB}4$	$R_{CB}5$	$R_{CB}6$	$R_{CB}7$	$R_{CB}8$	$R_{CB}9$	SUM
1	FRP prepreg	1	1	0	2	2	2	0	0	-2	**0.959**
2	Water cutting	1	2	2	1	1	-2	-1	1	1	**0.959**
3	SLS	1	2	1	1	-1	2	2	2	0	**0.820**
4	Wire-cut EDM	1	2	2	1	0	2	-2	1	0	**0.817**
5	SLM	1	1	1	-1	0	1	2	2	-1	**0.813**
6	Bonding	1	2	2	1	1	1	1	-1	1	**0.753**
7	SLA	1	2	2	0	-2	1	2	2	-1	**0.555**
8	Laser cutting	-1	2	2	1	0	-2	-1	2	1	**0.455**
9	Laser welding	1	2	1	1	0	1	1	-2	1	**0.200**
10	FDM	0	2	1	0	-2	0	1	2	-1	**0.137**
11	Investment casting	0	-1	1	-1	0	2	2	-2	1	**-0.239**
12	Extrusion	-1	-1	-1	2	0	1	-2	-2	2	**-0.643**
13	Injection moulding	-2	-1	-2	-1	0	1	-1	-2	2	**-1.167**
	Weighting factor	0.230	0.046	0.109	0.075	0.244	0.039	0.039	0.201	0.017	

5.1.3 FRP prepreg process

The top-rated process (cf. Table 5-2) for the production of a single PACS cell body structure is described in the following together with the related development process and the lessons learnt. An iterative approach for achieving suitable manufacturing parameters is introduced in Figure 5-2 to overcome the complexity of producing a PACS structure in a prepreg process. Processing the high potential FRP materials is thus enabled. Subsequently to the description of the critical structural elements and of the necessary iteration steps, the essential methods for the successful manufacturing of a single cell and a six cell single row cantilever structure are presented.

According to the examination of suitable materials for PACS (see Table 2-6), the unidirectional GFRP HexPly913 is identified to provide a high ratio of the square of strength to stiffness and thus is selected for this realization of a cell body structure. After defining the geometry for the single PACS cell, a mould is designed for producing a silicone core which serves as a winding mandrel for the GFRP material. Geometrical adaptions for compensating thermal expansion during the autoclave process are made on the basis of an FEM-simulation to ensure dimensional accuracy. The core is made of the two component silicone Elastosil 4642 from *Wacker*. Its elasticity and transversal contraction allows for gentle and non-destructive demoulding of the GFRP structure and leads to a smooth inner surface. Ply placement and autoclave process appeared to be the critical sub-processes to be controlled. These manufacturing steps are optimized according to Figure 5-2 for the single cell and for a double cell test specimen, before the production trials with the six cell target structure are performed and evaluated. The tool design, the parameters of the autoclave process, the draping techniques and the local layer structure represent the essential influence parameters that allowed reaching the desired production quality. The geometry and layup of the single cell specimen and of each cell of the cantilever structure are identical. Figure 5-1 illustrates the respective information.

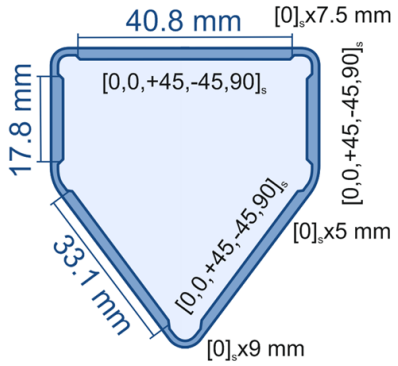

Figure 5-1: Geometry and stacking sequence for symmetrical GFRP PACS cell

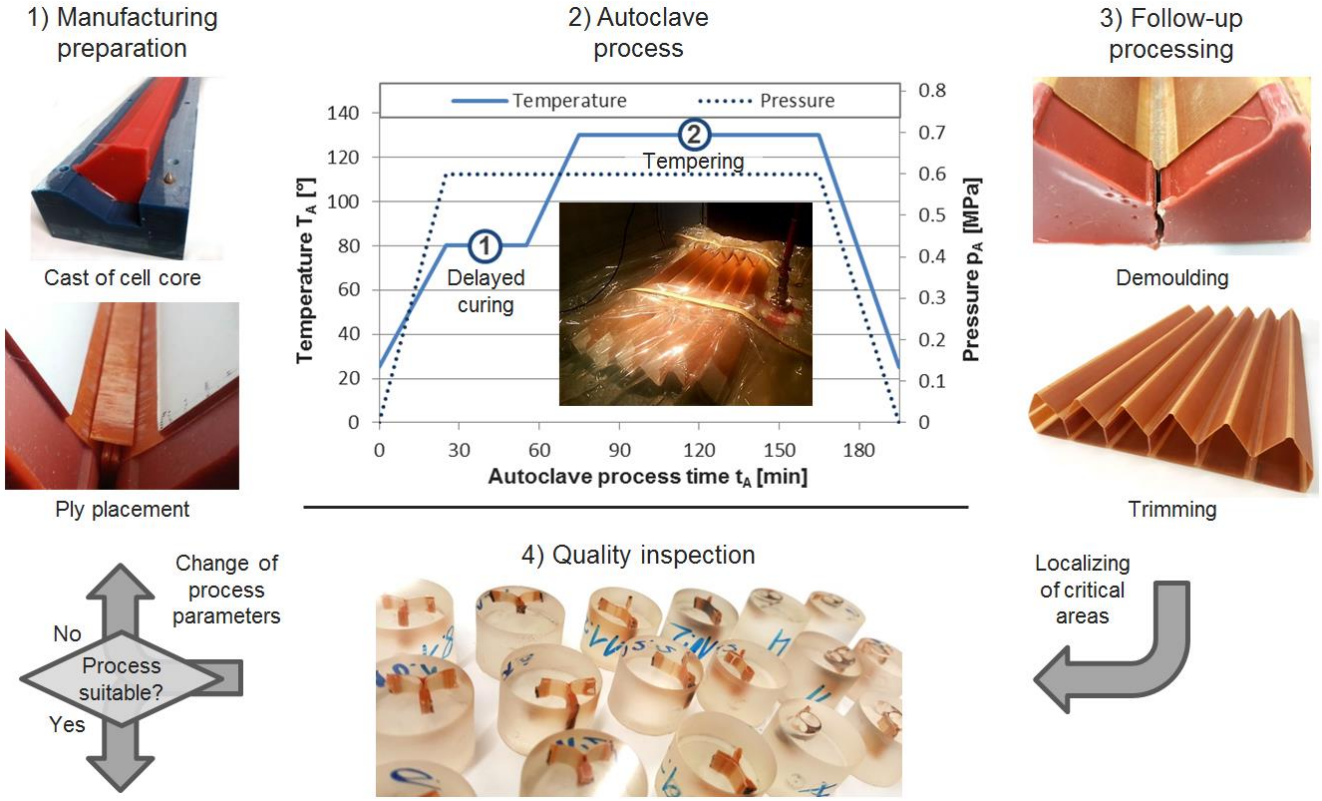

Figure 5-2: Iterative process development for realizing a single row PACS structure, including the manufacturing preparation, the autoclaving, the follow-up process and the quality inspection

Preforming all of the ten adjacent cell side plies to a single stack with multiaxial layup increases accuracy and facilitates the challenging process of draping. The precise manufacturing of the cell side crossovers and the flexure hinges is assessed as critical within the ply placement.

As presented in Figure 5-3, multiple production trials are necessary at a trimmed two cell structure to optimize the crosslinks of two and three cell sides that share the same edges. The final solution for the eccentric compliant hinges is shown in Figure 5-3, (1) and (2). As shown in the microscope pictures, the transition between cell side and hinge is realized by joining the bottom and top layer. The intermediate plies are not staggered near the transition zone in the final version. As it can be seen from the center-left depiction (1), the resin accumulation builds a small gusset of about 0.5 *mm* in size that takes over this function. The enveloping plies with cell circumferential fibre direction enclose the preformed cell side laminate and form a smooth resin braced transition between cell side and hinge.

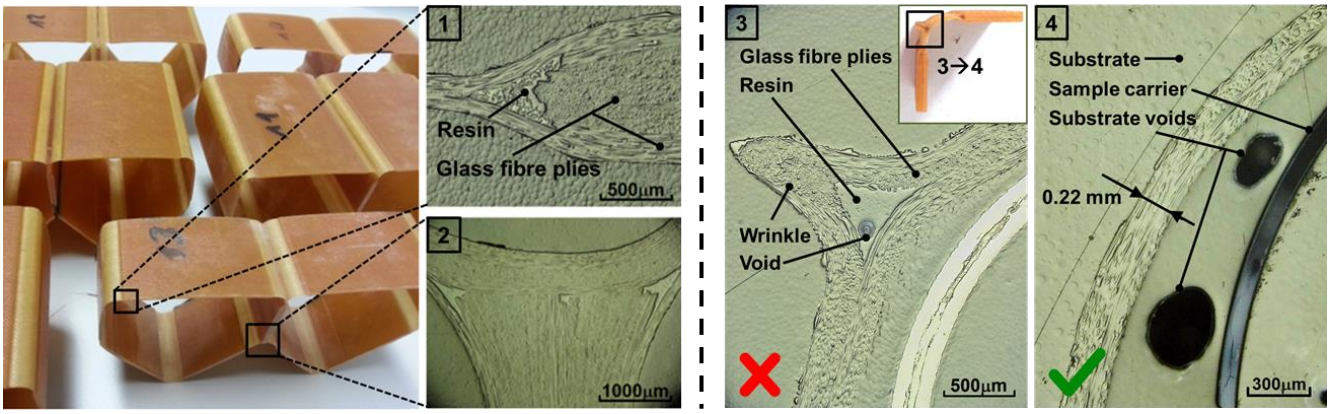

Figure 5-3: Manufacturing approaches (l.) and appropriate microscope photographs for the crossovers of two (1) and three (2) adjacent cell sides; wrinkle at flexure hinge (3) and optimal solution (4) as a result of repeated production trials

The more complex crosslink structure of three intersecting cell sides is depicted in illustration (2). Compared to the overall structure, this huge and stiff GFRP gusset with about $4\ mm$ in size turned out to be necessary as it has to withstand the autoclave pressure, which forces the cells to drift away from each other. A stable geometry for this gusset could not be implemented without the additional material accumulation. The microscope photographs are taken for quality inspection and show the successful implementation of the compliant hinge joint for the single and the six cell PACS.
Insufficient tautness of the hinge plies moreover results in wrinkles (3) at the sensible compliant hinge regions that could not be eradicated by increased drape efforts. These wrinkles, which preferably appear at the thin-walled flexure hinges, could be avoided by an adaption of the autoclave settings to the values that are shown in Figure 5-2. As an increased hinge stiffness and local load peaks result from such hinge imperfections, they cause deviations from the design model. The idea for overcoming this issue is to use the thermal expansion of the silicone core to stretch and straigthen the circumferential fibres of the cell structure before the resin is cured. In the first phase of the autoclave process, the autoclave is heated up to $T_A = 80\ °C$. The viscosity of the resin is reduced and the process of curing is delayed. Both conditions facilitate the fibres to be aligned in cell circumferential direction under the pressure of the extending silicone core (4). A raise of the autoclave temperature to $T_A = 130\ °C$ is initiated in the subsequent tempering phase, after the curing process is largely completed. The effects of the further thermal expansion of the silicone core on the geometrical accuracy are thus reduced. The autoclave pressure of $p_A = 0.6\ MPa$ is applied to the evacuated specimen for the whole process. It compacts the laminate and raises its fiber volume fraction.
An important parameter for the mechanical characteristics of PACS that could also be influenced by the prepreg process is the wall thickness of cell sides and hinges. As the thickness of a single ply of the HexPly913 material is $t = 0.125\ mm$, a nominal thickness of $t_{H,nom} = 0.25\ mm$ for the hinges and $t_{CS,nom} = 1.25\ mm$ for the cell sides is conceived (cf. Figure 5-1). The measured mean values for the cured structure that could be reached after the process development lie at $t_H = 0.22\ mm$ and $t_{CS} = 1.21\ mm$ and are tolerable for the subsequent investigations.
The follow-up processing, which is characterized by the demoulding and the trimming of the structure, is unproblematic. The silicone cores can easily be detached and pulled out of the cells due to their transversal contraction.

The critical structural elements within the production samples are mechanically separated and investigate in the form of microsections, as presented in Figure 5-3. The improvement strategy for the manufacturing process from the preparation and execution of production, to the quality inspection and suitability analysis is illustrated in Figure 5-2. It further holds the parameters that are used for the autoclave process and pictures the resulting PACS specimen. The single cell and the six cell single row cantilever prototype are built completely integrally according to the described process.

5.1.4 Water cutting

The great expense with the manufacturing of a PACS in a manual FRP prepreg process, which is found for single ($R_{CB}8$) and projected for series production ($R_{CB}9$), gave reason for a change of the production process. Water cutting allows for the processing of multiple materials, tolerates huge changes of wall thickness and can be applied for low and high volume production. Deficiencies regarding accuracy are overcome by the enhancement process that is illustrated in Figure 5-4. The description of the manufacturing strategy is followed by the identification of critical structural elements and the presentation of results.
This concept for manufacturing the PACS results in a layered structure. The total depth of the resulting PACS is controlled by the number of cuttings that are arranged behind another. Thread rods in cell-axial direction provide the necessary attraction force and bear the pressure-induced axial loads. The process of water cutting can be utilized for the machining of semi-finished products with a maximum wall thickness of the sheet material of $100\ mm$ for metals and $140\ mm$ for plastics and ceramics [172].

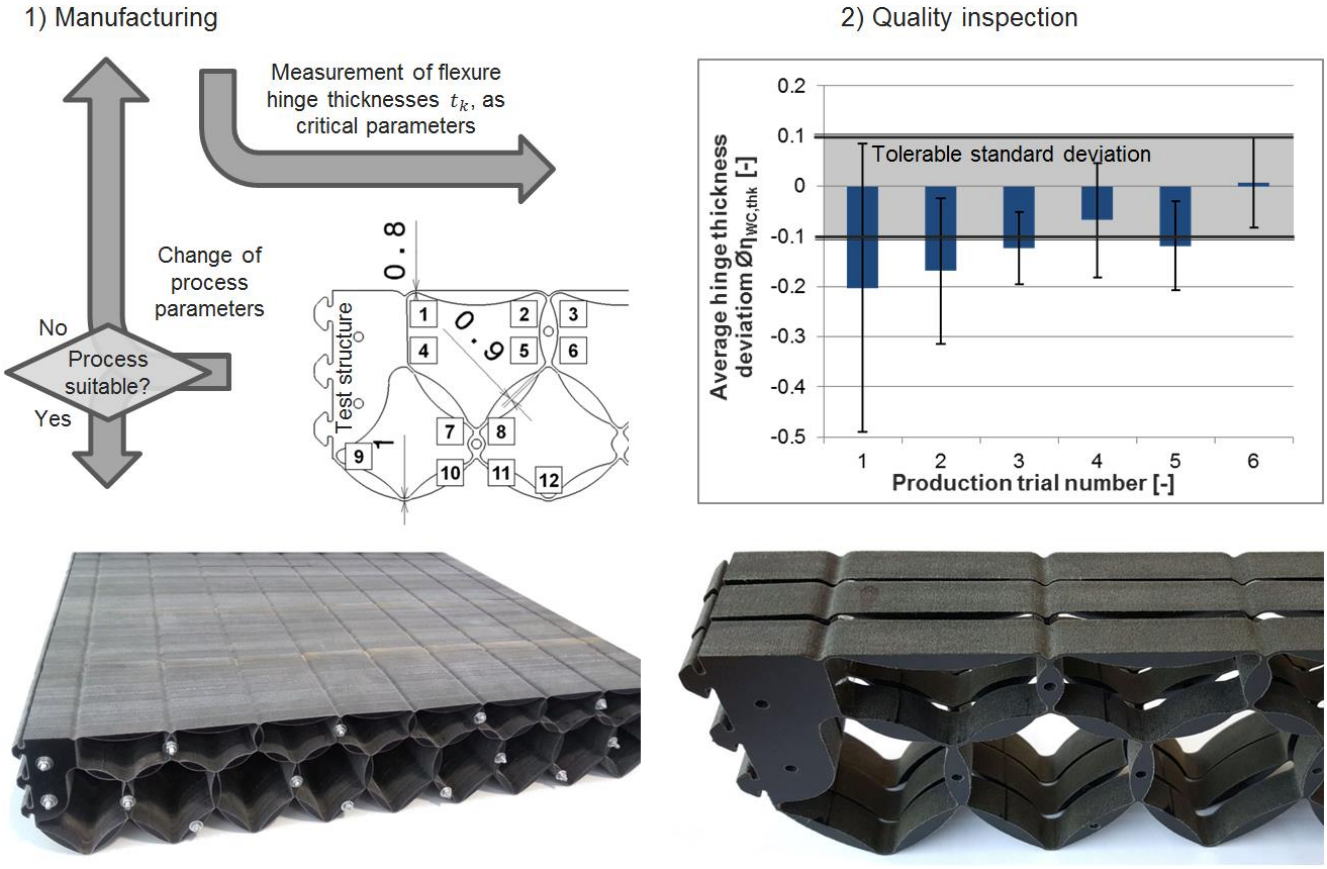

Figure 5-4: Development of the water cutting process, including the manufacturing, the subsequent inspection of quality and the resulting PA12 double row PACS structure

As the manufacturing precision decreases with increasing cut depth due to the divergence of the cutting jet, the thermoplastic polymer PA12 is processed in form of $10\,mm$ thick sheets. The PA12 material is selected because of its suitable strength and stiffness values and the associated optimal hinge thickness of $0.588\,mm$ that is calculated according to equation (2.39), for $s = 5\,mm$ and $\Delta u_c = 15°$. A tolerably increased thickness of $0.8 \ldots 0.9\,mm$ can be produced without suffering from huge thickness-proportional manufacturing inaccuracy $\eta_{WC,thk}$. The optimal hinge thickness for metals, however, lies at about $0.1\,mm$ and could not be achieved.

For the evaluation of the process quality, the accuracy of the hinge thickness is decisive. Figure 5-4 illustrates the location of the measuring points and provides the related average wall thickness deviation from the nominal value $Ø\eta_{WC,thk} = Ø\left(t_{WC,\boldsymbol{k}}/t_{WC,\boldsymbol{k},nom} - 1\right)$ for six different production trials. It further gives an overview about the number of iterations that had to be processed to reduce the related standard deviation to less than 10 %. The single segments that result from the adjusted water cutting process as well as the assembled layered structure are depicted in Figure 5-4. The presented double row structure is assembled from thirty segments that include bore holes for the thread rods. It is designed with a connection structure to allow for a modular construction and consists of eight pentagonal and nine hexagonal cells with a total length of $450\,mm$ and a height of $85\,mm$. The challenging task of sealing the segments is accepted in view of the huge advantages of only minor production complexity and of the flexibility to produce freely selectable cell lengths.

Satisfying process conditions for PACS are developed, led to repeatable results and allowed to realize the double row cantilever PACS specimen. The main disadvantage of this concept lies in the loss of the flexure hinges' capability to seal the cell body structure along the cell axis. The additional expense to recover the pressure-tightness reduces the value of this process for single and mass production.

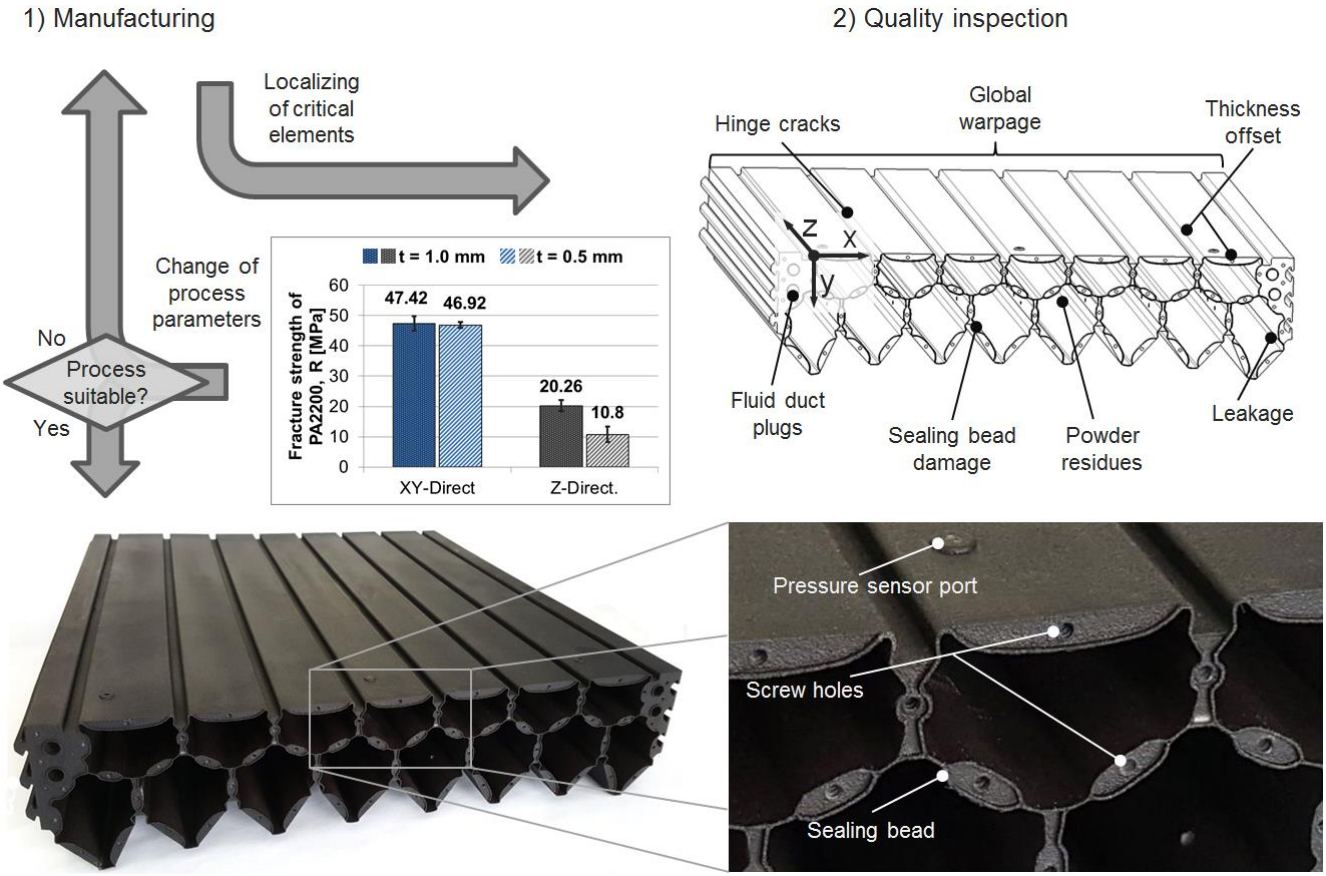

Figure 5-5: Development of the SLS process, including the manufacturing, the inspection of critical structural elements and the resulting PA2200 double row PACS structure

5.1.5 Selective laser sintering

Rapid prototyping processes are primarily conceived for low quantity production. In a SLS process the part is sliced in layers with a thickness of about $0.1\,mm$, which are manufactured sequentially from bottom to top. Thermoplastic powder, the basic material for the SLS, is applied to the build chamber before it is locally melted by a laser beam. With each layer, the part is growing within its supporting bed of powder material. The SLS process provides the possibility to produce complex geometries with undercuts and huge changes of wall thickness and allows for an integral design.
For the application for PACS this means that additional manufacturing steps for the integration of the pressure supply and the internal fluid ducts are redundant. In the following, the limitations of this process and the impact on the structural design are presented before the necessary sub-steps for qualifying the SLS for the specific demands of PACS are described and the resulting target structure is shown.
The material PA2200 is chosen because of its high ratio of the square of the tensile strength over the *Young*'s modulus. Tensile tests according to DIN EN ISO 527-2 with samples of different wall thicknesses, however, showed that the datasheets value regarding fracture strength of $R_{xy} = 48.0\,MPa$ [174] cannot be reached in each manufacturing direction. The merging quality of the thermoplastic material within each layer differs from that between the layers. Inhomogeneous mechanical properties result and depend on the part's orientation within the laser-sintering machine. Additionally, strength reductions are measured for thin-walled samples. The fracture strength of $R_{xy} = 47.42\,MPa$ in the xy-plane and $R_z = 20.26\,MPa$ in z-direction is determined for a flexure hinge thickness of $t = 1.0\,mm$. The strength values for a thickness of $t = 0.5\,mm$ lie below (cf. Figure 5-5). Detailed information about the material test is given in appendix I. The highly stressed flexure hinges, which primarily bear the cell-circumferential loads, are thus oriented to lie in the xy-plane and to avoid strength reductions.

Production trials are first performed at a double-cell structure to save resources. The adaption of the geometry in terms of hinge thickness and sealing bead, the selection of a suitable infiltration material, the SLS process parameters and the mechanical connection concept allowed developing this production process for the utilization for PACS. Hinge cracks, and local thickness offsets make it imperative to increase the minimum hinge and sealing bead thickness to at least $0.65\ mm$ for the SLS process. As a completely gas-tight structure cannot be produced for the thin-walled elements, the structure is infiltrated with *DIAMANT dichtol* in the follow-up process. Further issues like production-induced deformation, due to inappropriate heat treatment, fluid duct plugs, powder residues and sealing bead damage are eradicated in an iterative development of the production process. The cell body for the modular variable-surface PACS specimen, which is produced with the optimized process parameters, is shown in Figure 5-5. Two double-cell structures and four double row PACS are manufactured before the required quality could be reached.

The manufacturing process SLS, represents a valuable solution for realizing prototype structures and is thus used to realize the cell body structure for the PA2200 double row PACS. The main advantages of this production process are the geometrical accuracy, particularly in terms of hinge elements, the avoidance of production-induced deformations, the maximum component dimensions, the simple and effective sealing process, the possibility for integral design due to the manufacturability of undercuts and the benefits concerning single part production. With a tested burst pressure of $0.4\ MPa$ and the maximum pressure for experimental investigations of $0.25\ MPa$, the processible material allows for only moderate loads. For examinations in laboratory environment this is sufficient. With an increasing level of development, the material and thus the production process will necessarily have to change to raise the loadability and stiffness potentials of the PACS.

5.2 Manufacturing processes for cell closure membrane

The DSEC is selected in chapter 4.3 as the most efficient end cap of the herein investigated concepts for closing PACS cells. The herein presented demand analysis, the process valuation and the presentation of investigations on suitable manufacturing processes concentrate on the realization of the DSEC closure membrane. Under consideration of a modular PACS design and the necessity for single-part production the selected process is described in detail.

5.2.1 Demands on production processes

The investigation of the DSEC's properties and of suitable materials (cf. Table 4-2) for realizing this structure is presented in chapter 4.4. The closure membrane shall be built integrally to avoid additional sealing surfaces and mechanical connections. Although undercuts due to folding of the caps cannot be excluded, the demoulding is unproblematic, as the operational strains within the elastomeric cell closure exceed the necessary demoulding strains significantly. Expanding these boundary conditions, the requirements that are listed in Table 5-3 have to be fulfilled by an appropriate production process for the cell closure.

Table 5-3: Requirements on manufacturing process for cell closure structure

Label	Description
$R_{CC}1$	Global geometrical accuracy
$R_{CC}2$	Manufacturing dimensions
$R_{CC}3$	Quality of processible materials
$R_{CC}4$	Pressure tightness of component
$R_{CC}5$	Suitability for single-item production
$R_{CC}6$	Suitability for series production

Demands on geometrical accuracy of the closure and sealing structure (requirement 1 for production process of cell closure: $R_{CC}1$) are essential for the resulting stiffness and strength properties. Production-induced deformations may cause unacceptable shrinkage. Remedy can be provided by considering these deformations in the tooling design.
The manufacturable dimensions ($R_{CC}2$) limit the maximum size of the cell closure. Within the group of elastomers, materials with a high tensile strength are preferable, while the *Young*'s modulus is limited due to conceptual limitations (see chapter 4.4). A process which allows using several and mechanically advantageous materials is privileged ($R_{CC}3$). Depending on the applicable material and manufacturing process, the pressure tightness ($R_{CC}4$) is given either directly and without rework with the primary shaping or in a separate process. The suitability for single-item ($R_{CC}5$) and series production ($R_{CC}6$) completes the demands on the appropriate manufacturing process.

5.2.2 Relevant processes and valuation

The following valuation of manufacturing processes for the cell closure membrane is performed with respect to single-part production for the realization of functional demonstrators. The herein used weighting factors are determined according to Table G-2.
Four manufacturing processes for the cell closure are presented in Table 5-4. On the basis of simulative and experimental investigations, these variants are rated. The necessary information about the FDM process could be gathered during the investigation of suitable production processes for the cell body structure (cf. 5.1).

The most suitable alternative that is identified in in this valuation is the rapid prototyping process SLS. Though it is limited to the processing of particular materials it profits from high manufacturing accuracy and efficient single part production. With the material TPU-92A a thermoplastic elastomer with well suited mechanical characteristics can be processed. The production techniques vacuum casting and injection moulding enable the processing of various material systems. Thermoplastic elastomers have to be heated above their melting temperature. The subsequent cooling in the mould causes thermal shrinkage. With using reaction hardening materials like *Nitrile Butadiene Rubber* (NBR) or *Ethylene Propylene Diene Rubber* (EPDM) this issue may appear in the form of chemical shrinkage. Both processes profit from the capability to produce fluid-tight components and a high geometrical accuracy. Vacuum casting is preferentially used for single-part production, whereas injection moulding allows for quantity manufacturing. FDM as a rapid prototyping method is rejected for the production of cell closures because of the deficient properties of the processible materials and the insufficient gas-tightness of the resulting parts. The rating factors for Table 5-4 reach from 2 (completely fulfilled) to -2 (non-fulfilment).
For the realization of functional demonstrators the SLS process is identified to be the preferential manufacturing process for DSEC cell closure membranes. This process and its development are described in the following. The investigations on the discarded but investigated process variants vacuum casting and injection moulding are summarized in appendix H.

Table 5-4: Valuation of manufacturing processes for cell closure according to the underlying demand analysis and on the basis of weighting factors

	Manufacturing	**Performance w.r.t. requirements**						
No.	**process**	**$R_{CC}1$**	**$R_{CC}2$**	**$R_{CC}3$**	**$R_{CC}4$**	**$R_{CC}5$**	**$R_{CC}6$**	**SUM**
1	SLS	2	1	1	1	2	-1	**1.55**
2	Vacuum casting	1	1	2	2	1	0	**1.31**
3	Injection moulding	2	1	2	2	-1	2	**0.93**
4	FDM	1	1	-1	-2	2	-1	**0.61**
	Weighting factor	0.255	0.070	0.282	0.042	0.334	0.018	

5.2.3 Selective laser sintering

A description of the manufacturing technology SLS for processing thermoplastic materials, which keeps valid for the processing of the elastomer TPU-92A, is given in chapter 5.1.5. For the production of the cell closure membrane, this process is favoured because of its geometrical accuracy and its suitability for single-part production. Figure 5-6 illustrates the approach for the development of the manufacturing process. The investigation of material properties, together with an inspection of the manufacturing quality at a single and a double cell closure specimen allow for the necessary process optimization.
By using the exemplary structure of a single cell closure, the production process could be evaluated with reduced expense. The quality inspection thereby allows examining the manufacturing accuracy. Surface cracks, which cause strength reduction and leakage, occurred together with global shrinkage and porosity. Rough surfaces are subordinate in general, but lead to leakage when located at the sealing area. Due to the short distance between neighbouring folds, the heat dissipation during production is insufficient at specific regions. A merge of opposing cell closure walls results and limits the deformability of the closure unacceptably. Powder residues at mounting and sealing areas can normally be removed easily.
Production-induced deformations could initially not be determined during the manufacturing trials with the single cell closure, but with the complete double row membrane that is depicted in Figure 5-6. The total length of the closure membrane in x-direction exceeded the nominal length by $3.5\,mm$ (+0.9 %) and impeded the assembly with the cell body structure considerably. An extended heat treatment subsequently to the sintering process allowed for avoiding this global geometrical inaccuracy. With a wall thickness of less than $t_{CC} = 2.0\,mm$ the sintered parts are usually not self-sealing and have to be infiltrated for ensuring fluid-tightness.

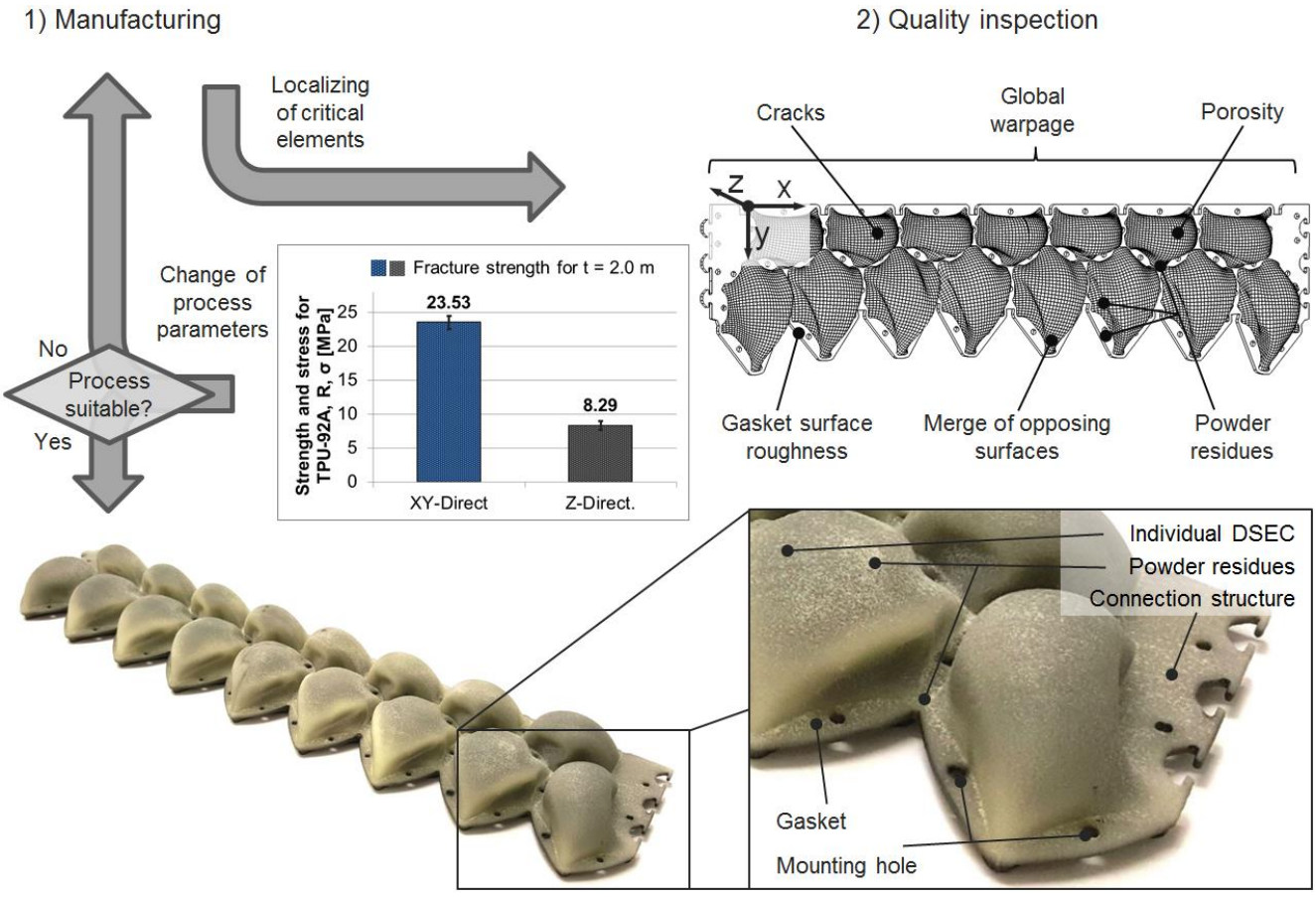

Figure 5-6: Development of the SLS process, including the manufacturing and the inspected critical structural elements; resulting TPU-92A cell closure membrane

Plasti Dip liquid rubber provides sufficient results and is compatible with the closure material. The orientation of the gasket area in parallel with the xy-plane of the sintering machine avoids surface roughness at this critical region. The highly orthotropic material properties are examined together with the nonlinear stress-strain behaviour in order to evaluate the mechanical quality of the resulting parts. The datasheet value for the material strength in z-direction of $R_{TPU-92A,z} = 15.0\,MPa$ could not be reached with the examined test specimens in contrast to the value in xy-direction of $R_{TPU-92A,xy} = 20.0\,MPa$, which is surpassed in the test (cf. Figure 5-6). The detailed information about the test setup, execution and analysis is presented in appendix I. The closure membrane is sealed fluid-tight in a follow-up process and assembled with the cell body structure as described in the following.

5.3 Assembly of PACS specimens

The manufacturing processes for the cell body structure and the closure membrane are discussed and the resulting components are available. In the following, a description of the assembly process shall provide information about the mechanical connection between both subsystems and the fluid tight sealing. The expense with the different assembly concepts is discussed and the improvement process is illustrated. A summary of the most important and fully assembled realizations of PACS completes this chapter and points out the related purposes and their significant properties in concentrated manner, before their use for the conceptual evaluation is described in chapter 6.

The first realization of a PACS demonstrator is assembled from the GFRP single row cell body and the non-reinforced tube solution, which is shown in Figure 4-4 (1a). The design process, the manufacturing and the experimental investigations are published in [162]. The cell body structure is designed manually and does not consider the local load flow for the creation of the hinge and the cell side geometry. The tube solution forms a closed system, is not in need of gas-tight cell walls and bears cell-axial forces by a separate thread rod. For the assembly of the cell body structure and the pressurization system with external fluid port, the tubes are simply slid into the cells. An axial fastening of the tubes within the cells is not necessary for laboratory tests, as residual axial forces are not present and the inflated bladder provides a certain clamping capacity. The separated construction of cell structure and pressurization system allows for a quick and uncomplicated assembly at the expense of limited pressures and a redundant cell-axial structure. Table 5-5 depicts the completely assembled single row PACS cantilever.

The cell body of the second PACS specimen is built from the PA12 slices that are produced in a water cutting process. Its cross-sectional geometry is also designed without consideration of the local load distribution. For sealing the non-gas-tight cell body structure and its connection to the DSEC closure membrane, *Plasti Dip* liquid rubber is used to coat the remaining openings. This process, which is performed after the assembly of the cell body slices and the closure membrane, is difficult, expensive, and above all leads to non-reproducible results. The double row cantilever is thus only used for conceptual proof and not for the evaluation of the design methods for PACS. The DSEC closure membrane is clamped to the cell body by thread rods. The advantages of material and weight reduction due to the substitution of a continuous tube by the local application of a closure membrane are accompanied by increased assembly efforts. Sixty-one thread rods are necessary to distribute the cell axial pressure loads and clamping forces and to reduce load-induced gaps. With this structure a multi-row PACS, which allows demonstrating the antagonistic principle of deformation and stiffening, is realized for the first time.

The modular variable-surface demonstrator is designed according to the herein presented generic design process. The load-based geometry computation for cell sides and hinges not only provides the possibility to reduce weight, but also allows for stress reduction at hinge elements. The use of the less appropriate material PA2200 for the cell body is thus enabled. An infiltration of this component is sufficient for achieving gas-tightness. As shown in Figure 4-23, the DSEC_OV closure membrane is designed self-centring and clamped to the cell body by the mounting frame.

Table 5-5: Most important realizations of PACS specimens and substantial properties

Image:	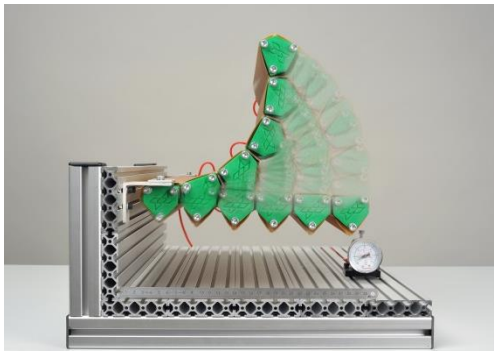	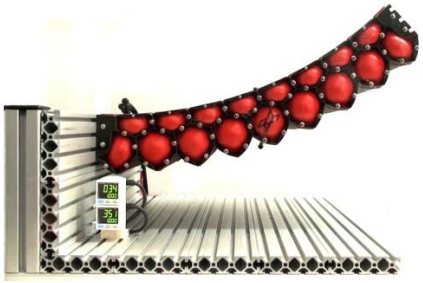	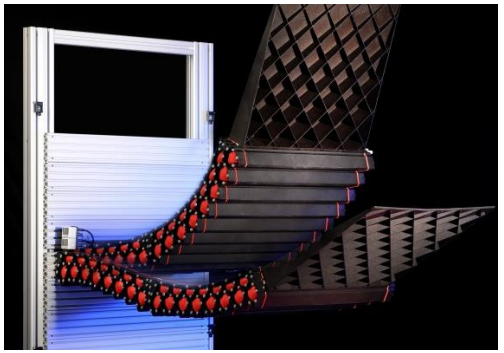
Designation:	Single row cantilever (HexPly913)	Double row cantilever (PA12)	Variable-surface demonstrator (PA2200)
Dimensions (w*h*d):	300 x 50 x 450 mm³	450 x 85 x 300 mm³	1200 x 100 x 500 mm³
Max. operat. pressure:	0.2 MPa	0.35 MPa	0.25 MPa
Cell body:	GFRP HexPly913, prepreg process Manual cross-sectional design Gas-tight	PA12 sheet material, water cutting Manual cross-sectional design Assembly of slices, expensive sealing	PA2200, SLS process Automated load-based design Infiltrated gas-tight
Cell closure:	Tube solution Latex tube and rigid clamping Additional load paths for axial forces	DSEC membrane TPU-92A, SLS process Thread rods bear axial forces	DSEC membrane (DSEC_OV) TPU-92A, SLS process Cell body bears axial forces
Assembly and sealing:	No mechanical linkage No common sealing surfaces External fluid flow	Mechanical link by thread rods Gasket seal and *Plasti Dip* liq. rubber Cell-body-internal fluid flow	Mechanical linkage by screws Gasket seal and sealing bead Cell-body-internal fluid flow
Preliminary investig.:	Single cell PACS, double cell PACS	Single cell PACS	Double cell PACS, PACS module
Main objectives:	Proof of concept Pressure-dependent deformation	Test of double-row modular PACS Investig. of DSEC closure membrane	Proof of generic design process Pressure-dependent stiffness

The elastic material for the closure membrane allows for its use as sealing gasket. Compared to the assembly and sealing process for the PA12 double row cantilever, the efforts are substantially reduced. With screwing the mounting frame, the closure membrane and the cell body together, a pressure tight PACS without redundant load carrying structures or sealing surfaces results. Taking advantage from the benefits of the SLS process, the fluid flow is designed to be manufactured integrally. The pressure ports for both cell rows are positioned at the connection structure, what prevents the pressure lines from abrasion and folding under operating conditions and provides good accessibility. One pressure port per cell row is sufficient and reduces interfaces to the shape-variable structure. The fluid transfer between the cells of one cell row is realized by holes in their common cell sides. For a modular PACS a second pressure port is required at the end of each cell row to transfer the fluid to the next PACS segment. All pressure ports are accessible at the mounting frame. The same sealing concept as for the cell closure is applied to ensure tightness between the mounting frame and the cell body. The single PACS modules are connected with their tongue and groove profiles by simply sliding it into one another. A rigid blade segment is mounted accordingly and completes the modular variable-surface demonstrator.

Table 5-5 shows the three demonstrators, summarizes their main properties and gives the decisive reasons for their realization. Additionally to the depicted demonstrators, preliminary specimens are manufactured, which base on the same production process and enable investigating subordinate technical issues. The following evaluation of the generic design process bases on the experimental investigation of PACS and thus the herein presented structural realizations.

6 Evaluation and progressive improvement of design methods

The generic design process for PACS includes the main subsections computation of truss geometry, cross-sectional design, sealing and pressurization and manufacturing and assembly techniques for realization. Starting with initially simplified computational approaches and design solutions that base on reduced requirements, the presented methods for conceiving each subsystem of PACS, are developed iteratively on the basis of the outcomes of simulative and experimental investigations. The performed numerical and physical experiments, its objectives, the utilised specimens, the test equipment and setup are presented in the following. The outcomes of these investigations build the basis for the specification of advanced requirements and assumptions and thus the progress of the design methods. The resulting iterative strategy for the development of design methods aims at the reduction of efforts by an identification of the necessary system complexity at an early stage of the design process (cf. chapter 1.4). For each of the main subsections of the design process, the deduced enhancements are subsequently described together with the underlying test results.
The repetitive validation process for the modelling and computation of the truss model, for the cross-sectional design, the proposed cell closure concept and the realization, are visualized in Figure 6-1. The performed experimental and simulative investigations, the related subjects and the type of examination are listed in Figure 6-1, left, and provide the basis for the verification and validation of the underlying design methods (cf. chapter 6.1). The related evaluation steps and the resulting effects on each major sub-process for the design of PACS are presented in Figure 6-1, right (cf. chapter 6.2).

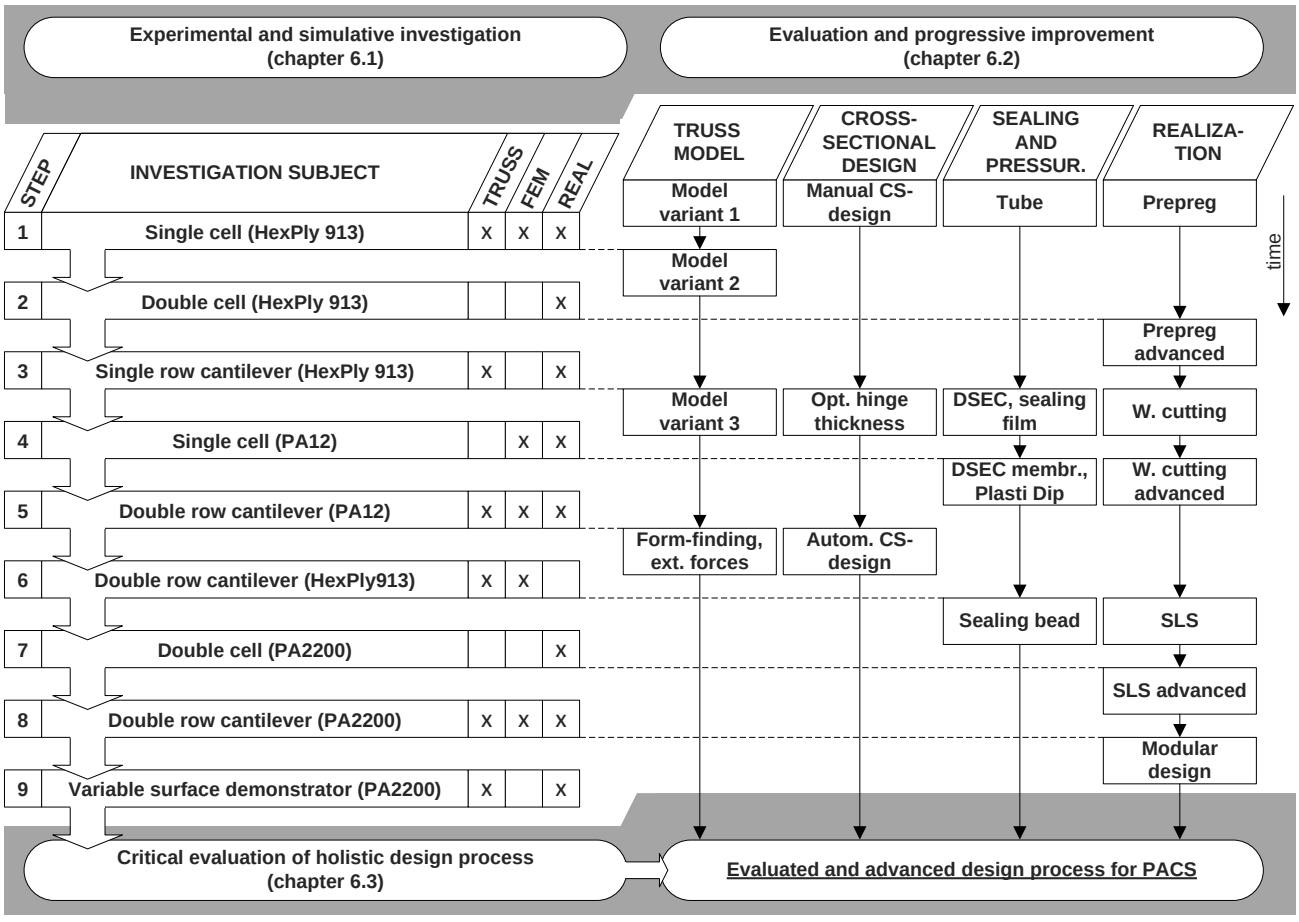

Figure 6-1: Evaluation subjects and effects on the progressive improvement procedure for the design process of PACS

A substantial aim of this chapter is to expand the information about the pure design process by giving reasons for the necessity of the underlying improvement steps and by declaring design sensitivities and factors of influence. A comparison of the results from the first and the final evaluation steps allows for concluding the procedure's effectivity and efficiency, before open issues with the most highly developed design process are discussed (cf. chapter 6.3).

6.1 Experimental and simulative investigation

The evaluation steps, which are shown in the left column of Figure 6-1 are presented in the following. The objectives of the experimental or simulative investigation, its implementation and the obtained outcomes are described. The essential information for the evaluation and improvement of the sub-processes for the design of PACS is thereby provided. The discussion of results is presented subsequently in chapter 6.2.

6.1.1 Single cell - HexPly913

The first demonstrator, the GFRP single cell, is realized to investigate the kinematical and mechanical behaviour of the PACS during pressurization. For the validation of the truss model, the pressure dependent deformation and the related material strains are measured. As illustrated in Figure 6-1, the adequacy of modelling variant 1 and variant 2, regarding the computation of deformations and stresses, is thus investigated to assess its applicability for the design process.
The implementation of an FEM-model of the examined structure allows for the additional analysis of simulated deformations and stresses on the basis of a model of higher order and with reduced assumptions (cf. chapter 2.1.2). For the objective of analysing the accuracy potentials of a more detailed modelling variant, the FEM-based approach provides the required comparative data.

Using *MSC Patran* for pre- and post-processing and *MSC Nastran* for the task of solving the FEM model, numerical simulations are performed. The geometry information for the single cell and the respective laminate setup are illustrated in Figure 5-1. The numerical calculation is significant for the validation process. It yields the detailed geometrical information, and thus the stiffness properties, of the structural elements hinge and cell side. The experimental results whereas may be influenced by manufacturing tolerances and unevenly distributed pressures. Within the structural model variants 1-4, hinge lines are considered as discrete one-dimensional elements. For the numerical evaluation a FEM-based structural model is built which considers the spatially distributed geometry of the compliant hinge. Two-dimensional shell elements are used therefore. They provide the necessary accuracy for the thin-walled structure and save computation efforts compared to three-dimensional elements. The assumptions of constant hinge stiffness and infinite cell side stiffness are thereby dropped. Both, the effective hinge position due to this geometry and the deformation of the hinge und face elements during pressurization are thus included. The element edge length of $0.7\ mm$ causes a number of 5.3e3 elements for the single cell and is carefully chosen after investigating the total deformation over element size. A doubling of element quantity leads to a tolerable deviation of the maximum stress of 1.7 %. The solver is selected to consider geometrical nonlinear deformations (SOL400).
Figure 6-2 shows the undeformed and deformed mesh of the FEM model as well as the related stress distribution at the comparative pressure of $0.35\ MPa$. The results are shown for the outmost ply in circumferential direction. The structural stresses and the overall deformation at the individual FRP laminae are examined.
The numerical investigations are accompanied by experimental tests. The implementation of a suitable manufacturing process for the GFRP single cell of $450\ mm$ depth and $\Delta u_{H,1,1,2} = 15°$ of asymptotic cell side rotation at hinge $j = 2$ (cf. Figure 6-4) provides the first realization of a PACS. The non-reinforced tube solution that is shown in Figure 4-4, (1a), is used for pressurization. The single cell, as the basic element of each PACS, is examined for its characteristics in terms of the pressure-dependent deformations and structural strains.

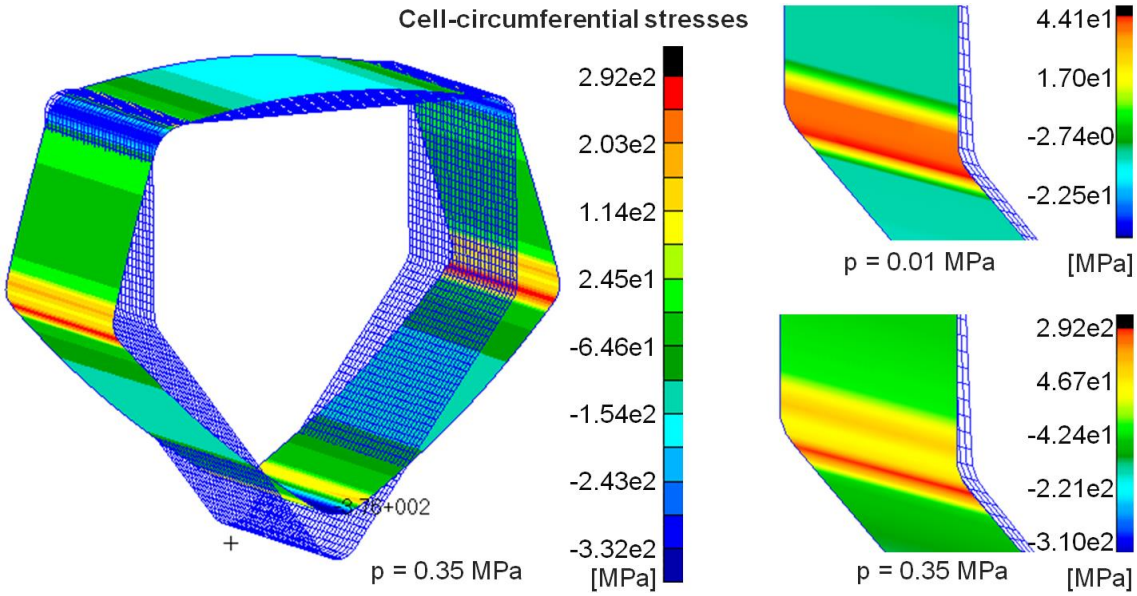

Figure 6-2: Maximum stresses in circumferential direction at the outer ply for different pressures from FEM simulation for the GFRP single cell

The regulator for controlling the air pressure within the PACS cell is a *SMC ITV0031-2BL-Q*. The barometer *B&B Thermotechnik DRTR-AL-10V-R10B* with analogue voltage output and the laser-supported distance meter *RF603* from *RIFTEK* provide the necessary data for capturing the cells pressure-dependent deformation characteristic. The structural strains are measured by twelve *1-LY11-0.6/120* strain gauges with a length of $0.6\,mm$ from *HBM*, which are connected in three-wire circuits and applied to the cell structure at the hinges $j = 2{,}4{,}6$ and at the cell side $j = 1$.

Figure 6-3 shows the test setup with the applied strain gauges, the distance meter, the pressure gauge and the GFRP specimen, which is clamped in its test bench. The analogue data from pressure and strain gauges as well as the digital input from the distance meter are received by the measurement system *CompactRIO* from *National Instruments*. The data is processed via *LabVIEW*.

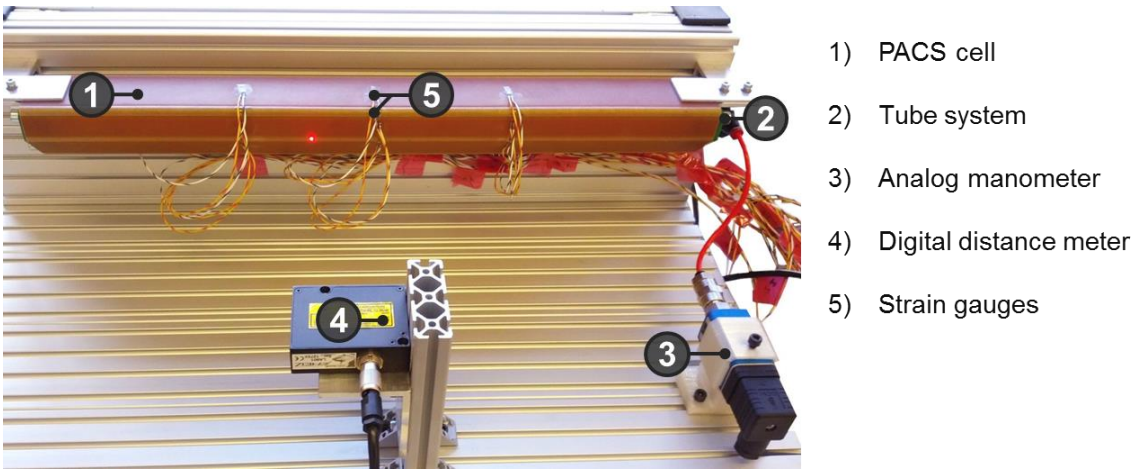

Figure 6-3: Single cell test specimen within test bench

The first parameter of interest for the comparison of the computational results and the experimental outcomes is the cell side rotation $\Delta u_{H,1,1,2}$. This parameter is chosen for the evaluation, because, compared to the absolute position of for example the cell's hinges, it does not depend on the scale of the structure. The course of the deformation over the applied pressure is plotted in Figure 6-4.
The illustrated data shows a deviation between the numerically computed values from the structural model variants 1 and 2 and the FEM-based results.

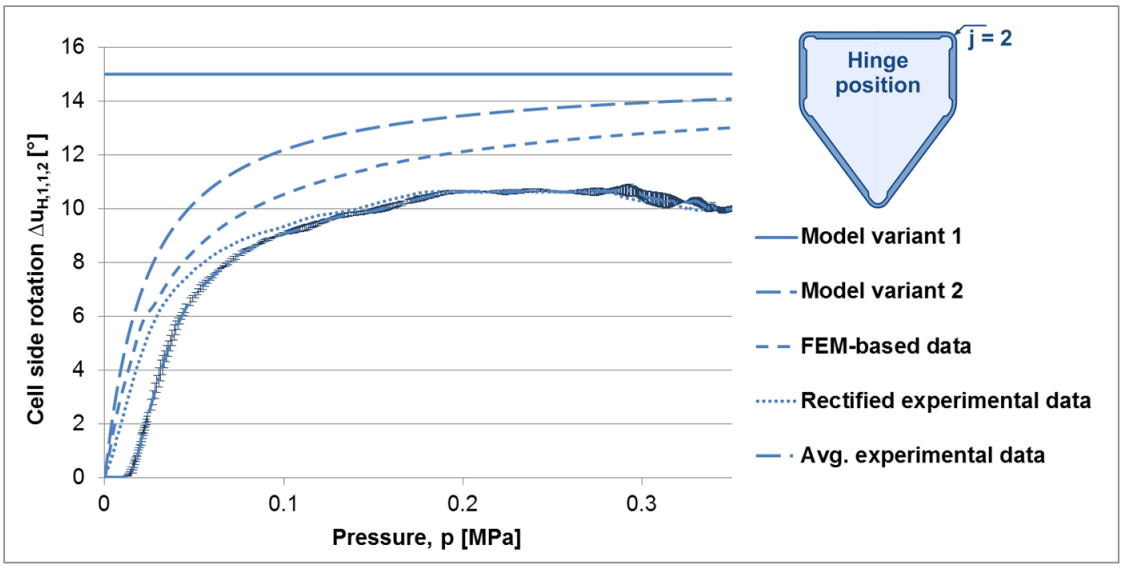

Figure 6-4: Comparison of analytical, numerical and experimental results for the cell side rotation $\Delta u_{H,1,1,2}$

The approach of model variant 1 cannot describe the pressure-dependent deformation of the, apart from that, unloaded single cell as an infinite amount of pressure is sufficient to cause the asymptotic deformation. The results from model variant 2 yield a significant improvement as confirmed by the comparison with the FEM-based outcomes. The data from the experimental investigations is rectified to consider the amount of pressure that is needed to inflate the elastomeric tube until it contacts the cell wall. The standard deviation is shown for the experimental raw data. The underlying data is measured for three different pressure tubes and one and the same PACS cell. Except for the values from modelling variant 1 and the final descend of the experiment-based graph, the basic courses of the curves coincide.

A maximum variance of $\eta_{u,exp.,FEM,2} = \Delta u_{H,1,1,2,exp}/\Delta u_{H,1,1,2,FEM} - 1 = -22.40\,\%$ of the experimental data over the FEM-based values occurs for $p = 0.35\,MPa$. The deviation between model variant 1 and the FEM-based value is $\eta_{u,Var1,FEM,2} = +15.32\,\%$. For model variant 2 a value of $\eta_{u,Var2,FEM,2} = +8.23\,\%$ results for the maximum pressure at hinge $j = 2$. The evaluation of these results is given in chapter 6.2. It gives reason for the development of the structural model for computing the truss geometry for PACS (see chapter 6.2.1).

The evaluation of the numerically calculated cell wall and hinge stresses allows assessing the significance of the computational results. The suitability of the current PACS design can further be investigated for its capabilities to avoid stress peaks. Figure 6-5 shows the maximum stress values in cell-circumferential direction at the outer surface of the cell. The results from the truss model and the FEM computations are plotted together with the strain gauge data. The strain gauges are applied at the mid of the outer surface of each flexure hinge. The resulting stresses are computed with knowledge of the *Young*'s modulus of HexPly913 according to *Hooke*'s law for uniaxial stresses. Analogous to Figure 6-4 the average experimental raw data is posted together with its standard deviation for hinge $j = 2$. Deviations between experimental and FEM-based data for increasing cell pressures exceed $\eta_{\sigma,exp,FEM,2} = \sigma_{H,1,1,2,exp}/\sigma_{H,1,1,2,FEM} - 1 > 20\,\%$ for all of the considered hinges. Regarding Figure 6-2 it can be seen that the experimental results are very sensitive to the positioning of the strain gauges. Manufacturing inaccuracies concerning the hinge thickness provide a further reliable declaration. The decreased stresses and increased deformation of the experimental structure are due to a reduced wall thickness at the hinge elements. An average value of $t = 0.22\,mm$ instead of the design thickness of $t = 0.25\,mm$ is measured at the real test specimen. The variance of face thicknesses is also measured and lies below $-3.2\,\%$ compared to the target value.

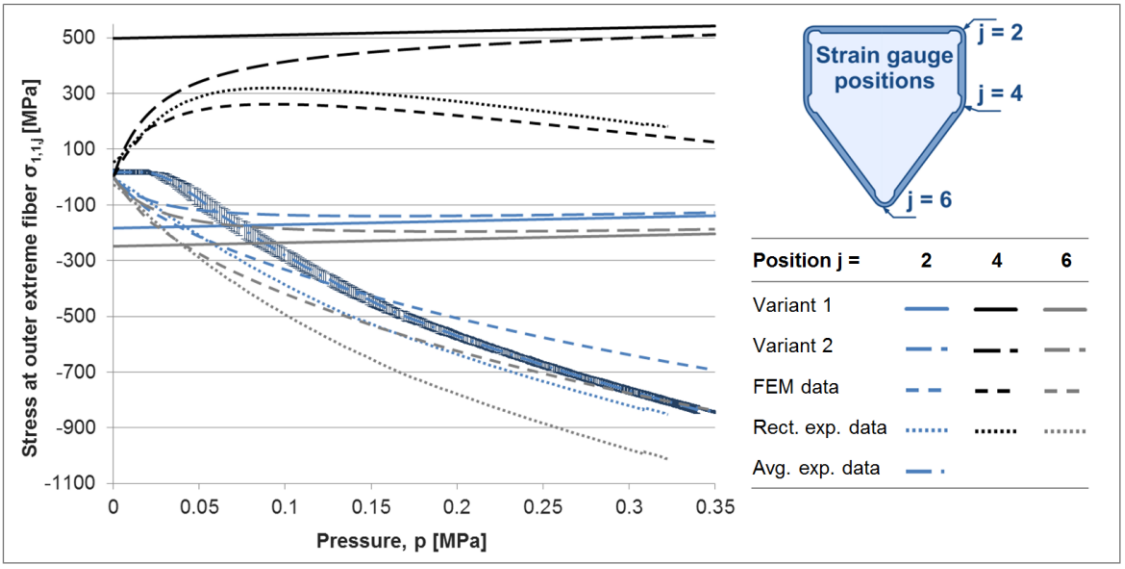

Figure 6-5: Max stress values $\sigma_{1,1,j}$ over pressure p from structural model variant 1 and 2, FEM model and experimental investigations at the outer surface of the flexure hinges j=2,4,6

An adaption of the AVW and FEM-based models according to the real thicknesses is not provided, because the deficiencies of the present design process, which starts with the geometry definition on the basis of the truss model, shall be analysed and illustrated.
Model variant 1 does not allow for the consideration of the bending stiffness. Thus, the bending-induced stresses for the asymptotic deformation can already be found for an infinitesimal amount of pressure. Although the stiffness of the flexure hinges is included in model variant 2, a maximum deviation of $\eta_{\sigma,Var2,FEM,2} = -81.60\,\%$ results at hinge $j = 2$ and $p = 0.35\,MPa$. All of the examined hinges show an equally high variation. The assumptions that underlie the truss model provide reasons for this mismatch of results. The discussion of these deviations is presented in the chapters 6.2.1 and 6.2.2.

6.1.2 Double cell - HexPly913

The objective behind the multiple realizations of the two-cell GFRP structure is the advancement of the manufacturing process. Numerical computations or experimental investigations are not performed.
As discussed in chapter 5.1.3, wrinkles at the hinge elements occur due to the compaction of the layup in the autoclave. Figure 5-3 illustrates this problem with showing some of the production trials. The modification of the recommended pressure and temperature in the curing process allows taking advantage from the expanding silicone core. A stretching of the cell-circumferential fibres can thus be reached and wrinkles are avoided. The arrangement of peel ply, bleeder, release film and breather in the vacuum bag layup is decisive for the resulting fibre volume fraction and the avoidance of laminate imperfections. The stacking of cell side plies reduces production efforts and causes an increase of accuracy. The strategy for the connection of multiple cells has significant influence on the mechanical and kinematical quality of the resulting structure. The selected geometries for the crossovers of hinges have to fulfil the kinematical requirements from the PACS design and additionally must withstand the pressure and temperature conditions in the autoclave process. The resulting structural design and process settings are presented in chapter 5.1.3. The enhancement of the prepreg process only enables the realization of the GFRP single row cantilever.

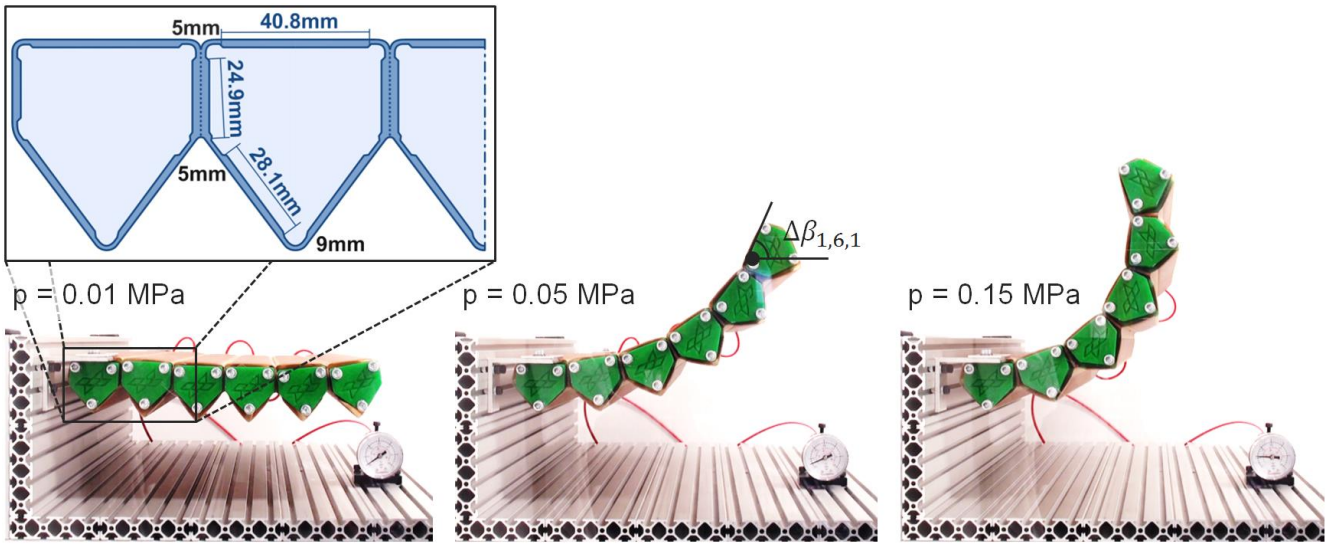

Figure 6-6: Cross-sectional design of the six-cell single row cantilever specimen and experimental investigation of pressure-dependent deformation

6.1.3 Single-row cantilever - HexPly913

Subsequently to the single and double-cell PACS, the six-cell single row GFRP structure is realized and investigated experimentally and on the basis of numerical computations. Besides the demonstration of the functional principle and the deformation potentials of PACS, the enhancement of the design process is an essential aim. The suitability of truss model variant 2 is investigated and compared with FEM-based and experimental results. The cross-sectional design is assessed together with the prepreg manufacturing process. An evaluation of the tube-based pressurization system for its suitability for further application is performed on the basis of this experimental test.

The FEM model for the computation of the pressure-dependent deformations and stresses is implemented equally as for the single cell (cf. Figure 6-2). With the element edge length of 0.7 mm, the number of shell elements for the cantilever sums up to 19.6e3. Further boundary conditions for the experimental test and the simulation can be obtained from chapter 6.1.1.
As a result from the investigations with the double-cell specimens, the design of adjacent cells has to be adapted to enable the realization of flexure hinges at crossovers. The consequent eccentric arrangement of these hinges and the varied cross-sectional design is illustrated in Figure 6-6 together with the test bench and three different states of shape of the PACS for increasing pressures. The laminate layup is equal to that of the single-cell GFRP specimen. As the mechanical strains could be measured already with the single cell, this demonstrator is used to validate the deformation behaviour of the cell compound. These experimental investigations summarize the results of the design process, the numerical computation, the manufacturing and the pressurization concept at an early stage of research on PACS. The rotational deformation of the first cell side of the sixth cell $\Delta\beta_{1,6,1}$ is measured for the evaluation, as it cumulates the distortions of all of the upstream cells and does not depend on the size of the structure.
The advantage of model variant 2 compared to model variant 1 is shown by the comparison of truss model and FEM-based results. Table 6-1 therefor summarizes the deformational results for the maximum test pressure of $p = 0.2\,MPa$. Note that inertial forces are not considered in any of the structural models. The comparison of FEM-based and experimental results leads to a deviation of $\eta_{\Delta\beta,exp,FEM} = (\Delta\beta_{1,6,1,exp}/\Delta\beta_{1,6,1,FEM}) - 1 = +13.22\,\%$. The increased deformation of the test specimen can again be explained by influences from the pressurization system and particularly by manufacturing inaccuracy, which leads to decreased hinge thickness and causes a reduction of bending stiffness. For the surface-related cell side of the sixth cell a rotational deformation of $\Delta\beta_{1,6,1} = 123°$ is

measured. With a deviation of $\eta_{\Delta\beta,Var1,FEM} = +38.07\ \%$ for variant 1 and $\eta_{\Delta\beta,Var2,FEM} = +23.84\ \%$ for variant 2, the model enhancement is significant.
It can be seen that the effects of different model assumptions on the equilibrium state of shape depend on the phase of pressurization (cf. Figure 2-17). For $p = 0.2\ MPa$ the deformation phase is not yet left and influence of inaccurate structural energy potentials are still in the same order of magnitude as the pressure dependent energy potentials. Compared to the results that are shown in Figure 6-4 increased deviations are thus reasonable.

Table 6-1: Comparison of deformation results for the single row GFRP cantilever at cell side one of sixth cell for p = 0.2 MPa

Source:	Var. 1	Var. 2	FEM	Exp.
$\Delta\beta_{1,6,1}$ [°]	150.0	134.54	108.64	123
$\eta_{\Delta\beta,exp}$ [%]	21.95	9.38	11.67	-

6.1.4 Single cell - PA12

Due to the residual geometrical inaccuracy and the huge manufacturing efforts with the GFRP specimens, a change of the production concept shall provide a remedy. Production trials for single slices with the cross-sectional shape of the cell body structure (cf. chapter 5.1.4), allow for the improvement of the manufacturing process. In parallel, the disadvantage of losing the sealing capabilities of the compliant hinges is addressed by investigating suitable solutions for this issue at a single PACS cell. The third objective with these specimens is the experimental evaluation of the FEM-based characterization of the DSEC cell closure concept.

Production trials provide a pragmatic way to ensure reaching a sufficient geometrical accuracy in the water cutting process, as shown in chapter 5.1.4. After reducing the thickness deviations $\eta_{\emptyset,thk}$ to less than $10\ \%$ at the critical hinge regions, the issue of sealing the jointed PA12 slices is examined. *DIAMANT dichtol* as well as *SICOMIN SR1710* epoxy resin turned out to be too brittle for sealing the flexure hinges. With the advantages of a constant thickness of $0.1\ mm$, adequate strength and elasticity, the adhesive polyvinylchloride (PVC) film *ORAJET 3105HT* is finally chosen for the gas-tight sealing of the PA12 single cell.
The experimental verification of the DSEC concept is performed in three steps. The investigation of the process-dependent material properties is investigated by experiment. The strength and stiffness values in horizontal and vertical direction for the hyper-elastic SLS-capable material TPU-92A are measured. The related test setup, the used equipment and the outcomes are described in appendix I. With knowledge of the necessary material properties, the FEM-based characterization of the cell closure is performed (see chapter 4.4). The outcomes of the underlying numerical computations confirm the concept selection and validate the DSEC as the most efficient shape-variable cell closure. Analogous to the simulation that is illustrated in Figure 4-19, an experimental test of the DSEC, the isotensoid and the flat plate concepts is performed. The according results are presented in the following.
These experiments have three objectives: the evaluation of the manufacturing and assembly concept, the proof of gas tightness and the measurement of the deformation characteristic of the cell-body cell-closure compound and thus the experimental validation of the underlying simulative investigations. Figure 6-7 depicts the experimental setup together with the examined specimens. In contrary to the test setup for investigating the single GFRP cell (see chapter 6.1.1), two *Althen AIT710-0101-60* inclinometers are used to log the angular deviation of the cell sides for varying pressures. Depending on the stiffness of the cell closure, the finite rigidity of the cell sides allows a deformation gradient along the cell-axial direction. For measuring this effect, the inclinometers are located at two positions, which are marked with (A) and (B), for cell edge and centre location.

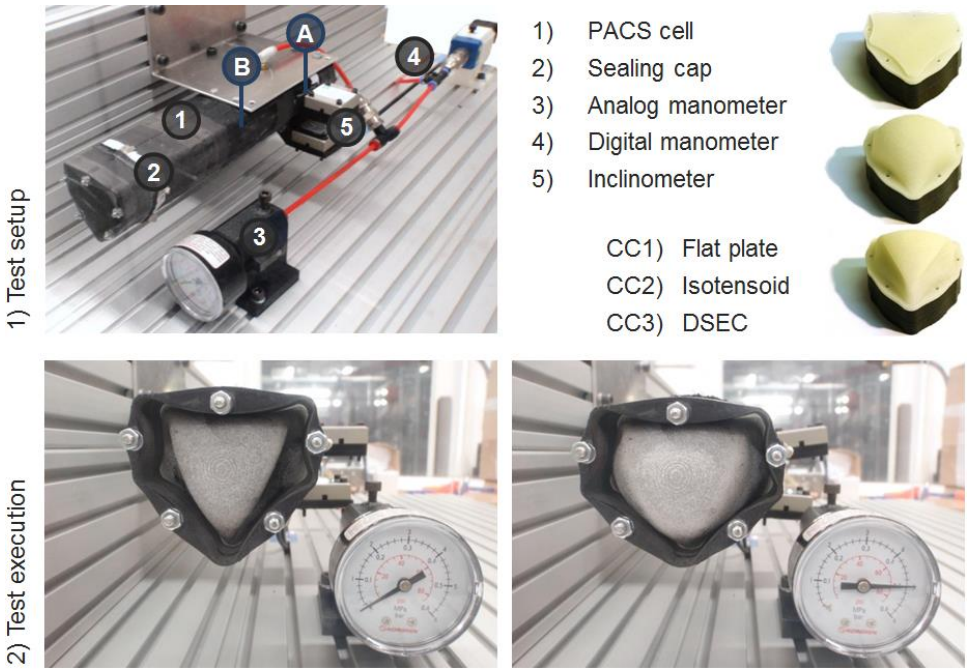

Figure 6-7: Experimental test setup for characterization of sealing concepts flat plate, isotensoid DSEC and DSEC_OV (1) and undeformed and deformed shape (2) of the DSEC_OV for p = 0 MPa and p = 0.5 MPa

The assembly and clamping concept is illustrated in Figure 4-23. It provides a dismountable, robust and pressure-tight structural connection. The flat plate cell closure is manufactured with a wall thickness of $t_{CC,fp} = 5.0\,mm$ and the isotensoid, DSEC and overdriven DSEC solution with a thickness of $t_{CC,isot} = t_{CC,DSEC} = t_{CC,DSEC\_OV} = 2.0\,mm$, to withstand the applied pressure without exceeding the approximated linear-elastic region of the material of $\sigma_{le,max} = 4.76\,MPa$. The deformation of the overdriven variant of the DSEC is shown in Figure 6-7. The related simulation that shows the transition of shape from the undeformed, folded state *st0* at $p_{st0} = 0\,MPa$ to the deformed state *st1* at $p_{st1} = 0.5\,MPa$ and the according stress distribution are illustrated in Figure 4-21.
The target pressure of $0.5\,MPa$ is reached for the isotensoid, the DSEC and the DSEC_OV closure variants. The manufacturing and assembly concept as well as the tightness of the proposed gasket sealing are thus verified for these concepts. Due to the huge in-plane stiffness of the flat plate closure, the gasket sealing can neither transfer the related forces nor compensate the differences in radial deformation between cell and seal. The maximum pressure for the experimental characterization is thus limited by leakage to $p_{fp,max} = 0.366\,MPa$ for this setup.

The outcomes of measuring the pressure-dependent deformation are given in Figure 6-8. The reason for these investigations is the comparison of the numerically calculated values for the undisturbed single cell and the DSEC_OV with the experimental results for the different cell closure variants. Thus, the pressure dependent deformation of cell and cell closure can be compared and the results from the FEM-based computation can be validated. Therefore, the simulation-based results are given for the DSEC_OV and the underlying PACS cell. The related outcomes of the experimental investigations of DSEC_OV, DSEC, isotensoid and flat plate at the edge and the centre position (see Figure 6-7, A and B) of the cell further allow for the evaluation of the closures' influence on the cell's deformations behaviour. By comparing the pressure-dependent deformation of the PACS cell with that of the closure concepts, the performance of the end caps can be evaluated.
The overdriven DSEC solution provides the highest pressure-dependent deformation potential compared to the other concepts. It is followed by the DSEC, the isotensoid and, far behind, the flat plate. The different deformation behaviour of isotensoid and flat plate closure compared to that of the underlying cell affects the performance and accuracy of the PACS's deformation.

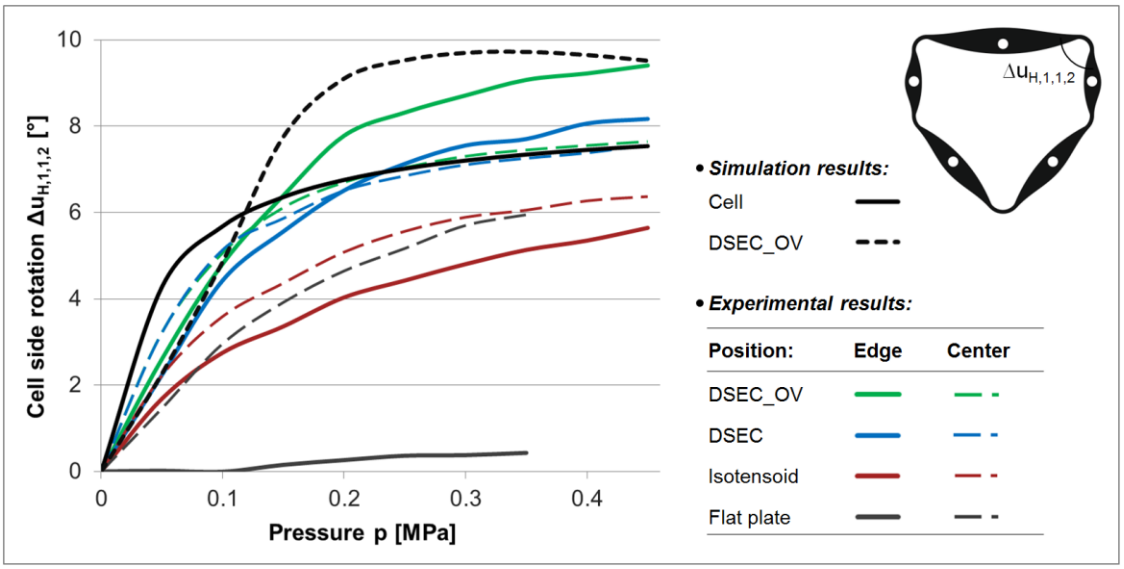

Figure 6-8: Experimentally measured cell side rotation $\Delta u_{H,1,1,2}$ over cell pressure p for two different measurement positions and reference data from FEM simulation

The measurement results for the centre and edge position of the cell confirm the negative influence of these cell closures on the global deformation behaviour. In contrary, the similarity of the deformation courses of PACS cell and both DSEC variants validate the capability of the DSEC to utilize the cell-inherent pressure to yield equal deformation behaviour on the basis of a double-curved membrane. The comparison of the different sealing concepts verifies the selection of the DSEC concept, which initially only based on the evaluation of FEM-based examinations (cf. chapter 4.3).

6.1.5 Double row-cantilever - PA12

The experimental evaluation of the water cutting process for the production of the cell body structure and the characterization and test of an efficient cell closure concept for the single PACS cell are performed. The first realization of a double row PACS is thereby prepared. After the implementation of the single row GFRP cantilever, it constitutes an important step towards the global system awareness that is needed for the holistic design process. Model variant 3, which takes the eccentric hinges at crossovers into account, is used for the computation of this structure's deformation. The geometry of the cell body is designed with having regard to the analytical formula for the optimal hinge thickness. FEM-based computations are performed to assess the quality of the improved design methods. The local load paths, as presented in chapter 3, are not considered for the cross-sectional design.

The DSEC membrane, a one-piece component for sealing the complete PACS, is tested at the PA12 double row structure. The integration of fluid ducts allows for a reduction of pressure ports to one port per cell row. The experimental investigation of the PA12 PACS structure is performed to evaluate the sealing and fluid flow concept.

On the basis of the experimental results from the single row cantilever, the numerical model for the computation of PACS is expanded for the consideration of eccentric hinges. Model variant 3 is investigated for its performance regarding the computation of deformations by a comparison with FEM-based results at the exemplary structure of the double row PA12 cantilever. The outcomes are already given in Table 2-5 and visualized in Figure 2-8. As this investigation is essential for the selection of the modelling technique it is presented in chapter 2, but is reused for the herein described evaluation of the design methods. A reduction of deviations from $\eta_{Var2,FEM,I} = \Delta\beta_{Var2,I}/\Delta\beta_{FEM,I} - 1 = +16.63\,\%$ for model variant 2 to $\eta_{Var3,FEM,I} = +9.47\,\%$ for variant 3 is calculated for the stiffening phase of the PACS. Also for the deformation phase an increase of accuracy is analysed. The deviation thereby decreases from $\eta_{Var2,FEM,II} = -15.88\,\%$ to $\eta_{Var3,FEM,II} = +0.59\,\%$.

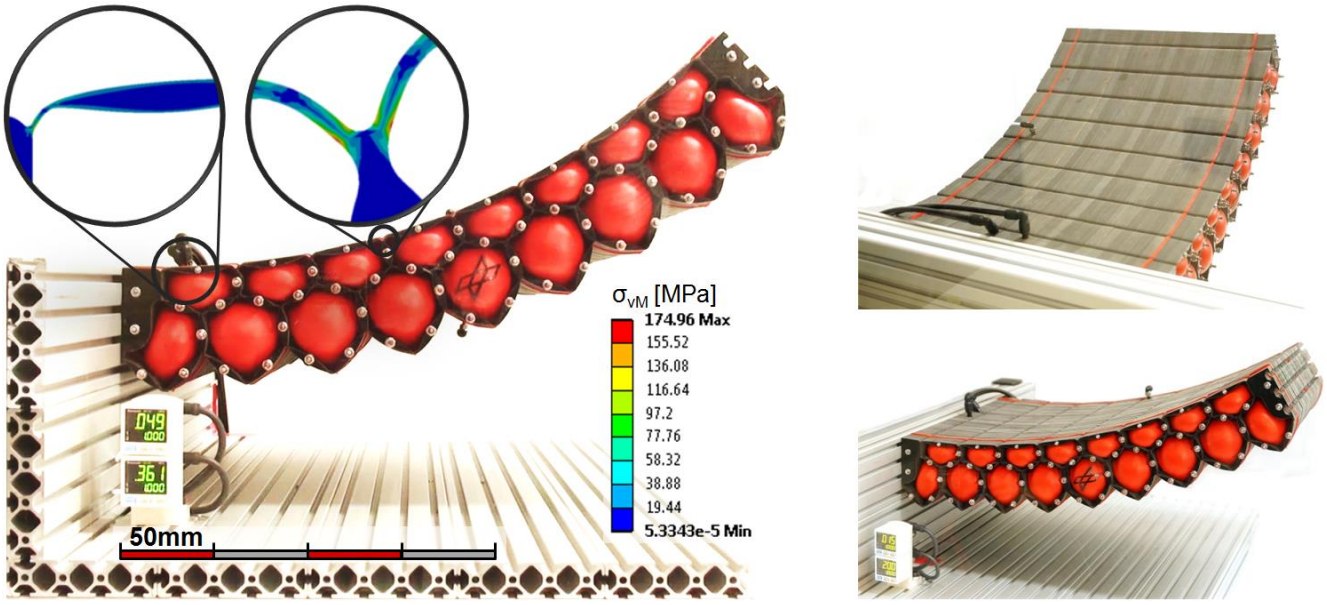

Figure 6-9: Experimental setup for investigating the double row PACS cantilever specimen with the dimensions 450 x 85 x 300 mm³ (w*h*d) and FEM-based stress distribution

As the cross-sectional design of the structure is generated without consideration of the local load flow and deformations, stress peaks at hinges are expected. The computation of the optimal hinge thickness according to equation (2.38) however reduces the averaged stresses within the hinge elements. The outcomes of the FEM-model are used to assess the stress distribution and to discuss the necessity of a load-based two-dimensional design. Figure 6-9 illustrates the structural stresses at a cell side and a hinge crossover for $p_{int,1} = 0.5\,MPa$ and $p_{int,2} = 0.25\,MPa$. The local increase of stresses within a hinge element is evaluated to more than 300 % and confirms the results from examining the single row GFRP structure. The design of cell sides is less critical, as the required bending stiffness leads to a significantly increased thickness and thus an extensive safety factor regarding stresses.

The validation of the structural models for the computation of the truss structure by the resulting experimental data is not reasonable, as the applied concept for sealing the cell body structure with elastomeric material has huge and non-quantifiable influence on the hinge stiffness. However, the major objectives with this specimen, the test of the DSEC membrane, the internal fluid flow and the functional principle of a double row PACS are not affected by this production-process-based issue. The sealing with an adhesive film according to the implementation for the PA12 single cell turned out to be not applicable for a cell depth of 300 mm and the conceived internal fluid flow. A new sealing method is thus established. By immersing the cell body structure in *Plasti Dip* liquid rubber, the complete PACS could be sealed in a single work step. Local accumulations of material especially at small radii however increase the hinge stiffness.

Two digital manometers are used to measure the applied pressures, $p_{int,1}$ for the first and $p_{int,2}$ for the second cell row. The maximum pressure values $p_{int,1,max} = 0.3\,MPa$ and $p_{int,2,max} = 0.36\,MPa$ lead to tip rotations of $\alpha_{p_{int,1,max}} = -11°$ and $\alpha_{p_{int,2,max}} = 45°$. The top view of this prototype with the dimensions of 450 x 85 x 300 mm³ gives a first insight into the sample application of an aircraft's control surface.

As it can be seen in Figure 6-9, the PACS is successfully assembled by clamping the DSEC membrane between the cell body structure and the mounting frame. The gas-tightness is only achieved by the subsequent immersion. The process of sealing cell body and closure in a single step is thus additionally complicated. The internal fluid flow is realized by openings in the cell sides of neighboured cells. The proof of concept and the applicability of multi-row PACS are shown by this exemplary PACS of a

double row cantilever. The necessity for the development of the production process for the cell body structure is identified. Only an improvement of the manufacturing quality will allow for the validation of the design methods for PACS. The following chapters include the related approaches.

6.1.6 Variable-camber wing PACS device - HexPy913

On the basis of truss model variant 3, the geometry for the variable-camber wing PACS device is computed and transferred to a cross-sectional design according to chapter 3. The automated load-based design of hinge and cell side elements under consideration of the truss model assumptions is therewith implemented and shall lead to stress reductions and to increased deformation accuracy. The pressure-dependent deformation and stresses are investigated in a two-dimensional FEM-based simulation. The results of this investigation enable to determine deviations between truss and FEM model and thus allow evaluating the enhancements due to this automated cross-sectional design method.

In equality to the truss model, the FEM model is implemented in the two-dimensional space with the FEM-software *ANSYS*. The PACS's cross-section is used as an input and modelled with linear plane elements (*Plane182*). The material parameters for HexPly913 in fibre-parallel direction are given in Table 2-6. These values can be used herein, as the fibre orientation of the critically-stressed hinge elements lies in the cross-sectional plane. The influence of the laminate layup within the cell side elements is neglected within this investigation.

The sensitivity analysis that is presented at the top of Figure 6-10 is processed for the internal pressure $\boldsymbol{p}_{int,I} = [1.0, 0.0]\ MPa$, which cause maximum deformation. As the deviation of the cell side orientation angle $\Delta\beta$ is used to examine the convergence behavior, the worst case is thus considered. The computational expense is normalized with the respective value of the selected element size. The sensitivity analysis leads to a necessary element edge length for hinge regions of $0.05\ mm$.
The element size is further controlled in dependency of the wall thickness. The FEM model is depicted below and shows the adaptive element resolution. A ratio of element size of 1:10 is chosen in accordance to the variance between hinge and mean cell side thickness for reducing simulation efforts. The geometrically non-linear deformation is considered by an iterative solution strategy. With an overall size of the structure of 435 x 100 mm² the number of 76.2e3 elements is used for this model.

Three different pressure ratios are determined to compare the FEM-based outcomes with those of the structural model according to variant 3:

I) the exclusive pressurization of the first cell row, with $\boldsymbol{p}_{int,I} = [1.0, 0.0]\ MPa$,

II) the pressurization of only the second row, with $\boldsymbol{p}_{int,II} = [0.0, 1.0]\ MPa$, and

III) the uniform loading of both rows, with $\boldsymbol{p}_{int,III} = [1.0, 1.0]\ MPa$.

External loads and forces of inertia are neglected for these investigations in order to provide consistence with the load set for the DP, which is used for creating the cross-sectional design and marked in Figure 6-11. Besides the design pressure ratio, also the load states, which lead to the maximum deformation, are subsequently used for the comparison of computational results.
In equality to the evaluation shown in Figure 6-10 the angle $\Delta\beta$ is used for the evaluation of deformations. It results from the summation of the deflection of the complete cell compound and thus represents the cumulative deformational deviation. Figure 6-11 shows that the deviations between truss and FEM model increase for rising pressure values. For the pressure factor $PF = 1$, a deviation of $\Delta\beta_{Var3,FEM,I} = \Delta\beta_{Var3,I} - \Delta\beta_{FEM,I} = -3.42°$, $\Delta\beta_{Var3,FEM,II} = 3.94°$, and $\Delta\beta_{Var3,FEM,III} = 0.90°$ is measured for the three load states. The reduction of the angular deviation to 26.3 % and 22.8 % for the DP (III) compared to the off-design load sets attest the efficiency of the presented design process in terms of deformation accuracy. The reasons for the deviations and the divergence of the resulting values are discussed in the subsequent chapters.

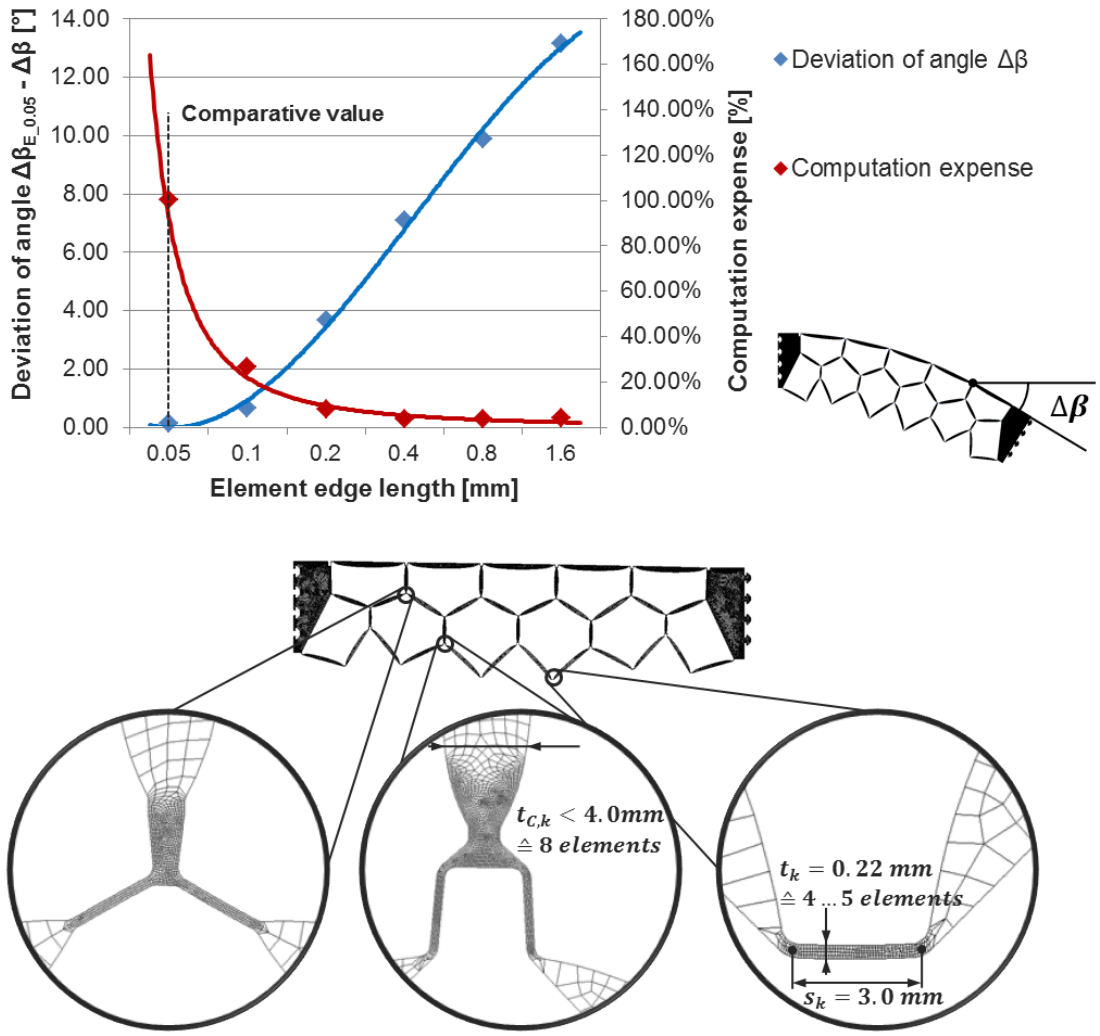

Figure 6-10: Sensitivity analysis for FEM model and model description

Equally to the global deformation, the deviation of maximum structural stresses rises with the amount of pressure (see Figure 6-12). For the three examined pressure ratios it is minimal for the design load state (III). For the pressure factor $PF = 1$, the global maximum of the stresses for truss and FEM model (FEM: principal stresses) deviate by $\Delta\sigma_I = 2019.84\ MPa$, $\Delta\sigma_{II} = 1998.92\ MPa$ and $\Delta\sigma_{III} = 392.51\ MPa$. Local stress peaks surpass the strength value of the utilized GFRP material HexPly913. The length-dependent cell side thickness is calculated according to chapter 3.2 with a safety factor of $SF_{CS} = 8$ for causing high axial and bending stiffness. The load-based dimensioning leads to a constant analytically computed stress distribution in the extreme fibre of $\sigma_{Var3,CS,max} = 150.0\ MPa$. Figure 6-13 includes the FEM-based stress results for the two marked cell sides. Between hinges and central cell side regions with controlled thickness, a geometrical transition zone causes stress peaks. For the major part of the cell sides, the stress distribution over cell side length, as well as the extreme fibre values are constant and accord with the underlying analytics.

For the design pressure load the stress distribution is also homogeneous over the hinge length. As shown in Figure 6-14, both of the selected positions for the uniform pressurization of the two cell rows show smooth stress gradients. The maximum principal stress of $\sigma_{FEM,P,max,III} = 1020.17\ MPa$ results for $\boldsymbol{p}_{int,III} = [1.0, 1.0]\ MPa$. The maximum value for the stress colouring is set to this value in order to show the effects of the load-based PACS design. The position and value of the peak stresses are labelled within the depiction. As the hinge orientation and curvature is designed for one single load state, the cross-sectional geometry is non-optimal for modified loads. For the off-design pressure ratio (I), at position two, the direction of principal stresses does not correspond to the hinge orientation.

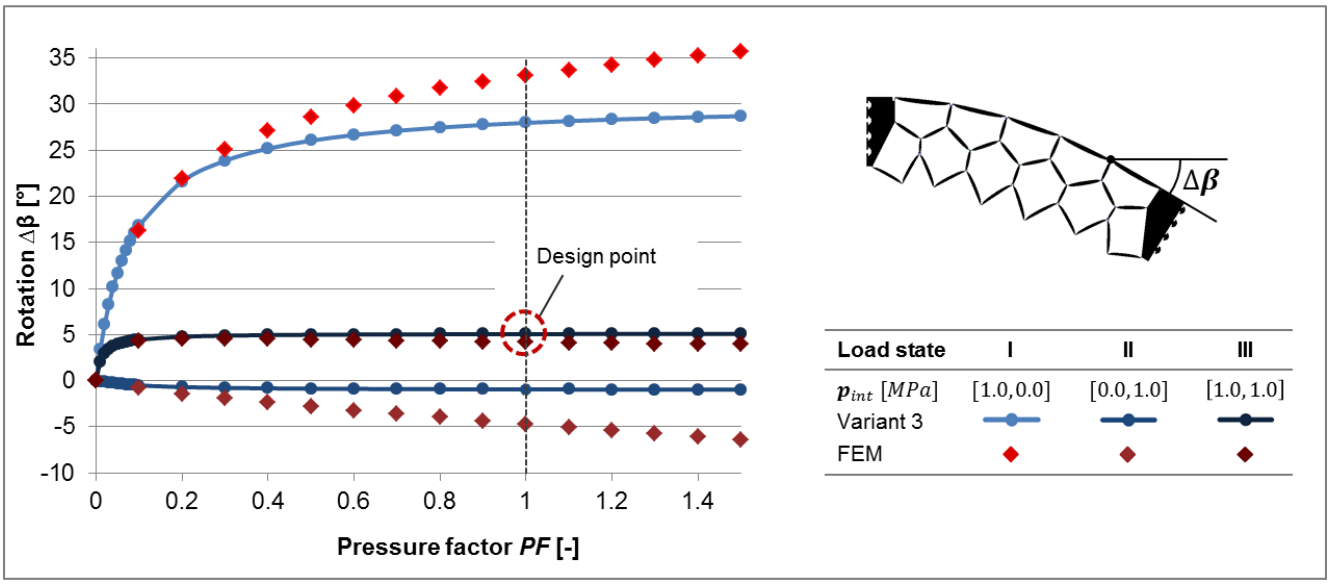

Figure 6-11: Comparison of computational results for pressure-dependent deformations resulting from truss and FEM model

The global tension peak stress of $\sigma_{FEM,P,max,I} = 2623.76\,MPa$ thus surpasses the DP value by the factor 2.82. For the pressure ratio (II) the maximum stress is $\sigma_{FEM,P,max,II} = 2573.43\,MPa$. The maximum stresses are reduced to $\sigma_{FEM,P,max,III}/\sigma_{FEM,P,max,I} = 38.9\,\%$. The advantages regarding stress reduction of a force and deformation-based cross-sectional PACS design are thus proven.

The strength of the FRP material HexPly913 is given with $R_{||} = 1200\,MPa$ and marked within Table 2-6. The simulated stresses exceed this value substantially. The pressure load that relates to the DP can be applied without exceeding the material strength, whereas the off-design loads lead to local overstressing. As for a given PACS cell only a reduction of the pressure load or of the hinge bending angle provides a remedy, these stress peaks could reduce the performance of a PACS.

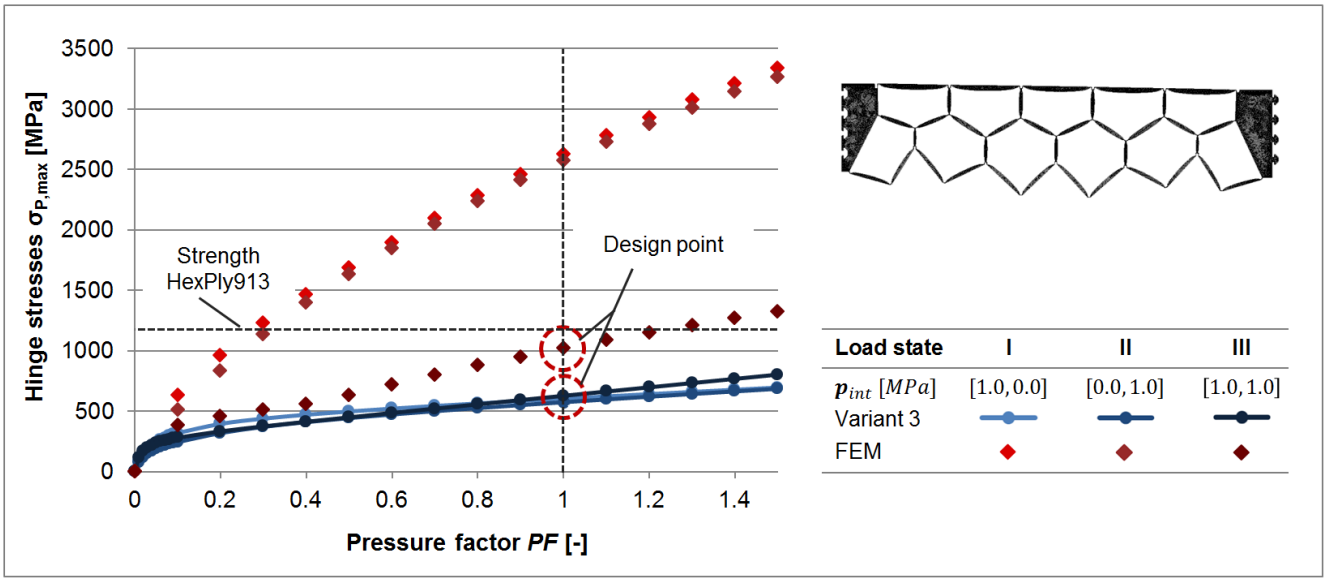

Figure 6-12: Comparison of computational results for pressure-dependent stresses resulting from truss and FEM model

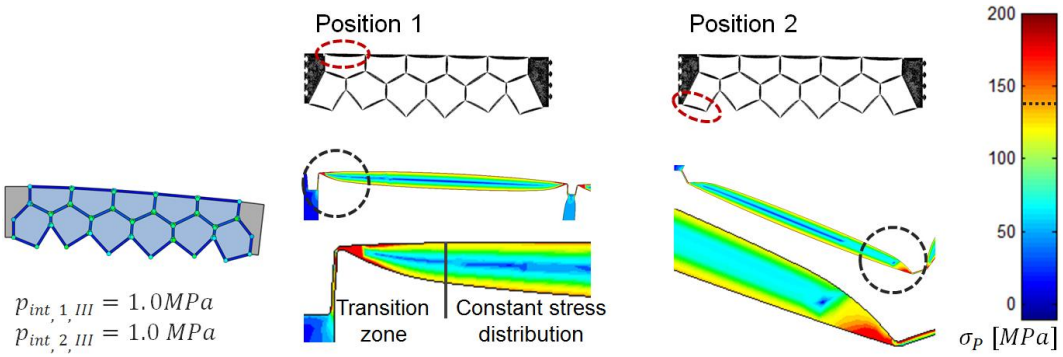

Figure 6-13: Stresses within two different cell sides of upper and lower cell row

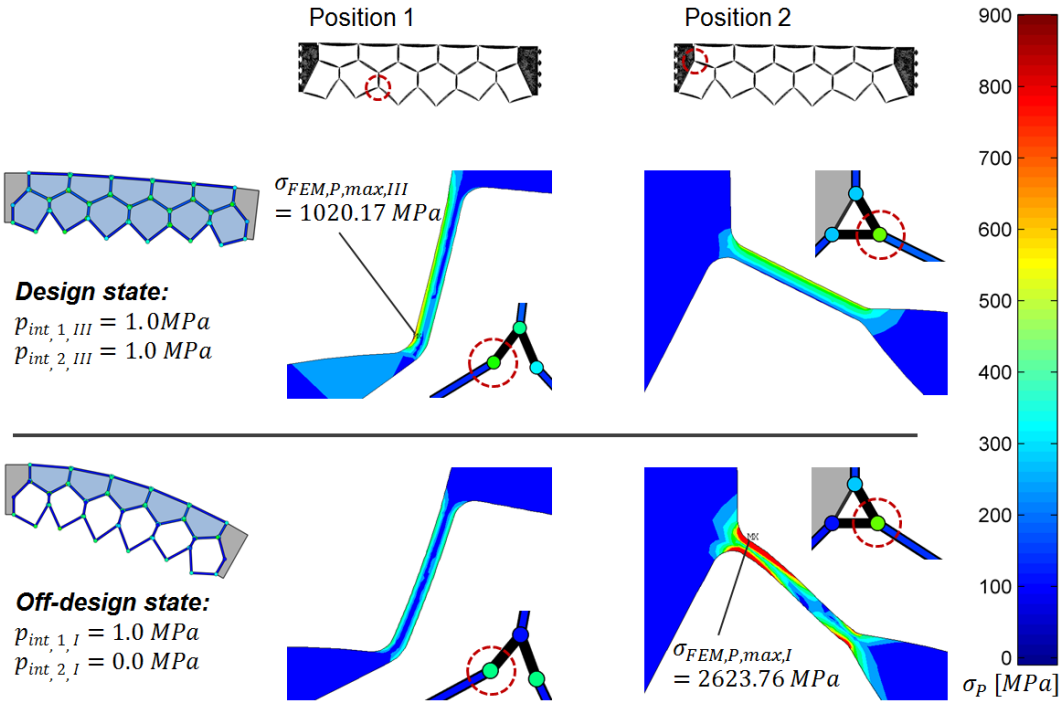

Figure 6-14: Stress distribution for two pressure states at the positions of maximum stresses

Geometry-related singularities or an inappropriate element size are eliminated to be responsible for these peak stresses as they could have been identified within the sensitivity analysis. A reason for the possible overestimation of stresses may lie in the assumed linear elasticity of the material model. The concentration of the maximum stresses to geometrically small areas compared to the hinge thickness allows for the assumption, that loads could be redistributed more homogeneously in a real-life structure. Nonetheless, the effects of local overloads on the fatigue strength of the flexure hinges are not investigated and cannot conclusively be assessed. Also the consequences of an inhomogeneous load distribution for the hinges' bending stiffness are unknown. These issues should be addressed by the future work on PACS.

Both, the increase of the deformation accuracy and the avoidance of stress peaks are shown by comparing the deviations between FEM and truss model results for design and off-design conditions. For the design load case, it could be found that the structural stresses within the cell sides and the flexure hinges reasonably match with those that are calculated on the basis of the structural model variant 3 and equation (2.72). The stress peaks, which are identified for off-design load states by FEM simulation and surpass the analytically computed values many times over, have significant influence on the design of PACS and are discussed in chapter 6.2.2. Further potentials for the cross-sectional design for PACS that result from this issue are presented therein.

6.1.7 Double cell - PA2200

Due to the issues with the assembly and gas-tight sealing of the cross-sectional slices for the production of the cell body structure, the water cutting process is substituted by the SLS process. It allows for the integral production of a sealed cell body structure and is thus used for the further realization of PACS specimens. Also the tightness between cell body and cell closure structure shall be ensured without the use of additional, hinge stiffening sealing material. The utilization of the moderately suitable PA2200 material (cf. Table 2-6) is enabled by stress reductions due to the load-based design for PACS. The production quality, the tightness of the cell body and the sealing bead for the gas-tight assembly with the DSEC membrane are investigated at the preliminary structure of the double cell PA2200 PACS. A successful implementation of the double cell PACS, allows for the subsequent design and realization of a double row structure according to the holistic design process.

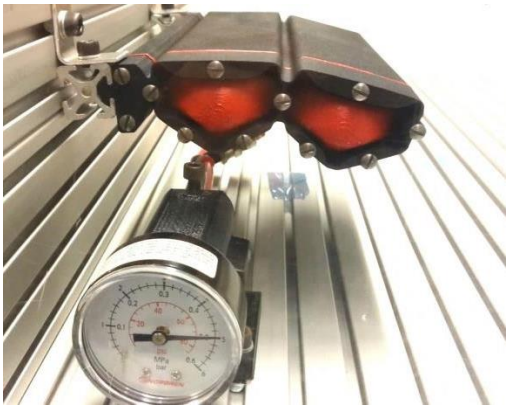

Figure 6-15: Double-cell PA2200 PACS specimen with a cell pressure of p = 0.5 MPa

As illustrated in Figure 5-5, the SLS process provides the capability for the integral manufacturing of the mounting holes, the fluid channels and the sealing bead in a single production step. The assembly process is investigated for the first time at the double cell specimen that is shown in Figure 6-15. In comparison to the sliced PA12 structures it is significantly simplified and accelerated. Up to the burst pressure of the structure of $p_{max} = 0.6\,MPa$, the specimen showed to be completely gas-tight. Both, the infiltrated cell body structure and the connection to the DSEC membrane, which is successfully complemented by the sealing bead structure, could be tested without the necessity for rework. As a preliminary test for the revised design, production and assembly concept, this investigation of the double cell PACS specimen paves the way for the subsequent evaluation of the holistic design process at the exemplary structure of the double-row PA2200 cantilever.

6.1.8 Double-row cantilever - PA2200

Based on the described strategy for the holistic design of PACS, a real-life demonstrator is designed, manufactured and experimentally examined. As the double-row PA12 cantilever could not be used for the measurement of the load-dependent deformations, the double-row PA2200 specimen is the first multi-row PACS, which enables this experimental investigation. As a result, the holistic design process for PACS shall thus be evaluated.
The results from three sources of data are compared, the truss model, a two-dimensional FEM model and the experimental test. The simulation and realization of this PACS device validates the underlying methods, regarding the dimensioning of the truss structure according to model variant 3. Influences from the cell closure membrane and its periphery, the mounting frame, boreholes and screws as well as the fluid ducts are not considered in the two-dimensional computations and shall be quantified experimentally. Manufacturing processes are already evaluated for the single-part production of a double row PACS cell compound and for the related closure structure. The fluid flow and sealing solution shall be evaluated as well as the stiffness influences from the cell closure membrane. As a major characteristic of the cell compound, the load-dependent deformation behaviour is investigated. The application of point loads verifies the computational models regarding external forces.

The PACS demonstrator is conceived to consist of seven pentagonal and eight hexagonal cells, describes a flat surface with its upper cell sides for the unloaded state of shape and has an overall length of 400 mm. The target shapes are described by a circular arc with an angular deflection of the upmost cell sides per pentagonal cell of $\Delta\alpha_{st1} = 5°$ for the first pressure state, with $\boldsymbol{p}_{int,st1} =$

[0.5,0.0] MPa, and of $\Delta\alpha_{st2} = -5°$ for the second pressure state, with $\boldsymbol{p}_{int,st2} = [0.1,0.5]\ MPa$. The pressure vectors are determined to provide the necessary energy for the structure to deform between the given target states of shape. On this basis, also other cell pressures could be defined, which allow for the successful optimization of the structure's geometry. The shape-variable structure is supported at one end. Forces of inertia and subsequently described external loads are considered.

After creating the cross-sectional design of the PACS according to the methods that are provided in chapter 3, a two-dimensional FEM model is implemented using the software *ANSYS* (cf. Figure 6-16). The double-row cantilever structure is represented by plane elements (*Plane182*). The sensitivity analysis for the element size is depicted in Figure 6-16 and bases on the loads due to the pressure vector $\boldsymbol{p}_{int,st2}$. It leads to an element edge length of $0.1\ mm$ for hinges and $1.0\ mm$ for cell sides. In the appropriate FEM model the functional hinge regions are described by at least seven and the cell sides by four to eight plane elements over the thickness. The FEM-based outcomes provide the basic information for the comparison of the pressure-dependent deformation behaviour of the two-dimensional PACS cell-body and the real-life structure with cell closure membrane and fluid ducts.

For the realization of the double-row cantilever structure, the SLS process provides a time and cost-efficient solution. With the material PA2200 (cf. Table 2-6), a hinge length of $s = 4.0\ mm$, an average cell diameter of $D \approx a_{CS,1,i,1} = 50\ mm$ and a maximum hinge distortion of $\Delta u_{c,max} = 15.46°$ the maximum operating pressure for the optimal hinge thickness of $t_{opt} = 0.40\ mm$ is approximated to $p_{max} = 0.32\ MPa$, according to equation (2.39). The cross-sectional design is generated using a uniform hinge thickness of $t_H = 0.7\ mm$. Functional flexure hinges can be guaranteed for thicknesses from $0.65\ mm$ in the SLS process with an *EOS P 760* laser sintering machine. For the pressure-tight sealing between cell compound and closure, an increase of hinge thickness is advantageous as it allows for a more durable sealing bead. The preliminary test with the double cell PACS exceeds the analytically computed strength value. Due to the non-linear stiffness properties of PA2200 (cf. appendix I), which leads to a redistribution and reduction of peak stresses, a failure value of $p_{max} = 0.6\ MPa$ is reached.
The necessity for screw holes limits the minimum cell side wall thickness to $t_{CS,min} = 6\ mm$. Subsequent to the shape-optimization process for the DSECs, according to [167], the fluid ports and ducts are implemented in the cell compound and the closure membrane to realize the pressure connection and the respective air flow. The real-life implementation of the structure is shown within the test setup for the experimental investigations in Figure 6-17.

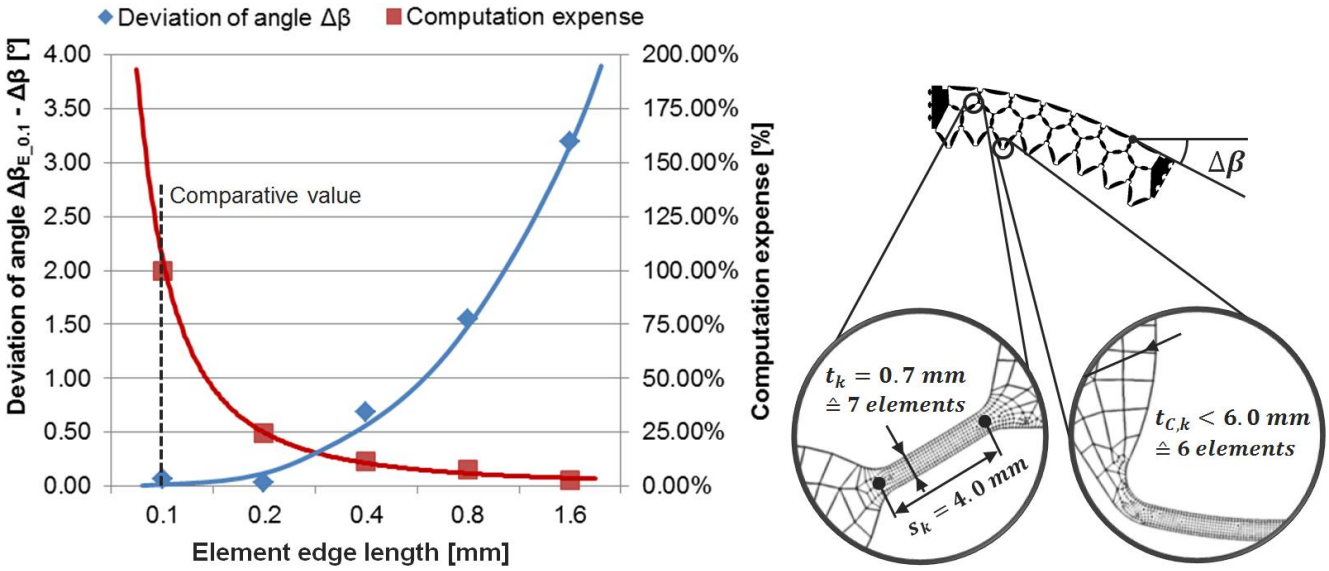

Figure 6-16: Sensitivity analysis for adjusting the element size and resulting FEM model

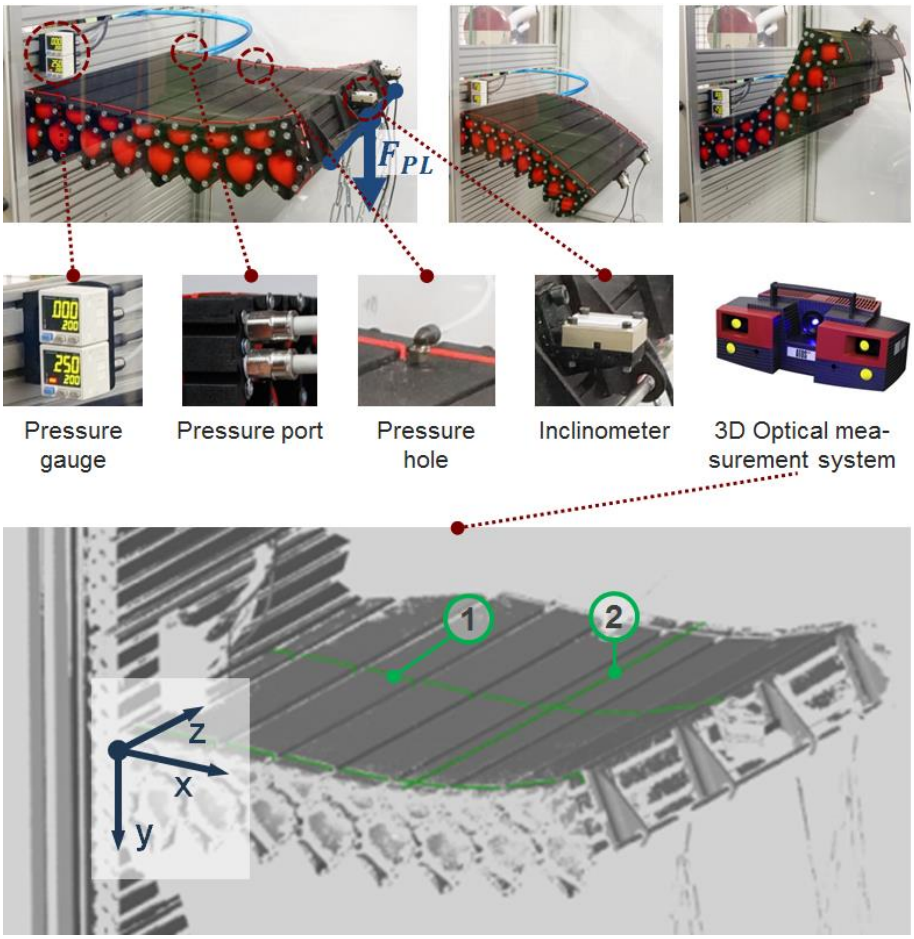

Figure 6-17: Modular PACS unit of the variable-surface demonstrator; test setup (t.) and results from optical measurement (b.)

The test specimen is attached to the test bench at one side and equipped with two *Althen AIT710-0101-60* inclinometers to record the angular deflection at its opposing end. At the back of the depicted mounting wall, two *B&B Thermotechnik DRTR-AL-10V-R10B* pressure gauges are used to measure the actual pressure values and provide the necessary information for controlling the fluid transfer at the pressure ports. The data from the pressure gauges and the inclinometers is received by a *National Instruments CompactRIO* and is processed with *LabView*. The pressure regulator is a *SMC ITV0031-2BL-Q*. The accessory pressure gauges *Panasonsic DP102EP* with digital display at the front of the test bench afford visual feedback. In addition to the evaluation of local distortions, the optical measurement system *GOM Atos* is used to digitize the upper surface of the PACS at specific load states (see Figure 6-17). The desired information resulting from this measurement technology is the surface deformation in the xy- and yz-plane. The xy-shape, Figure 6-17, (1), evaluates and extends the information from the inclinometers, whereas the yz-shape, Figure 6-17, (2), of the PACS indicates influences from the closure membrane on the global deformation behaviour.

The specimen is loaded with the internal pressure $\boldsymbol{p}_{int}$ and the external point (2D) respectively line load (3D) F_{pl}. The maximum pressure for each cell is limited to $p_{max} = 0.25\,MPa$. Four attachments are used to distribute the external load evenly over the depth of the connection structure. The test procedure is divided into five stages. After measuring the deformational state of the unloaded structure, three different pressure ratios with five sub-steps each are investigated. With a constant pressure of $p_{int,2} = 0.25\,MPa$, which is applied to the cells of the second cell row, the effects of changing external loads on the deformation are examined subsequently. In equality to the examinations in chapter 6.1.6 the pressure ratio is kept constant within each stage, while the amount of pressure is altered by multiplying the pressure vector with the pressure factor PF.

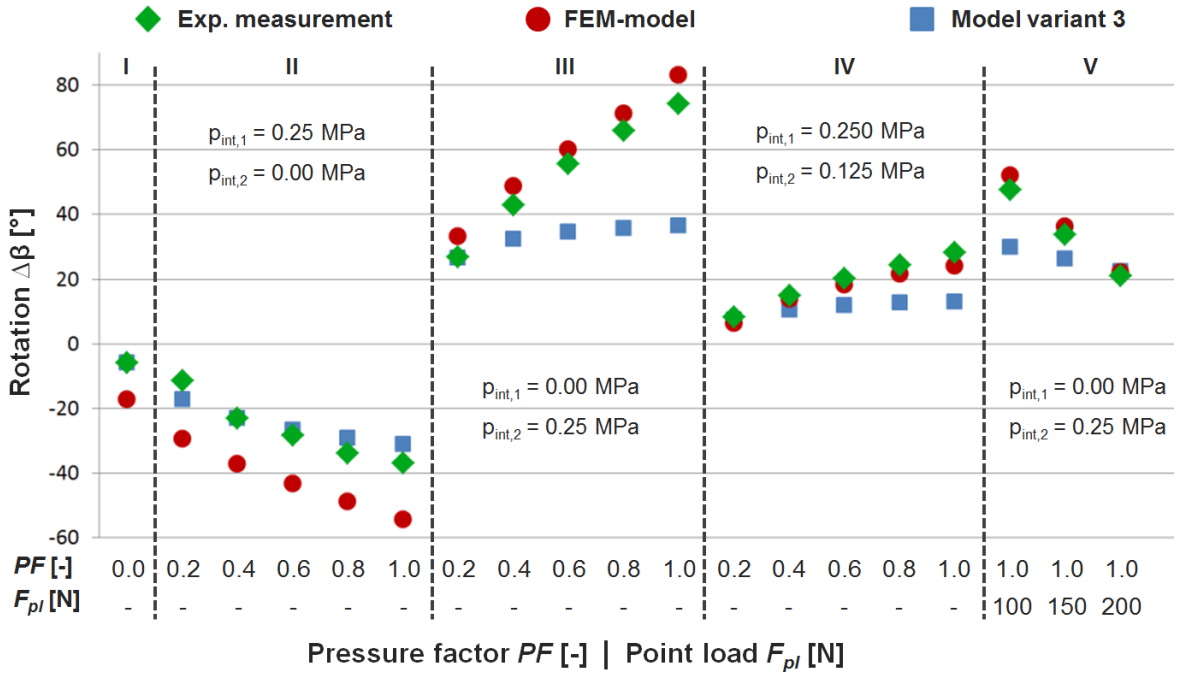

Figure 6-18: Rotational deformation at the free end of the experimental PACS for different pressure settings and point loads, from truss model, FEM model and experimental test

The rotation $\Delta\beta$ provides the distortion angle at the free end of the PACS device. Figure 6-18 summarizes the results from the truss model, the FEM model and the experimental investigations. The deviation of the results that base on the structural model variant 3 from the experimentally measured and the FEM-based values are discussed in chapter Figure 6-3. Reasons for the differences between experiment and FEM simulation are provided in the following.

Huge initial deviations between FEM and truss model can be obtained from Figure 6-18 for the second pressurization phase (II). The computed deformation values are significantly higher than the experimentally measured results. The first reason for this lies in the deformation hysteresis that is examined for this PACS structure and is due to the utilization of polymeric and elastomeric materials. A value of $\Delta\beta_{hys} = \pm 8°$ could be measured for the unloaded structure (I). An increase of loads reduces the related influence on the flexure hinges' bending moments and thus on the deformation behaviour. The stiffness of the cell closure membrane provides the second reason for this deviation. Only the first cell row is pressurized in this phase. Due to its small lever arm, the moments about the neutral fibre of the PACS are low. The closure membrane that belongs to the second cell row is further away from the surface and thus yield increased stiffness against the deformation of the PACS.
Also for the third load phase (III), the FEM-based deformation results surpass the experimentally deduced values. In this case, the second cell row is pressurized and provides high moments for the deformation of the cell closures of both cell rows. The influence of the necessary energy potential that is needed to deform the closure membrane decreases with increasing pressure-induced energy potential. Consequently, the resulting deviation is directed equally but is of lower amount.
The same arguments can be used to explain the fifth phase (V). The additional external loads lead to a further reduction of the cell closure's influence on the deformation of the PACS.
Within phase four (IV) the difference between the results from both sources is still small, but the experiment-based values are now greater than those of the FEM simulations. As presented in chapter 5.3, an overdriven DSEC variant (DSEC_OV) is utilized to investigate the possibility for compensating the stiffness effects from the cell closure. For the pressurization of both cell rows, it can be seen that the additional moment from the cell closure (cf. Figure 4-20) leads to an excessive deformation that increases for rising pressures (cf. Figure 6-19, bottom). The possibility for compensating the closure stiffness is thus proven, although the impact is too high for these load cases.

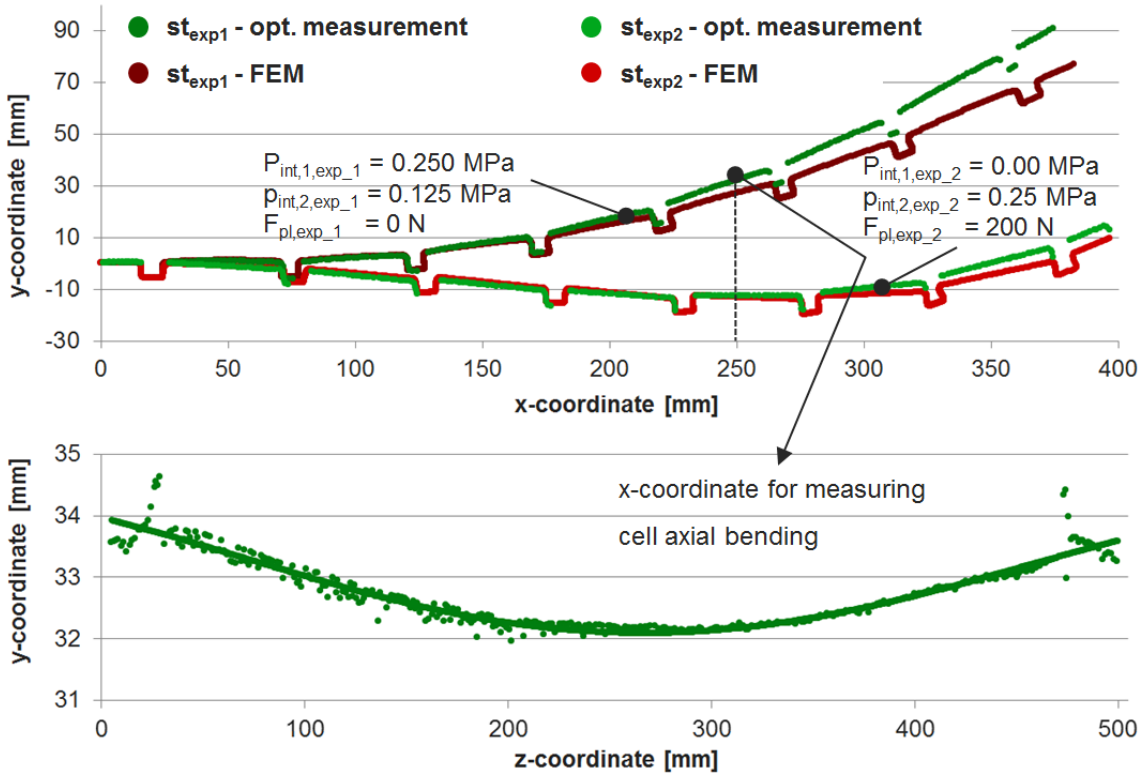

Figure 6-19: Optical measurement and FEM-based results for xy- (1) and yz-plane (2) of the upper surface of the double-row PA2200 cantilever

These investigations show that appreciable losses of accuracy result when the structural stiffness of the cell closure is not considered. The inclusion of these stiffness values in the FEM computations and in the holistic design process shall be realized in the further research on PACS in order to increase the quality of the structural simulation.

For the deviation analysis a three-dimensional measurement of the specimens' upper surface for two load states shall provide the information about the global deformational shape. The consideration of deviations between clamping and inclinometer in the xy-plane allows discarding and determining reasons for variances and demonstrates the applicability of the inclinometer data for the evaluation (see Figure 6-19). Measurements in the yz-plane are used to visualize the bending of the upper cells about the x-axis and to quantify effects of the cell closure on the global deformations. The subsequent discussion of results (cf. chapter 6.2) evaluates the outcomes, identifies reasons for deviations and points the way ahead.

6.1.9 Variable-surface demonstrator - PA2200

The shape-variable surface demonstrator (see Figure 6-20) is implemented to examine the concept for the possibility of realizing modular structures and gives an outlook for potential applications.
The verification of the PACS functionality in a modular architecture, the demonstration of its shape-changing capabilities and the intermediate step towards a morphing aerofoil is implemented by the demonstrator that is depicted in Figure 6-20. The modular device is assembled from two of the introduced and examined PA2200 double-row cantilever specimens. Although the target shapes of the structure are designed for pressures of $p_{max} = 0.5\ MPa$, the manufacturing quality caused a limitation of the internal pressure to $0.25\ MPa$. The resulting shape of the experimental demonstrator for four different pressure loads are compared with the computational outcomes on the basis of the truss model.

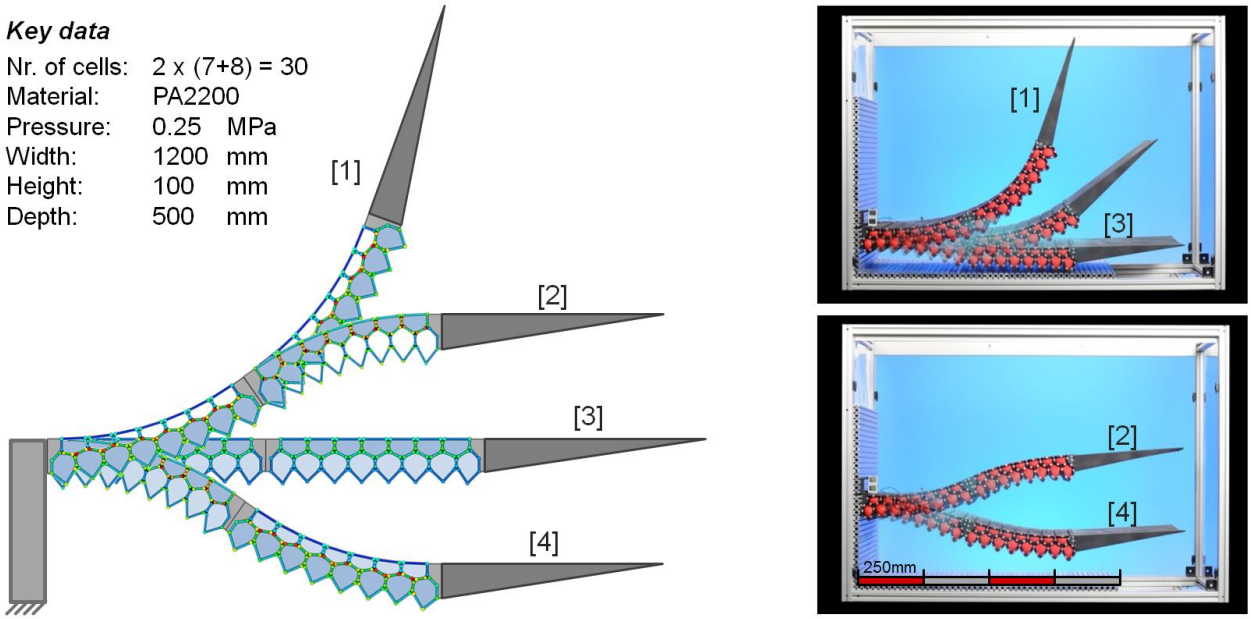

Figure 6-20: Computational results for structural deformations and experimental outcomes for the modular variable-surface PACS demonstrator

Deviations regarding deformation and structural stresses of this specimen are investigated on the basis of a single segment (cf. chapter 6.1.8). The variable-surface demonstrator shows the deformation potentials of PACS in general, the capabilities of the concept for interlinked structures and gives an outlook for the reduction of design and manufacturing efforts by a modular construction system. Figure 6-21 shows this PACS specimen within its test bench in full size.

6.2 Evaluation and progressive improvement

The outcomes of the relevant experimental and simulative investigations on PACS are presented together with the related design methods in chapter 6.1. The necessary information for the progressive improvement process, according to Figure 6-1, right, is thus given. In the following, the results are evaluated and the sensitivities of the design steps to specific assumptions are determined. The conclusions for the development and progressive improvement of the structural model, the cross-sectional design, the sealing and pressurization system and the realization of PACS are deduced and presented herein.
The necessity for the enhancement of each sub-process for the design of PACS is further illustrated by presenting the characteristics of the initial and the most highly developed methods. A comparison of the first and final implementations thus summarizes the effects of the progressive improvement procedure on the holistic design process for PACS.

6.2.1 Progress of computing the truss geometry for PACS

The structural model is used for the shape optimization of the truss geometry of PACS and for its simulation and characterization. Invalid assumptions for this process step that cannot be legitimized in the proceeding design stages cause inaccuracy regarding target deformations and structural stresses. Beginning with model variant 1, the PACS are reduced to a truss structure that consist of cell side line elements with infinite stiffness and point elements of infinitesimal rotational stiffness that represent the flexure hinges. The complete list of assumptions for the different structural models is given in chapter 2.1.2. The initial computational approach is implemented for handling single row structures without considering external forces.

The experimental and simulative investigation of the single GFRP cell (see chapter 6.1.1) gives reasons for model improvements. At first, the deviation of deformations between the structural model

variant 1 and an FEM-simulation are regarded. With this initial structural model, a pressure-dependent deformation cannot be computed. An infinitesimal amount of pressure is sufficient to cause the single cell to move to a state of shape of maximum enclosed volume as it can be seen in Figure 6-4. Dropping the assumption of infinitesimal rotational stiffness of hinge elements, model variant 2 is consequently implemented and substantially enhances the accuracy of results. Reasons for the remaining deviation can be found by observing the resulting stress distribution from the FEM model at the hinge elements. Figure 6-2 shows the stresses at hinge $j = 4$ for increasing pressures. The initially distributed stresses move from a centric position and concentrate at the lower boundary of the hinge element. As the non-uniform stress distribution is due to locally concentrated deformations, the flexure hinge is not loaded evenly over its whole length. Only a reduced length of the hinge is used for bending and thus an increased effective hinge stiffness results. Together with the information about the effects of hinge stiffening, which are shown in Figure 2-17, the FEM-based result of decreased deformation and increased stresses (cf. Figure 6-5) thus corresponds with the expectations. The assumption of constant hinge bending over the hinge length is mainly responsible for the remaining discrepancy.
The assumption of infinite cell side stiffness also affects the cell's deformation. Additional strain gages at the mid of face $j = 1$ give reasons for the suspicion that the deformation due to a pressure-dependent bending moment at the cell sides leads to an additive charge of hinge $j = 2{,}6$ and a discharge of hinge $j = 4$ (cf. Figure 6-2). Furthermore, the tension and bending-based change of the cell sides' chord lengths is not considered within model variant 2.
The uneven pressurization of the PACS due to the use of the tube pressurization system in particular, and the geometrical inaccuracy of the GFRP cell, which is caused by manufacturing issues, yield additional deviations between FEM and experimental results.
Due to the significant rise of the model complexity and the possibility to fulfil the assumptions of constant hinge bending and rigid cell sides with adapting the subsequent design methods, model variant 2 is unchanged for the moment. The alternative concept for the pressurization of PACS shall provide remedy for the uneven pressurization.

A further drop of assumptions is initiated after the experimental investigation of the single row GFRP cantilever (cf. chapter 6.1.3). In addition to the already discussed reasons for deviations, the eccentricity of the flexure hinges at crossovers causes an incorrect representation of the kinematics of PACS. This eccentricity is indispensable for the cross-sectional design of more than two intersecting cell sides because the flexibility of the compliant hinges is limited at the crossover structure. The consideration of this eccentric position of hinge points lowers variances for the computed deformations and stresses. The assumption of centric hinges at crossovers is thus dropped to meet the demands from the cross-sectional design.

In preparation for the investigation of the variable-camber wing structure, the structural model is developed for the consideration of inertial forces, external point loads and aerodynamic forces. The computational approach for shape optimization is further expanded by the capability to handle double row structures. The previously used variant of combining individually computed cell rows for the double row PA12 cantilever did not provide satisfying results regarding accuracy and operability.

The process steps of shape optimization and structural characterization are initially handled on the basis of a truss-like structural model for single cell rows that consist of rigid cell sides and flexible hinge elements. The effects of the development of this model on the deformation accuracy and thus also on the computed hinge stresses are summarized in Table 2-5. Two pressure sets for the stiffening (I) and deformation phase (II) of a double row PACS are applied and the results are compared with the outcomes of an FEM-based simulation. An increase of accuracy from $\eta_{Var1,FEM,I} = +37.14\ \%$ to $\eta_{Var3,FEM,I} = +9.47\ \%$ of deviation and from $\eta_{Var1,FEM,II} = +85.88\ \%$ to $\eta_{Var3,FEM,II} = +0.59\ \%$ is analysed and points out the sensitivity of the structural model to the related assumptions. The expansion of the structural model for the consideration of further load types and multiple cell rows provides essential capabilities for its utilization in the design process for PACS.

6.2.2 Effects of the cross-sectional design on deformations and stresses

The transfer from the structural model to the cross-sectional geometry is realized with respect to the underlying model assumptions. For the first three GFRP specimens hinges and cell sides are designed manually. As this initial approach does not consider local loads, stress peaks cannot be avoided and potentials for weight saving are disregarded.
Thick uniform layups for the rigid cell sides and thin-walled rounded geometries for hinges are initially used. In the course of the realization of the single row GFRP structure, a stress-based approach for the design of the cell side thickness is formulated. Weight reduction is enabled due to better material utilization. An increase of the bending stiffness coincidently favours the assumption of cell side rigidity. In particular, the analytical approach for the computation of the optimal hinge thickness, which results in equation (2.38), is beneficial. The consequent reduction of stresses in the critical hinge elements leads to an expansion of the maximum applicable pressure and thus the operational envelope of PACS.

The FEM-based and experimental outcomes of the investigation of the single cell GFRP structure (cf. Figure 6-2) illustrates, that the shape and orientation of the hinge elements and not only its thickness is decisive for its effective stiffness and also for the resulting maximum stresses. The assumption of constant bending over the hinge length is thus not compatible with the initial design of flexure hinges. The extraction of local hinge and cell side forces for a given DP allows for the load-based shape optimization of PACS. The underlying methods are first applied for the variable-camber wing PACS device.
As depicted in Figure 6-11, differences of the rotational deformations in the comparison of the design load state with two off-design settings are reduced to 26.3 % and 22.8 %. Though the loads on the structure for the DP overweight those of the other two pressure ratios, the resulting stresses are reduced and the values of truss and FEM model match significantly better. The investigation of the associated load flow, which is summarized in Figure 6-12, verifies the simultaneous decrease of stresses. For the DP, a reduction of stresses to 38.9 % and 39.6 % is evaluated, considering the off-design load states (I) and (II). It shall be noticed that the load-based cross-sectional design can only produces relief for one design state. A change in loading and deformation, which leads to lateral forces within the hinge elements, causes irregular stresses that concentrate in the transition zone between hinges and cell sides. This cannot be completely avoided, as the huge structural deformations that are necessary to provide the functionality of PACS lead to a range of different structural loads. The geometry whereas can only be optimized for one load and deformation state. For all other loads and related deformations that differ from this DP, the geometry is non-optimal and the inevitable lateral forces yield stress concentrations.
In consequence, the maximum pressure or hinge bending angle for a given PACS cell has thus to be limited to a lower value, according to equation (2.72). The performance of the PACS would thus be reduced. An optimization of the DP which considers multiple load states is not investigated herein but could result in a further reduction of stresses regarding the complete deformation envelope of a PACS.
Similarly, the accuracy of the truss model in terms of deformations bases on the optimal position, alignment and curvature of the flexure hinges. Figure 6-11 and Figure 6-18 show the effects of variances from the DP on the deformation accuracy of model variant 3.

Three major aims are reached with the automated load-based design, compared to the initial variant. The shape-optimization allows reducing structural stresses, what results in an expanded functional envelope for PACS and saves weight. With controlling the hinge orientation, curvature and effective position (cf. chapter 3.1), the identified need for a constant hinge bending could be reached for the DP. Enhancements regarding deformation accuracy and stress reduction are obtained. The transfer of the underlying methods in an automated sub-process for the design of PACS facilitates the efficient creation of generic PACS.

6.2.3 Test and progress of the sealing and pressurization concept

The initial implementation for the sealing and pressurization concept for PACS is characterized by the external fluid flow with individual pressure ports for each cell and the tube sealing with rigid end caps as cell closure solution. Not all of the identified demands on this sub-system, which are illustrated in Figure 4-1, are thereby completely fulfilled. The sensitivities of the PACS to specific requirements is investigated by experiment and simulation. The major objectives with the pressurization concept, that have to be addressed by all solutions, concern the deformation behaviour and the maximum applicable pressure.

The outcomes of the experimental examination of the single GFRP cell show that the tube system fulfils the main expectations of tightness and deformability, but holds disadvantages regarding pressure limitations, lightweight design and pressure distribution. Figure 6-4 illustrates the influence of the tube solution on the pressure-dependent deformation of the PACS. The silicone bladder is not able to transfer the applied pressure to the structure without an initial offset. For increasing pressures, the contact zones of tube and cell sides are unknown and depend on the cell geometry as well as on the perimeter and the mechanical properties of the tube. The assumption for the truss model of uniformly distributed pressure loads at hinges and cell sides cannot be fulfilled adequately by this pressurization concept. Together with the limitation of the cell pressure to $p = 0.2\,MPa$ and the necessity of redundant load paths for bearing cell-axial forces, substantial reasons for the improvement of the sealing and pressurization are obtained.

In an experimental investigation at the single cell PA12 specimen the selected best solution, the DSEC closure, is compared with the flat plate and an isotensoid end cap to verify the FEM-based investigations. The pressure-dependent deformation course of this cell is illustrated in Figure 6-8, confirms the influence of the closure concept on the change of shape and attests the negligible influence of the DSEC on the cell's deformation for $p > 0.3\,MPa$. The DSEC is thereby tested for a maximum pressure of $p = 0.5\,MPa$, which is sufficient for this investigation as the stiffening phase is reached. With using a more suitable material or by increasing the wall thickness, the DSEC can be adapted flexibly for bearing increased pressure values.
As the cell is assembled from single slices, an adhesive film is used to seal the cell body.

Combined to the DSEC membrane, the cell closure is developed for the use at the double row PA12 cantilever. Compared to the tube solution, the number of parts and thus the assembly efforts are significantly reduced. The internal fluid flow allows for the reduction of pressure ports to one per cell row. The disadvantageous sealing of the cell body slices and the connection to the DSEC membrane is addressed in the further improvement step.

The double-row cantilever, which is produced in an SLS process from PA2200, is infiltrated gas-tight. For sealing the parting area between cell body and closure, the membrane functions as gasket seal. In combination with the sealing bead around each cell, which is shown in Figure 5-5, the need for rework is avoided. The integral fluid flow allows for the substitution of redundant pressure ports and reduces the required installation space.
The analysis of the results from the two-dimensional FEM computation and the measured test data for this specimen (see Figure 6-18) shows good accordance. Increased deviations are only measured for pressure set (II). Thereby only the upper cell row is pressurized. The structural closure membrane stiffness of the second cell row acts against the deformation with a high lever arm towards the neutral fibre. For the applied low pressure values, the combination of DSEC stiffness and lever arm causes the illustrated deformational deviation.

A reduction of deviations between FEM-based and experimental results for the double row PA2200 cantilever specimen from $\eta_{exp,FEM,tube} = -22.40\,\%$ for $p = 0.35\,MPa$ and the initial realization, to $\eta_{exp,FEM,DSEC,III} = -12.01\,\%$ and $\eta_{exp,FEM,DSEC,IV} = -14.46\,\%$ for $p = 0.25\,MPa$ is significant but

should be treated with caution. The different materials, manufacturing processes and related accuracies have influence on this comparison. The sensitivity of the deformation behaviour to the pressurization system is analysed and remedy is provided by the DSEC. The pressure limitation is extended and an internal fluid flow allows reducing the number of pressure ports compared to the initial design. The reduction of parts due to the self-sealing concept of the DSEC-membrane allows for the efficient assembly of the PACS due to functional integration.

6.2.4 Qualification of realization concepts

Basing on the investigation of suitable materials for compliant PACS (cf. Figure 2-11) the GFRP material HexPly913 is selected for the first realization. The associated prepreg process is well suited for the production of geometrical complex FRP structures with notable thickness gradients. Influences from the manufacturing concept have to be considered in the design process. The limitation of applicable materials, the geometrical boundaries regarding the minimum wall thicknesses, the feasibility of undercuts or cutting depths and boundary values for thickness gradients have repercussions on the design process for PACS. For a successful implementation of PACS, the manufacturing restrictions are already considered in the shape-optimization process. The progress regarding the manufacturing concepts is presented in the following.

Production trials at a double-cell structure allow for the improvement of the prepreg process before the single row structure is realized (see chapter 5.1.3). Both, accuracy enhancements and the determination of practicable design solutions for the eccentric hinges are objectives of these examinations. For the resulting kinematical behaviour of the PACS the variability and accuracy of the hinge thickness is decisive. Due to the layered construction, only discrete thickness changes are possible. The minimum wall thickness depends on the thickness of the individual layer and is $0.125\,mm$ for the herein used GFRP prepreg. The geometrical accuracy depends on the processing and the draping precision, but in general is sufficient for the application of PACS. Deviations of $-12\,\%$ for the hinge thickness are measured at the single-row cantilever. Undercuts for the realization of an internal fluid flow system are possible. The process preparation, its execution and the follow-up work are expensive, even for a single cell and especially for a single-row cantilever. The necessity of removable mould cores for each cell complicates these production steps.

In order to qualify a production process for rapid realizations of single specimens, the water-cutting process is investigated. As described in chapter 5.1.4, production trials allowed to decrease geometrical inaccuracies at the hinge elements to less than $10\,\%$. The minimum wall thickness depends on the material type and thickness of the cut sheet and is determined to $0.8 \ldots 0.9\,mm$ for PA12 slices with a thickness of $10\,mm$. Undercuts are not processible by water cutting what causes the necessity for rework. Huge efforts with the assembly and sealing of the PA12 slices and the resulting intolerable stiffness input leads to the rejection of this concept for the production of PACS.

With the enhanced cross-sectional design and the related reduction of structural stresses, less appropriate materials could be used for the realization of the test specimens. The SLS process, which is presented in chapter 5.1.5 allows to realize wall thicknesses of $t \geq 0.65\,mm$. Undercuts, which are necessary for the realization of the internal fluid ducts, are feasible and the occurring thickness gradients are unproblematic.

Compared to the initial prepreg production process, the SLS provides the possibility to realize even complex-shaped cross-sectional designs with integral fluid flow and sealing beads in a single production step. The repeatability of this process compared to the manual GFRP prepreg process leads to increased accuracy. The disadvantage of only moderate characteristics of the processible PA2200 material can be tolerated with regard to the applicable cell pressures that are sufficient for the experimental investigations. Depending on the application of PACS, the need for varying materials may require a revision of the manufacturing concept.

6.3 Critical evaluation of the holistic design process

Two of the presented test structures, the variable-camber wing PACS device (cf. chapter 6.1.6) and the PA2200 double-row cantilever (cf. chapter 6.1.8) are created by using the most highly developed methods for the design of generic PACS. A critical evaluation is performed by analysing the simulative and experimental results from these test structures, with respect to substantial objectives with the design process. Deviations from these global aims are identified and reasons are presented. The connection to the underlying model assumptions is established where appropriate and potentials for improvement are presented.

Objective I: Accurate computation of deformations

An essential part of the design process for PACS is the approach for shape optimization. Independent of the utilized methods, the related deformational accuracy is identified as a major objective. The deviation between measured and target states of shape builds the basis for evaluating the process performance regarding this aim. Therefor a systematic listing of reasons for these deviations is presented in the following.

Deformational deviations between FEM simulation and truss model results are analysed to lie between $\Delta\beta_{Var3,FEM,III} = 0.90°$ and $\Delta\beta_{Var3,FEM,II} = 3.94°$ for the variable-camber wing PACS and the underlying load conditions that are described in chapter 6.1.6. The stiffness and the position of the hinge elements are decisive for the resulting deformation. For flexure hinges, a reduction of properties to these two parameters is accompanied by simplifications. Possible sources for variations, which result from the presented modelling variant, are given in Table 6-2 together with their abbreviation. The first five reasons all refer to the utilization of flexure hinges for PACS, which profit from advantages like pressure tightness and integral design. These advantages are paid with a complex stiffness behaviour, which is reduced to a linear-elastic approach within the truss model (see chapter 2.1.2). The reasons for deformational deviations R-D-H1 and R-D-H2 are sourced in the change of the hinge stiffness due to a non-optimal hinge orientation and curvature and the resulting non-uniform bending over the hinge length. Another effect is the relocation of effective hinge positions with respect to the neighbouring cell sides, initiated by R-D-H3 to R-D-H5.

Since the computation of deformations bases on the length of cell sides, an elongation of cell side elements inevitably influences these results. The divergent pressure-dependent deformation course, which is shown in Figure 6-11, confirms these issues. Bending of cell sides not only results in a change of a cell side's chord length, but also induces rotational deformations on hinge elements. With modelling the cell sides as rigid beams within the structural model, the presented cell-side-based effects R-D-CS cannot be considered. The increase of the deviations with rising amounts of pressure verifies the relevance of a more detailed mechanical description of hinge and cell side elements for the accuracy of the computational results.

Table 6-2: Reasons for deformational deviations and responsible assumptions

Reason for deviation		**Responsible assumptions for truss model**
Label	**Description**	
R-D-H1	Hinge curvature does not suit principal stresses	A-H4
R-D-H2	Hinge orientation does not suit principal stresses	A-H4
R-D-H3	Assumed hinge length does not include transition zone	A-H4, A-H5
R-D-H4	Elongation of flexure hinge	A-H2, A-H4
R-D-H5	Migrating of effective hinge position	A-H4
R-D-H6	Plastic deformation of hinges	A-H6
R-D-CS1	Elongation of cell sides	A-CS2
R-D-CS2	Bending of cell sides	A-CS1
R-D-CC1	Stiffness of closure membrane	A-CC1,
R-D-CC2	Pressure-induced forces from closure membrane	A-CC2

Additional reasons for deformational inaccuracy are found with the investigations of the PA2200 double-row cantilever. The plastic deformation of hinge elements is due to the described hysteresis (cf. chapter 6.1.8) of polymeric materials (R-D-H6).
The experimental stages two to four confirm the presented reasons for deviations between structural model variant 3 and FEM model. In contrary to the virtual variable-camber wing PACS device, the actual material PA2200 is of lower stiffness. The cell side effects R-D-CS become more important. Together with the hinge-based influences, they affect the deformed shape of the PACS.
Variations between FEM data and the experimental values attest the influence of the cell closure on the overall deformation. The reasons for this lie in the negligence of the closure membrane in the FEM model and can be summarized to the cell closure-dependent reasons for deviations R-D-CC. As described in chapter 4.2.7 the DSEC is designed to utilize the cell pressure to support deformations. For a low cell-internal pressure, the membrane's structural stiffness is dominant and leads to a reduction of the PACS's deformation. The related effects are illustrated in Figure 6-18. The experimentally measured deformation thus deceeds the FEM-based results for low pressures and for single-pressured cell rows. It shall be noticed, that stiffness effects from the second cell row thereby result in higher moments due to the larger lever arm of the underlying forces.
For increasing pressure loads, the effects from the closure stiffness decrease and are exceeded by pressure-induced forces, what can be observed in test stage four. The utilization of the DSEC-OV, with a convergent deformational state of shape that exceeds that of the underlying PACS cell, is responsible for a similar effect that leads to the excessive deformation of the examined PACS specimen.

The reasons for deformational deviations of the values that are computed on the basis of model variant 3 compared to the FEM-based outcomes and the experimental test data are summarized in Table 6-2. The assumptions which underlie the structural model are assigned to these reasons and point the way for the future model development in terms of the deformation accuracy. The additional computational expense for dropping each of these assumptions is high and should be contrasted with its benefits.

Objective II: High range of deformations
The second objective with the design process for PACS results from the desire to reach a high grade of deformation and thus an extensive actuator strain. PACS are conceived to change the shape of single-curved structures by bending about a neutral fibre. All deformations are thus achieved by the change of this surface's curvature. Comparing all of the realized structures, the single row GFRP cantilever provides the maximum experimentally tested change of curvature of $\Delta\kappa_{max} = 7.16\,m^{-1}$ with $\Delta\alpha_{max} = 20.5°$ per cell of $50\,mm$ width. With an additional cell row, the deformation-based stresses within the flexure hinges increase and the deformability is reduced by strength limitations. For the realization of the double row PA2200 cantilever, the rotational deformation $\Delta\alpha_{max} = 15.87°$ per pentagonal cell with a width of $50\,mm$ sums up to a change of curvature of $\Delta\kappa_{max} = 5.54\,m^{-1}$. The conceptual limits are thereby far from being achieved. As described, the deformability of a PACS depends on the size of the cells and the characteristics of the used material. Smaller cell structures can be designed to provide substantially increased changes of curvature. The selection of the applied material and the related manufacturing process influence the achievable values significantly. Limitations are additionally given by the basic layout of the PACS. The herein investigated combination of pentagonal and hexagonal cell tubes may be surpassed by alternative cell geometries.

Objective III: High load capacity
The PACS is loaded in three different ways. The cell inherent pressure initiates deformations and is used to control the stiffness of the structure (cf. chapter 2.1.3). External forces act locally or in distributed manner on the PACS. The utilization of flexure hinges leads to additional loads within hinge elements due to bending. The material strength limits the bearable stresses and defines the functional envelope for PACS as illustrated in Figure 2-11. In order to reduce structural stresses due to the applied loads an approach for the load-based cross-sectional design is implemented.
At the variable-camber wing PACS specimen, the effects of the load-based design are investigated. A maximum stress reduction for the DP of 38.9 % compared to an off-design load case is analysed.

Stress peaks as depicted in Figure 6-14 concentrate at flexure hinges. The load-based cross-sectional design produces relief for only one design state. A change in loading and deformation, which leads to lateral forces, causes irregular stresses within hinge elements, which concentrate near the transition zone between hinge and cell side. However, the stress distribution in cell sides is regular and can be adequately controlled by dimensioning the cell side thickness of each cell for the maximum applicable pressure.
It could be shown that the load-dependent design of the PACS's cross section provides the desired results of stress reduction. The definition of a design state, which involves the complete load envelope of a PACS would allow for the reduction of stress peaks in a global consideration.

Objective IV: High structural stiffness
PACS are conceived to possess a minimum of structural stiffness in order to minimize the necessary actuation energy. The interaction of structural and pressure-dependent stiffness is investigated experimentally. Figure 6-18 shows the outcomes of the double-row PA2200 cantilever test. The structure is loaded with external forces of up to $400\ N/m$, which are applied at its right connection structure. The higher the strength reserve of the PACS under consideration of deformations and external loads, the higher the cell-inherent pressures can be. A reduction of deformations and loads thus allow for an increase of stiffness.
The stiffness of the structure, or in other words, the blocking force of the PACS actuator is essential for the specification of the efficiency of a shape-variable structure. A further enhancement of the cross-sectional design as well as the substitution of flexure hinges by conventional pinned hinges may provide a remedy for the present limitations, if this is necessary for a specific application.

Objective V: Identification of suitable production processes
The relationship between the manufacturing process and the selection of materials, and the effects of the resulting limitations on the cross-sectional and three-dimensional design of PACS are discussed in chapter 5. As a high-potential process for realizing cell body structures with outstanding mechanical properties, the prepreg process is investigated. Besides the associated production expense, this process is in many respects advantageous and thus top-rated. However, for the design process of PACS the SLS manufacturing technique is selected. With its suitability for single-part production, the capability for realizing undercuts, the gas-tightness of the resulting structure and a high geometrical accuracy, this process is well appropriate. The moderate material properties can thus be tolerated for the purpose of the evaluation of PACS. For the manufacturing of the cell closure membrane, the SLS allows to process the thermoplastic elastomer TPU-92A, with an elongation at break of more than $200\ \%$. Depending on the target application and on the according weighting factors for the process selection (cf. Table G-1 and Table G-2), the favoured production process may be altered.

Objective VI: Extensive automation of design process
Due to the complexity of the PACS's kinematic the utilization of numerical methods for the creation of its cross-sectional design is advantageous. Moreover, the preferential cell closure concept, the DSEC, can hardly be designed without computational assistance. Also for the manufacturing of PACS digital data is needed to describe the geometry. The generic design process is thus conceived to combine the individual process steps by providing interfaces between them. The cross-sectional design is thereby generated on the basis of the truss geometry from the shape-optimization process. The resulting shape of the single cells is forwarded to the FEM-software for the design of the DSEC und further to the computer-aided design (CAD) tool *Catia V5* from Dassault Systèmes. Only the integration of the fluid ducts, the sealing bead, and the pressure ports is realized manually to finish the three-dimensional digital cell body model. The cell closure membrane is designed from a point cloud that results from the shape-optimization process for the DSEC. Further details on the application of the design process are given in chapter 7.
With the presented design process for PACS, a high grade of automation is already achieved. Depending on the necessary design flexibility, also the final steps regarding the CAD-based integration of cell body and cell closure membrane may be automated within the future work on PACS.

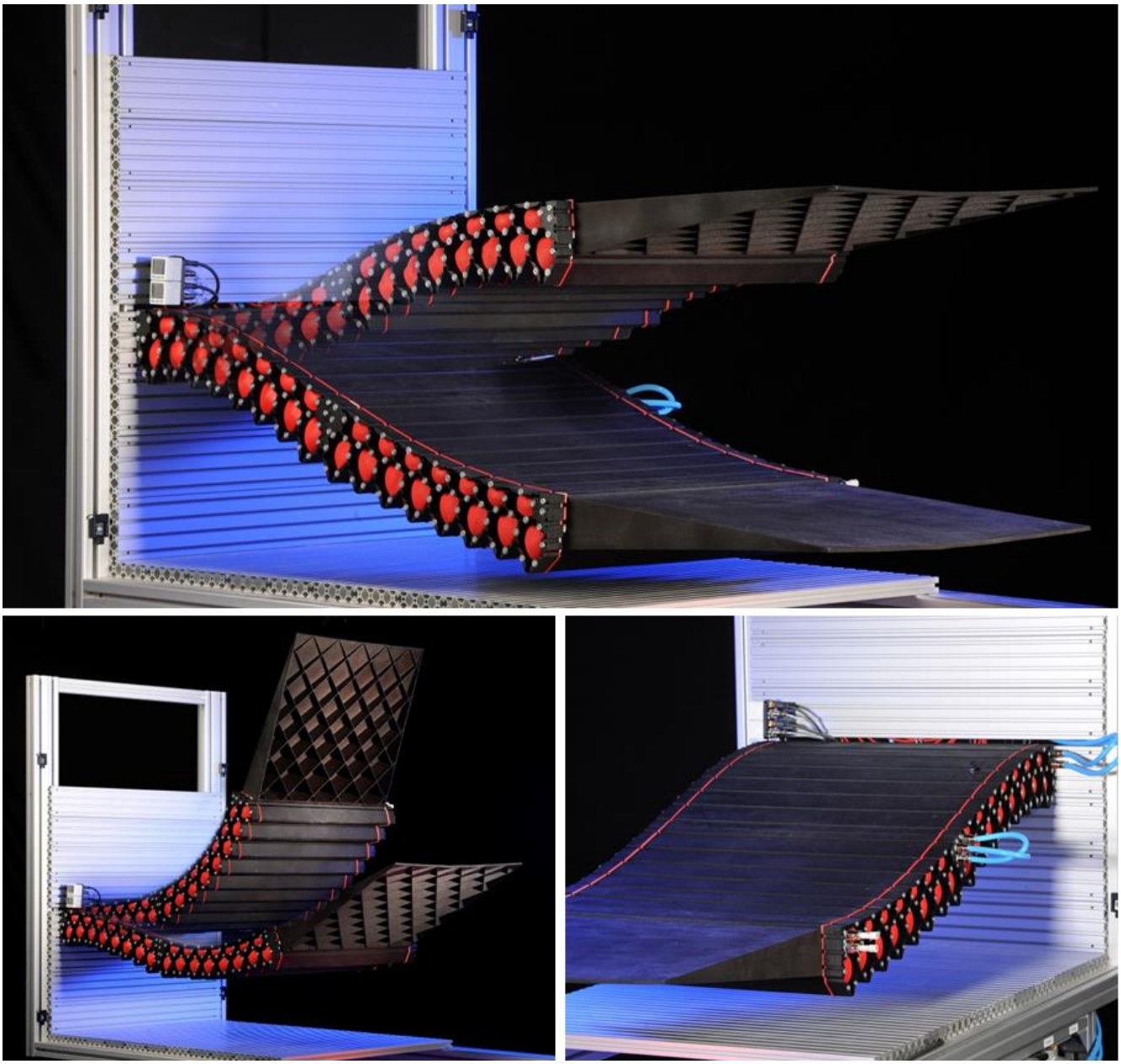

Figure 6-21: Modular PACS demonstrator for the realization of a shape-variable surface; length x depth x height = 1200 x 500 x 100 mm³; total mass = 9.2 kg

Objective VII: High specific efficiency and power

A comparison of fluidic and other actuator types for their efficiency in general is given in Figure 1-5. Fluidic actuators are therein identified to profit from high actuation strain and power density. With the double-row PA2200 cantilever with a total weight of $4\,kg$, an external load of $200\,N$ is raised by $0.3\,m$ in one second. With a resulting power density $1.5\,Wkg^{-1}$, the current realization lies far below the values of typical pneumatic actuators with $2x10^{3}\,Wkg^{-1}$ to $3x10^{4}\,Wkg^{-1}$. Notice that the investigation and increase of the power density and the efficiency of the PACS is no major objective of the performed work. As the substantial design issues are now solved, the further investigations have to aim at the detailed research on these performance parameters. With the load-based design for PACS and the related material saving, the first step towards performance increase is done.

As described in chapter 6.1.9, the evaluation of the generic design process is concluded with the realization of the modular variable-surface demonstrator [175]. Figure 6-21 depicts the pressure-actuated structure, with the dimensions of 1200 x 500 x 100 mm³ and a maximum pressure of $p = 0.2\,MPa$, for varying states of shape as a result of the progressive improvement of design methods.

7 Application of the generic design process

The research results on the sub-processes for the design of PACS are combined to the subsequently presented toolchain in order to simplify and accelerate the structural development. As each of the utilized methods is presented in detail previously, the subsequently presented application description for the toolchain shall illustrate its capabilities, characterize the essential sub-steps and provide the necessary information about the utilized software and the implemented interfaces. The remaining manual sub-steps are presented and illustrate the current grade of automation. Dependencies between the design steps and the resulting boundary conditions are summarized.
The so far investigated structures allowed to analyse and improve the quality of the underlying design methods but could not demonstrate the applicability of the toolchain for the design of PACS for more complex applications. Therefore, the presentation of airborne and ground-based use cases shall illustrate the flexibility of the toolchain in terms of its application for different target structures.

7.1 Toolchain for the design of PACS

According to the research methodology that is illustrated in Figure 1-20 and the division of the design process to its main sub-steps, the toolchain is described in the following four subsections (cf. chapter 2 to 5). The computation of the truss geometry, its transfer to the cross-sectional design for PACS, the solution for sealing and pressurization, up to the generation of the output data for the realization are provided subsequently. Figure 7-1 illustrates the procedure and presents the respective flow of information for the exemplary structure of a double-row PACS cantilever.
Although the presented methods allow for an extension for multiple cell rows, the herein described toolchain is implemented for the design of single-cell, single-row and double-row PACS.

Step I: Computation of truss geometry
Three sub-steps can be deduced for the computation of the truss geometry. Basing on the design of the truss model, the gradient-based shape-optimization process for the PACS is initiated. The simulation and characterization of the resulting two-dimensional structure allows analysing the PACS for any off-design load case including arbitrary external loads.

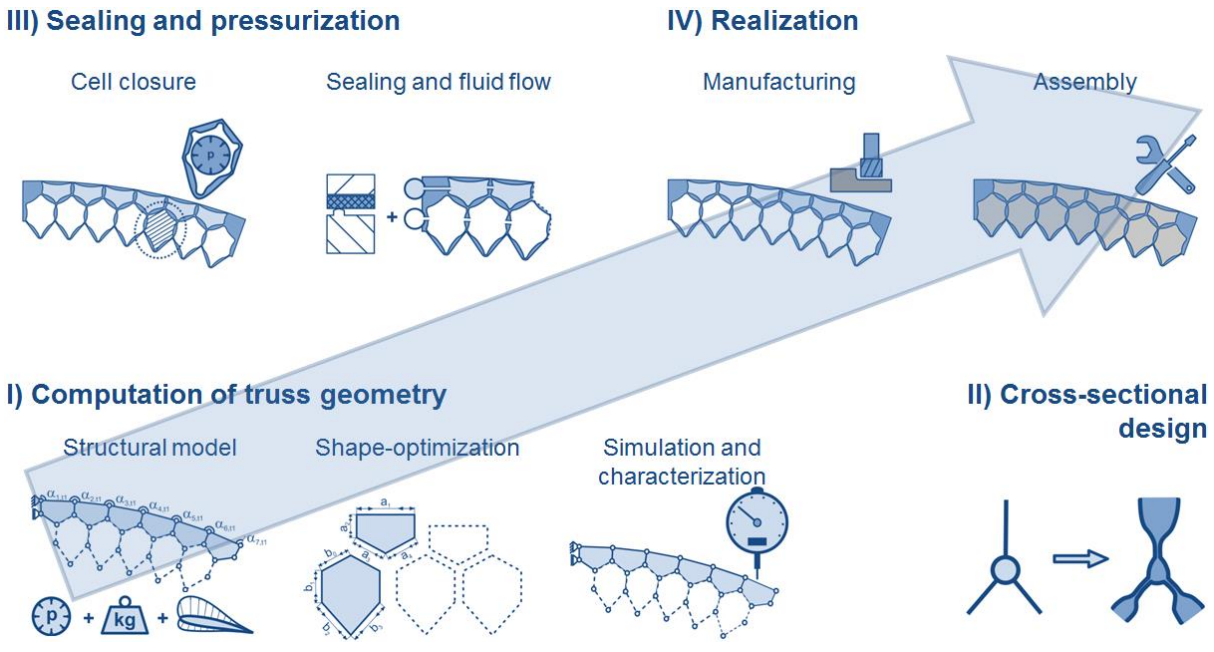

Figure 7-1: Process chain for the holistic design of PACS

The complete process of computing the truss geometry is implemented in *MathWorks MATLAB*. For the computation of aerodynamic pressure loads an interface to the software *XFOIL* is realized. As the subsequent design step is also implemented in *MATLAB*, no further interfaces to other programs are necessary for this sub-step of the design process.
With the model implementation, all of the necessary input for the shape optimization and the simulation and characterization is determined. The current implementation enables for the design of a double-row PACS with a number of n_1 cells in the first and $n_2 = n_1 + 1$ in the second cell row. However, the approach can be extended for additional cell rows. The required input data that allows for fully determining the structural model according to Figure 2-10, is listed in Table 7-1. The independent surface state variables, which are given by the hinge and crossover surface angles, have to be defined for the manufacturing state of shape, as well as for both target shapes. The number format that is used for the related data is a double-precision floating-point format which occupies 64 bits. The two parameters for specifying the hinge geometry are hinge length and eccentricity and have to be provided for each hinge. The optimal hinge thickness is calculated according to equation (2.38). Point and line loads, in this two-dimensional model, are applied for both target states and include internal and external loads. Boundary conditions from manufacturing can be considered by limit values for the wall thickness. The computed optimal hinge thickness can thus be adapted to provide feasible designs.

Table 7-1: Necessary input data for model design and related contents, data type and size of the vector or the matrix

No.	Input data	Contents	Data type	Size
1	Number of cells	Number of cells per cell row	integer	2
2	Cell size	Cell side lengths (surface)	double	n_1
3	Hinge angles	Independent state variables (surface)	double	$3 * (n_1 + 1)$
4	Crossover angles	Independent state variables (surface)	double	$3 * (n_1 - 1)$
5	Hinge geometry	Hinge length, hinge eccentricity	double	$2 * (13n_1 + 1)$
6	Point loads	Point load vector for each node	double	$2 * [(13n_1 + 1) \times 2]$
7	Line loads	Internal and external pressure loads	double	$2 * (15n_1 + 7)$
8	Material properties	*Young*'s modulus, material strength	double	2
9	Thickness limits	Manufacturing limitations t_{min}, t_{max}	double	2

In order to decrease the input effort, the number of absolutely necessary parameters is reduced to fourteen. The individual parameters for defining the cell side, hinge and crossover geometry are thereby filled with linearly changed respectively constant values. The implemented user interface that is presented the appendix 0 (see Figure J-), provides an input mask for these parameters. For more detailed settings, the thereby generated variables can be modified manually. All further steps for the computation of the truss geometry are automated.
The output data of the shape-optimization process is listed in Table 7-2. The cell side lengths, which represent the optimization variables, are computed for the complete structure except for the predefined surface elements. The inner independent state variables, which describe the hinge and crossover angles and are not determined by the definition of the target shape, are also altered during the optimization. With the respective variables and the information about the manufacturing and target shapes, the PACS can be completely described for all three states of shape.

Table 7-2: Output data from shape optimization and related contents, data type and size of the vector or the matrix

No.	Output data	Contents	Data type	Size
1	Cell side lengths	Cell side lengths (inner)	double	$6n_1 + 5$
2	Hinge angles	Independent state variables (inner)	double	$3 * (2n_1 - 1)$
3	Crossover angles	Independent state variables (inner)	double	$3 * (4n_1)$

With the optimized shape of the structure and the related information about the deformations due to target loads, only three states of shape are known. In a third sub-step, the design tool can be used to investigate the structural behaviour for varying internal and external loads. The deformational characteristic and the stiffness properties of the optimized PACS can thus be computed. Besides the hinge and crossover angles, which determine the equilibrium state of shape of the structure, hinge and cell side stresses are computed (see Table 7-3).

Table 7-3: Output data from simulation and characterization, related content, data type and size of vector or matrix

No.	Output data	Contents	Data type	Size
1	Hinge stresses	Hinge stresses for given load state	double	$13n_1 + 1$
2	Cell side stresses	Cell side stresses for given load state	double	$7n_1 + 5$
3	Hinge angles	Independent state variables	double	$3n_1$
4	Crossover angles	Independent state variables (inner)	double	$5n_1 - 1$

With knowledge of the manufacturing shape of the PACS, its deformation characteristic and the appearing structural loads, the truss model can be transferred to a cross-sectional load-based design in the next step.

Step II: Cross-sectional design

The input for this sub-step is given by the shape-optimized truss model and provided in form of variables that are presented in Table 7-2 and Table 7-3. As the software for the computation of the cross-sectional geometry is also MATLAB, the interface is defined by the given set of variables. The automated transfer of the truss model to a two-dimensional design of PACS under consideration of the local load flow, deformations, bearing conditions and manufacturing requirements allows for load reductions. Deviations regarding the deformation behaviour of truss model and cross-sectional structure are reduced by fulfilling the underlying geometrical assumptions.

The methodology behind the model transfer is presented in chapter 3. As described in that section, the two-dimensional geometry for the PACS bases on a single load state. This load state has to be defined manually and the equilibrium state of shape for this DP has to be computed to provide the required local structural forces. The already presented data fields for the input of point and line loads can be used to define the design load case. The material strength is used to determine the wall thickness of the cell sides. Limitations for the minimum cell side thickness allow considering the required space for screw holes for attaching the cell closure membrane. Also narrows near the flexure hinges, which affect the functionality of the cell closure membrane, can be avoided by defining the minimum distance of opposing cell side walls. With this information, the process of sizing hinges and cell sides is performed. After that, the implementation of the connection structure and the merge of the three structural elements are processed automatically. The function of creating the cross-sectional geometry of a PACS is integrated in the same user interface that allows for the computation of the truss geometry. Figure J-1 illustrates this highly automated part of the toolchain for the design of PACS.

As an output, the resulting geometry, which is determined by lines, circular arcs and splines, is transferred to an *APDL*-file (Ansys Parametric Design Language) that can be compiled by ANSYS. The thereby transferred contour and area information (see Figure 7-2) is used for the computation of the DSEC closures and for an FEM-based verification of the results from the truss model. The reliability of the design shall thus be increased before the PACS is realized.

Step III: Sealing and pressurization

Basing on the cross-sectional geometry of the PACS, the DSEC closure membrane is generated in a first step, before the three-dimensional design for the cell body and the mounting frame structure is determined to fulfil the sealing and fluid flow demands. Figure 7-2 illustrates this third step of the toolchain that leads to the three-dimensional design of the PACS. The input for the computation of the DSEC closures within *ANSYS* is given by the two-dimensional PACS geometry. For computing the

shape of each individual cell closure, the underlying cell contour is automatically extracted, an initially flat membrane is generated to close the contour, cell walls are integrated and LBCs are applied. After meshing the structure, the iterative process for generating the ERI end cap (see Figure 4-7) is initiated. The DSEC is computed subsequently. The resulting geometrical information is output in the form of a point cloud. To provide an interface to the CAD software that is used for the further design sub-steps, the information is saved in the *Initial Graphics Exchange Specification* (IGES) format. As the point cloud includes the position and shape of the cell contour, the manual assembly of the individual end caps to the DSEC closure is simplified. The entire process, from integrating the interface file, which contains the two-dimensional geometry, up to the output of the IGES-files for each DSEC, is controlled by an APDL program and runs without further user-input.

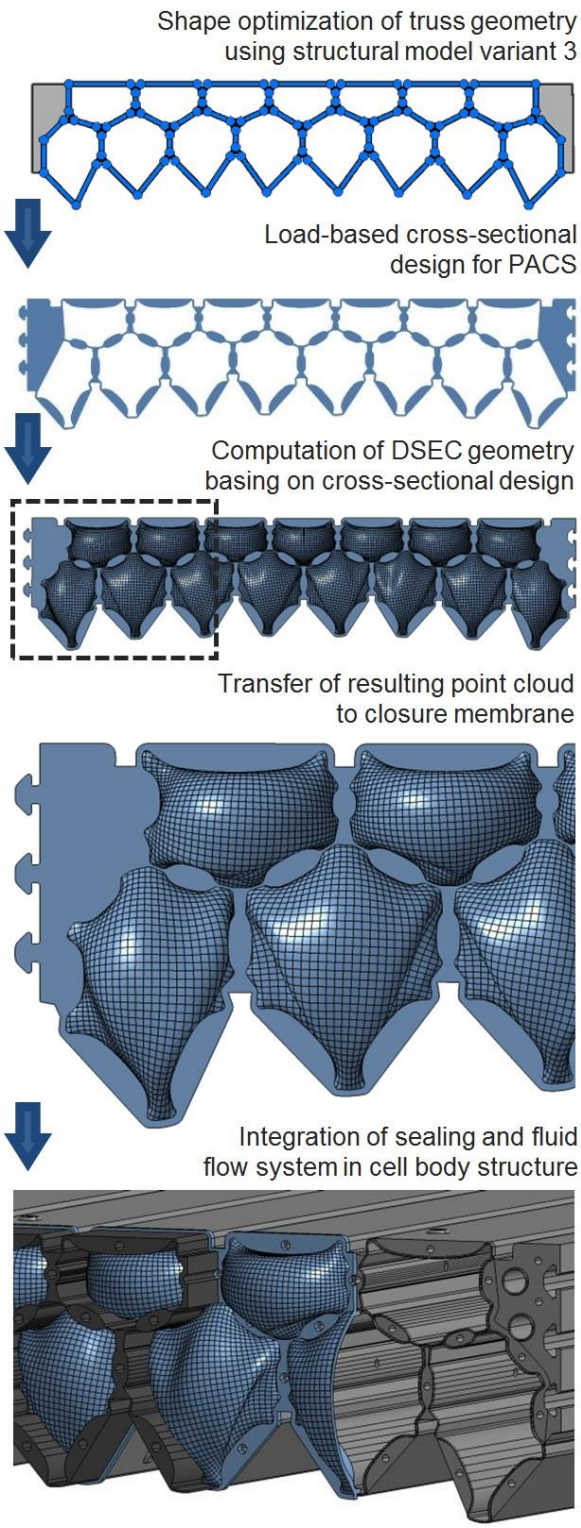

Figure 7-2: Design process for the sealing and pressurization concept

As illustrated in Figure 7-2, the point clouds together with the underlying cross-sectional geometry are handed over to *Dassault Systèmes CATIA V5R21* by using the IGES data format as an interface. The following manual process steps are necessary to create the DSEC membrane from the point clouds of the single end caps and to design the cell body structure. For the creation of the three-dimensional design of the DSEC membrane, two operations have to be performed. The transfer of the point clouds to individually shaped surfaces and their combination with the underlying cross-sectional area (cf. Figure 7-2, middle) is followed by the definition of offset conditions for the transfer to the three-dimensional body. This membrane thickness can be extracted from the underlying FEM computations for generating the DSECs. The necessary distance between opposing cell sides is adjusted in the cross-section design to allow for the offset without causing overlapping structures. The required holes for the assembly of the DSEC membrane with the cell body are also added manually. The design of the first PACS component is thus finished and the geometrical information is output in the *Standard for the Exchange of Product Model Data* (STEP) format.

The cell body structure is generated by extruding the cross-sectional area. Screw holes for the assembly of the components are integrated. The implementation of fluid ducts, pressure and measuring ports enable the fluid supply of each cell. The sealing bead avoids leakage at the cell sides and in particular near the screw holes. It provides the necessary contact pressure to seal the area between cell body and closure membrane. With the same cross section as the cell body, the mounting frame is generated similarly. The geometrical information about both components is outputted in the form of STEP-files.

The resulting three-dimensional design of the components cell body, closure membrane and mounting frame is shown in Figure 7-2, bottom, for the exemplary structure of the double-row PA2200 cantilever specimen. The output information is saved in the STEP-format as interface for the subsequent manufacturing preparation.

Step IV: Realization
The geometry for all components is provided and enables the realization of the PACS structure. The selection of the production process for each part has to be defined in an early stage of the design process. Mutual dependencies due to the limitation for specific groups of material, the achievable accuracy and the possibility to manufacture even complex geometries integrally influence the entire design process. Due to these relationships, the holistic design process has to include the realization. A requirement analysis and the respective properties of several manufacturing processes are given in chapter 5. Process characteristics and boundary conditions are discussed therein. Manual work steps for creating a real-life PACS at this stage of the toolchain depend on the manufacturing process.

A highly automated toolchain is implemented for the generic design of PACS, which allows for the shape optimization, characterization and closure of these structures. Manual work steps remain necessary for the three-dimensional design of cell body and cell closure and for the realization.

7.2 Use cases

Apart from the variable-camber wing structure, all of the so far investigated PACS are designed to deform from a straight shape into circular arcs with predefined curvature. Further, the cell sides that belong to the PACS surface are all of equal length. With the implementation of the toolchain for the holistic design of PACS, the possibility to realize shape-variable cellular structures that exceed the geometrical complexity of these specimens is created. The following section shall illustrate the functionality and flexibility of the design process on the basis of different applications for PACS.

Four structure examples from the different fields of application, automotive, aeronautics, energy and construction, are processed through the design tool to illustrate its operability. The structures are selected to consist of varying materials and to possess different dimensions. The necessary actuation pressures changes with the necessary energy potential, the required stiffness and with the size of the cells and are thus also varied over the example structures. Small modular and large integral as well as structures with constant and tapered cell size are designed to proof the flexibility of the design process. The significant parameters as well as the initial and target-shape functions are provided. In the following, the computational results are presented from the shape-optimization on the basis of the truss model up to the transfer to the cross-sectional design.
The PACS use-case structures are arranged according to their dimensions. The computational outcomes and the most relevant properties of the specimens are summarized in Table 7-4.

As a sample application for the automotive section, an adaptive car spoiler is conceived to replace the conventionally used kinematic system. The position of a currently applied retractable rear spoiler is controlled relative to the car's velocity, it increases the downforce on the rear tires and provides an attractive design feature. In a modular construction, two PACS devices that consist of fifteen and thirteen cells are designed to form a continuously deformable spoiler. With a width of $360\ mm$ and a maximum height of $60\ mm$, both structures are designed for low space requirements. The maximum pressure of $0.5\ MPa$ has to be provided by the on-board pressure supply. The resulting metal construction is designed to move between to circular arcs. The outcomes from the shape-optimization process and the cross-sectional design of the PACS for the adaptive car spoiler are illustrated in Table 7-4, A1. The utilized material Ti6Al4V can be processed by EDM. In comparison to the existing conventional solutions, gaps can be avoided, what results in aerodynamic and design enhancement potentials.

Table 7-4: Application of the toolchain for the holistic design of PACS for different structure examples

Designation:	**A1) Adaptive car spoiler**	**A2) Variable-camber wing (*Sagitta*)**
Application:	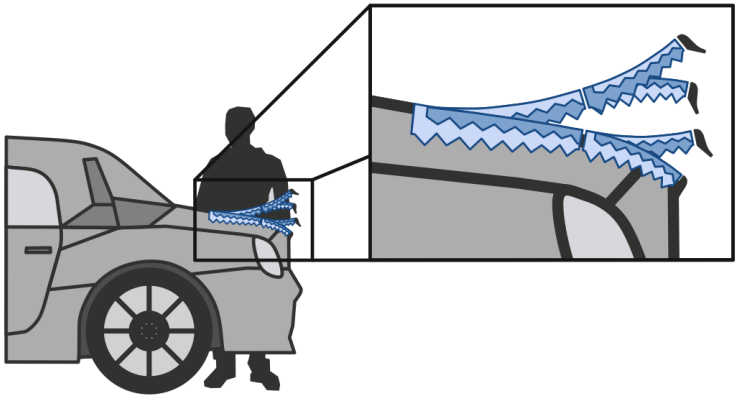	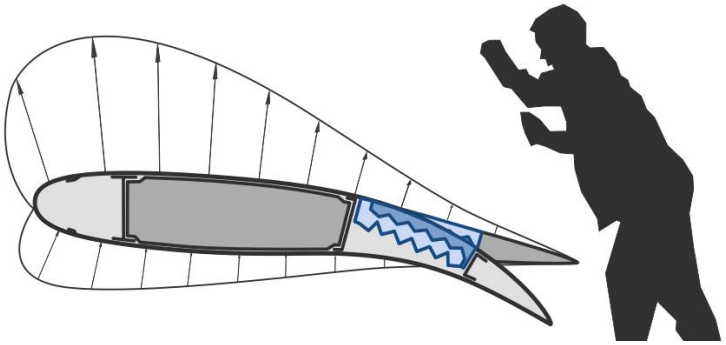
Cross-sectional design:		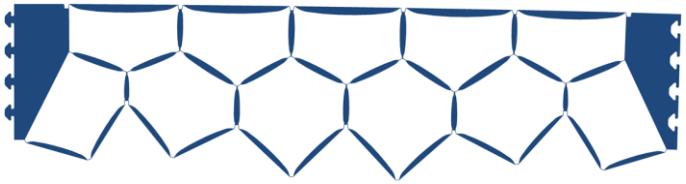
Dimensions (w*h):	360 x 60 mm²	400 x 100 mm²
Cell quantity:	(7 pentagonal, 8 hexagonal) + (6 pentagonal, 7 hexagonal)	5 pentagonal, 6 hexagonal
Cell size & taper:	35 mm, f_{taper} = 0.75	75 mm, f_{taper} = 1.0
Max. pressure:	0.5 MPa	1.0 MPa
External forces:	Aerodynamic forces	Aerodynamic forces
Target shapes:	$\sqrt{1-x^2}-1$, $-\sqrt{1-x^2}+1$, $x\epsilon[0,0.1]$	$f_{NACA\,0012}(x)$, $f_{NACA\,0012}(x)+\left[\sqrt{1-x^2}-1\right]$, $x\epsilon[0.6,0.9]$
Material:	Ti6Al4V	HexPly913
Product. process:	Wire-cut EDM	Prepreg process
Main advantages:	Potentials for aerodynamic enhancement Infinitely variable surface and avoidance of gaps	Efficiency increase and noise reduction Enhanced agility and camouflage

Designation:	**A3) Wave energy converter**	**A4) Petal canopy**
Application:	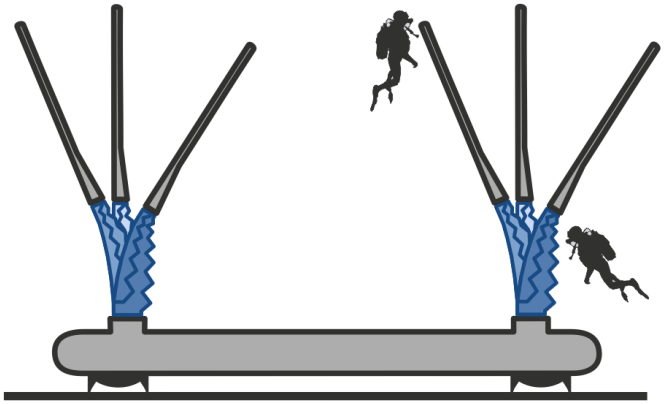	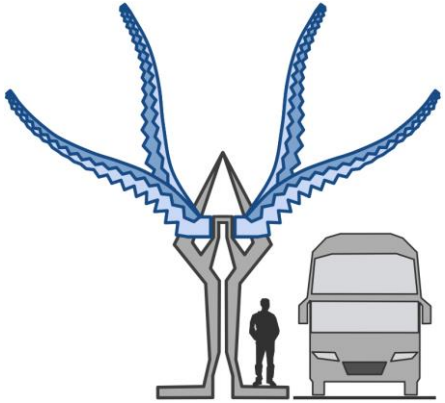
Cross-sectional design:	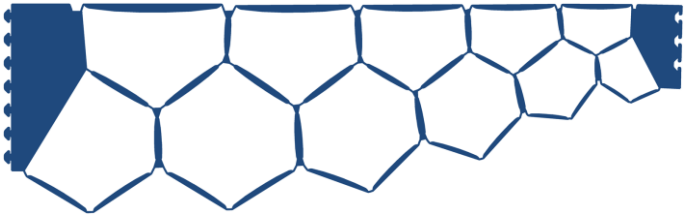	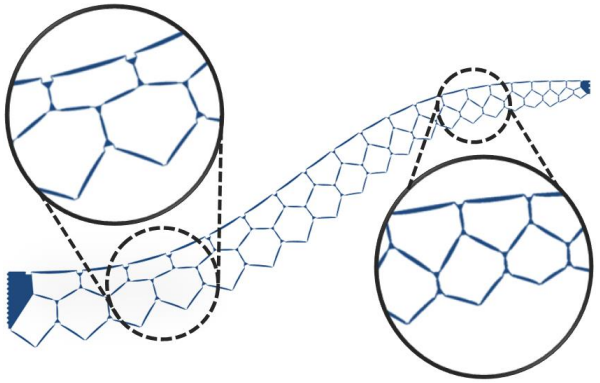
Dimensions (w*h):	2000 x 750 mm²	4950 x 700 mm²
Cell quantity:	5 pentagonal, 6 hexagonal	19 pentagonal, 20 hexagonal
Cell size & taper:	500 mm, f_{taper} = 0.5	400 mm, f_{taper} = 0.3
Max. pressure:	2.0 MPa	1.0 MPa
External forces:	Hydrodynamic	Inertial forces, snow load
Target shapes:	$x, x, x\epsilon[0,1]$	$-sin(x)/3, sin(x)/3, x\epsilon[1/3\,\pi, 7/3\pi]$
Material:	HexPly913	HexPly913
Product. process:	Wet laminating	Prepreg process
Main advantages:	Reversed use of deformation for pressure generation Integral gap-free design advantageous for seabed conditions	Functional integration Design aspects for public places

The variable-camber wing structure, as an aeronautical application for PACS, is already introduced in chapter 2. It is used as target structure for the elaboration of the design process and functions as application example for the explanation of the subsequently described methods. Its dimensions of $400\,mm$ of width and $100\,mm$ of height allow for the integration into a NACA 0012 profile with a length of $1200\,mm$, to reach consistence with the boundary conditions of the UAV *Sagitta*. The maximum pressure of $1.0\,MPa$ can be applied to five pentagonal and six hexagonal cells. The pressure-induced change of shape, between the NACA form and a superimposed circular arc, leads to a considerable increase of lift forces (see Figure 2-19). The structure is supposed to be built from the GFRP material HexPly913 in a prepreg process. With the variable-camber wing PACS device an expansion of the flight envelope, noise reduction and an increase of flight efficiency can be reached.

In the third sample application the PACS is used as pressure generator instead of an actuator. The cells in both cell rows are designed to contain maximum volume in its initial vertical state of shape. Any deformation of the structure due to external forces results in a reduction of the included volume. The idea about this kind of PACS is to convert the hydrodynamic energy of waves into the potential energy of compressed fluid for electricity generation. Comparable concepts with similar dimensions like the *WaveRoller* [176] and the *Oyster* [177], which base on conventional kinematic mechanisms, are reviewed in [178]. The PACS as the core element of the wave power plant is $2000\,x\,750\,mm^2$ in size and consists of five cells in the first and six cells in the second cell row. With a maximum cell size of $500\,mm$ the cells are designed to withstand a maximum pressure of $1.0\,MPa$. The integral gap-free design is advantageous for seabed conditions. The saltwater-resistant GFRP material is conceived to be processed in a wet laminating process. This concept is covered by patent application [179].

The fourth use case that is illustrated in Table 7-4 is the shape-variable petal canopy. For the application of the roofing of a bus or train station a PACS with 19 pentagonal and 20 hexagonal cells is designed to provide a total span of $4950\,mm$ at a height of less than $750\,mm$. As the largest of the introduced PACS structures, the petal-like construction allows to close up the roofing in sunny weather and to provide protection against rain, when brought down. The tapered design of the profile is chosen as it considers the increasing bending moments towards the clamping at the root of the structure. Towards the tip, the maximum cell size of 400 mm is reduced by the taper factor $f_{taper} = 0.3$. The actuation pressure is limited to $1.0\,MPa$. The retracted, closed shape is chosen as the manufacturing state of shape, what guarantees a lift of the roofing in case of pressure loss. The pressurization of the second cell row, with an increased lever arm towards the neutral fibre of the PACS allows for high upward moments and thus to bear inertial forces, rain and snow loads. The sinusoidal shape of the structure ensures the drainage of rainwater. As a well suitable material for PACS, the HexPly913 is conceived to be utilized for the realization of the petal canopy structure.

8 Conclusion and Outlook

The contents of this work, the novelties and major achievements are summarized in the following. The subsequent recapitulation of open issues, which should be addressed in the future work, is further extended by the perspectives for the concept of PACS.

8.1 Results and achievements

The research interest on morphing structures for aeronautical applications rose significantly during the last fifteen years. Reasons for this are the expected potentials for saving operating costs due to efficiency increase, a reduction of exhaust and noise emission and the expansion of the flight envelope. The avoidance of gaps and the continuous change of curvature provide additional benefits in terms of an aircraft's radar signature.

Motivation, research methodology and overview

With compliant PACS, a lightweight concept for shape-variable structures is developed and theoretically investigated by Pagitz et al. [1]. The combination of three major advantages differentiates PACS from the available morphing structures. First, the concept is characterized by a blended actuator-structure construction, which utilizes the high specific power density and the large actuation strain of fluidic actuators. Second, the dilemma of the concurrent demands for deformability and load capacity is circumvented by the release of specific degrees of freedom. Third, the concept of PACS allows for the definition of multiple target shapes that can be varied continuously by controlling a small number of input parameters. The physical background, a basic shape-optimization algorithm and a proposal for possible applications are covered by previous research achievements.

The motivation for this work results from the presented conceptual benefits and the open issues, which have to be solved, before the realization of a PACS is enabled. The identification of critical influence factors, the assessment of the reliability of outcomes and the investigation of conceptual limitations are performed within this work. Subsequently, a design process is implemented, which allows for the realization of PACS and thus the experimental evaluation and validation of concept.

The herein developed comprehensive methods allow for the holistic design of PACS for the first time. In an iterative approach, which bases on the evaluation of methods by numerical and experimental investigations at an early stage of the research process, these methods are improved step-by-step. The evaluation of functional subs-systems as well as of the overall design process is performed to analyse the accuracy of results and to verify the quality of the underlying methods. The described methodology allows for the effective realization of PACS. The assembly of the design methods to a toolchain enables the highly automated design of PACS from the definition of boundary conditions over the shape optimization and the realization of the cell closure up to the production preparation.

The implementation of an alternative method for the shape-optimization and the characterization of PACS, which bases on the AVW, allows for reducing model assumptions, for increasing the accuracy of the results and provides accelerated convergence for computational outcomes. For the cross-sectional design for PACS the local deformations and load distributions are evaluated to reduce stresses peaks and enhance the deformational precision. A novel concept for the sealing of pressurized cells with variable base frame is investigated. The individually shaped end caps not only allow for the reduction of additional in-plane stiffness, but also utilize the cell-inherent pressure to support the deformation of the underlying cell. With the investigation of manufacturing techniques, additional boundary conditions for the realization of PACS are identified and solutions for the successful implementation of test specimens are provided. The FEM-based and experimental evaluation of the design process is performed to improve and validate the underlying design methods. The major achievements in the respective fields are summarized in the following.

Computation of truss geometry

In order to decrease the computational efforts and to accelerate the computationally expensive shape-optimization process, the underlying structural model is reduced to a two-dimensional truss model. The AVW, which bases on the evaluation of the DOF-dependent potential energy of a structure, is compared with the initially published AVM and an FEM-based variant. For the objectives of the computation of the highly geometrical-nonlinear deformations, the calculation of structural stresses and the implementation of the shape-optimization algorithm, the AVW provides the favoured solution. Different levels of detail are implemented with a decreasing extent of model assumptions. The increased computational expense is justified with the enhanced precision of outcomes that are examined for this model. The initial variant with infinitesimal hinge stiffness and rigid cell sides is expanded in two steps for the consideration of finite hinge stiffness and eccentric hinge positions. An improvement of accuracy from $37.14\,\%$ to $9.47\,\%$ of deviation for a high pressure state and from $85.88\,\%$ to $0.59\,\%$ for a second low pressure state, clearly confirms the benefit of increased model complexity.

At the exemplary structure of a variable-camber wing PACS device, the implementation of the model is described in detail. Independent and dependent state variables are determined for both, the simulation of deformations and the shape-optimization procedure. The coupling of DOFs due to the kinematical linking of multiple cells and the determination of boundary conditions is described and enables to reduce the number of unknown variables. The used materials have significant influence on the performance of the PACS. The analytical computation of stresses on the basis of the pressure-loaded and deformed single cell allows the definition of a functional envelope. Depending on the type of material, its stiffness and strength, the deformability and pressure capacity can be determined. FRP materials lead to the highest performance, followed by metal, plastics and ceramic. Elastomeric materials, with a *Young*'s modulus of less than $1\ GPa$, are excluded from the further considerations as they do not provide the necessary tensile stiffness that is necessary to bear the applied pressure loads. For a cell diameter of $50\ mm$ the maximum rotational hinge deformation of $20°$ and a hinge length of $5\ mm$ the optimal hinge thickness for the UD-GFRP material HexPly913 is computed to $0.41\ mm$. The strength of the material theoretically allows for the maximum cell-inherent pressure of $9.82\ MPa$. The necessary formulations for the implementation of the flexure hinge stiffness and the consideration of the cell-inherent pressure are presented. External loads like inertial forces, point loads and aerodynamic pressures are included to expand the numerical model for increased design flexibility. As a substantial step of the design process, the shape-optimization approach that uses the gradient-based *Newton* method is described. In addition to a reduced numerical deviation of less than $1e\text{-}5\ \partial\Pi/\partial u$ of residual energy potential at each rotational DOF, the number of the necessary optimization iterations for convergence is extremely reduced from $2{,}000$ to $20{,}000$ in the underlying publications to about ten, depending on the *Young*'s modulus of the material. This is basically enabled by the coupling of dependencies between independent state variables in the sensitivity matrix. Especially for increased model complexity, the effects of this enhancement are significant. On the basis of the same model, the simulation of the resulting structure for varied load conditions is achieved by using a changed set of optimization parameters. In contrary to the shape-optimization process, the global potential energy of the structure is reduced by the variation of only rotational DOFs. The cell side lengths are kept constant. For varying load sets, the characterization of the structure regarding its deformation behaviour and stiffness against external loads is investigated. The three pressure-dependent phases, deformation, transition and stiffening can be observed. Also the load-dependent structural stresses can be evaluated in the characterization step. Factors of influence like the shape of the cell, the hinge and cell side geometry, the material, the manufacturing and target shapes and the external loads are identified and related to the resulting effects on the structural characteristics and deformation behaviour.

Cross-sectional design

The methods for the transfer of the truss model to a design for the cross-sectional area of the PACS are determined. The major objective is to fulfil the assumptions from the truss model for achieving a high

grade of accordance and thus to provide a precise control of deformations. In addition to the influence on the deformation behaviour of the PACS, peak stresses are reduced by the appropriate design of hinges, cell sides and the transition between them. Five demands on the hinge design are determined. Structural stresses shall be homogeneous over the hinge length. Flexure hinges shall be aligned parallel to the applied forces. The curvature of the hinges shall be adjusted for the applied forces and for the local deformations. The effective hinge position shall correspond with that of the truss model. The wall thickness of cell sides shall ensure high bending and longitudinal stiffness.
The respective design methods are deduced and integrated into a design tool, which allows for the automated transfer from the truss model to the cross-sectional geometry. A reduction of structural stresses within the most highly stresses hinges to $35.45\,\%$ and $35.68\,\%$ is measured for the comparison of two off-design load states with the design load state. The deviation of deformations is simultaneously reduced to $21.04\,\%$ and $28.07\,\%$. The observed homogenous stress distribution over the hinge lengths for the design state confirms the effectiveness of the underlying methods.
Although the structural stresses within the cell sides are lower and less critical, the requirements on the design of cell sides are decisive for the deformation behaviour. High bending and longitudinal stiffness shall guarantee approximately constant cell side lengths, which represent substantial parameters for the kinematic system and are thus responsible for the deformation behaviour. A lightweight structural design results from the sizing of cell sides according to the load-based definition of wall thicknesses. A constant maximum cell side stress for all cell sides and for optional design loads results. The cross-sectional area is expanded by a connection structure that fulfils the bearing conditions of the truss model. The automated export of the geometry information allows for its further use for FEM-based computations and the creation of the geometrically adjusted cell closure solution.

Sealing and pressurization

Available solutions for the sealing of pressurized shape-variable cell tubes are rejected as they implicate two critical problems. Either they are only suitable for test bench implementations, as additional structures are necessary to bear cell-axial loads, or the maximum pressure is limited to less than $0.1\,MPa$. A demand analysis for the specific needs of PACS is performed and results in requirements for pressure allocation, mechanical properties and geometrical boundaries. The conflict of the demands for in-plane flexibility, which is essential to allow for deformations, and high strength and stiffness in cell-axial direction, is identified as major issue. As the state-of-the-art solutions do not provide suitable concepts, a tube-based solution is initially designed, realized and tested, which allowed for pressures up to $0.35\,MPa$. Due to its disadvantages regarding inhomogeneous pressure allocation, the need for secondary load bearing structures and wear, the examinations for an enhanced closure solution are initiated.
A novel concept for sealing shape-variable base frames is developed, characterized and patented. Basing on a specifically developed approach for the creation of isotensoid cell closure geometries, which can be regulated for optional size, the DSEC solution is designed to fulfil strength and stiffness requirements. The successfully implemented aim with the DSEC is to utilize the cell-inherent pressure to support the deformation of the end cap. A pressure-dependent deformation behaviour results for the cell closure, which is nearly identical with that of the underlying PACS cell. The methods for the FEM-based shape computation are presented, the characterization of the resulting geometry is processed and the design sensitivities are investigated. Compared to the competitive solutions of isotensoid and flat plate, the differential moments, which have to be provided by the cellular structure, are reduced to $8.57\,\%$ and $0.85\,\%$. An assembly concept which utilizes the sealing capabilities of the elastomeric closure material is applied for the DSEC structure. The assembly and sealing of the complete PACS with a closure membrane is thereby realized in a single work-step. Experimental tests with pressures up to $0.6\,MPa$ confirm the outcomes of the theoretical investigations.
The results from the investigation of shape-variable sealings only enable the realization of PACS. A highly-efficient solution is found that allows for huge cell-inherent pressures without impeding the deformation of the underlying cell structure. The provided methods can be reused for the design of isotensoid structures or related applications in terms of shape-variable sealings.

Realization

Manufacturing restrictions have significant influence on the design of the cell body structure. The processible materials, the realizable wall thicknesses and achievable geometrical accuracy cause repercussions on the shape-optimization process. The possibility to manufacture geometrical undercuts and the limitation of machining depths has to be considered in the three-dimensional design. An investigation of production techniques for comparable cellular structures is not published previously to this work. A requirement analysis, preliminary manufacturing investigations for property identification and the subsequent weighted evaluation of concepts allows determining the FRP-prepreg, the water-cutting and the SLS process as the most appropriate procedures for single-part production. Manufacturing trials are processed and enable the enhancement of design and quality. One PACS specimen for each of the top-rated processes is realized to perform the experimental evaluation of the numerically investigated methods.

In an equal procedure the SLS process is identified as the most suitable production process for the manufacturing of the cell closure membrane. A key requirement for the examined processes is the ability to produce structures with undercuts because the folds of the DSEC are responsible for the pressure-induced deformation. A DSEC membrane is realized, which is produced from TPU-92A, is completely gas-tight and fulfils the demands on geometrical accuracy. The surface quality enables the coincident use of the elastomeric membrane as sealing gasket.

The enhanced assembly strategy results in a reduction of installation expense from weeks, for the double-row PA12 cantilever, to hours, for the double-row PA2200 PACS specimen.

The most important realizations are the single row HexPly913 cantilever, as the first realization of PACS, the double row PA2200 cantilever, as the first multi row structure, and the variable-surface demonstrator. The final realization, with the dimensions of 1200 x 100 x 500 mm^3 is completely designed according to the herein presented toolchain for the design of PACS. The proof of the generic design process, the evaluation of the pressure dependent stiffness properties and the demonstration of the deformation potentials are the major achievements with this specimen.

Evaluation and progressive improvement of design methods

A procedure for the conception and the progressive improvement of the holistic design process is introduced, which bases on an iterative evaluation of the underlying methods and ultimately allows for the effective realisation of PACS. Beginning with an initial complexity reduction through the division into subsystems, the underlying methods for the design process for PACS are evaluated repeatedly by numerical and experimental investigations. This process is started at an early stage of the research on PACS. The reasons for choosing this approach lie in the increased research flexibility and the evaluation-based quality enhancement. This is demonstrated for the subsystems computation of truss geometry, sealing and pressurization and realization.

Before the functionality of the design process is proven, the evaluation steps for the advancement of the design methods are described. Starting with a single HexPly913 cell, these methods are extended for a single-row structure and finally for a double-row PACS. The inclusion of external forces in the shape optimization and the simulation process expands the applicability of the numerical approach for a variety of target structures. With the implementation of the design process for the DSEC closure, a huge step towards increased cell pressures, weight reduction and deformational accuracy is done. The manufacturing processes are varied and the improved cross-sectional design finally allowed for the use of the moderately suitable PA2200 material and the realization of the most recent demonstrator, the variable-surface PACS.

In the subsequent critical evaluation, the objectives with the design process are opposed with the achieved outcomes and open issues are identified. With a power density of $1.5\,Wkg^{-1}$, the current realizations cannot make full use of the potentials of fluidic actuation. A demonstration of the design process for PACS by means of use-cases summarizes and concludes the research results. At the highly differing example structures of the adaptive car spoiler, the variable-camber wing, the wave power plant and the petal canopy, the flexibility and functionality of the design process is proven.

8.2 Open issues and prospect

Open issues regarding the current design process are identified in the critical evaluation. In the following, the summary of the therein described challenges is complemented by the analysis of research potentials due to modifications of the current design. The discussion of promising applications for PACS and of the necessity for investigations about the related benefits and for specific development issues completes the prospect.

Open issues with the current design of PACS

The accurate computation of deformations is determined as a major objective for the design process. The determination and reduction of structural stresses are necessary to utilise and expand the concept-related performance. Potentials for improvement regarding the modelling of hinge and cell side elements as well as the cell closure membrane are identified.

In the current structural model, the flexure hinges are reduced to a single rotational DOF with linear-elastic stiffness properties. The curvature, orientation and load-based deformation of hinge elements are not considered within the numerical approach for the computation of deformations and structural stresses. The cross section of the PACS is further optimized for only one DP. The shift of the effective hinge position during the change between undeformed and deformed state is of small magnitude but influences the kinematical system and thus leads to an inaccurate global deformation for off-design load states. The determination of the conceivable length of a flexure hinge is non-trivial, as the transition zone between hinge and cell side elements has to be considered. Due to its influence on the stiffness properties an extended approach would increase the achievable deformation accuracy. Nonlinear elastic and plastic strains at the flexure hinges cannot be simulated with the present structural model. Adequate accordance of FEM- and truss-model-based values could be found only for the DP. Fatigue investigations would improve the design process and ensure to utilize but not to exceed the load limits of a PACS after a high number of alternation loadings. For all of these issues, an expansion of the structural model, which allows specifying the flexure hinges' mechanical behaviour in detail, would produce relief. FEM-based simulations and experimental examinations on flexure hinges are necessary to provide the required data for the verification and enhancement of methods.

The assumed rigidity of cell sides causes deviations that depend on the *Young*'s modulus of the used material, on the stresses, which result from the current load state and on the cross-sectional design. The influence of longitudinal and bending strains on the global deformation is quantified and should be considered in the future design process. A two-dimensional FEM-based implementation for the calculation of deformations and for the shape optimization would enhance the design process. The additional computational expense should be contrasted with the increase of accuracy.

The interaction between the pressure-dependent deformation behaviour of the cell closure and the underlying cell is currently not included in the structural model for shape-optimization though it affects the resulting equilibrium state of shape. An optimization of the presented DSEC design for variable instead of constant wall thickness would further allow for increased structural flexibility and a reduction of stresses.

Additional research potentials

The basic geometry of the herein investigated PACS can be described as a compound of pentagonal cells in the first and hexagonal cells in the second cell row. An adaption of this design holds benefits regarding stress reduction, increased deformation potential and avoidance of gaps. Figure 8-1 shows a PACS with tetragonal cells for the first cell row. The computational results from an FEM model are illustrated for the application of an adaptive car spoiler. The shape-optimization approach and the cross-sectional design are adjusted for the novel geometry. The load-based orientation of the topmost hinges in parallel with the surface necessitates the change to a tetragonal geometry and further avoids surface gaps. Hinge-perpendicular loads due to transverse forces within the neutral fibre are prevented. An increase of the deformation potential to about 200 % is measured during preliminary investigations [180]. Further examinations allow evaluating the impact on the characteristics of PACS.

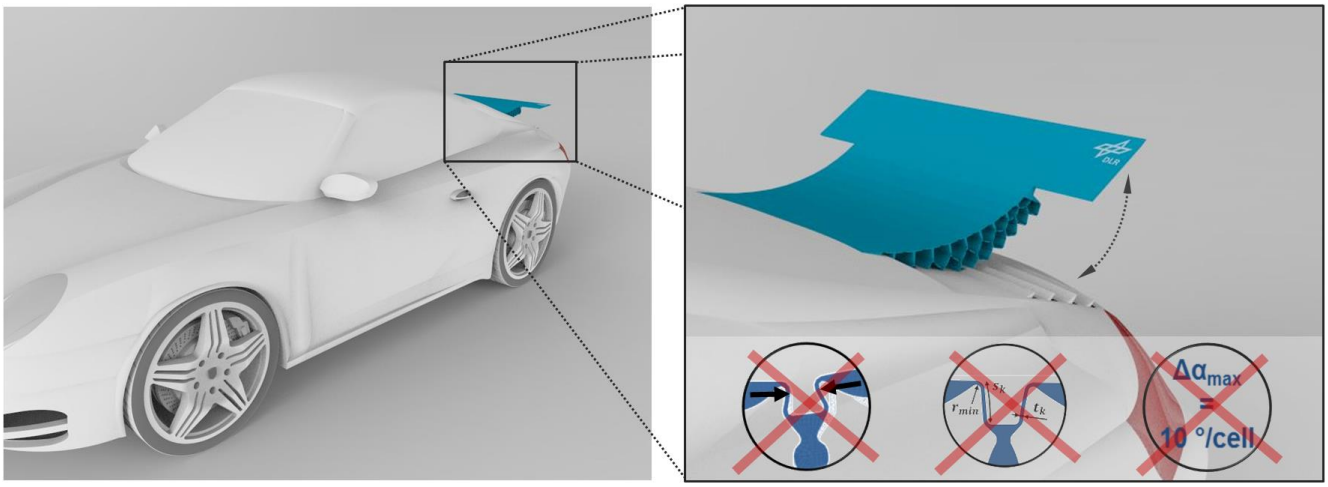

Figure 8-1: Modification of basic cell geometry for tetragonal cells in the first cell row, shown at the exemplary application of an adaptive car spoiler

Essential advantages of compliant PACS with flexure hinges are given by the in-plane fluid tightness and the possibility for integral design. As an increase of the hinge thickness, which would result in reduced pressure-based stresses, simultaneously raises the stresses due to bending, the ability to size compliant PACS is severely limited. The use of conventional hinges would allow for increased pressures and deformations and thus holds the potential to significantly enhance the performance of PACS. The non-integral design of the cell body further reduces the manufacturing requirements. Investigations regarding the sealing of conventional pinned hinges have to be performed.
The presented cross-sectional PACS design primarily bases on the applied loads. A greater focus on design simplifications and on the increase of the mechanical strength could lead to a decrease of the currently high production expense and to an extension of the functional envelope. The replacement of the rigid cell sides by flexible textile structures is one design option that should be considered.
PACS are conceived to alter the shape of single-curved structures. For the shape variation of double-curved structures a similar concept is described by Pagitz et al. [150]. The research on such structures is in its beginnings and only performed theoretically for the described case. Investigations in this field may result in the cancellation of the limitation for two-dimensional deformations.

Applications for PACS

An extract of possible applications for PACS is presented and covers the automotive, the aerospace, the energy and the architecture sector. As the technology of shape-variable structures in general is not state-of-the-art, currently realized representatives usually base on mechanisms and rigid-body motion. Opening up new areas of application for PACS is an important task for future investigations as it only allows exploiting the related benefits.
A decisive aspect for the identification of applications is the sophisticated characterization of the structural properties. In addition to the already investigated actuation forces, examinations on the basis of analytical equations or *Computational Fluid Dynamics* (CFD) should be performed to analyse the fluid flow within the cells and thus the resulting actuation speeds. Also dynamic effects, which are caused by the fluid-structure-interaction, can be examined. In this context, an efficiency enhancement and a limitation of the maximal deformations can be achieved by filling “dead” volumes within the cells with foam material. The comprehensive investigation of the power density and the efficiency of PACS should include the weight and efficiency of the peripheral system, which is needed for the pressure supply and regulation.
For each application of PACS an error case strategy is of relevance. A solution for preventing leakage, redundant mechanisms like travel stops and a segmented design increase the reliability of the shape-variable structure. Maintenance and repair concepts can further raise the value of this structural concept. The realization of a variable-camber wing for a wind tunnel test would not only demonstrate the performance of PACS at a particular application but also raise the technological readiness level.

Appendix

A Finite element method

The FEM is explained at the exemplary beam structure that is illustrated in Figure A-1. A suitable element to describe the given structural system is the bar element. In the presented case, it holds the necessary minimum of only one DOF per node and thus reduces the computational efforts. The stiffness $K_{Bar,ab}$ of the single element with nodes a and b, cross sectional area A and length l, can be calculated by [153]:

$$K_{Bar,ab} = \frac{\partial^2 W}{\partial x_a \partial x_b} = EA \int_l \frac{\partial \varepsilon_{11}}{\partial x_a} \frac{\partial \varepsilon_{11}}{\partial x_b} \mathrm{d}x = \frac{EA}{l^2} \int_l \frac{\partial (x_2 - x_1)}{\partial x_a} \frac{\partial (x_2 - x_1)}{\partial x_b} \mathrm{d}x, \text{ to} \tag{A.1}$$

The stiffness matrix for this element results in

$$\boldsymbol{K}_{Bar} = \begin{bmatrix} \frac{EA}{l} & -\frac{EA}{l} \\ -\frac{EA}{l} & \frac{EA}{l} \end{bmatrix}. \tag{A.2}$$

The strain ε_{11} in bar axial direction, is determined according to *Hook*'s law [181] with knowledge of the beam's cross section A, the beam length l and the applied material's *Young*'s modulus E. Figure A-1 depicts the exemplary setup for two bars.

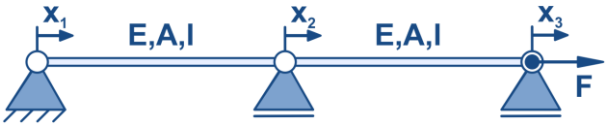

Figure A-1: Exemplary two-bar problem for the explanation of an FEM computation

The global stiffness matrix for an FEM model can be found by the superposition of the element stiffness matrices. For the given system it is

$$\boldsymbol{K} = \begin{bmatrix} \frac{EA}{l} & -\frac{EA}{l} & 0 \\ -\frac{EA}{l} & \frac{2EA}{l} & -\frac{EA}{l} \\ 0 & -\frac{EA}{l} & \frac{EA}{l} \end{bmatrix}. \tag{A.3}$$

The evaluation of equation (2.1) results in

$$\begin{Bmatrix} F_1 \\ 0 \\ F \end{Bmatrix} = \frac{EA}{l} \begin{bmatrix} 1 & -1 & 0 \\ -1 & 2 & -1 \\ 0 & -1 & 1 \end{bmatrix} \begin{Bmatrix} 0 \\ x_2 \\ x_3 \end{Bmatrix}. \tag{A.4}$$

With the computation of the inverse matrix $\boldsymbol{K}^{-1}$ the system of equations can be solved. For this exemplary case, the low number of DOFs allows to deduce an analytical solution. The displacements at the second and third roller supports are $x_2 = l/EA$ and $x_3 = 2l/EA$. The reaction force at the fixed support is $F_1 = F$.

B Approach of volume maximization for structural optimization

In order to select the most advantageous approach for the structural optimization of PACS, the AVM is compared with the AVW in chapter 2.1.1. Both variants are used to compute the force vector $\boldsymbol{f}$, which is the optimization variable and vanishes for the equilibrium state of shape of the structure. The difference of both approaches lies in the computation of $\boldsymbol{f}$, the related numerical efforts and the expandability of the underlying equations for including internal and external forces. Further, the strategy for the shape-optimization problem is solved differently. This section completes the information about the structural optimization according to Pagitz et al. [1] and thus clarifies the differences of both approaches.

Computation of deformations

An iterative solving process that uses *Newton*'s method is applied for the computation of deformations. The vector of unknown rotational DOFs $\boldsymbol{u}_{z+1}$ for the iteration step $z+1$ is thus computed by

$$\boldsymbol{u}_{z+1} = \boldsymbol{u}_z - \boldsymbol{K}(\boldsymbol{u}_z)^{-1}\boldsymbol{f}(\boldsymbol{u}_z), \text{ with} \tag{B.1}$$

$$\boldsymbol{K} = \sum \boldsymbol{K}_{Pent} + \sum \boldsymbol{K}_{Hex} = \sum p_{Pent} \frac{\partial^2 V_{Pent}}{\partial \boldsymbol{u}_{Pent}^2} + \sum p_{Hex} \frac{\partial^2 V_{Hex}}{\partial \boldsymbol{u}_{Hex}^2}. \tag{B.2}$$

For the calculation of the increment $\Delta\boldsymbol{u} = \boldsymbol{u}_{z+1} - \boldsymbol{u}_z$ of the rotational DOFs for the current state z, the stiffness matrix $\boldsymbol{K}$ is computed and can be found as the weighted second derivative of the respective volumes. It is shown by Pagitz et al. that for the given cell side lengths $\boldsymbol{a}$ the equilibrium state that is defined by the vector of cell side angles $\boldsymbol{u}$, can be calculated iteratively.
Following equation (B.1) the possibility to consider additional loads is not described. The advantage of an efficient computation of the cells' volumes V (cf. [1]) is outclassed by the missing possibility to optimize a PACS for a real operating condition including various external loads. Supplementary equations are necessary to expand the AVM for the consideration of further load types what would increase the calculation effort.

Shape optimization

For the objective of shape optimization a different approach than the one presented in chapter 2.4 is chosen by Pagitz et al. Their shape-optimization method bases on the computation of the *Hessian* matrix $\boldsymbol{H}$, which considers the change of the surface independent state variables $\boldsymbol{u}$ that are determined by the definition of the target shape, due to the change of cell side lengths $\boldsymbol{a}$:

$$\boldsymbol{H} = \begin{bmatrix} \frac{\partial \boldsymbol{f}_{Pent}}{\partial \boldsymbol{a}_{Pent}} & \frac{\partial \boldsymbol{f}_{Hex}}{\partial \boldsymbol{a}_{Hex}} \end{bmatrix} = \begin{bmatrix} p_{Pent} \frac{\partial^2 V_{Pent}}{\partial \boldsymbol{u}_{Pent} \partial \boldsymbol{a}_{Pent}} & p_{Hex} \frac{\partial^2 V_{Hex}}{\partial \boldsymbol{u}_{Hex} \partial \boldsymbol{a}_{Hex}} \end{bmatrix}. \tag{B.3}$$

Together with the stiffness matrix for both current states of shape $\boldsymbol{K}_{st1,st2} = [\boldsymbol{K}_{st1} \quad \boldsymbol{K}_{st2}]$ the sensitivity matrix $\boldsymbol{S}_{st1,st2}$, which relates the change of cell side lengths to the change of the surface independent state variables, is computed:

$$\boldsymbol{S}_{st1,st2} = \boldsymbol{K}_{st1,st2}^{-1}\boldsymbol{H}. \tag{B.4}$$

As the stiffness matrix $\boldsymbol{K}_{st1,st2}$ is not quadratic, the *Moore-Penrose* method is utilized to compute the pseudo inverse matrix. The 2-norm of the matrix is thus minimized. Computing the increment $\Delta\boldsymbol{a} = \boldsymbol{a}_{z+1} - \boldsymbol{a}_z$ for the current cell side lengths $\boldsymbol{a}_z$ and the associated cell side angles in equilibrium state allows to iteratively approaching the target shape. $\boldsymbol{r}_{VM}$ is the residuum shape vector, which describes the difference between the angles of current and target state of shape. The vector of cell side lengths $\boldsymbol{a}_{z+1}$ for the iteration step $z+1$ is

$$\boldsymbol{a}_{z+1} = \boldsymbol{a}_z - \boldsymbol{S}_{st1,st2}\boldsymbol{r}_{VM,st1,st2}. \tag{B.5}$$

Compared to the shape-optimization procedure that is used for the herein presented design process for PACS (cf. chapter 2.4), this approach distinguishes by the computation of the sensitivity matrix $\boldsymbol{S}_{st1,st2}$. According to the approach by Pagitz et al. it is sufficient to relate a change of the inner cell side lengths $\boldsymbol{a}_1$ to the change of the surface independent state variables $\boldsymbol{u}_0$ (cf. chapter 2.2.1). The effects of a change of the cell side lengths on the inner independent state variables $\boldsymbol{u}_1$ are thereby ignored. As a result, a substantially increased number of iterations if necessary and the optimization converges to a non-vanishing value for the force vector $\boldsymbol{f}$. For the given optimization objectives the equilibrium state can thus not be computed exactly.
Pagitz et al. [145] investigated the convergence behaviour of their optimization approach at an exemplary double row PACS with circular target shapes that consists of 60 pentagonal in the first cell row. Depending on the applied materials and thus the hinge bending stiffness, the number of necessary iterations lies between 2,000 and 20,000. Both, a residual energy potential Π and a non-vanishing residuum vector $\boldsymbol{r}$ are presented and confirm the advantages of the optimization approach presented in chapter 2.

C Double row PACS cantilever for comparison of structural models

According to the examinations of Pagitz et al. [1] the deformations of a double row PACS are computed with the herein used structural model, which bases on the AVW. The structure with ten pentagonal cells in the first and ten hexagonal cells in the second cell row is shown in Figure C-1. Each of the cells within the same cell row are of identical shape. Besides the geometrical information that is given in terms of the cell side lengths, LBCs are illustrated. A line load of $F = 5\,kN/m$ is applied to the unattached end of the cantilever. The hinges are assumed to be frictionless and possess infinitesimal rotational stiffness. Two states of shape are computed for the pressure vectors $\boldsymbol{p}_{int,st1}$ and $\boldsymbol{p}_{int,st2}$.

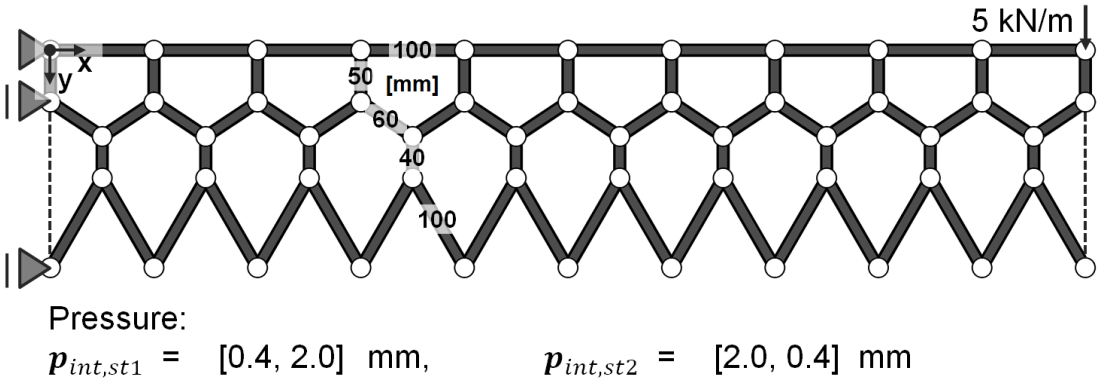

Figure C-1: Initial geometry and load settings for the computation of deformations for the comparison the AVW and the AVM

D Generic double row PACS

The convergence behaviour of the shape-optimization process is investigated in chapter 2.4.3. Basing on a generic double row PACS, the effects of different initial geometries and of varying hinge stiffnesses on the optimization process are examined. The exemplary PACS consist of $n_1 = 5$ pentagonal cells in the first cell row and $n_2 = 6$ cells in the second row. Figure D-1 illustrates the geometries that are described by three different sets of initial model parameters. The baseline set of initial parameters that define the first structure Geo_0, top, is adapted under the designation Geo_+ (Figure D-1, bottom-left) for a better initial correlation with the optimization objective. The third set of initial model parameters, Geo_- (Figure D-1, bottom-right), is defined to investigate the effects of poorly chosen initial model parameters. The cell side lengths, which are used for describing the initial model parameters, are given in Table D-2, Table D-3 and Table D-4.
In addition to the variation of the initial geometry, the hinge stiffnesses are altered to investigate their effects on the optimization procedure. On the basis of the baseline geometry Geo_0, the double row PACS is optimized for infinitesimal stiffness ($E_0 = 0\ GPa$) and for the Young's moduli $E_1 = 10\ GPa$ and $E_2 = 20\ GPa$. Table D-1 shows the test matrix for the investigations.

The optimization objective is defined by the two deformational target shapes *st1* and *st2*, which are both described by circular arcs. For the pressure vector $\boldsymbol{p}_{int,st1}$ the structures shall bend downwards by $\Delta u_{0,st1} = 5°$ per cell of the upper cell row. The total rotation of $\Delta\beta = 25°$ results for the right bearing. For the internal pressure load $\boldsymbol{p}_{int,st2}$, the surface deformation is given by $\Delta u_{0,st2} = -5°$ per pentagonal cell.

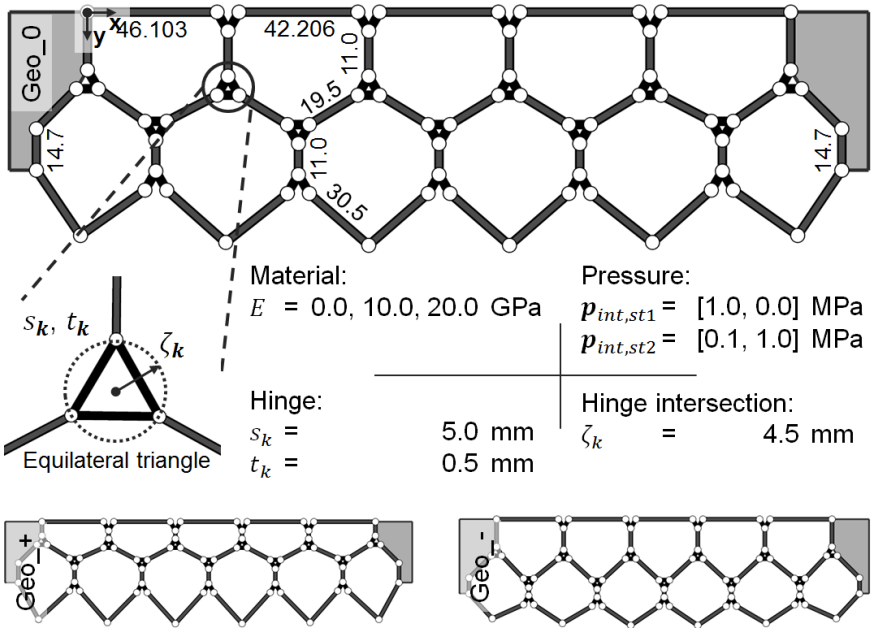

Figure D-1: Three different initial sets of model parameters for investigating the convergence behaviour of the shape-optimization procedure at the exemplary structure of a generic double row PACS

Table D-1: Test matrix for examining the convergence behaviour of the optimization procedure

	Geo_-	**Geo_0**	**Geo_+**
$\boldsymbol{E_0 = 0.0\ GPa}$		X	
$\boldsymbol{E_1 = 10.0\ GPa}$	X	X	X
$\boldsymbol{E_2 = 20.0\ GPa}$		X	

Table D-2: Cell side lengths of initial configuration Geo_0

Number of cell i	Cell side length $a_{CS,k}$ at cell side j [mm]					
h=1	**1**	**3**	**5**	**7**	**9**	**11**
1	46.103	11.000	19.500	19.500	15.500	
2	42.206	11.000	19.500	19.500	-	
3	42.206	11.000	19.500	19.500	-	
4	42.206	11.000	19.500	19.500	-	
5	46.103	15.500	19.500	19.500	-	
h=2	**1**	**3**	**5**	**7**	**9**	**11**
1	14.700	19.500	-	11.000	30.500	30.500
2	-	-	-	11.000	30.500	30.500
3	-	-	-	11.000	30.500	30.500
4	-	-	-	11.000	30.500	30.500
5	-	-	-	11.000	30.500	30.500
6	-	-	19.500	14.700	30.500	30.500

Table D-3: Cell side lengths of improved initial configuration Geo_+

Number of cell i	Cell side length $a_{CS,k}$ at cell side j [mm]					
h=1	**1**	**3**	**5**	**7**	**9**	**11**
1	46.103	6.000	19.500	19.500	10.500	
2	42.206	6.000	19.500	19.500	-	
3	42.206	6.000	19.500	19.500	-	
4	42.206	6.000	19.500	19.500	-	
5	46.103	10.500	19.500	19.500	-	
h=2	**1**	**3**	**5**	**7**	**9**	**11**
1	14.700	19.500	-	11.000	31.500	31.500
2	-	-	-	11.000	31.500	31.500
3	-	-	-	11.000	31.500	31.500
4	-	-	-	11.000	31.500	31.500
5	-	-	-	11.000	31.500	31.500
6	-	-	19.500	14.700	31.500	31.500

Table D-4: Cell side lengths of poorly chosen initial configuration Geo_-

Number of cell i	Cell side length $a_{CS,k}$ at cell side j [mm]					
h=1	**1**	**3**	**5**	**7**	**9**	**11**
1	46.103	16.000	23.500	23.500	20.500	
2	42.206	16.000	23.500	23.500	-	
3	42.206	16.000	23.500	23.500	-	
4	42.206	16.000	23.500	23.500	-	
5	46.103	20.500	23.500	23.500	-	
h=2	**1**	**3**	**5**	**7**	**9**	**11**
1	11.700	23.500	-	6.000	25.500	25.500
2	-	-	-	6.000	25.500	25.500
3	-	-	-	6.000	25.500	25.500
4	-	-	-	6.000	25.500	25.500
5	-	-	-	6.000	25.500	25.500
6	-	-	23.500	11.700	25.500	25.500

E Variable-camber wing PACS

The following data summarizes the computational data about the variable-camber wing PACS device for 0.6 to 0.9 of the chord length of a NACA 0012 profile and a maximum deflection of $\beta_2 = 15°$. The utilized material, the initial geometry and the LBCs are defined prior to the shape-optimization process. Figure E-1 holds the global geometrical information, Table E-1 lists point loads at the connection structure, Table E-2 summarizes aerodynamic pressures and Table E-3 gives the required information about initial cell side lengths. The resulting cell side lengths, which are modified in the shape-optimization process, are presented in Table E-4. The variable cell sides are marked in italics to distinguish them from fixed parameters that are predefined by restrictions of the connection structure or the neutral fibre.

The effects of the cell-internal pressure on the structural stiffness of the variable-camber PACS device are investigated in chapter 2.6.4. Figure E-2 illustrates the equilibrium states of shape that are calculated with structural model variant 3 for constant external loads and different cell-inherent pressures. According to Figure 2-25, which summarizes the pressure-dependent deformation behaviour of the variable-camber wing PACS, the pressure ratios of the two target loads are kept constant whereas the pressure vectors are multiplied with different pressure factor *PF*.

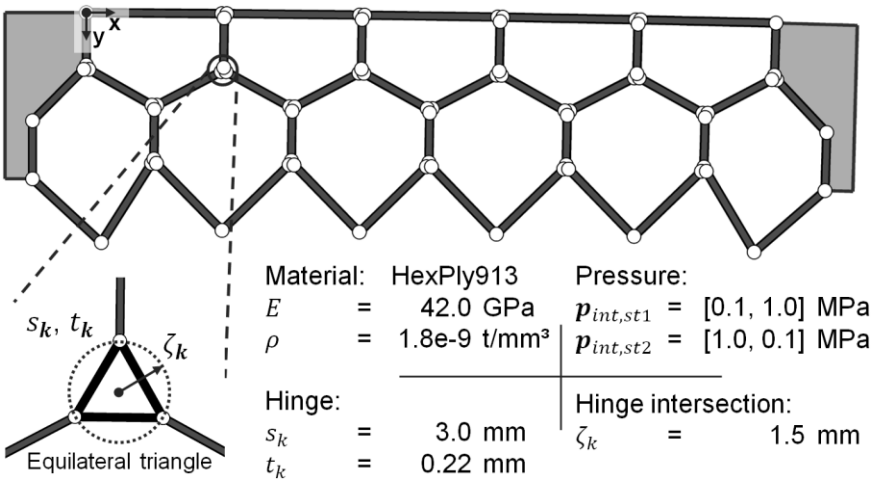

Figure E-1: Initial settings for shape-optimization procedure of variable-camber wing PACS device

Table E-1: Point loads at right hand connection structure

	Point load vectors $f_{pl,k}$ [N/m]			
	st1		**st2**	
$k = [h,i,j]$	x-comp	y-comp	x-comp	y-comp
[1,5,3]	-0.831	-4.528	-11.309	425.137
[1,5,5]	-0.575	-0.050	-267.899	-7.511

Table E-2: Aerodynamic pressure loads for both states of shape

		Aerodynamic pressure $p_{ad,k}$ at cell side *j* [Pa]					
		st1			st2		
Number of cell *i*	h=1	**1**	**2**	**10**	**1**	**2**	**10**
	1	715.6	615.8	-	2884.3	2679.4	-
	2	516.9	420.7	615.8	2492.6	2172.4	2679.4
	3	322.9	217.4	420.7	1866.7	1412.3	2172.4
	4	117.8	-6.2	217.4	966.1	546.7	1412.3
	5	-152.3	-	-6.2	122.7	-	546.7

Table E-3: Cell side lengths as used for the initial model parameters

	Cell side length $a_{CS,k}$ at cell side *j* [mm]						
Number of cell *i*	h=1	**1**	**3**	**5**	**7**	**9**	**11**
	1	71.093	25.957	38.077	38.077	27.457	
	2	69.794	25.957	38.077	38.077	-	
	3	69.794	25.957	38.077	38.077	-	
	4	69.794	25.957	38.077	38.077	-	
	5	71.093	27.457	38.077	38.077	-	
	h=2	**1**	**3**	**5**	**7**	**9**	**11**
	1	30.457	-	-	25.957	49.175	49.175
	2	-	-	-	25.957	49.175	49.175
	3	-	-	-	25.957	49.175	49.175
	4	-	-	-	25.957	49.175	49.175
	5	-	-	-	25.957	49.175	49.175
	6	-	-	-	30.457	49.175	49.175

Table E-4: Cell side lengths of optimized configuration, variables that are modified during optimization are marked in italics

	Cell side length $a_{CS,k}$ at cell side *j* [mm]						
Number of cell *i*	h=1	**1**	**3**	**5**	**7**	**9**	**11**
	1	71.093	*24.263*	*34.285*	*37.127*	27.457	
	2	69.794	*27.041*	*37.170*	*40.768*	-	
	3	69.794	*27.382*	*37.221*	*37.452*	-	
	4	69.794	*23.284*	*42.705*	*37.322*	-	
	5	71.093	27.457	*38.363*	*35.874*	-	
	h=2	**1**	**3**	**5**	**7**	**9**	**11**
	1	30.457	-	-	*15.797*	*43.146*	*43.126*
	2	-	-	-	*22.454*	*45.088*	*45.094*
	3	-	-	-	*23.186*	*46.907*	*46.939*
	4	-	-	-	*22.026*	*47.044*	*47.024*
	5	-	-	-	*15.377*	*44.561*	*44.763*
	6	-	-	-	30.457	*42.918*	*42.890*

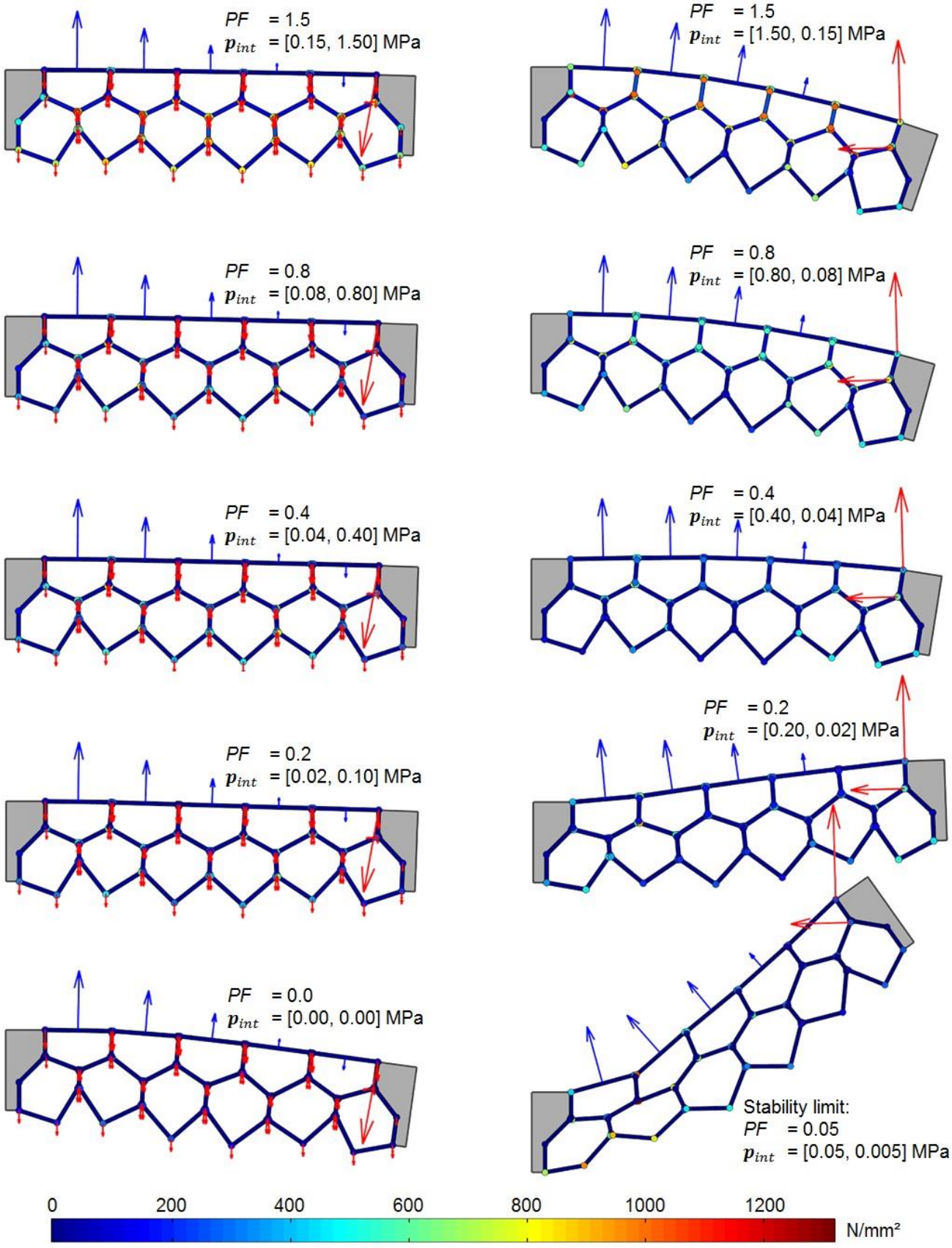

Figure E-2: Deformation of variable-camber wing PACS due to the external loads of the target load states *st1* (l.) and *st2* (r.) and different internal pressures p_{int}

F Structural model and computation process for of isotensoid cell closure

The methods for the FEM-based shape optimization of the isotensoid cell closure for PACS are described in chapter 4.2.5. Figure F-1 illustrates the initial shape of the closure, which is equal to the flat plate, and provides information about the utilized finite elements and the underlying LBCs.

The input data for the optimization is given by the cell contour and the target pressure p_t. The area that is enclosed by the cell contour is meshed with linear three-node shell elements, which represent the initial geometry of the cell closure structure. The nodes that lie on the cell contour are supported rigidly for all translational DOFs. Rotational DOFs are released, to allow for the shell elements to redirect according to the applied loads.
In order to consider the geometrical requirements ($R_{CC}C1$) on the cell closure (cf. chapter 4.1), the structural model is supplemented by elements that allow to describe the cell walls. Therefore, the cell wall is represented by four-node shell elements. Similar to the underlying cell contour, the translational DOFs of this structure are clamped. To avoid an intersection of cell closure and cell wall, contact elements are superimposed to both structures. The contact condition is defined to allow frictionless gliding. The element edge length is 1 mm for the cell closure and 5 mm for the cell wall structure.

As presented in chapter 4.2.5, a geometrical deviation of $\left|\Delta r_{isot,z}/r_{isot,t}\right| = 4.72\text{e}-8$ related to the target closure height of $r_{isot,t} = 25\,mm$ is reached after $z = 14$ iterations. Figure F-2 shows the cell closure structure for the iteration steps $z = 0$ to $z = 8$ and thus visualizes the change of geometry during the optimization process.

No.	Element type	Nodes	Ansys desig.
1	Shell	3	Shell181
2	Shell	4	Shell181
3	Contact	3	Targe170
4	Contact	4	Conta173

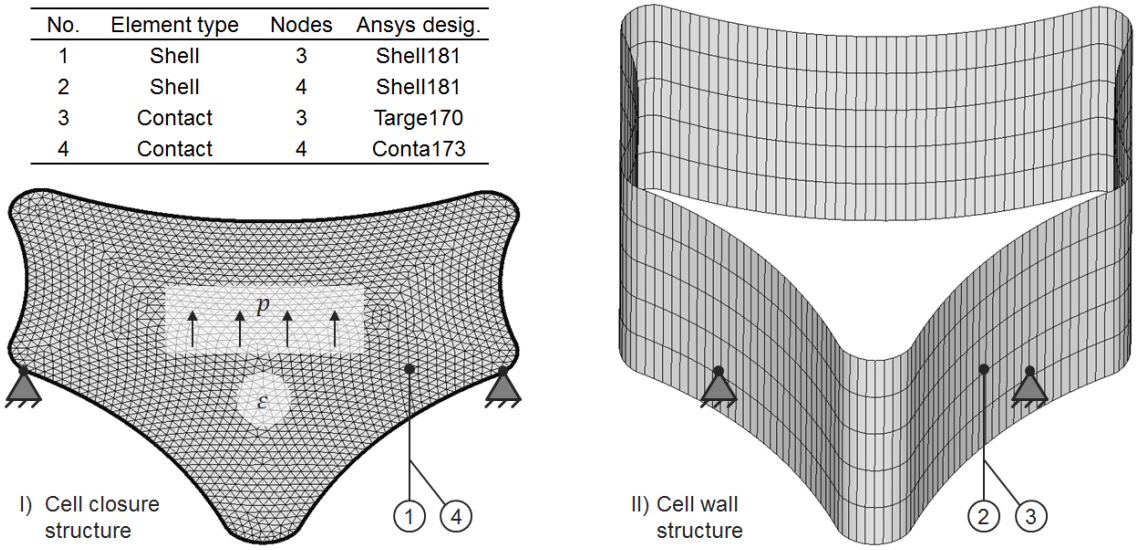

Figure F-1: Description of utilized elements and LBCs for the structural model that is used to compute the isotensoid cell closure

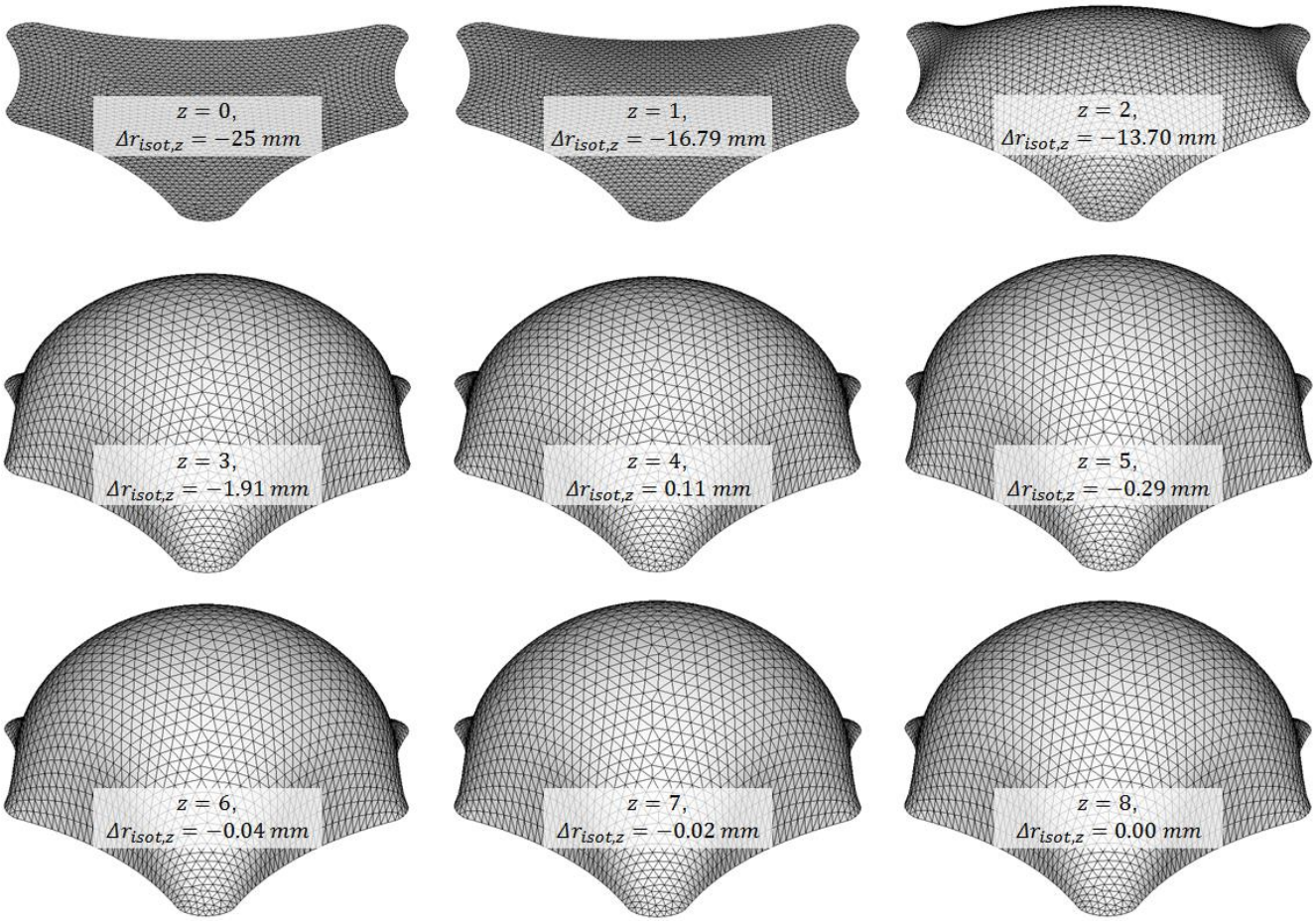

Figure F-2: Shape variation during optimization process for the isotensoid cell closure structure for the iteration steps z = 0 to z = 8

G Weighting factors for valuation of production process

The comparison of requirements for manufacturing processes for cell body and cell closure structure (see chapter 5) allows for the determination of weighting factors. Table G-1 includes the comparison of couples of requirements for the production of the cell body structure, which leads to the weighting factors for the individual demands. The weighting factors for the cell closure are defined in Table G-2.

Table G-1: Comparison of requirements for cell body production processes for determination of weighting factors (Valuation: 1/9 = extremely irrelevant … 9 = extremely important)

Requirements	$R_{CB}1$	$R_{CB}2$	$R_{CB}3$	$R_{CB}4$	$R_{CB}5$	$R_{CB}6$	$R_{CB}7$	$R_{CB}8$	$R_{CB}9$	WF
$R_{CB}1$	**1**	**7**	**4**	**4**	**1**	**5**	**7**	**1**	**9**	
$R_{CB}1$/SUM	0.244	0.239	0.288	0.203	0.251	0.183	0.266	0.226	0.173	**0.230**
$R_{CB}2$	**1/7**	**1**	**1/5**	**1/4**	**1/7**	**2**	**2**	**1/4**	**4**	
	0.035	0.034	0.014	0.013	0.036	0.073	0.076	0.057	0.077	**0.046**
$R_{CB}3$	**1/4**	**5**	**1**	**5**	**1/4**	**1**	**3**	**1/3**	**7**	
	0.061	0.171	0.072	0.253	0.063	0.037	0.114	0.075	0.135	**0.109**
$R_{CB}4$	**1/4**	**4**	**1/5**	**1**	**1/5**	**3**	**1**	**1/3**	**7**	
	0.061	0.137	0.014	0.051	0.050	0.110	0.038	0.075	0.135	**0.075**
$R_{CB}5$	**1**	**7**	**4**	**5**	**1**	**7**	**7**	**1**	**9**	
	0.244	0.239	0.288	0.253	0.251	0.256	0.266	0.226	0.173	**0.244**
$R_{CB}6$	**1/5**	**1/2**	**1**	**1/3**	**1/7**	**1**	**1**	**1/7**	**3**	
	0.049	0.017	0.072	0.017	0.036	0.037	0.038	0.032	0.058	**0.039**
$R_{CB}7$	**1/7**	**1/2**	**1/3**	**1**	**1/7**	**1**	**1**	**1/4**	**3**	
	0.035	0.017	0.024	0.051	0.036	0.037	0.038	0.057	0.058	**0.039**
$R_{CB}8$	**1**	**4**	**3**	**3**	**1**	**7**	**4**	**1**	**9**	
	0.244	0.137	0.216	0.152	0.251	0.256	0.152	0.226	0.173	**0.201**
$R_{CB}9$	**1/9**	**1/4**	**1/7**	**1/7**	**1/9**	**1/3**	**1/3**	**1/9**	**1**	
	0.027	0.009	0.010	0.007	0.028	0.012	0.013	0.025	0.019	**0.017**
Σ R_{CB}:	**4.097**	**29.250**	**13.876**	**19.726**	**3.990**	**27.333**	**26.333**	**4.421**	**52.000**	**1**

Requirements — Weighting factors

Table G-2: Comparison of requirements for cell closure production processes for determination of weighting factors (Valuation: 1/9 = extremely irrelevant … 9 = extremely important)

Requirements	$R_{CC}1$	$R_{CC}2$	$R_{CC}3$	$R_{CC}4$	$R_{CC}5$	$R_{CC}6$	WF
$R_{CC}1$	**1**	**5**	**1**	**5**	**1/2**	**9**	
$R_{CC}1$/SUM	0.222	0.271	0.290	0.236	0.125	0.329	**0.255**
$R_{CC}2$	**1/5**	**1**	**1/7**	**3**	**1/5**	**7**	
	0.044	0.054	0.041	0.142	0.050	0.256	**0.070**
$R_{CC}3$	**1**	**7**	**1**	**5**	**1**	**9**	
	0.222	0.379	0.290	0.236	0.251	0.329	**0.282**
$R_{CC}4$	**1/5**	**1/3**	**1/5**	**1**	**1/7**	**7**	
	0.044	0.018	0.058	0.047	0.036	0.256	**0.042**
$R_{CC}5$	**2**	**5**	**1**	**7**	**1**	**9**	
	0.443	0.271	0.290	0.331	0.339	0.214	**0.334**
$R_{CC}6$	**1/9**	**1/7**	**1/9**	**1/7**	**1/9**	**1**	
	0.025	0.008	0.032	0.007	0.038	0.024	**0.018**
Σ R_{CC}:	**4.511**	**18.476**	**3.454**	**21.143**	**2.954**	**42.000**	**1**

Requirements — Weighting factors

H Discarded production processes

Investigated production processes for cell body structure

A brief summary of rejected but examined manufacturing processes shall list their disadvantages for the current needs within the scope of single-part production and point out their potentials for future application. In addition to presenting the processes that are utilized for the production of demonstrators, the herein given examination of further techniques allows assessing alternative concepts for their suitability for quantity manufacturing. Figure H-1 illustrates the results from investigating three production techniques each, for processing plastics and metals. Characteristic values for the utilized materials can be found in Table 2-6.

The first three manufacturing processes are selected for the processing of plastic materials. FDM is an additive rapid prototyping process for handling fusible materials. Plastic filament or metal wires can be applied to a building platform in layers. Within the examined process, the thermoplastic material ULTEM 1010 from Stratasys is used, as it holds a high ratio of tensile strength over *Young*'s modulus (cf. Table 2-6). Manufacturing trials showed that the local strength properties fall considerably below the datasheet values. The reason for this lies in the positioning of start points, which are defined by the slicing software and represent cut points for the filament. The strength of the locally discontinuously produced material is decreased to about two thirds of the continuously produced material [182]. The bearable maximum cell pressure depends on the square of this reduction factor, as shown in equation (2.39). Without a reliable strategy for avoiding these discontinuities at the critical flexure hinge elements, this process with its related materials does not suit the requirements. A novel FDM-based technology, which is distributed by *Markforged*, allows for the integration of glass and carbon fibres. Together with an appropriate software solution it may produce relief for the current issues.
For the sliced construction of a PACS cell body, a series of panel cuttings is produced in a laser cutting process with a CO2 cutting system from *Eurolaser GmbH*. The cross section of the cellular structure is therefore cut out of PA12 sheets with a thickness of $10\ mm$. Due to the divergence of the laser beam for increasing distance from its focal point, an hourglass- or cone-shaped cut contour results. This effect is strengthened by the refraction of the beam in the polymeric material. A minimum wall thickness of $t_{H,min} = 1.0\ mm$ for a sheet thickness of $10\ mm$ is identified. For a decrease of sheet thickness to $5\ mm$, the accuracy of this process is sufficient to manufacture wall thicknesses of about $0.5\ mm$. With this, the laser cutting is outnumbered by the water cutting process and thus rejected.
For the demand for quantity manufacturing, injection moulding is investigated in theoretical manner. The company *RICONE GmbH* is commissioned to perform feasibility studies about the manufacturability of a double row PACS in an injection moulding process. Simulations showed that the mould cavity can be filled completely with the recommended material *DuPont* Hytrel 7246. Draft angles normally lie above the minimum of 1°. For a depth of $d = 500\ mm$, this limit value would result in a thickness reduction of $\Delta t = 8.7\ mm$ for hinges and cell sides. It can be seen that such a boundary condition is not compatible with the assumption of an approximately constant hinge thickness. High demoulding forces allow avoiding draft angles for limited structural depths but increase the risk for production defects. Further, unavoidable casting seams reduce the strength of flexure hinges substantially. For this degradation of performance, a process- and material-dependent range of 10 % to 90 % is given by *RICONE GmbH*. Shrinkage of 1.6 % can be expected for *DuPont* Hytrel 7246 [183]. Extensive efforts regarding the tool design and the determination of process parameters may lead to a successful implementation, but are not economically viable at the present state of concept.

According to Table 2-6 and equation (2.39), the processing of metals raises the cell body's load capacity for a reduced optimal wall thickness and causes higher deformability and increased bearable pressure loads. For the SLM process a minimum hinge thickness of $t_{H,min} = 0.5\ mm$ for the utilization of the titan alloy CL 40TI (Ti6Al4V) is obligatory. High degrees of filling which result in a volume fraction of voids of less than 0.5 % and a density of 96 % to 99 % are documented by

Kasperovich et al. [184] and lead to yield strengths of $R = 800\,MPa$ to $R = 1000\,MPa$. As this process momentarily is far from standard application and restricted to special alloys, the raw materials, the manufacturing and the subsequent heat treatment are still expensive and result in costs of approximately $200\,€/kg$. For future applications and prototypes, the advantages of this process may justify its costs.
Slightly better results are reached with the wire-cut EDM process that can be used for cutting electrically conductive materials. A flexure hinge with a thickness of $t_{H,min} = 0.3\,mm$ can be manufactured with adequate accuracy for a workpiece depth of $d = 500\,mm$. A double cell structure that is manufactured in a production trial and made from the aluminium alloy EN-AW-7075 is illustrated in Figure H-1. As this process does not allow for manufacturing integral sealing beads or fluid ducts, these structural elements have to be realized in a separate production step.

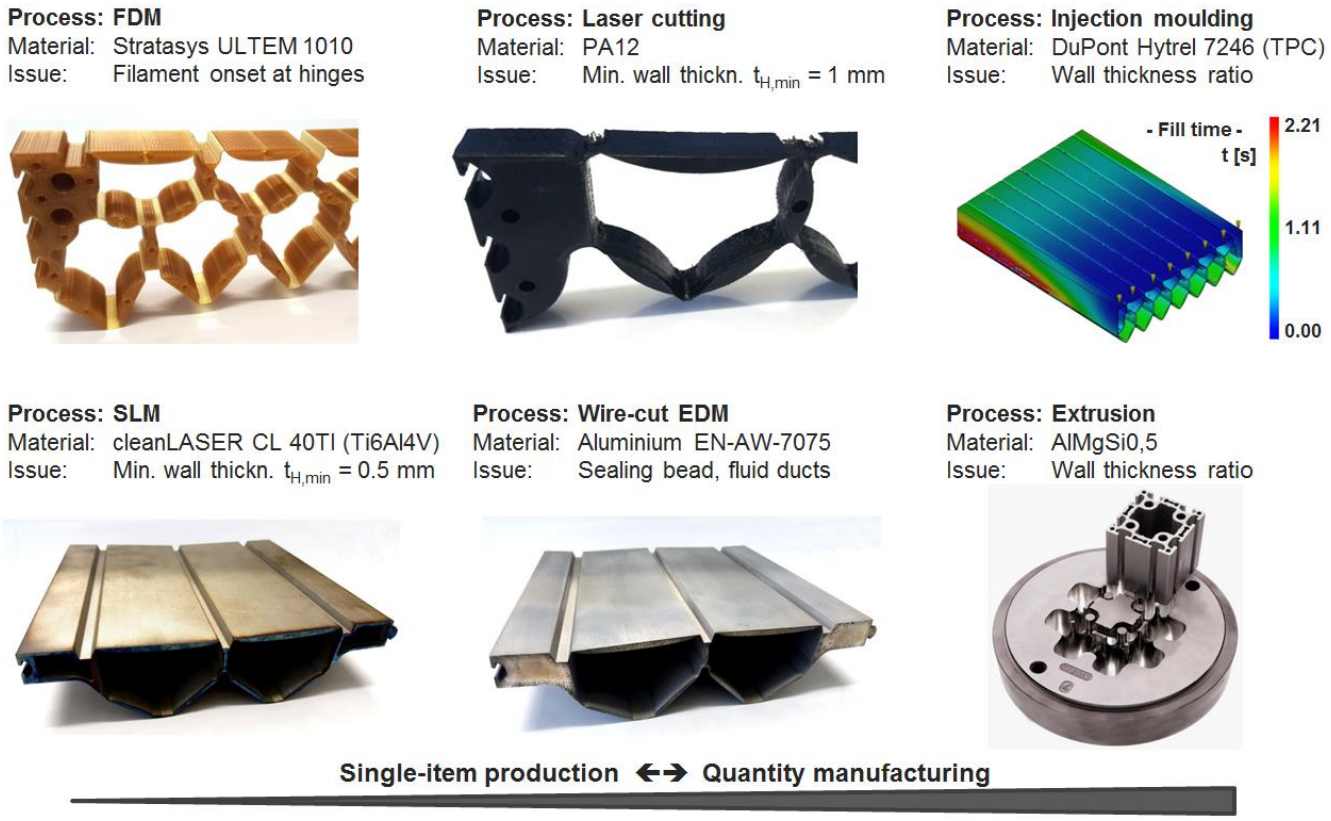

Figure H-1: Production processes and specimens from production trials for FDM, laser cutting, injection moulding, SLM, EDM and extrusion (from top left to bottom right)

Aluminium profiles with complex geometries are produced by extrusion in great diversity. As illustrated in Figure H-1 for an exemplary geometry, profiles of optional length can be manufactured in a continuous process. The complexity of the illustrated part is on the same level as the PACS. The standard aluminium alloy for extrusion AlMgSi0,5, with a square of strength to stiffness ratio of 0.57, is hardly appropriate for the application of PACS. Other alloys or also plastics can be processed by extrusion and could yield suitable production results.
The so far presented manufacturing processes are not the first choice for single-part production but summarize the investigational outcomes. Processes, which are utilized for the realization of cell body structures, are presented in chapter 5.1.

Investigated production processes for cell closure structure

With their suitability for mass production, the ability for processing various materials and the capacity to manufacture gas-tight parts without secondary processing, vacuum casting and injection moulding hold huge potentials for the future production of the cell closure membrane.

Vacuum casting in a broader sense belongs to the rapid prototyping processes. The main advantage over direct manufacturing methods, which are not in need of a mould construction, is the processability of diverse two-component plastics. Disadvantages like orthotropic strength degradation due to inhomogeneous fusion are avoided. Parts of elastic and stiff thermosets with isotropic mechanical properties can be produced. Starting with a positive mould that can be manufactured in a rapid prototyping process, the usually two-part negative mould is casted from this master by using silicone. Depending on the geometrical complexity of the component, ten to twenty functional parts can be casted in such a mould, before it becomes unusable through normal wear.

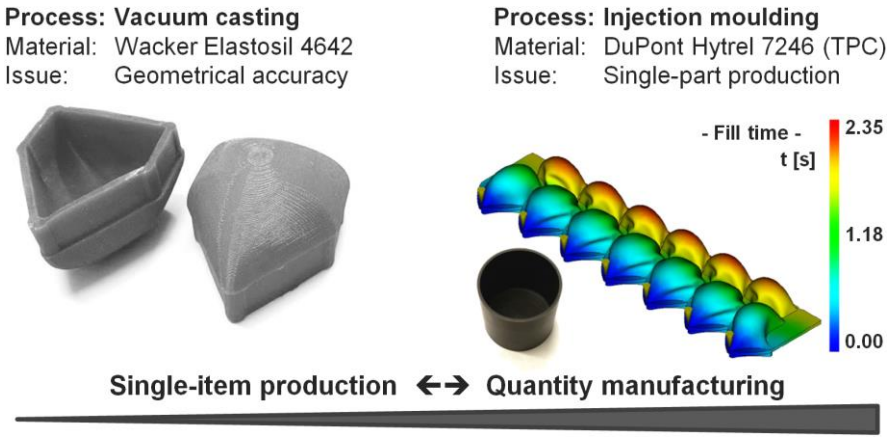

Figure H-2: Production processes and specimens from production trials for vacuum casting and injection moulding (from left to right)

Due to the elasticity of the mould, the DSEC with its slight geometrical undercuts is realizable also for stiff cast materials. An exemplary implementation of a single end cap that is made of Wacker Elastosil 4642 is shown in the left depiction of Figure H-2. The higher expenditure and lower geometrical accuracy compared to the SLS are decisive for the rejection of this process.

The injection moulding process is introduced for the manufacturing of the cell body structure previously in this section and rejected because of unrealizable draft angles and intolerable casting seams. In contrast, this process is well suited for the mass production of a cell closure membrane. With a high geometrical accuracy of the injection-moulded part, the processability of various materials and the capacity to produce fluid-tight components, this manufacturing method fulfils all of the quality requirements. Undercuts or draft angles don't represent a problem as the necessary deformations for demoulding do not surpass the operational strains. Figure H-2, right, depicts the simulation results for the casting process. The ability to produce also parts that are made of NBR, which is normally used for seals and gaskets, is shown at the exemplary part of the illustrated black cylindrical closure. A fill time of 2.35 s for a complete membrane is computed by *RICONE GmbH*. Tooling costs of 25 $k€$ to 35 $k€$ for the illustrated membrane with the dimensions of 450 x 90 x 30 mm^3 were decisive for rejecting this process for the manufacturing of individual demonstrator components.

I Material tests

For the determination of material properties experimental tests are performed. The thermoplastic PA2200 and the thermoplastic elastomer TPU92-A are investigated as datasheet values are incomplete. Neither is the nonlinear stress-strain behaviour given, nor are reliable fracture strength values provided. Both materials are utilized for the realization of PACS specimen and thus for its design and the FEM-based characterization. The herein presented data is examined for these simulations to provide a reliable database.

Static testing of PA2200

The thermoplastic polyamide PA2200 is developed for the SLS process. The PACS test specimens double cell, double-row cantilever and variable-surface demonstrator are manufactured from this material (cf. chapter 6). As the results from the experimental test shall evaluate the numerical investigations, accurate material properties have to be used for the simulation to avoid incorrect model parameters. The main objectives with this material test are the examination of the non-linear and direction-dependent stiffness behaviour and the according strength values. Furthermore, the influence of thin wall thicknesses of $t < 1\ mm$ on the material strength is analysed, as the critically loaded hinge regions are thereby affected.

Figure I-1 illustrates the resulting values. A significant difference between the fracture strength of vertically and horizontally built specimens can be assessed. Due to the insufficiently merged or degraded PA2200 powder in z-direction, the strength of these specimens is reduced to 48.2 %, compared to the datasheet value of $R_z = 42.0\ MPa$ [174]. For the thin-walled specimen with a thickness of $t = 0.5\ mm$, a reduction to 25.7 % results. As an outcome of this investigation, all cell body structures are manufactured with horizontal alignment within the machine bed. The strength value in xy-direction of $R_{xy} = 48.0\ MPa$ from the datasheet could almost be confirmed.

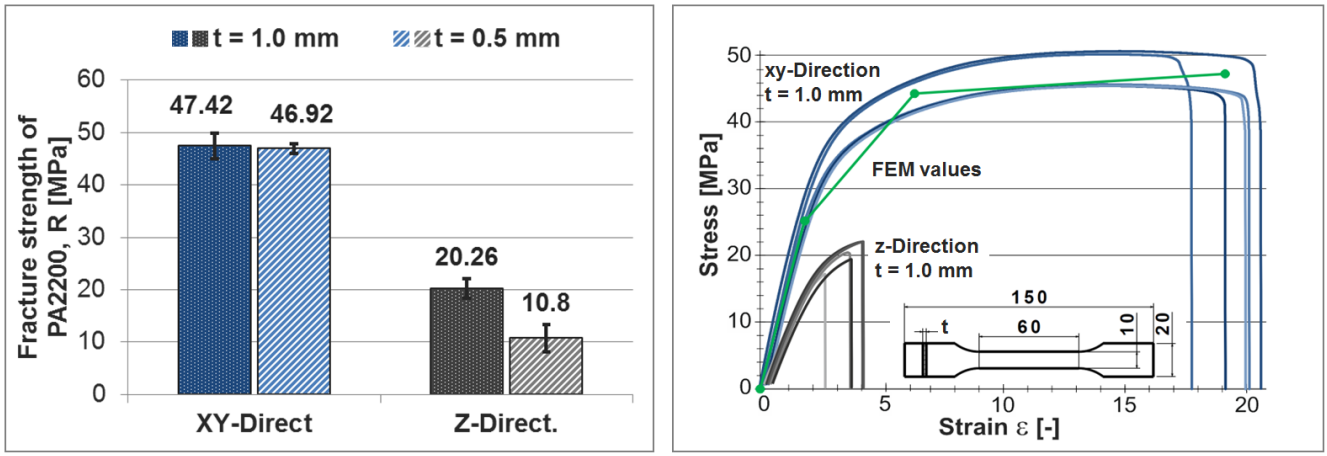

Figure I-1: Results from the experimental characterization of the laser-sintered material PA2200 in a tensile test according to DIN EN ISO 527-2 for xy- and z-direction

The experimentally analysed stress-strain curve is linearized for its use in the FEM simulations. Therefore, the measured values that relate to the specimens that are manufactured in xy-direction are evaluated. For the herein investigated vertically aligned cell body structures, the influence of the material properties in z-direction is neglected. The resulting values are summarized in Table I-1.

Table I-1: Stress-strain linearization for PA2200

	Step 0	Step 1	Step 2	Step 3
Strain [%]	0	1.67	6.25	19.17
Stress [MPa]	0	25.0	44.2	47.42

Optical measurement of TPU-92A

The thermoplastic polyurethane TPU-92A provides satisfying material characteristics for the manufacturing of the cell closure membrane. As this material is handled in a SLS process, the material characteristics strongly depend on the process parameters. For the FEM-based evaluation of the DSEC concept, the hyperplastic material properties as well as the direction-dependent characteristics of the TPU-92A have to be examined. The test conditions and the geometry of the specimens are determined according to the test norm DIN EN ISO 527-2. The optical measurement system GOM Aramis is used to analyses a monochrome dot pattern on the sample so as to compute the longitudinal and lateral strains, ε_x and ε_y. *Young*'s modulus and *Poisson*'s ratio can thus be derived. Figure I-2 shows a summarizing chart of the optical strain measurements.

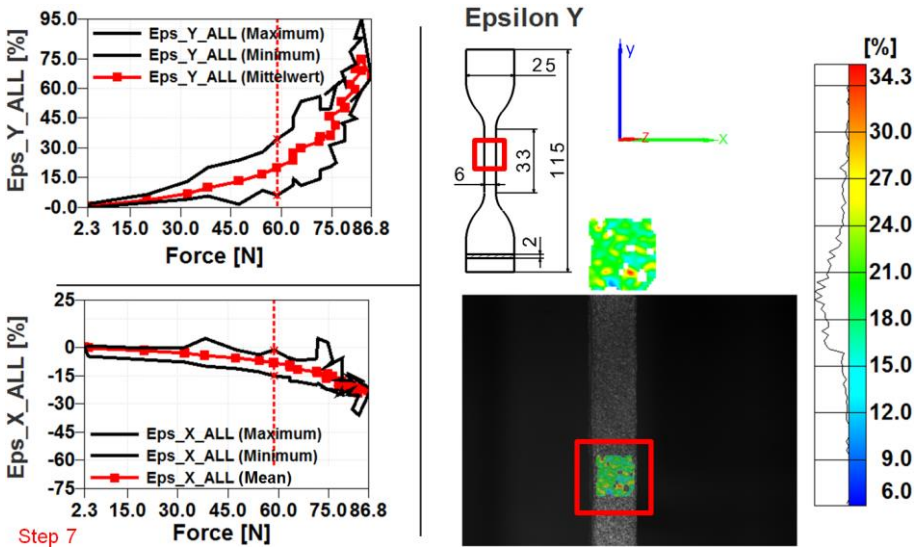

Figure I-2: Results from the optical measurement of longitudinal and lateral strain at a horizontally sintered TPU-92A specimen

The optical measurement is stable for strains below 100 %. Flaking patterns, which occur at higher deformations, prevent from measuring values above 100 % strain with the optical system. The ultimate elongation of the material though lies between 200 % and 400 %. The data from the optical system is used in two ways. First, it enables the calculation of the *Poisson*'s ratio. Second, as Figure I-3 shows, it is used for a fitting of optically and mechanically measured test data.

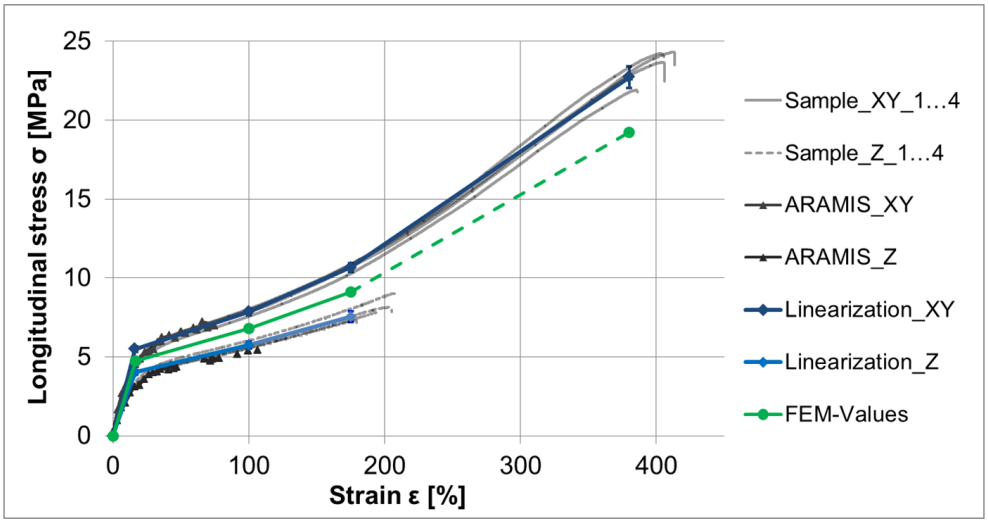

Figure I-3: Stress-strain plots for specimens that are manufactured in xy-direction and z-direction and according linearized data for FEM simulations

As the orientation of the component in the SLS machine affects the material characteristics and an anisotropic mechanical behaviour results. Two sets of specimens, which are manufactured in the horizontal xy-direction and the vertical z-direction of the machine bed, are thus used. Figure I-3 condenses the outcomes for both material orientations and the mechanically and optically measured data. The linearization of the stress-strain curves leads to the resulting input data for the FEM computations. The initial gradient for finding the yield point of the highly nonlinear material stiffness is evaluated between $\varepsilon_{y1} = 0\ \%$ and $\varepsilon_{y2} = 10\ \%$. As the linearized data for the specimens of the two orientations differ by about $25\ \%$ of stress, the final values that are used in the FEM model are mean values of the two linearized functions.
An initial *Young*'s modulus of $E = 29.08\ MPa$ results and a *Poisson*'s ratio of $\nu = 0.38$ is derived. The linearized stiffness properties of TPU-92A for the FEM simulations of cell closures, which are presented in chapter 4.4, are given in Table I-2. Physical implementations of different closure concepts made from this material are experimentally investigated in chapter 6.1.

Table I-2: Stress-strain linearization for TPU92-A

	Step 0	Step 1	Step 2	Step 3	Step 4
Strain [%]	0	16.37	100	175	380
Stress [MPa]	0	4.76	6.80	9.11	19.25

J Design tool for PACS

The input mask with a reduced number of parameters for the rapid model design is shown in Figure J-1. Besides the required number of cells, one value for the size plus one for a taper factor is sufficient. The hinge and crossover angles, which determine the shape of the neutral fibre in the manufacturing state, are deduced from the course of an entered formula. The related deformations between initial and target states of shape are given with two parameters, which define the rotational deformation per cell of the first cell row. The cell side lengths and the independent state variables, which are not part of the neutral fibre, define the initial shape of the PACS and are determined automatically by the design tool. For the hinge lengths and the eccentricities one value each is sufficient.
Forces of inertia can moreover be added automatically by providing the acceleration vector. The mass of the PACS is computed with the information about the density of the utilized material. For the application of point loads, a separate input mask allows to select individual hinge elements to add a specific point load vector. Line loads in terms of internal or external pressure loads are applied to cell side elements. For the definition of the internal pressure, two values, one for each cell row, are required. Aerodynamic pressures can be computed automatically using XFOIL, by giving the shape formula or point cloud of the underlying aerofoil and the chord length segment, which shall be replaced by the PACS. The input mask further allows initiating the shape optimization respectively the simulation processes. The transfer of the truss model to the cross-sectional design can be initiated after the design load case is determined and the according equilibrium state of shape is computed.
For visual feedback, the current shape of the truss structure can be plotted at each point of the design process. The underlying set of parameters can be saved and previous data sets can be loaded.

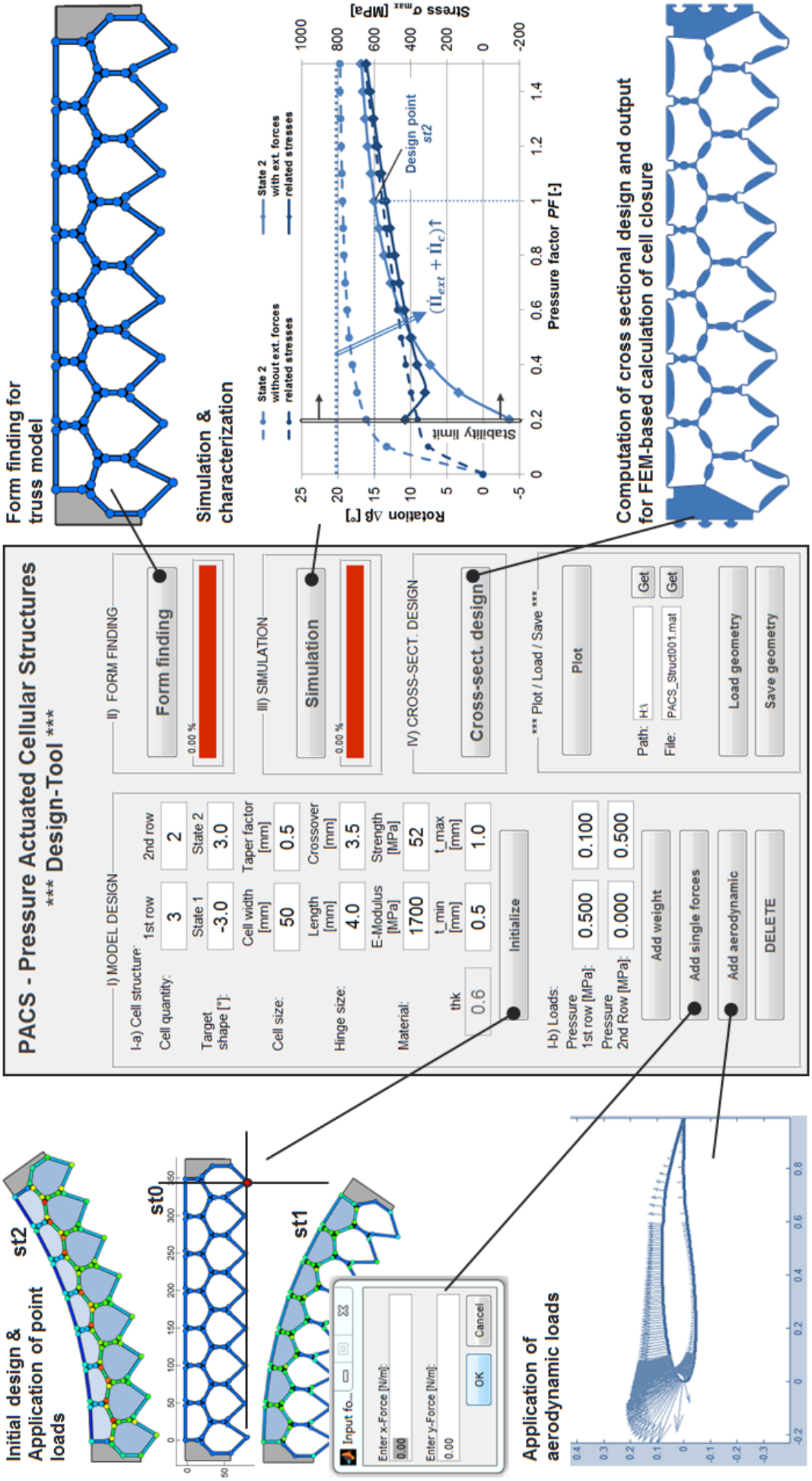

Figure J-1: User interface for controlling the computation of the truss geometry and the computation of the cross-sectional design

List of Tables

List of Figures

Bibliography

[1] Pagitz M. et al., Pressure-actuated cellular structures. *Bioinspiration and Biomimetics*, vol. 7, no. 1. 2012 March: Art.Nr.: 016007.

[2] Kientz O.L., Aeroplane Wing. Kansas, USA, *1,790,309*. 1931 January 27.

[3] Kress R.W. et al., Variable sweep wing design. *AIAA - Aircraft Prototype and technology*, 1983 March: 43 - 61.

[4] Seigler T. M., Dynamics and Control of Morphing Aircraft. University. Blacksburg; 2005.

[5] McGowan et al., Perspectives on Highly Adaptive or Morphing Aircraft. In *NATO RTO AVT-168 Symposium*; 2009 April; Lisbon.

[6] Weisshaar T.A., Morphing Aircraft Technology - New Shapes for Aircraft Design. *Multifunctional Structures / Integration of Sensors and Antennas*, 2006 December: O1-1 – O1-20.

[7] Janocha H., Aktoren - Grundlagen und Anwendungen. 1st ed. Janocha. Berlin: Springer Verlag; 1992.

[8] BWM AG, BMW Design: Vision Cars. [Online].; 2015 [cited 2016 February 29. Available from: http://www.bmw.de/de/topics/faszination-bmw/bmw-design/visionen/bmw-vision-cars.html.

[9] Szodruch J., The influence of camber variation on the aerodynamics of civil transport aircraft. In *AIAA 23rd Aerospace Sciences Meeting*; 1985; Reno, Nevada. Code: 6416.

[10] Gano S.E. et al., Optimized unmanned aerial vehicle with wing morphing for extended range and endurance. In *9th AIAA/ISSMO Symposium on Multidisciplinary Analysis and Optimization 2002*; 2002; Atlanta, Georgia. Code: 103018.

[11] Moorhouse D. et al., Benefits and design challenges of adaptive structures for morphing aircraft. *Aeronautical Journal*, vol. 110, no. 1105. 2006 March: 157 - 162.

[12] Müller D., Das Hornkonzept, Realisierung eines formvariablen Tragflügelprofils zur aerodynamischen Leistungsoptimierung zukünftiger Verkehrsflugzeuge. 2000. http://elib.uni-stuttgart.de/opus/volltexte/2000/712/pdf/Diss_Mueller_25.01.2000.pdf.

[13] Greff E., The development and design integration of a variable camber wing for long/medium range aircraft. *Aeronautical Journal*, vol. 94, no. 939. 1990 November: 301 - 312.

[14] Thornton S.V., Reduction of structural loads using maneuver load control on the Advanced Fighter Technology Integration. Technical Memorandum. Edwards, California: NASA; 1993. Report No.: 4526.

[15] Barrett R. et al., Biomimetic FAA-certifiable, artificial muscle structures for commercial aircraft wings. *Smart Materials and Structures*, 2014 June 17: Art.Nr. 074011.

[16] Breitsamter C., Aerodynamic efficiency of high maneuverable aircraft applying adaptive wing trailing edge section. In *24th Congress of International Council of the Aeronautical Sciences*; 2004; Yokohama, Japan. Art.Nr. 2004-4.3.2.

[17] Madsen H.A. et al., The potentials of the controllable rubber trailing edge flap (CRTEF). In *European Wind Energy Conference and Exhibition 2010, EWEC 2010*; 2010; Warsaw, Poland. 2165 - 2175.

[18] Tani Y. et al., Aerodynamic noise reduction for high lift devices using morphing flap concept. In *29th Congress of the International Council of the Aeronautical Sciences, ICAS 2014*; 2014; St. Petersburg ,Russia. Code: 108502.

[19] Ai Q. et al., Airfoil noise reduction using morphing trailing edge. In *21st International Congress*

on Sound and Vibration 2014, ICSV 2014; 2014; Beijing, China. Code: 110147.

[20] Knott E.F. et al., Radar cross section. 2nd ed. Publishing. Raleigh, North Carolina: SciTech Publishing; 2004.

[21] Rütten M. et al., Numerical flow investigation of morphing leading edges for the enhancement of maneuverability of unmanned combat air vehicles. In *30th AIAA Applied Aerodynamics Conference 2012*; 2012; New Orleans, Louisiana. 2341 - 2357.

[22] Chen S. et al., Numerical simulation on the radar cross section of variable-sweep wing aircraft. *Journal of Aerospace Technology and Management*, vol. 7, no. 2. 2015 April: 170 - 178.

[23] Gramüller B. et al., Design process and manufacturing of an unmanned blended wing-body aircraft. In *Deutscher Luft- und Raumfahrtkongress 2015*; 2015; Rostock, Germany.

[24] AIRBUS Group, Airbus Group - Sagitta: Airbus Defence and Space open collaboration project. [Online].; 2015 [cited 2015 August 13. Available from: http://www.airbusgroup.com/int/en/news-media/media~item=jcr%3A3095d1f2-a930-4c90-92b3-087a017f654d~.html.

[25] Gern F.H. et al., Computation of actuation power requirements for smart wings with morphing airfoils. *AIAA Journal*, vol. 43, no. 12. 2005 December: 2481 - 2486.

[26] Huber J. E. et al., The selection of mechanical actuators based on performance indices. *The Royal Society*, vol. 453, no. 1965. 1997 October: 2185-2205.

[27] Hollerbach et al., A comparative analysis of actuator technologies for robotics. In *The robotics review 2*. Cambridge: MIT Press Cambridge; 1992. 299-342.

[28] Hunter I.W. et al., A comparison of muscle with artificial actuators. In *Solid-State Sensor and Actuator Workshop, 5th Technical Digest, IEEE*; 1992; Hilton Head Island, South Carolina. 178 - 185.

[29] Vos R., Mechanics and applications of pressure adaptive honeycomb. PhD Thesis ed. Kansas. Lawrence, Kansas: University of Kansas; 2009.

[30] Shepherd R.F. et al., Using explosions to power a soft robot. *Angewandte Chemie - International Edition*, vol. 52, no. 10. 2013: 2892 - 2896.

[31] Brissenden R.F. et al., Assessment of variable camber for application to transport aircraft. Contractor Report. Seattle, : Boeing Commercial Airplane Company, Preliminary Design Department; 1980.

[32] Stanewsky E., Aerodynamic benefits of adaptive wing technology. *Aerospace Science and Technology*, vol. 4, no. 7. 2000 October: 439 - 452.

[33] Bauer C. et al., A new structural approach to variable camber wing technology of transport aircraft. In *9th AIAA/ASME/ASCE/AHS/ASC Structures, Structural Dynamics, and Materials Conference and Exhibit* ; 1998; Long Beach, California. 474 - 482.

[34] Barrett R., Active aeroelastic tailoring of an adaptive Flexspar stabilator. *Smart Materials and Structures*, vol. 5, no. 6. 1996 December: 723 - 730.

[35] Elzey D.M. et al., A bio-inspired, high-authority actuator for shape morphing structures. In *PROCEEDINGS OF SPIE SPIE - The International Society for Optical Engineering: Smart Structures and Materials 2003 Active Materials: Behavior and Mechanics*; 2003; San Diego, California. Code: 61913.

[36] Monner H.P., Realization of an optimized wing camber by using formvariable flap structures. *Aerospace Science and Technology*, vol. 5, no. 7. 2001 October: 445 - 455.

[37] Vasista S. et al., Topology-optimized design and testing of a pressure-driven morphing-aerofoil trailing-edge structure. *AIAA Journal*, vol. 51, no. 8. 2013 August: 1898-1907.

[38] Ramrakhyani D.S. et al., Aircraft structural morphing using tendon-actuated compliant cellular trusses. *Journal of Aircraft*, vol. 42, no. 6. 2005 November: 1615 - 1621.

[39] Ajaj R.M. et.al., The Zigzag wingbox for a span morphing wing. *Aerospace Science and*

Technology, vol. 28, no. 1. 2013 July: 364-375.

[40] Nguyen N. et al., Aeroelastic analysis of a flexible wing wind tunnel model with variable camber continuous trailing edge flap design. Moffett Fiel, CA: NASA, Intelligent systems devision; 2015.

[41] Barbarino et al., A review of morphing aircraft. *Journal of Intelligent Material Systems and Structures*, vol. 22, no. 9. 2011 June: 823 - 877.

[42] McGowan A.-M. et al., NASA's Morphing Project Research Summaries in Fiscal Year 2002. Hampton:; 2002.

[43] Thill C. et al., Morphing skins. *The aeronautical journal*, vol. 112, 2008 March: Art.Nr.1129.

[44] Reinboth, Flickr. [Online].; 2008 [cited 2015 July 23. Available from: https://www.flickr.com/photos/techmuseum/2979155343/.

[45] Anschütz O., Wikipedia. [Online].; 1894 [cited 2015 July 23. Available from: https://commons.wikimedia.org/wiki/File:Otto_is_going_to_fly.jpg.

[46] Hannah M.O., Expanding wing for aeroplanes. Missouri, USA, *1,773,530*. 2030 August 19.

[47] Lyon D.G., Variable shaped airfoil. Iowa, USA, *3,179,357*. 1965 April 20.

[48] Frost et al., Airfoil variable cambering device and mehtod. Texas, USA, *4,247,066*. 1981 January 27.

[49] Boeing Commercial Airplane Company, Assessment of variable camber for application to transport aircraft. NASA Contractor Report. Hampton, Virginia: NASA, Preliminary Design Department; 1980. Report No.: 158930.

[50] Gilbert W.W., Mission adaptive wing system for tactical aircraft. *Journal of Aircraft*, vol. 18, no. 7. 1981 July: 597 - 602.

[51] Boeing Advanced Systems Company, AFTI/F-111 Mission adaptive wing briefing to industry. Final Report for Period 86 to 88. Ohio, USA: Flight Dynamics Laboratory, Mission Adaptive Wing Program Office; 1988. Report No.: F33615-78-C-3027.

[52] Powers S.G. et al., Flight test results from a supercritical mission adaptive wing with smooth variable camber. Technical Memorandum. California, USA: NASA; 1992. Report No.: 4415.

[53] Previtali F. et al., Performance of a three-dimensional morphing wing and comparison with a conventional wing. *AIAA JOURNAL*, vol. 52, no. 10. 2014 October: 2101 - 2113.

[54] Statkus F.D. et al., Continuous skin, variable camber airfoil edge actuating mechanism. Washington, USA, *4,351,502*. 1982 September 28.

[55] Cole J.B., Variable camber leading edge assembly for an airfoil. Washington, USA, *4,706,913*. 1987 November 17.

[56] Zimmer H., Transverse force-connected body with variable profiling, particularly an airplane wing. Friedrichshafen, Germany, *4,252,287*. 1981 February 24.

[57] Kintscher M.et al., Design of a smart leading edge device. In Heidelberg. *Adaptive, tolerant and efficient composite structures*. Berlin: Springer-Verlag; 2012. 381 - 390.

[58] Monner et al., Design of a smart droop nose as leading edge high lift system for transportation aircrafts. In *Collection of Technical Papers - AIAA/ASME/ASCE/AHS/ASC Structures, Structural Dynamics and Materials Conference*; 2009; Palm Springs, California. Art.Nr. 2009-2128.

[59] Heintze O. et al., Die Vorbereitung der Faserverbundstruktur einer flexiblen und spaltfreien Flügelvorderkante auf ihren ersten großskaligen Bodenversuch. In *Deutscher Luft- und Raumfahrtkongress 2010*; 2010; Hamburg, Germany.

[60] Monner H.P. et al., Groundtest of a composite smart droop nose. In *53rd AIAA/ASME/ASCE/AHS/ASC Structures, Structural Dynamics and Materials Conference 2012*; 2012; Honolulu, Hawaii. Code: 98132.

[61] Thuwis et al., Optimization of a variable-stiffness skin for morphing high-lift devices. *Smart*

Materials and Structures, vol. 19, no. 12. 2010 December: Art.Nr.: 124010.

[62] Kintscher et al., Investigation of multi-material laminates for smart droop nose devices. In *29th Congress of the International Council of the Aeronautical Sciences, ICAS 2014*; 2014; St. Petersburg, Russia. Code: 108502.

[63] Weber D. et al., Droop Nose for application to Laminar Wing of future Green Regional A/C. In *Council of European Aerospace Societies, CEAS: Greener Aviation*; 2014; Darmstadt, Germany.

[64] Santer M.J. et al., Topology optimization of adaptive compliant aircraft wing leading edge. In *48th AIAA/ASME/ASCE/AHS/ASC Structures, Structural Dynamics, and Materials Conference*; 2007; Waikiki, Hawaii. Code: 70016.

[65] Saggere L. et al., Static shape control of smart structures using compliant mechanisms. *AIAA Journal*, vol. 37, no. 5. 1999 May: 572 - 578.

[66] Vasista S. et al., Topology optimisation via the moving iso-surface threshold method: Implementation and application. *Aeronautical Journal*, vol. 118, no. 1201. 2014 March: 315 - 342.

[67] Berg D. et al., Design, fabrication, assembly and initial testing of a SMART rotor. In *29th ASME Wind Energy Symposium*; 2011; Orlando, Florida.

[68] Berg J.C. et al., Field test results from the Sandia SMART rotor. In *51st AIAA Aerospace Sciences Meeting including the New Horizons Forum and Aerospace Exposition 2013*; 2013; Grapevine, Texas. Code: 98224.

[69] Monner H.P. et al., Development and design of flexible fowler flaps for an adaptive wing. In *Smart Structures and Materials 1998 Industrial and Commercial Applications of Smart Structures Technologies*; 1998 March; San Diego, California. Code: 59757.

[70] Wang Y. et al., The design and flight analysis of a new adaptive wing. In *52nd AIAA/ASME/ASCE/AHS/ASC Structures, Structural Dynamics and Materials Conference*; 2011; Denver, Colorado. Code: 95047.

[71] Kintscher et al., Low speed wind tunnel test of a morphing leading edge. In *Proceedings of the 2013 AIDAA Conference*; 2013 September; Naples, Italy.

[72] Sanders B. et al., Aerodynamic performance of the smart wing control effectors. *Journal of Intelligent Material Systems and Structures*, vol. 15, no. 4. 2004 April: 293 - 303.

[73] Musgrove R.G., Apparatus for producing pivotal movement. Arlington, Texas, *3,944,170*. 1976 March 16.

[74] Musgrove R.G., The Eccentuator - A new concept in actuation. In *Collection of Technical Papers - AIAA/ASME/ASCE/AHS/ASC Structures, Structural Dynamics and Materials Conference*; 1980; Seattle, Washington. 933 - 937.

[75] Kudva J.N., Overview of the DARPA Smart Wing Project. *Journal of Intelligent Material Systems and Structures*, vol. 15, no. 4. 2004 April: 261 - 267.

[76] Bartley-Cho J.D. et al., Development of high-rate, adaptive trailing edge control surface for the smart wing phase 2 wind tunnel model. *Journal of Intelligent Material Systems and Structures*, vol. 15, no. 4. 2004 April: 279 - 291.

[77] Di Matteo N. et al., Design and analysis of a morphing flap structure for high lift wing. In *51st AIAA/ASME/ASCE/AHS/ASC Structures, Structural Dynamics and Materials Conference*; 2011; Orlando, Florida. Art.Nr. 2010-3096.

[78] Bei Z. et al., Research on a new servo mechanism named eccentuator. In *64th International Astronautical Congress 2013, IAC 2013*; 2013; Beijing, China. 6295 - 6311.

[79] Liu S. et al., Optimal design of compliant trailing edge for shape-changing. *Chinese Journal of Aeronautics*, vol. 21, no. 2. 2008 April: 187 - 192.

[80] De Gaspari A. et al., Design, manufacturing and wind tunnel validation of an active camber morphing wing based on compliant structures. In *25th International Conference on Adaptive*

Structures and Technologies, ICAST 2014; 2014; The Hague, Netherlands. Code 110367.

[81] Gandhi F., Centrifugal force actuated variable span helicopter rotor. State College, Pennsylvania, *US 2009/0290981 A1*. 2009 November 26.

[82] Gandhi F. et al., Design, development, and hover testing of a helicopter rotor blade chord extension morphing system. *Smart Materials and Structures*, vol. 24, no. 3. 2015 March: Art.Nr. 035024.

[83] Han C. et al., Experimental study of a telescopic wing inside a channel. *Journal of Aircraft*, vol. 44, no. 3. 2007 May: 1029 - 1030.

[84] Guiler R. et al., Wind tunnel analysis of a morphing swept wing tailless aircraft. In *23rd AIAA Applied Aerodynamics Conference*; 2005; Toronto, Ontario. 946 - 959.

[85] Raither W. et al., Morphing wing structure with controllable twist based on adaptive bending-twist coupling. *Smart Materials and Structures*, vol. 22, no. 6. 2013 June: Art.Nr. 065017.

[86] Boller C., Adaptronic systems in aeronautics and space travel. In Springer. *Adaptronics and smart structures*. Berlin: Springer; 2007. 371 - 393.

[87] Leletty R. et al., Piezoelectric Actuators. In Springer. *Adaptronics and smart structures*. New York: Springer; 2007. 107 - 125.

[88] Dicker M. et al., Large wind turbine structural load control: Trailing edge deformation mechanism for active variable-camber blade. *Wind Engineering*, vol. 38, no. 4. 2014 August: 425 - 440.

[89] Kota S. et al., Design and application of compliant mechanisms for morphing aircraft structures. In *Smart Structures and Materials 2003: Industrial and Commercial Applications of Smart Structures Technologies*; 2003; San Diego, California. 24 - 33.

[90] Perner M. et al., Approach for a smart device for active vibration suppression as an add-on for robot-based systems. *Journal of Mechanical Science and Technology*, vol. 28, no. 11. 2014 November: 4407 - 4413.

[91] Natterer F.J. et al., Configuration of a shear web based actuation system. In *Active and Passive Smart Structures and Integrated Systems 2010*; 2010; San Diego,California. Art.Nr.: 764329.

[92] Barrett R. et al., Missile flight control using active flexspar actuators. *Smart Materials and Structures*, vol. 5, no. 2. 1996 April: 121-128.

[93] Hesselbach J., Shape Memory Actuators. In Springer. *Adaptronics and smart structures*. Berlin: Springer; 2007. 145 - 163.

[94] Kudva J.N. et al., Design, fabrication, and testing of the DARPA/Wright Lab 'smart wing' wind tunnel model. In *38th Structures, Structural Dynamics, and Materials Conference*; 1997; Kissimmee, Florida. Art.Nr.: 1198.

[95] Jardine A.P. et al., Smart wing shape memory alloy actuator design and performance. In *Smart Structures and Materials 1997: Industrial and Commercial Applications of Smart Structures Technologies*; 1997; San Diego, California. 48 - 55.

[96] Urnes J. et al., A mission-adaptive variable camber flap control system to optimize high lift and cruise lift-to-drag ratios of future N+3 transport aircraft. In *51st AIAA Aerospace Sciences Meeting including the New Horizons Forum and Aerospace Exposition 2013*; 2013; Grapevine, Texas. Code: 98224.

[97] Kaul U.K. et al., Drag optimization study of variable camber continuous trailing edge flap (VCCTEF) using OVERFLOW. In *32nd AIAA Applied Aerodynamics Conference 2014*; 2014; Atlanta, Georgia. Code: 106134.

[98] Ivanco T.G. et al., Validation of the lockheed Martin morphing concept with wind tunnel testing. In *48th AIAA/ASME/ASCE/AHS/ASC Structures, Structural Dynamics, and Materials Conference*; 2007; Waikiki, Hawaii. 6464 - 6480.

[99] Lendlein A. et al., Formgedächtnispolymere. *Angewandte Chemie*, vol. 114, no. 12. 2002 June:

2138 - 2162.

[100] Bye D.R. et al., Design of a morphing vehicle. In *48th AIAA/ASME/ASCE/AHS/ASC Structures, Structural Dynamics, and Materials Conference*; 2007; Waikiki, Hawaii. 321 - 336.

[101] Love M.H. et al., Demonstration of morphing technology through ground and wind tunnel tests. In *48th AIAA/ASME/ASCE/AHS/ASC Structures, Structural Dynamics, and Materials Conference*; 2007; Waikiki, Hawaii. 337 - 348.

[102] Reed J.L. et al., Adaptive wing structures. In *Smart Structures and Materials 2005 - Industrial and Commercial Applications of Smart Structures Technologies*; 2005; San Diego, California. 132 - 142.

[103] Pelrine R. et al., Dielectric elastomer artificial muscle actuators: Toward biomimetic motion. In *Smart Structures and Materials 2002: Electroactive Polymer Actuators and Devices (EAPAD)*; 2002; San Diego, California. 126 - 137.

[104] Austin F. et al., Comparison of smart wing concepts for transonic cruise drag reduction. In *Smart Structures and Materials 1997: Industrial and Commercial Applications of Smart Structures Technologies*; 1997; San Diego, California. 33 - 40.

[105] Cho S. et al., Development of micro inchworm robot actuated by electrostrictive polymer actuator. In *Electroactive Polymer, Actuators and Devices-Smart Structures and Materials 2001*; 2001; Newport Beach, California. 466 - 474.

[106] Pierce R.C., Expansible cover. USA, *2,211,478*. 1940 August 13.

[107] Bubert E.A., Highly extensible skin for a variable wing-span morphing aircraft utilizing pneumatic artificial muscle actuation. 2009. Master thesis, University of Maryland, College Park, Maryland.

[108] Kang R. et al., Design, modeling and control of a pneumatically actuated manipulator inspired by biological continuum structures. *Bioinspiration and Biomimetics*, vol. 8, no. 3. 2013 September: Art.Nr.: 036008.

[109] Woods B.K.S. et al., Advanced kinematic tailoring for morphing aircraft actuation. *AIAA Journal*, vol. 52, no. 4. 2014 April: 788 - 798.

[110] Woods B.K.S. et al., Wind tunnel testing of the fishbone active camber morphing concept. In *54th AIAA/ASME/ASCE/AHS/ASC Structures, Structural Dynamics and Materials Conference*; 2013; Boston, Massachusetts, USA. Art.Nr.: 2013-1908.

[111] Shan Y. et al., Variable stiffness structures utilizing fluidic flexible matrix composites. *Journal of Intelligent Material Systems and Structures*, vol. 20, no. 4. 2009 March: 443 - 456.

[112] Kirn J. et al., Development of flexible matrix composites (FMC) for fluidic actuators in morphing systems. *International Journal of Structural Integrity*, vol. 2, no. 4. 2011: 458 - 473.

[113] Feng N. et al., A bio-inspired, active morphing skin for camber morphing structures. *Smart Materials and Structures*, vol. 24, no. 3. 2015 March: Art.Nr.: 035023.

[114] Madsen H.A. et al., Towards an industrial manufactured morphing trailing edge flap system for wind turbines. In *European Wind Energy Association Conference and Exhibition 2014, EWEA 2014*; 2014; Barcelona, Spain. Code: 111012.

[115] Ilievski F. et al., Soft robotics for chemists. *Angewandte Chemie - International Edition*, vol. 50, no. 8. 2011 February: 1890 - 1895.

[116] Deimel R. et al., A compliant hand based on a novel pneumatic actuator. In *2013 IEEE International Conference on Robotics and Automation, ICRA 2013*; 2013; Karlsruhe, Germany. 2047 - 2053.

[117] Shepherd R.F. et al., Multigate soft robot. *Proceedings of the National Academy of Sciences of the United States of America*, vol. 108, no. 51. 2011 December: 20400 - 20403.

[118] Onal C.D. et al., Soft mobile robots with on-board chemical pressure generation. In *15th International Symposium on Robotics Research*; 2011; Flagstaff, Arizona. 1 - 16.

[119] Reinhard et al., Adaptive pneumatic wing for fixed wing aircraft. USA, *US 6,199,769*. 2001 March 13.

[120] Dittrich K., Cellular actuator device amd methods of making and using same. USA, *US 7,055,782*. 2006 June 6.

[121] Vos R. et al., Pressure adaptive honeycomb: A novel concept for morphing aircraft structures. In *27th Congress of the International Council of the Aeronautical Sciences 2010*; 2010; Nice, France. 1792 - 1801.

[122] Barrett R. et al., Method and apparatus for pressure adaptive morphing structure. Europe, *EP 2,459,442*. 2012 June 6.

[123] Vos R. et al., Method and apparatus for pressure adaptive morphing structure. USA, *US 8,366,057*. 2013 February 5.

[124] Philen M. et al., Variable stiffness adaptive structures utilizing hydraulically pressurized flexible matrix composites with valve control. In *47th AIAA/ASME/ASCE/AHS/ASC Structures, Structural Dynamics and Materials Conference*; 2006; Newport, Rhode Island. 6387 - 6397.

[125] Breuer J. et al., An inflatable wing using the principle of tensairity. In *48th AIAA/ASME/ASCE/AHS/ASC Structures, Structural Dynamics, and Materials Conference*; 2007; Waikiki, Hawaii. 4994 - 5005.

[126] Vos R. et al., Mechanics of pressure-adaptive honeycomb and its application to wing morphing. *Smart Materials and Structures*, vol. 20, no. 9. 2011 September: Art.Nr.: 094010.

[127] Sun J. et al., Active inflatable auxetic honeycomb structural concept for morphing wingtips. *Smart Materials and Structures*, vol. 23, no. 12. 2014 December: 125023.

[128] Luo Q. et al., Adaptive pressure-controlled cellular structures for shape morphing I: Design and analysis. *Smart Materials and Structures*, vol. 33, no. 5. 2013 May: Art.Nr.: 055014.

[129] Luo Q. et al., Adaptive pressure-controlled cellular structures for shape morphing: II. Numerical and experimental validation. *Smart Materials and Structures*, vol. 33, no. 5. 2006 May: ArtNr.: 055012.

[130] Vasista S. et al., Design considerations of a pressure driven morphing wing structure. In *28th Congress of the International Council of the Aeronautical Sciences 2012*; 2012; Brisbane, Australia. 2174 - 2183.

[131] Zhang H.W. et al., A new multiscale computational method for mechanical analysis of closed liquid cell materials. *CMES - Computer Modeling in Engineering and Sciences*, vol. 68, no. 1. 2010 October: 55 - 93.

[132] Zhang H.W. et al., A multiscale method for the numerical analysis of active response characterization of 3D nastic structures. *Smart Materials and Structures*, vol. 21, no. 8. 2012 August: Art.Nr.: 085009.

[133] Lv J. et al., Shape and topology optimization for closed liquid cell materials using extended multiscale finite element method. *Structural and Multidisciplinary Optimization*, vol. 49, no. 3. 2014 March: 367 - 385.

[134] Lv J. et al., A multiscale co-rotational method for geometrically nonlinear shape morphing of 2D fluid actuated cellular structures. *Mechanics of Materials*, vol. 79, 2014 December: 1 - 14.

[135] Nachtigall W. and Pohl G., Bau-Bionik. 2nd ed. Springer-Verlag. Heidelberg: Springer-Verlag; 2013.

[136] Rossmann T. and Tropea C., Bionik - Aktuelle Forschungsergebnisse in Natur-, Ingenieur- und Geisteswissenschaft. 1st ed. Springer-Verlag. Heidelberg: Springer-Verlag; 2005.

[137] Howard, Penetration of hard substrates by a fungus employing enormous turgor pressures. *Proceedings of the National Academy of Sciences of the United States*, 1991 December: 11281-11284.

[138] Stahlberg R. et al., Nastic Structures: The Enacting and Mimicking of Plant Movements. In Bar-

Cohen Y. *Biomimetics - Biologically inspired technologies*. Boca Raton: Taylor & Francis Group; 2006. 473-493.

[139] Webb J.W., Flickr.com. [Online].; 2008 [cited 2016 February 29. Available from: https://www.flickr.com/photos/webbaliah/2368172833/in/photostream/.

[140] Company, Carolina.com. [Online].; 2015 [cited 2016 February 29. Available from: http://www.carolina.com/images/product/large/30-3886.jpg.

[141] Karlsson M. et al., The maximum polygon area and its relation to the isoperimetric inequality. Göteborg, Sweden: Chalmers University of Technology and Göteborg University, Department of Mathematics; 2005. Report No.: ISSN 1652-9715.

[142] Vos R. et al., Topology optimization of pressure adaptive honeycomb for a morphing flap. *Proceedings of SPIE - The International Society for Optical Engineering*, vol. 7977, no. 1. 2011 March: Art.Nr.: 79771J.

[143] Scheepstra et al., Topology design of pressure adaptive honeycomb for a morphing fowler flap. In *52nd AIAA/ASME/ASCE/AHS/ASC Structures, Structural Dynamics and Materials Conference*; 2011; Denver, Colorado. Art.Nr.: AIAA 2011-2130.

[144] Pagitz M. et al., A morphing structure and method for morphing a structure. Netherlands, *2006936*. 2012 Dec 28.

[145] Pagitz M. et al., Compliant pressure actuated cellular structures. [Online].: *arXiv 1403.2197*; 2014 [cited 2015 August 06. Available from: http://arxiv.org/abs/1404.6448v1.

[146] Pagitz M. and Kappel E., Design of pressure actuated cellular structures. [Online]. 1403.4033v1: *arXiV*; 2014 [cited 2015 August 06. Available from: http://arxiv.org/abs/1403.4033v1.

[147] Pagitz M., Design of pressure actuated cellular structures. [Online].; 2015 [cited 2015 August 06. Available from: http://arxiv.org/abs/1403.4033.

[148] Pagitz M., Compliant pressure actuated cellular structures. [Online].; 2015 [cited 2015 August 06. Available from: http://arxiv.org/abs/1403.2197.

[149] Pagitz M. et al., A modular approach to adaptive structures. *Bioinspiration and Biomimetics*, vol. 9, no. 4. 2014 December: 046005.

[150] Pagitz M. et al., Shape-changing shell-like structures. *Bioinspiration and Biomimetics*, vol. 8, no. 1. 2013 March: Art.Nr.: 016010.

[151] Schimmelpfennig M. et al., Volumenausdehnung von Paraffinen aus Steigrohr-Messungen. *Jahrbuch für den Praktiker*, 2007 February: 417 - 429.

[152] Eschenauer H.A., The "Three Columns" for treating problems in optimum structural design. *Lecture Notes in Engineering*, vol. 47, 1989 June: 1-21.

[153] Wissmann J. et al., Finite Elemente in der Strukturmechanik. 1st ed. Berlin: Springer Verlag; 2006.

[154] Sun Z. et al., Modeling of fatigue damage in a polymer matrix composite. *Materials Science and Engineering A*, vol. 361, no. 1-2. 2003 November 15: 302-311.

[155] Hövelmann A. et al., Aerodyamic characteristics of the SAGITTA diamond wing demonstrator configuration. In *Deutscher Luft- und Raumfahrtkongress*; 2012; Berlin.

[156] Madsen H.A. et al., Implementation and test of the XFOIL code for airfoil analysis and design. Annual report. Risoe, Denmark: Forskningscenter Risoe, National Laboratory for Sustainable Energy; 1995 September. Report No.: ISBN 87-550-1830-0.

[157] da Rocha-Schmidt L. et al., A shape variable gap cover concept for aerodynamic control surfaces based on shear deformation. In *63. Deutscher Luft- und Raumfahrtkongress*; 2014; Augsburg.

[158] item24, item Industrietechnik GmbH. [Online].; 2016 [cited 2016 März 24. Available from: http://www.item24.de/.

[159] Wittel H. et al., Roloff / Matek Maschinenelemente. 20th ed. Wiesbaden: Vieweg+Teubner Verlag; 2011.

[160] Timoshenko S. et al., Theory of plates and shells. New York: McGraw-Hill Book Company; 1989.

[161] Festo AG & Co KG, Fluidic Muscle DMSP/MAS. [Online].; 2015 [cited 2015 December 7. Available from: https://www.festo.com/rep/en_corp/assets/pdf/info_501_en.pdf.

[162] Gramüller B. et al., PACS - Realization of an adaptive concept using pressure actuated cellular structures. *Smart Materials and Structures*, 2014 November 1: 115006.

[163] Bletzinger et al., A general finite element approach to the form finding of tensile structures by the updated reference strategy. *International Journal of Space Structures*, 1999 April 28.

[164] Wüchner R. et al., Stress-adapted numerical form finding of pre-stressed surfaces by the updated reference strategy. *International Journal for Numerical Methods in Engineering*, no. 64. 2005 May 9: 143-166.

[165] Kruzelecki J. et al., Shape and thickness optimization of thin-walled pressure vessel end closures. In *EngOpt 2012 – 3rd International Conference on Engineering Optimization*; 2012; Rio de Janeiro.

[166] Konzelmann et al., Freiformbarer DLR-Wabentank – Aufbau, Eigenschaften und Charakteristika des CNG-Tanks. In *VDI-Wissensforum Tank- und Kraftstoffführende*; 2014; Filderstadt.

[167] Gramüller B. et al., Shape-variable seals for pressure actuated cellular structures. *Smart Materials and Structures*, vol. 24, no. 9. 2015 July: Art.Nr.: 095005.

[168] Tempel A., Entwicklung und Umsetzung eines Konzeptes zur Bedruckung einer formvariablen Röhrenstruktur. Internal report. Braunschweig: German Aerospace Center, Luft- und Raumfahrt; 2014. Report No.: IB 131-2015/72.

[169] Delker A., Experimentelle Evaluierung von Konzepten zum axialen Verschluss druckaktuierter zellulärer Strukturen (PACS), sowie Anwendung am doppelreihigen Kragarmdemonstrator. Bachelor thesis. Braunschweig: TU Braunschweig, Maschinenbau; 2015.

[170] Wiedemann J., Leichtbau - Elemente und Konstruktion. 3rd ed. Springer-Verlag. Berlin: Springer-Verlag; 2007.

[171] Gramüller B. et al., Formveränderliche Verschlusskappe und Zelle. Germany, *application number 10 2015 102 189.7*. 2015 February 16.

[172] Fritz A.H. et al., Fertigungstechnik. 9th ed. Springer-Verlag. Berlin: Springer-Verlag; 2006.

[173] Westkämper E. et al., Einführung in die Fertigungstechnik. Wiesbaden: Vieweg+Teubner; 2010.

[174] Oceanz, http://www.oceanz.eu/. [Online].; 2015 [cited 2015 October 18. Available from: http://www.oceanz.eu/files/upload/11/oceanz-pa2200.pdf.

[175] Gramüller B. et al., Holistic design and implementation of pressure actuated cellular structures. *Smart Materials and Structures*, vol. Volume 24, no. Issue 12. 2015 December: Art.Nr.: 125027.

[176] Ylänen M. et al., Determining optimal operating pressure for AaltoRO - A novel wave powered desalination system. *Renewable Energy*, vol. 69, no. 1. 2014 April: 386-392.

[177] Cameron L. et al., Design of the next generation of the oyster wave energy converter. In *3rd International Conference on Ocean Energy*; 2010; Bilbao, Spain. 1-12.

[178] Folley M. et al., The design of small seabed-mounted bottom-hinged wave energy converters. In *Proceedings of the 7th European Wave and Tidal Energy Conference*; 2007; Porto, Portugal. 1265-1274.

[179] Gramüller B. et al., Wellenenergiewandler und Verfahren zur Wandlung von Wellenenergie. Germany, *patent application 102016207662.0*. 2016 May 3.

[180] Gramüller B. et al., Enhanced design methods for pressure-actuated cellular structures and evaluation. In *Sampe Long Beach 2016*; 2016; Long Beach, California. 1-16.

[181] Pepper D.W. et al., The finite element method - Basic concepts and applications. 1st ed. New York: Taylor & Francis Group; 2006.

[182] Stratasys, Engatech.com. [Online].; 2016 [cited 2016 April 24. Available from: http://engatech.com/wp-content/uploads/2015/11/ULTEM1010.pdf.

[183] DuPont, DuPont.com. [Online].; 2016 [cited 2016 April 24. Available from: http://dupont.materialdatacenter.com/profiler/7xKZv/material/pdf/datasheet/Hytrel7246.

[184] Kasperovich G. et al., Improvement of fatigue resistance and ductility of TiAl6V4 processed by selective laser melting. *Journal of Materials Processing Technology*, vol. 220, 2015 June: 202-214.